Imperial College London

Department of Chemical Engineering

Characterisation of Solute Transport in Heterogeneous Porous Media by Multidimensional Imaging and Modelling

Author

Takeshi Kurotori

Supervisor

Dr. Ronny Pini

A thesis submitted in fulfillment of the requirements for the degree of

Doctor of Philosophy

July, 2019

Declaration of Originality

I hereby declare that the PhD thesis, entitled: **Characterisation of Solute Transport in Heterogeneous Porous Media by Multidimensional Imaging and Modelling** is entirely my own work and is performed under the supervision of Dr. Ronny Pini at the Department of Chemical Engineering, Imperial College London. Any published works presented in this thesis are given full acknowledgements, as stated at the beginning of each chapter.

Copyright Declaration

Abstract

The study of solute transport in porous media continues to find applications in both traditional and emerging engineering problems, many of which occur in natural environments. Key applications include CO_2 sequestration, enhanced oil recovery and soil remediation. Transport is a fundamental component in the analysis of these systems, because it provides the driving force for physical and chemical interactions between the fluid and the solid phase. However, the inherent heterogeneity of the subsurface leads to what is classically referred to as anomalous transport, which challenges classic interpretations of both field and laboratory experiments. In this context, novel laboratory protocols are needed to probe transport in heterogeneous medium by measuring the spatial structure of the concentration field in the medium, rather than relying exclusively on the analysis of breakthrough curves (BTCs).

In this thesis, a combined experimental and modelling study of solute transport in a range of porous media has been presented, including sandstone and carbonate rocks, to cover a range of pore structures. At the core of the experimental work is the combination of two imaging methods, X-ray Computed Tomography and Positron Emission Tomography. While the former is used to characterise rock properties spatially, the latter allows visualising the temporal evolution of the full tracer plume within the medium in three dimensions. To this aim, a core-flooding system has been built to carry out pulse-tracer tests over a wide range of Péclet numbers ($Pe = 15 - 500$) using brine- and radio-tracers. In addition to the experiments on the three rock samples (Bentheimer Sandstone, Ketton Limestone and Edwards Carbonate), control experiments on uniform beadpacks were carried out to verify the accuracy of the in-situ measurements.

The experimental BTCs have been analysed in the framework of residence time distribution functions, which revealed mass transfer limitations in the microporous carbonates in the form of a characteristic flow-rate effect. Three transport models: the Advection Dispersion Equation (ADE), the Multi-Rate Mass Transfer (MRMT) and the Continuous Time Random Walk (CTRW) framework have been thoroughly evaluated with both the BTCs and the internal concentration profiles. It is shown that the ADE provides an accurate description of the results on the beadpack and the sandstone. The data on the carbonates are better described by the MRMT, which uses a fraction of stagnant, intra-granular pore space and an external fluid film resistance model to account for mass transfer between the flowing fluid and the porous particles. The CTRW theory, applied here for the first time to carbonate cores, provides a further improvement in describing the BTC, because of its ability to account for unresolved heterogeneities. In the application of the models, a distinction was made between parameters that are rocks-specific (e.g., the dispersivity) and those that depend on the flow rate, by treating the former as global fitting parameters in the optimisation routine. Accordingly, the obtained results provide a more consistent picture than what the current literature may suggest regarding the use of these models to the analysis of BTCs.

The dataset obtained from the PET has been used to quantify the extent and rate of mixing in the different porous media. The 3-D images clearly reveal the presence of spreading caused by subcore-scale heterogeneities. To quantify their effects on the core-scale dispersion, various measures has been used, namely the dilution index (Π), the spreading length-scale (K) and the intensity of segregation (I). It was observed that the microporosity has a pronounced effect on mixing, thereby greatly accelerating the time scale to reach the asymptotic regime. Notably, both Π and K scale vary linearly with the square-root of time, indicating the suitability of a Fickian-based model to quantify macrodispersion. This observation suggests that the strength of heterogeneity in the rock samples investigated is moderate and that anomalous transport has evolved to normal behaviour on a length-scale $\mathcal{O}(l) \sim 10$ cm ($\sim$ length of the samples). In this context, to provide a more comprehensive picture of anomalous transport in laboratory rock samples, future studies should aim at increasing the spatial resolution of the measurement. Non-invasive, imaging tools such as PET are likely to go a long way in addressing this problem and provide significant opportunities to advance our understanding of miscible displacements in consolidated porous media, thus including those involving additional phenomena, such as adsorption and chemical reactions.

Acknowledgements

Without any doubt, I would like to first acknowledge my supervisor, Dr. Ronny Pini for giving me the opportunity to start a new chapter of my life, and for always being there to support me throughout my Ph.D. I have learnt a lot from him in all aspects. My research would nothave been possible without him by any means.

I would like to thank Dr. Christopher Zahasky and Prof. Sally Benson for hosting my research visits at Stanford University. I am very thankful for their warm welcome and for sharing their fantastic PET facility to carry out the dynamic experiments. Most of the PET results presented would not have been possible without their kind assistance.

Special thanks to Dr. Saurabh Shah for the guidance with micro-CT scans, Mr. Vincenzo Cunsolo for the support associated with medical-CT imaging and Mr. Joshua Momodu for the mercury intrusion porosimetry measurements. I would also like to thank Dr. Nicholas Keat and Dr. Nathalie Matusiak at Imanova Ltd. for the indispensable help in preparing the radio-tracers, and for the discussions and guidance with the PET scans.

And of course, my colleagues in the Complex Porous Media group for all the discussions related to research, life, future..., and for their morale support. I would like to acknowledge (in alphabetical order): Humera Ansari, Emily Chapman, Anna-Maria Eckel, Alireza Hejazi, Junyoung Hwang, Nerine Joewondo, Caroline Jones, Lisa Joss, Rebecca Liyanage and Swapna Rabha for giving me all the great memories during my four years of Ph.D. I gratefully thank the project administrator, Bhavna Patel for the help with travel arrangements, purchase orders and for the friendship. She has been always approachable whenever needed.

I would like to express my greatest gratitude to my parents who have educated, encouraged and given me their full love and support to get me where I am today. I want to say my warmest thanks to my father. Even though you are very far away now, you are always in my heart. I owe you a lot.

Finally, I would like to acknowledge the funding through Qatar Carbonates and Carbon Storage Centre (QCCSRC) provided jointly by Qatar Petroleum, Shell, and the Qatar Science and Technology Park.

Publications

***Kurotori, T.**, Zahasky, C., Hosseinzadeh Hejazi, S. A., Shah, S. M., Benson, S.M., Pini, R. Measuring, imaging and modelling solute transport in a microporous limestone, Chemical Engineering Science 196 (2019) 366-383.*

***Kurotori, T.**, Zahasky, C., Benson, S. M., Pini, R. (2018). Three-Dimensional Imaging of Solute Transport in Reservoir Rocks by Positron Emission Tomography. 14th Greenhouse Gas Control Technologies Conference, Melbourne 21-26 October 2018 (GHGT-14).*

*Zahasky, C., **Kurotori, T.**, Pini, R., Benson, S.M. Positron emission tomography in water resources and subsurface energy resources engineering research, Advances in Water Resources 127 (2019) 39-52.*

*Wenning, Q. C., Madonna, C., **Kurotori, T.**, Pini, R. (2019). Spatial mapping of fracture aperture changes with shear displacement using X-ray computerized tomography. Journal of Geophysical Research: Solid Earth, under review.*

***Kurotori, T.**, Zahasky, C., Benson, S. M., Pini, R. Modelling solute transport in laboratory rock cores using continuous time random walk and multi-rate mass transfer models, to be submitted.*

***Kurotori, T.**, Zahasky, C., Benson, S. M., Pini, R. Experimental observations of the spatial structure of the concentration field during solute transport in microporous rocks by positron emission tomography, under preparation.*

Table of Contents

List of Figures

List of Tables

List of Symbols

a	correlation length	a	specific surface area (Chapter 7)
A	cross-sectional area	A_{Bq}	radioactivity in becquerel
A_p	surface area of a particle	c	solute concentration (decay-corrected)
$\widetilde{c}$	solute concentration (predicted)	c_{D}	solute concentration (detected)
c_{o}	feed concentration	c_{p}	solute concentration in the micropores
c^{PET}	solute concentration (PET)	CT_{air}	CT number of air
CT_{water}	CT number of water	$\overline{CT}_{\mathrm{dry}}$	CT number of core saturated with air
$\overline{CT}_{\mathrm{wet}}$	CT number of core saturated with water	d	core diameter
d_{e}	equivalent grain diameter	d_{p}	grain diameter
D^0	tracer diffusion coefficient	$\mathbf{D}_h$	hydrodynamic dispersion tensor
D_{L}	longitudinal dispersion coefficient	$\mathbf{D}_m$	mechanical dispersion tensor
D_{T}	transverse dispersion coefficient	D_{TH}	horizontal transverse dispersion coefficient
D_{TV}	vertical transverse dispersion coefficient	D_ψ	dispersion coefficient (CTRW)
$\mathcal{D}$	molecular diffusion coefficient	$\mathcal{D}_{\mathrm{eff}}$	effective diffusion coefficient
e^+	positron	e^-	electron
E	RTD function	E_Θ	normalised RTD function
f_j	fraction of micropore volume in grain class j per unit of micropore volume	${}^{18}_{9}\mathrm{F}$	fluorine isotope
$\mathbf{g}$	gravitational acceleration vector	G	Gravity number
h	sample thickness	I	intensity of segregation
I_f	transmitted X-ray beam intensity	$\mathbf{I}$	identity matrix
I_o	initial X-ray beam intensity	J	objective function (optimiser)
$\mathbf{j}_{\mathrm{adv}}$	advective flux vector	$\mathbf{j}_{\mathrm{diff}}$	diffusive flux vector
$\mathbf{j}_h$	hydrodynamic dispersion flux vector	$\mathbf{j}_m$	dispersive flux vector
k	permeability along flow direction	k_{m}	effective mass transfer coefficient

k_o	overall mass transfer coefficient	K	spreading length scale
$\mathbf{k}$	permeability tensor	K_corr	concentration correction factor (PET)
l	characteristic length scale	L	core length
M	mass of tracer	$\tilde{M}$	Memory function (CTRW)
M_μ	mobility ratio	N_A	Avogadro number
N_g	number of grid points (model)	N_j	number of grain classes (model)
N_p	number of data points	N_q	number of flow rates (optimiser)
N_v	number of voxels	$^{18}_{8}\mathrm{O}$	oxygen isotope
p	pressure	p_conf	confining pressure
P_j	probability distribution function of solute mass	P_c	capillary pressure
Pe	Péclet number, $v\alpha/\mathcal{D}$	$\mathrm{Pe}_{\mathrm{d_p}}$	Péclet number, $vd_\mathrm{p}/\mathcal{D}$
Pe_ψ	Péclet number, $v_\psi d_\mathrm{p}/\mathcal{D}$	q	volumetric flow rate
r_p	pore throat radius	Re	Reynolds number
Sc	Schmidt number	Sh	Sherwood number
S_nw	non-wetting phase saturation	S_w	wetting phase saturation
t	time coordinate	T	truncation time (CTRW)
t_1	mean transit time of solute particles (CTRW)	$t_{1/2}$	radioisotope half-life
t_2	"cutoff" time (CTRW)	t_adv	advection time scale
t_diff	diffusion time scale	t_D	dead time
t_i	time frame	$\mathbf{u}$	superficial velocity vector
$\mathbf{v}$	interstitial velocity vector	$\overline{v}$	interstitial velocity in the direction of flow
v_e	neutrino	v_ψ	transport velocity (CTRW)
V_core	volume of core	V_D	dead volume
V_inj	tracer volume injected	V_p	volume of a particle
V_plug	volume of a small plug	V_vox	voxel volume
$\underline{x}$	3-D space coordinate	z	space coordinate along the direction of flow
α	dispersivity	α_L	longitudinal dispersivity
α_T	transverse dispersivity	α_ψ	longitudinal dispersivity (CTRW)
β	extent of heterogeneity (CTRW)	γ	gamma photon
γ_surf	surface tension	Γ	dilution index

Δp	pressure drop	Δt	time interval
Δx	grid size (model)	$\Delta\widetilde{\Pi}$	dilution index deviation
$\Delta\rho$	density difference	ε	relative error
Θ	normalised time (pore volume)	Λ	average sorption rate (CTRW)
μ	fluid viscosity	μ_1	solute viscosity
μ_2	solvent viscosity	μ_I	linear attenuation coefficient of X-ray beam
ξ	tortuosity	Π	normalised dilution index (reactor ratio)
$\widetilde{\Pi}$	scaled reactor ratio	ρ	fluid density
ρ_{env}	bulk density	ρ_{sk}	skeletal density
σ	inhomogeneity factor	σ_{Δ_n}	CT noise
σ_{ϕ_n}	porosity uncertainty (X-ray CT)	σ_ψ	inhomogeneity factor (CTRW)
ς^2	second moment of concentration	τ	mean residence time (theoretical)
τ_{c}	dimensionless time, $t_{\mathrm{diff}}/t_{\mathrm{adv}}$	τ_{exp}	mean residence time (experimental)
τ_{inj}	mean residence time of injection pulse	ϕ	intergranular porosity
ϕ_{p}	intragranular porosity	ϕ_{T}	total porosity
ϕ_{vox}	voxel-level porosity	ϕ_{z}	slice-averaged porosity
Ψ	sphericity index		

List of Abbreviations

ADE	Advection Dispersion Equation
BS	Bentheimer Sandstone
BTC	breakthrough curve
CCS	Carbon Capture and Storage
CT	Computed Tomography
CTRW	Continuous Time Random Walk
DDMT	Dual Domain Mass Transfer
EB	Edwards Brown Carbonate
EOR	enhanced oil recovery
fADE	Fractional Advection Dispersion Equation
FBP	filtered back projection
FOV	field of view
GA	Genetic algorithm
GSD	grain size distribution
GUI	Graphical User Interface
KL	Ketton Limestone
LOR/VOR	line of response/ volume of response
MIM	Mobile-Immobile model
MIP	mercury intrusion porosimetry
MRI/NMR	Magnetic Resonance Imaging/Nuclear Magnetic Resonance
MRMT	Multi-rate Mass Transfer
ODE	ordinary differential equation
OSEM	ordered subsets expectation maximisation
PDF	probability density function
PET	Positron Emission Tomography
PSD	pore size distribution

PV	pore volume
REV	representative elementary volume
RV	Random Walk theory
SNR	signal to noise ratio
SPECT	Single Photon Emission Computed Tomography

Chapter 1

Introduction

The study of flow and transport in porous media is relevant to many large-scale industrial operations, with applications spanning from chemical engineering (e.g. deep filtration (Herzig et al., 1970), mass transport through membranes (Brenner and Gaydos, 1977) and gel chromatography (Knox, 1999)) to subsurface (geo)engineering. The latter are the main scope of this thesis and include the spreading of contaminants in soils during groundwater flow (Bredehoeft and Pinder, 1973), the geological sequestration of CO_2 for Carbon Capture and Storage (CCS) (Bui et al., 2018), and solvent (such as N_2, CO_2, steam or water) injection into oil reservoirs for Enhanced Oil Recovery (EOR) (Muggeridge et al., 2013). Due to the inherently complex characteristics of geologic formations, it remains very challenging to accurately predict fluid transport in the subsurface. Challenges include accounting for patterns of heterogeneity over a wide range of length-scales, complicated pore structures (with pores as small as a few nanometers), and coupled physical phenomena, such as transport with chemical reactions that may significantly alter the porous network of the rock. While field tests are essential to ensure the viability of the given operation at scale, laboratory experiments are needed to shed light on flow mechanisms in complex porous systems and on their controls.

The goal of this PhD project is to improve our fundamental understanding of solute transport in heterogeneous and microporous porous media. As described in Chapter 2, studies on using representative core samples are very limited as compared to those using unconsolidated systems (e.g. sand-packs), accordingly, dataset of transport coefficients shows significant scatter. Most signif-

icantly, the technical difficulty of probing the mixing process within three-dimensional porous media has so-far precluded a thorough experimental investigation of the role of heterogeneities on solute transport. A rigorous assessment of mixing in complex porous media, such as rocks, is of crucial importance, because it provides the driving force for chemical reactions that take place in subsurface flows, such as mineral dissolution and/or precipitation.

To fill this gap of knowledge, in this PhD work, a novel experimental approach has been developed and deployed that integrates conventional pulse-tracer tests with the simultaneous imaging of flows. The imaging techniques used are X-ray Computed Tomography (X-ray CT) and Positron Emission Tomography (PET). While the former is nowadays widely applied to quantify non-destructively the local distribution of volumetric (and static) properties within opaque porous media (e.g. saturation and porosity), PET enables the dynamic imaging of flow pathways and the associated mixing and spreading processes in three dimensions. Notably, PET is a known technology in the medical imaging field, but its use in the geosciences for quantitative studies has not received much attention. In this context, studies are needed that use a range of rock materials and fluids to evaluate the potential of PET to address challenging problems in subsurface transport.

1.1 Thesis outline

In Chapter 2, the fundamental theories governing solute transport processes during miscible displacement in porous media are described. A review of the existing literatures is presented, including both numerical and experimental techniques to characterise solute transport in laboratory cores and the main research gaps are identified.

One of the major aspects of novelty of this thesis is the utilisation of a combination of multiscale imaging techniques to allow full access to properties and processes within an opaque porous medium. In Chapter 3, the working principles of the three instruments deployed in this study, namely (i) micro X-ray CT, (ii) medical X-ray CT, and (iii) PET are presented. This is followed by the description of the methodology proposed for image reconstruction, processing and the characterisation of various spatial and temporal properties of rocks. To better highlight the performance of PET for characterising the spatio-temporal evolution of concentration distributions

of a solute plume, quantitative and qualitative comparisons of the results are made on two rock cores, against that obtained by classical X-ray CT.

Chapter 4 presents the multi-functional core-flooding system that has been designed and commissioned for the pulse-tracer tests performed in this thesis. Specifically, details are presented for the custom-made aluminum core-holder, and the various ancillary components mounted in the flow loop. This chapter describes also the key design factors considered to conduct pulse tracer tests, including the choice of fluid pair, gravitational and viscous effects, dead volume and excess dispersion analysis, and a evaluation of experiment operating conditions. To support this discussion, results from calibration tests are presented.

In Chapter 5, results are presented and discussed for a set of control experiments conducted on a well-defined granular beadpack. To this aim, we applied (i) micro X-ray CT to characterise grain size distribution, (ii) clinical X-ray CT to quantify 3-D porosity distribution, and (iii) a series of pulse tracer tests (with the Péclet numbers, $25 < \mathrm{Pe} < 250$) coupled with PET to dynamically image the temporal and spatial distribution of solute plume in 3-D. The obtained results are then systematically evaluated using (i) material balance calculations, (ii) residence time distribution (RTD) analysis, (iii) tracer effluent history and internal concentration profiles, and (iv) measures of global mixing state. The experimental data are also verified against the classic Advection Dispersion Equation (ADE).

In Chapter 6, an integrated multiscale, multidimensional experimental approach is presented to characterise the structural complexity of the three rock samples to be used in the pulse-tracer experiments, including Bentheimer Sandstone, Ketton Limestone and Edwards Brown Carbonate. Helium pycnometry, Mercury Intrusion porosimetry and micro X-ray CT were applied to estimate properties, such as skeleton and bulk density, sphericity index, as well as and grain and pore size distributions of mm-size plug. Medical X-ray CT was also applied to obtain a distribution of porosity values of larger cores at a spatial resolution of about 8 mm^3.

Chapter 7 and 8 present a systematic investigation of "anomalous" transport observed on the three characteristic rock cores using breakthrough curve analysis. The dataset includes pulse-tracer tests carried out over a wide range of Péclet numbers, i.e. $\mathrm{Pe} \approx 15-500$. The experimental observations are interpreted by using three transport models, namely the Advection Dispersion

Equation (ADE) and the Multi-rate Mass transfer Model (MRMT) (Chapter 7), and the Continuous Time Random Walk theory (Chapter 8).

The 3-D dynamic behaviour of the spatial structure of the concentration field obtained from PET is evaluated in Chapter 9. In particular, the temporal evolution of the solute plume within the three rock samples used in this study is quantified by various mixing measures, such as the concentration probability density function, the dilution index, the intensity of segregation and the spreading length scale. The experimental observations are compared to predictions obtained from the one-dimensional models discussed in the previous chapter, thereby providing a unique opportunity to test their predictive capability. A new spreading measure is also presented that is on the concept of dilution index to assess the extent of incomplete mixing in heterogeneous porous media.

In Chapter 10, the main achievements of this PhD thesis are summarised and suggestions for future work are presented.

Chapter 2

Background and Literature Review

This chapter provides an overview of the key mechanisms that characterise the transport of solute during miscible displacements in porous media. The fundamental theories used in the modelling of solute transport in a porous medium, including the governing equations are introduced. A literature review is then presented in the following subjects, which are closely associated with the work performed in this PhD thesis:

1. Modelling of anomalous transport in heterogeneous and microporous rocks
2. Experimental measurements of solute dispersion in rocks including sandstones and carbonates
3. Multidimensional imaging techniques used for the characterisation of solute transport in porous media

2.1 Classification of rocks

Geological porous media are predominated by sandstone and carbonate formations, with each of them accounting for about 50% of the world total oil reserves (Perrodon, 1983). They are known as sedimentary rocks and have been formed over millions of years by deposition and accumulation of sediments in deltas, river estuaries, and in marine environments (i.e. seas or oceans), followed by burial and compaction. Such rocks consist of grains made of minerals

and organic materials, and of crystalline cement that binds the grains together (Mathur, 2008). Fine-grained clay-sized particles (i.e. the matrix) may also be present within the interstitial pore space between the grains. A schematic diagram illustrating the fundamental components that can be found in a sedimentary rock is depicted in Figure 2.1.

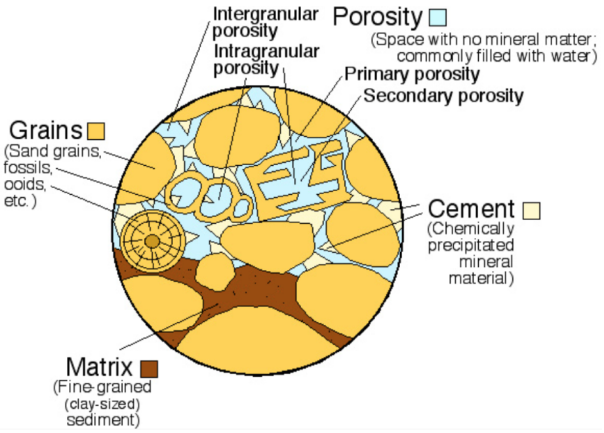

Figure 2.1: The four fundamental components present in a sedimentary rock, namely porosity, grains, matrix and cement. Figure taken from Martinez (2016).

2.2 Key mechanisms of solute transport in porous media

2.2.1 Advection

Advection refers to the transport of solutes due to the fluid's bulk motion and is driven by the advective hydraulics of the displacing fluid. The advective flux is given by:

$$\mathbf{j}_{\text{adv}} = \mathbf{v}c \tag{2.1}$$

and the corresponding advective transport equation reads as:

$$\frac{\partial c}{\partial t} = -\nabla \mathbf{j}_{\text{adv}} \tag{2.2}$$

where $\mathbf{v}$ is the velocity vector field with components (v_x, v_y, v_z), c is the solute concentration (a scalar, $c = c(x, y, z)$) and t is the time coordinate. The symbol, ∇ refers to the vector differential operator.

2.2.2 Hydrodynamic dispersion

Classically, mixing in a porous medium is characterised by means of hydrodynamic dispersion (Bear, 1972). The latter is a process that affects miscible flows in a porous medium, e.g. by effectively smearing out displacement fronts. The study of dispersion has attracted significant interest in various disciplines and it is treated at length in a large number of textbooks on fluid flow in porous media (e.g. (de. Marsily, 1986; Sahimi et al., 1986; Bear, 1972; Dullien, 1992; Fetter, 1999)). According to Bear (1972), one of the earliest works of dispersion phenomena was presented by Slichter (1905), who used electrolyte solutions as a tracer to track the movement of groundwater. There, it was observed that the tracer downstream of a given injection point gradually spreads and occupies an ever-increasing portion of the flow field. This phenomenon is referred to as dispersion and results into local variations of the tracer concentration (Bear, 1972).

The underlying microscopic mechanisms that are associated with hydrodynamic dispersion are molecular diffusion and mechanical dispersion, which are traditionally lumped together into a single parameter called hydrodynamic dispersion coefficient, $\mathbf{D}_h$:

$$\mathbf{D}_h = \mathcal{D}\mathbf{I} + \mathbf{D}_m \tag{2.3}$$

where $\mathcal{D}$ and $\mathbf{D}_m$ are the molecular diffusion and mechanical dispersion coefficient, respectively. $\mathbf{I}$ is the identity matrix. The hydrodynamic dispersion coefficient is a second-order tensor, which in a three-dimensional Cartesian coordinate system takes the form:

$$\mathbf{D}_h = \begin{bmatrix} D_{h,xx} & D_{h,yx} & D_{h,zx} \\ D_{h,xy} & D_{h,yy} & D_{h,zy} \\ D_{h,xz} & D_{h,yz} & D_{h,zz} \end{bmatrix} \tag{2.4}$$

When the direction of the dispersion is aligned with the direction of the velocity field, this tensor can be simplified to:

$$\mathbf{D}_h = \begin{bmatrix} D_{\mathrm{L}} & 0 & 0 \\ 0 & D_{\mathrm{TH}} & 0 \\ 0 & 0 & D_{\mathrm{TV}} \end{bmatrix} \tag{2.5}$$

where D_{L} is the *longitudinal* hydrodynamic dispersion coefficient (i.e. parallel to the direction of flow), and D_{TH} and D_{TV} are the horizontal and vertical transverse hydrodynamic dispersion coefficient (i.e. perpendicular to the direction of flow), respectively.

Molecular diffusion, is independent of fluid velocities, is associated with the random motion of molecules (Brownian motion), and is driven by a concentration gradient. In general, such process can be represented by the Fick's first law; in vector notation, the equation is given by:

$$\mathbf{j}_{\mathrm{diff}} = -\mathcal{D}\nabla c \tag{2.6}$$

where $\mathbf{j}_{\mathrm{diff}}$ denotes the diffusive flux vector, and ∇c is the concentration gradient vector. In porous systems, a so-called *effective* diffusion coefficient is used to account for the tortuous nature of the pore space, i.e.

$$\mathcal{D}_{\mathrm{eff}} = \frac{\mathcal{D}\phi}{\xi} \tag{2.7}$$

where ϕ is the porosity and ξ is the tortuosity ($\xi > 1$). The *effective* diffusion coefficient is always less than that of molecular diffusion coefficient as diffusion along the tortuous path is greater (Dullien, 1992).

The second mechanism, mechanical dispersion, refers to the tendency for fluids to spread out from the bulk flow due to variations in the advective velocity at the pore scale. In a porous medium, different "streamline" velocities can be caused by a number of baseline microscopic characteristics of the pore space:

- Effect of pore lengths causing some fluid particles to follow a more direct path than other fluid particles.
- Effect of pore-wall friction causing velocity fluctuations within a single pore throat. This is analogous to solute transport through a circular pipe where a parabolic velocity profile were shown (Taylor, 1953) (referred to as the Taylor dispersion). It has also been demonstrated from pore-scale modelling that the dispersion is higher in the pores where wall friction is greater (Bijeljic et al., 2004).
- Different pore dimensions resulting in local variations of fluid velocity.

Mathematically, the process resulting from mechanical dispersion is treated in a similar manner as for molecular diffusion, where a constant mechanical dispersion coefficient ($\mathbf{D}_m$, independent of concentration) is assumed:

$$\mathbf{j}_m = -\mathbf{D}_m \nabla c \tag{2.8}$$

Where $\mathbf{j}_m$ denotes the dispersive flux of solute. In the literature, the *hydrodynamic* dispersion flux, $\mathbf{j}_h$, is usually defined, which combines diffusion and mechanical dispersion (Bear, 1972):

$$\mathbf{j}_h = -(\mathbf{D}_m + \mathcal{D}\mathbf{I})\nabla c = -\mathbf{D}_h \nabla c \tag{2.9}$$

2.3 Governing equations for solute & solvent transport

At the pore scale, the transport of fluids can be correctly described using Navier-Stokes equations. In practice, these equations are solved by combining them with a model that enables the reconstruction of the pore space of a given porous medium. The most predominant methods used in the literature are pore-network models (i.e. (Fatt, 1956; Blunt, 2001; Valvatne and Blunt, 2004)) and direct numerical simulation (DNS) (i.e. (Pan et al., 2004; Boek and Venturoli, 2010; Ramstad et al., 2012)). Both models are based on simulating the free flow field by using the pore space information obtained from imaging techniques, such as X-ray computed microtomography. While DNS simulate transport through the three-dimensional pore space obtained directly from these images, the pore-network models use the topologically equivalent network of pores (Blunt, 2001).

The application of these approaches on a larger scale ($\mathcal{O} \sim 1$ cm and above) is still out of reach, because of the associated computational costs (Xiong et al., 2016). Moreover, at the core scale, revealing detailed information of the pore geometry is not trivial (Dentz et al., 2011). Accordingly, the pore scale transport equations are upscaled by averaging the effective parameters over a Representative Elementary Volume (REV), which is *"the smallest volume over which a measurement can be made that yields a value that is representative of the whole"* (Hill, 1963). For random bead-/sand-packs, that is about $5 \times 5 \times 5$ grains (Clausnitzer and Hopmans, 1999) whereas a much larger REV is expected for rocks (i.e. $\sim 11 \times 11 \times 11$ grains for Berea sandstone (Pini and Madonna, 2016)). Until now, a number of upscaling methods

have been proposed; some common approaches include volume averaging (Whitaker, 1999) and homogenisation theories (Hornung, 1997).

When Reynolds number is less than unity (typical for reservoir flows). Darcy's equation can be derived to describe fluid flow through porous media at the continuum scale:

$$\mathbf{u} = -\frac{\mathbf{k}}{\mu}(\nabla p - \rho \mathbf{g}) \tag{2.10}$$

Where $\mathbf{u}$ is the flux (discharge per unit cross-sectional area); ∇p is the pressure gradient vector; μ and ρ are the fluid viscosity and density, respectively; $\mathbf{g}$ is the gravitational acceleration vector and $\mathbf{k}$ is the permeability tensor. The flux, $\mathbf{u}$, is often referred to as the Darcy velocity, which is related to the pore (interstitial) fluid velocity by:

$$\mathbf{v} = \frac{\mathbf{u}}{\phi} \tag{2.11}$$

Traditionally, the flow of a solute through a porous medium is described by the well-known Advection Dispersion Equation (ADE). The ADE, in the absence of chemical reaction, in its three-dimensional form (Cartesian coordinate system) reads,

$$\frac{\partial c}{\partial t} = -\nabla \cdot (\mathbf{v}c - \mathbf{D}_h \nabla c) \tag{2.12}$$

The first term on the right hand side of Eq. 2.12 represents the advection term, while the second term describes mass transport due to hydrodynamic dispersion. The underlying assumption of the advection dispersion approach is that hydrodynamic dispersion obeys Ficks law, and it is treated as a constant parameter, being spatio-temporally independent (Dullien, 1992). In the literature, hydrodynamic dispersion coefficient has found to be a function of velocity, and the general expression for the hydrodynamic dispersion (i.e. Eq. 2.3) can be rewritten by the following form (Bear, 1972):

$$D_j = \mathcal{D}_{\text{eff}} + \alpha_j \overline{v} \quad \text{with} \quad j = \text{L, T} \tag{2.13}$$

Where the subscript j denotes the longitudinal and transverse components of dispersion. $\overline{v}$ is the mean interstitial velocity in the principal direction of flow. The constant, α_j is the dispersivity,

which is a measure of the heterogeneity of a pore space and can therefore be interpreted as a characteristic property of the porous medium. For solute transport in unconsolidated systems (e.g. random bead-/sand-packs), the longitudinal/transverse dispersivites can be directly related to the microscopic properties of the porous medium, such as the mean particle diameter (Perkins and Johnston, 1963). For consolidated systems (e.g. sandstones and carbonates rocks), this reconciliation is less straightforward, partly because the mean grain diameter looses significance; this is discussed further in the sections below.

2.3.1 Different flow regimes in porous media

The study of hydrodynamic dispersion can be mapped into different flow regimes, depending on the dominant mechanism of transport. The latter is defined by the dimensionless Péclet number, which describes the ratio between advection and diffusion over a given distance, l (the so-called characteristic mixing length scale) (Sahimi et al., 1986), i.e:

$$\mathrm{Pe} = \frac{\overline{v}l}{\mathcal{D}} \tag{2.14}$$

For homogeneous systems, such as unconsolidated bead-/sand-packs, the average grain diameter, d_p has been commonly used as the characteristic length scale, l (Perkins and Johnston, 1963). However, the definition remains unresolved for rocks, where different metrics have been proposed, including the average pore/grain diameter (Legatski and Katz, 1967), the dispersivity, α_L (Honari et al., 2013), as well as the correlation length of a porous medium (Bijeljic et al., 2013). For diffusion-dominated transport ($\mathcal{O}(\mathrm{Pe}) \sim 10^{-1}$) (Perkins and Johnston, 1963)), the advective term in Eq. 2.13 can be removed, and the following expression is obtained:

$$\frac{D_j}{\mathcal{D}} = \frac{\phi}{\xi} \tag{2.15}$$

At larger Péclet numbers ($\mathcal{O}(\mathrm{Pe}) \sim 10^{1}$) (Perkins and Johnston, 1963)), the transport is governed by advection,

$$\frac{D_j}{\mathcal{D}} = \frac{\alpha_j \overline{v}}{\mathcal{D}} = \sigma \mathrm{Pe} \tag{2.16}$$

where $\alpha_j = \sigma l$ and σ is a constant parameter that relates the characteristic length scale of the porous medium l to the core-scale dispersivity ($0.5 < \sigma < 1.2$ for uniform sand-/bead-packs, while $\sigma > 1$ for rocks (Perkins and Johnston, 1963; Pini and Madonna, 2016; Zahasky and Benson, 2018)). Generally, reservoir flows can be characterised by both transport regimes (Pini and Krevor, 2019).

2.4 Adapting dispersion concepts in rocks

2.4.1 Asymptotic and preasymptotic transport in porous media

Although hydrodynamic dispersion represents a practical and widely adopted concept for characterising mixing during miscible displacements, the quantification of dispersion coefficients requires careful appraisal, particularly for heterogeneous porous media. As outlined in Section 2.2, hydrodynamic dispersion results from microscopic variations in the fluid velocity within the pores of the medium which in turns lead to spatial and temporal non-uniformity in the cross-sectional pore concentration profiles (Dentz et al., 2018). The term, "incomplete mixing" has been introduced to describe this phenomenon (Le Borgne et al., 2011). Most significantly, the common perception is that the solute particles need to travel a given number of pores within the medium in order to reach local concentration equilibrium. The latter determines the scale at which the transport can be characterised by an average quantity (Berkowitz et al., 2006). This is known as the asymptotic condition and is more commonly referred to as the Fickian scale, because it defines the condition for the correct application of the classical Fickian-based transport approach. The establishment of asymptotic regime is a consequence of diffusion process which acts to effectively 'homogenise' microscopic velocity variations, similar to the behaviour that is observed in the flow through a channel (as demonstrated in the work presented by Taylor (1953)). In the so-called preasymptotic regime (also referred to as non-Fickian regime), the dispersion coefficient is found to increase over time and distance travelled (Han et al., 1985; Berkowitz et al., 2000; Bijeljic and Blunt, 2006), and it therefore does not represent the proper quantitative measure to describe solute mixing (Tartakovsky et al., 2008; Battiato et al., 2009; de Anna et al., 2013).

The complex nature of rocks is such that the argument above can be applied also at scales

larger than the pore, from the core- up to the field-scale. At these scales spatial variations in the permeability are responsible for variations in fluid velocity in the medium and introduce length-scale effects in the hydrodynamic dispersion coefficient. In general terms, these can be associated with the characteristic time- and/or length- scales of the system under study, namely:

$$\text{for advection time scale:} \qquad t_{\text{adv}} = \frac{l}{v} \tag{2.17a}$$

$$\text{for diffusion time scale:} \qquad t_{\text{diff}} = \frac{l^2}{2\mathcal{D}} \tag{2.17b}$$

where v is the interstitial fluid velocity, t_{adv} and t_{diff} are the times needed for a solute particle to traverse a characteristic length scale, l by advection and diffusion, respectively. Accordingly, the dimensionless parameter, i.e. $l^* = t_{\text{diff}}/t_{\text{adv}}$ is introduced to define the critical time-(or length-) scale at which the transport of solute has reached into an asymptotic regime. In other words, l^* defines the support scale at which the representative elementary volume (REV) is assumed to be well-mixed. In a porous medium, a REV scale is typically selected such that the porosity can be well-defined (Dullien, 1992). One of the objectives of this study is to quantify this scale for the description of solute transport in consolidated rock samples used in core analysis ($\mathcal{O}(l) \sim 1$ cm$-$1 m).

2.4.2 Limits of advection dispersion approach

The classic method of characterising solute transport relies on the use of advective-dispersion approach. This is applicable to homogeneous systems and/or to porous media where heterogeneity has a uniform spatial distribution. In these situations, the transport process can be fully described by means of a single parameter (i.e. dispersivity) (Dullien, 1992). As pointed out in the previous section, this situation is rarely encountered in the subsurface, because rocks exhibit geologic heterogeneities at all scales (from nanometer to meters) with correlation lengths often approaching the size of a laboratory samples (Murphy et al., 1984). This gives rise to what is commonly referred to as "anomalous" transport (Dentz et al., 2011). The latter is used to describe any behaviour that cannot be captured by the advection-dispersion equation (ADE), which treats dispersion in a way fully analogous to diffusion in Fick's law (Neuman and Tar-

takovsky, 2009). In fact, the anomalous behaviour in rocks has been readily demonstrated across the full range of relevant spatial scales, from the interpretation of tracer tests in the field (e.g. Adams and Gelhar (1992); Cirpka and Kitanidis (2000b); Gouze et al. (2008b)) to the analysis of unidirectional miscible displacements in laboratory samples (e.g. Silliman and Simpson (1987); Walsh and Withjack (1994); Pini et al. (2016)). Due to the additional "macrodispersion" effects caused by heterogeneity, it has been unequivocally shown that hydrodynamic dispersion alone does not prove to be a sufficient measure for characterising the mixing process in rocks (Kitanidis, 1994; Dentz et al., 2011; Le Borgne et al., 2011), primarily because it does not contain information on the spatial structure of the concentration field within the medium (Le Borgne et al., 2011). Knowledge of the actual distribution of solutes represents an essential need for the accurate estimation of chemical and physical interactions between fluids and between the fluids and the rocks (Cirpka et al., 2008; Rolle et al., 2009; Dentz et al., 2011; Chiogna et al., 2011b). Some typical examples of these chemical processes include the convective dissolution of CO_2 rich brine in saline aquifers (Liyanage et al., 2019), ion adsorption on mineral surfaces (Sposito et al., 1999), and precipitation/dissolution of $CaCO_3$ in carbonate reservoirs (Berkowitz et al., 2003); they are all triggered by mixing between two miscible fluids. However, obtaining such information with the level required for quantitative analysis is not trivial, and represents an experimental challenge, as demonstrated in later sections.

2.4.3 Concepts of spreading, mixing & dilution

While hydrodynamic dispersion reveals the transport mechanisms that originate from the microscopic processes within the pores (shown in the left of Figure 2.2), the transport of solute in a heterogeneous porous medium at larger scales can be described by two processes, i.e. spreading and mixing (or dilution), thereby introducing an additional mechanism to describe the "macrodispersion" phenomenon. As can be demonstrated from a snapshot of an evolving tracer plume inside a bi-layered beadack shown in Figure 2.2, spreading gives rise to plume deformation (change in the overall shape of the plume), while mixing results in smoothing out of the concentration gradient (discolouring of the solute plume). In other words, the former controls the spatial distribution of the solute plume due to local velocity variations, mixing governs the spatial distribution of the solute within the plume. In Figure 2.3 are shown the four conceptual

concentration maps that illustrate how a tracer pulse injected into a hypothetical heterogeneous porous medium can be affected by different transport mechanisms at the continuum scale.

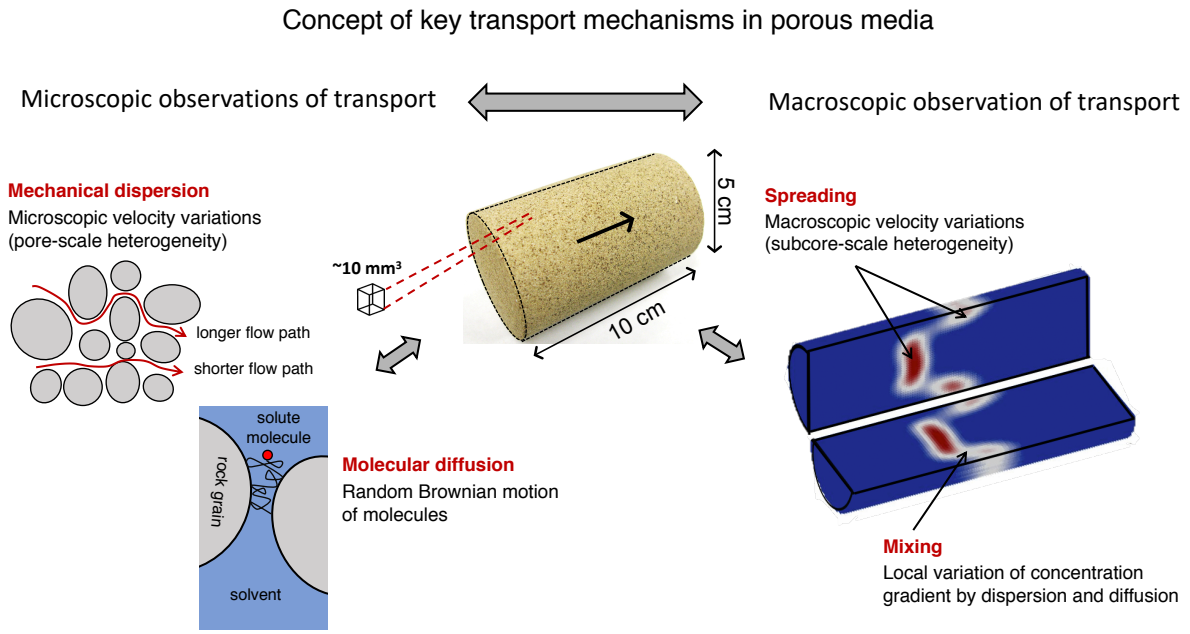

Figure 2.2: Snapshots of different characteristic transport mechanisms that can be observed at different scales of measurements. The image on the right represents a snapshot of an evolving tracer plume within a bi-layered beadpack.

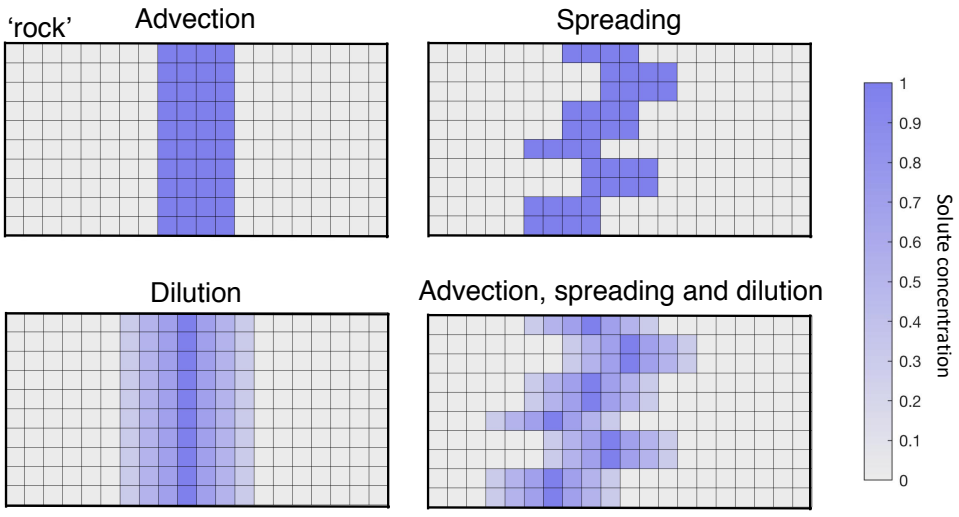

Figure 2.3: Conceptual diagram illustrating the different mechanisms of transport present in a porous medium during solute transport.

2.5 Modelling anomalous transport in rocks

The reliability of the measured dispersivity coefficient in rocks relies heavily on the numerical approach used. This is evidenced by the recent works of Honari et al. (2013, 2015), where the obtained dispersivity varied significantly depending on how the experimental dataset is interpreted, i.e. $\alpha_{\mathrm{L}} = 0.063 - 0.159$ (Ketton Limestone) and $\alpha_{\mathrm{L}} = 0.057 - 0.120$ cm (Estaillades Limestone). In the literature, many theories have been proposed to describe the processes that govern the experimental observations of anomalous phenomena. These methods can be subdivided into two main categories, namely stochastic (probabilistic) and deterministic approaches.

The continuous time random walk (CTRW) framework appears to be one of the most widely used theory to predict dispersive flows in heterogeneous porous media. There, the transport problem is modelled as a stochastic process, meaning that the movement of solute particles in the porous medium is treated as a random variable in time and space. The distribution of latter is associated with a probability density function (PDF), that can be determined, depending on the nature of the system, or the behaviour of the breakthrough curve measured (Berkowitz et al., 2006). In the CTRW formalism, the Fickian assumption no longer holds because the impacts of microscopic (pore-scale) heterogeneities are accounted by a series of 'slow' and 'fast' movements of solute particles controlled by the density function (Cortis and Berkowitz, 2005). Similar to other stochastic approaches, the effective quantities, such as concentration represent an ensemble average, and therefore is best applied to transport problems when the heterogeneity of a system exhibit no clear spatial correlations (i.e. statistically 'homogeneous' medium) (Levy and Berkowitz, 2003). The application of CTRW in a deterministic manner (e.g. by accounting the spatial distribution of heterogeneities within the size of interest) remains an ongoing research (Berkowitz et al., 2006). In the literature, the use of CTRW framework to interpret dispersion in rocks is very scarce, with only few validation works against simulation results computed from pore-scale modelling on a Berea sandstone (Bijeljic and Blunt, 2006) and on a Portland limestone (Bijeljic et al., 2011); these numerical studies were limited to a cubic sample with the side length of about 3 mm. To best of our knowledge, the work by Cortis and Berkowitz (2005) presents the only study where experimental measurements of solute transport in laboratory rock cores are interpreted in the context of CTRW. Other effective (stochastic) transport formulations, such

as the fractional advection-dispersion equation (fADE, e.g. (Benson et al., 2000; Metzler and Klafter, 2000)) and the multi-rate mass transfer (MRMT, e.g. (Coats et al., 1964; Haggerty and Gorelick, 1995)) approach, has proven to be the special form of the CTRW (Berkowitz et al., 2006). Briefly, the fADE approach models the spatial and temporal distribution of solute particles by means of modifying the fractional derivative in the classical ADE. The order of the fractional derivative, also known as the Lévy index varies between $1 - 2$, which is governed by the nature of a breakthrough curve (BTC). In contrast, the MRMT model introduces an additional term to the ADE to account for the mass transfer resistance that arises between the bulk fluid and the microporous regions where the transport are assumed to be immobile. The MRMT model has been commonly used to describe transport in carbonates; these rocks are in fact characterised by the presence of both inter- and intra-granular porosity, the latter enabling mass exchange only by diffusion. Yet, the fraction of stagnant pore space is often let to depend on the fluid velocity (Baker, 1977; Batycky et al., 1982; Bretz and Orr, 1987; Honari et al., 2015) and the physical meaning of the obtained parameter values has therefore been questioned (Yellig and Baker, 1981). Further details of the MRMT theory can be found in Chapter 7.

Solute transport in heterogeneous porous media has also been extensively interpreted using the streamtube approach (e.g. Simmons et al. (1995); Cirpka and Kitanidis (2000a); Ginn (2001)). The latter assumes fluid transport to take place in a series of streamtubes characterised by different travel times (Kitanidis et al., 2012). In this case, mixing occurs within each streamtube in one direction where instantaneous (complete) mixing is assumed, whereas mass transfer between the streamtubes is neglected. The ADE is solved for each streamtube independently, and the effluent concentration profile is then obtained by integrating the average concentration of each streamtube over the entire system. Amongst others, the most referred techniques are the stochastic convective streamtube approach (e.g. (Ginn et al., 1995)) and the advective-dispersive streamtube approach (e.g. (Cirpka and Kitanidis, 2000a)). The difference is that the former does not account for the effect of longitudinal dispersion within each streamtube (Simmons et al., 1995). The underlying assumption of the model is that non-Fickian behaviour originate from tracer spreading caused by macroscopic heterogeneity, which are effectively captured by the different streamtube velocities. However, this is done at the cost of neglecting mixing between them. As a practical consequence, this may lead to significant underestimation

of mixing (Cirpka and Kitanidis, 2000a), particularly for mixing-controlled systems, i.e. microporous rocks. Traditionally, the distribution of the streamtube travel times are characterised by a probability density function, that is often obtained from the mathematical technique, known as deconvolution of a tracer effluent curve (Kitanidis et al., 2012).

More recently, an approach has been proposed to generate streamtubes in a rock sample based on the (known) permeability field (Pini et al., 2016). Driven by the development of non-invasive imaging techniques, a permeability map can nowadays be generated from capillary-pressure measurements during core-flooding experiments and the use of the J-Leverett scaling relationship (Pini and Benson, 2013). This (deterministic) streamtube approach represents a departure from earlier studies that rely on stochastic information and the combination with *in situ* imaging techniques allows for a direct link between the transport parameters (e.g. hydrodynamic dispersion) and the spatial heterogeneity of rocks.

2.6 Dispersion experiments in rocks

The traditional approach for quantifying transport properties of rocks relies on the use of laboratory tracer tests coupled with a numerical or analytical solution of a transport model. In such tests, a tracer is injected in the inlet core of a porous system in the form of a pulse- or step-change in the concentration, and the BTCs are measured with time. Hydrodynamic dispersion coefficient is used as a fitting parameter, so as to obtain a best match between measured and predicted concentration values. A practical implication of anomalous transport is that the tracer BTCs are characterised by asymmetry and long tailing of the concentration at late times. As an example of general validity, Figure 2.4 presents a set of such observations found in the BTCs for a Berea sandstone core and a Ketton carbonate sample. As shown, while the ADE fails at describing the experimental BTCs, the non-Fickian models, such as the CTRW and the MRMT models outlined in the previous section, provide much better descriptions of the experimental dataset. However, the puzzling observation here is that there is an evident lack of consistency in the choice of the method used to describe experiments on a given rock type. For the most typical rock core used in laboratory dispersion measurements, i.e. Berea Sandstone, all the modelling approaches described above have been reported; the corresponding range of

dispersivity values spans almost one order of magnitude ($\alpha_L = 0.04 - 0.4$ cm), as evidenced in a collection of literature data reported in Table 2.1.

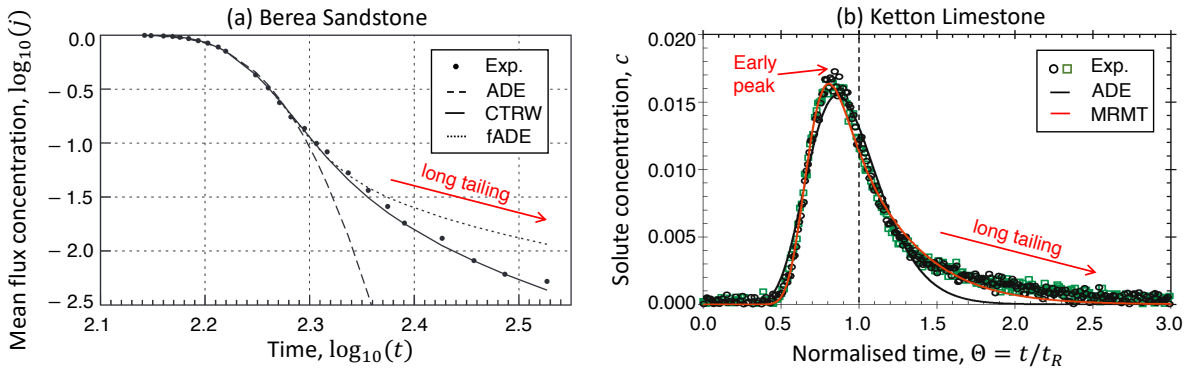

Figure 2.4: Examples of literature effluent breakthrough curves measured on (a) Berea Sandstone and (B) Ketton Limestone, following a step and a pulse injection of solute into the cores, respectively. The figure is used to demonstrate the anomalous transport behaviour of rocks, in which the classic ADE model fail to describe. The results are presented as log-transformed time over mean flux concentration for (a) and reduced time (normalised by the mean residence time of solute particles) over concentration for (b). The symbols refer to the experimental measurements whereas the lines are the ADE or the non-Fickian models described in Section 2.5. The plots are adapted from Cortis et al. (2004) (figure a) and Honari et al. (2015) (figure b), respectively.

Table 2.1: Longitudinal (α_L) and transverse (α_T) dispersivity measured from tracer tests in cylindrical cores of Berea sandstone (B-S) using both liquids (liq.) and gases (gas). The Péclet number is defined as $\mathrm{Pe}_\alpha = v\alpha/\mathcal{D}$ or $\mathrm{Pe} = vd_p/\mathcal{D}$ The following values are assumed: bulk diffusion coefficients $\mathcal{D}$(gas) $= 1 \times 10^{-4}$ cm^2/s, $\mathcal{D}$(liquid) $= 1 \times 10^{-5}$ cm^2/s and rock's grain diameter, $d_p = 150$ μm. The size of the samples are reported as $d \times L$(diameter $\times$ length). Table adapted from Pini and Krevor (2019).

Fluid	$d \times L$ [cm^2]	Pe_α [–]	Pe [–]	α_L [cm]	α_T [cm]	Reference
liq.	4×76	1-34	3-101	–	0.005	Grane (1961)
gas	3.8×60	60-443	7-48	0.14	–	Legatski and Katz (1967)
liq.	3.8×25	300	11	0.40	–	Donaldson et al. (1976)
liq.	5×23	131-1270	7-71	0.27	–	Baker (1977)
gas	7.6×18	0.4-35	0.04-3	0.17	–	Batycky et al. (1982)
liq.	1.25×14	9-2268	1-243	0.14	–	Hulin and Plona (1989)
liq.	2×6	2-103	0.3-14	0.11	–	Gist et al. (1990)
gas	3.8×10	0.03-3	0.01-1	0.04	–	Honari et al. (2015)
liq.	5×9	61-155	9-23	0.10	–	Pini et al. (2016)
liq.	7.6×20	0.1-29	0.5-100	–	0.004	Boon et al. (2017)

This uncertainty affects also experimental observations on carbonate rocks, which have been studied less extensively. In fact, characterisation of dispersion in carbonate rocks is additionally challenged by the existence of more complex pore structures (Bijeljic et al., 2013), trimodal pore size distribution, thus exhibiting intra-granular porosities (sub-micron pores within grains) and/or macroscopic vugs (visible pore space that are significantly bigger than the corresponding

grains or crystals) (Lucia, 1983). The study of miscible displacements in laboratory cores of carbonate rocks started in the 1970s, with the work by Brigham (1974); Baker (1977); Spence and Watkins (1980) who conducted a series of tracer tests over a range of Péclet numbers. The MRMT model was applied to describe the tracer tests, resulting in much larger dispersivity values as compared to sandstones (up to 25 times higher when compared to a Berea Sandstone). This work was extended by Bretz and Orr (1987); Bretz et al. (1988), by reporting the first attempt to evaluate the impacts of small-scale heterogeneity on solute transport. The conclusion from these studies is that the connectivity of the pore space and the wide pore size distributions (PSDs) are responsible for the early breakthrough and the pronounced concentration tails, respectively. A different mechanism was indicated by Gist et al. (1990), who found that a wide PSD does not induce early breakthrough nor the long time tail in carbonates. In this study, the effluent profiles of less heterogeneous carbonate samples (Austin chalk and Indiana limestone) having a wider bimodal pore-size distribution did not show pronounced tailing, while anomalous behaviour was observed in carbonate rocks with significant fine scale (mm) heterogeneities.

Another discrepancy that highlights the complex nature of carbonate rocks is the discussion on the velocity dependency of the dispersion coefficient. While some authors have shown that the relationship can be approximated by a linear function (Brigham, 1974; Baker, 1977; Spence and Watkins, 1980; Bretz and Orr, 1987; Bretz et al., 1988), others have used a power-law correlation between dispersion coefficient and fluid velocity, i.e. $D_{\mathrm{L}} \propto v^n$ with the exponent, n that increases with increasing heterogeneity of the porous medium (e.g. $n = 1 - 1.4$) (Gist et al., 1990; Bijeljic et al., 2004, 2011; Honari et al., 2015). As a direct consequence of the inconsistencies revealed in the literature, a significant scatter in the dispersion dataset has been reported for carbonate rocks, i.e. longitudinal dispersivity coefficients: $\alpha_{\mathrm{L}} = 0.05 - 4.35$ cm (Gist et al., 1990; Baker, 1977; Brigham, 1974; Spence and Watkins, 1980; Bretz and Orr, 1987; Honari et al., 2015) (data collated from 6 literature sources on 15 core samples).

To resolve these discrepancies, different experimental approaches have been proposed. In the early work by Hulin and Plona (1989); Leroy et al. (1992), the "dispersion-echo" technique has been applied, in which a tracer-pulse was injected into the sample and the flow was reversed after a finite time. There, they used a packed-bed of a stratified porous medium and a relatively homogeneous rock core (i.e. Berea sandstone) and demonstrated that the extent of the

solute plume is partly recoverable, leading to smaller values of dispersivity. Similar techniques have also been adapted to measure tracer effluent profiles at the field-scale (Liu et al., 2010; Hansen et al., 2016; Schroth et al., 2000; Shakas et al., 2016) (known as push-pull or single-well injection-withdraw tracer tests). Alongside these studies, efforts have been made to develop multidimensional techniques that allows direct and dynamic visualisation of the solute plume inside a porous medium. Some of the recent works include bench-scale (transparent) tank experiments (packed with sand- or glass-beads) that involve monitoring of a dye tracer imaged by high-speed cameras (Zinn et al., 2004; Catania et al., 2007; Trevisan et al., 2015, 2017) or measurements based on optical transmission technologies (Zinn et al., 2004; Haberer et al., 2011). While these investigations provide valuable insights on the fundamental transport mechanisms occurring at the pore- and subcore-scale, they are limited to 2-D, and therefore, present a major challenge for studying anisotropic rocks. Moreover, the optical measurements constrain the medium of interest to only translucent materials, e.g. glass-beads (Zinn et al., 2004).

2.7 *In situ* visualisation of core-scale solute transport in rocks using imaging techniques

One of the major limitations in the classical characterisation of hydrodynamic dispersion is that spreading and mixing cannot be easily decoupled. This is attributed to the fact that it is inherently difficult to infer what is happening inside a porous medium. To complement the understanding from tracer breakthrough analysis, recent advancements include the implementation of multidimensional imaging techniques, which enable direct observations of the evolution of the solute plume within the porous medium in both space and time. Techniques that can be used to obtain this information include X-ray Computed Tomography (X-ray CT), nuclear magnetic resonance imaging (MRI/NMR) and more recently nuclear emission imaging methods, such as Positron Emission Tomography (PET) and Single Photon Emission Computed Tomography (SPECT). Above all, X-ray CT is by far the most widely applied in geological applications, and has nowadays become an integral part of core-analysis workflows (Akin and Kovscek, 2003; Shafer, 2013). Standard protocols have been established using X-ray CT to quantify the spatial variability of various physical characteristics of rocks (e.g. porosity, permeability), the distribu-

tion (e.g. saturation) of fluids pumped through them, as well as the interactions between them (e.g. capillary pressure-saturation relationship), both at the pore- (e.g. Bertels et al. (2001); Blunt et al. (2013); Berg et al. (2016)) and subcore-scale (e.g. Krause et al. (2009); Pini et al. (2012); Krause et al. (2013); Pini and Benson (2013)). While being a proven technology in the medical field, the advancement of X-ray CT has contributed significantly to the current understanding of challenging geological problems such as how CO_2 can be trapped into saline aquifers or how oil reserves can be extracted more effectively from the reservoir. Alongside these, X-ray CT has also been occasionally used to visualise plume migration during miscible and immiscible displacements in both sandstones (Toshiya et al., 2000; Berg et al., 2013) and carbonates (Hidajat et al., 2004; Fourar and Radilla, 2009; Ott et al., 2015). However, the main challenges are the achievement of the required temporal resolution and of sufficient image contrast without disturbing the flow field. As a matter of fact, X-ray CT can only be applied to capture fluid movement at very slow flow rates (e.g. (Ott et al., 2015) used a flow rate of 0.45 ml/min). Although more recent scanners provide much quicker time resolution ($\mathcal{O} \sim 10$ s to image a full core with length of about 15 cm with our in-house scanner, Toshiba Aquilion 64 TSX-101A), a dopant (e.g. a heavy salt, such as potassium iodine, KI) is often needed to enhance the image contrast between the two fluids. As demonstrated in the next chapter, this does not provide sufficient resolution to study miscible displacements in rocks quantitatively, particularly for systems that experience significant mixing. At such conditions, unwanted buoyancy effects may also arise that would inherently affect the displacement behaviour. Furthermore, the application of MRI/NMR methods to study geologic materials is limited by the presence of paramagnetic species (such as clays, pyrite), which can largely distort the quality of the obtained 3-D images (Reeves and Chudek, 2001; Nestle et al., 2003; Gladden and Mitchell, 2011).

In comparison, PET, a nuclear imaging technique, offers the potential to overcome these issues by providing a spatial resolution comparable to clinical X-ray CT instruments ($\mathcal{O} \sim 1$ mm), while requiring minimal doses of radiotracer ($\mathcal{O} \sim 10^{-12} - 10^{-13}$ mol/mL) and enabling high temporal resolution ($\mathcal{O} \sim 10$ s) (Gründig et al., 2007; Boutchko et al., 2012; Ilankoon et al., 2013; Fernø et al., 2015a). Recent years have seen an increased use of PET to the study of flow and transport processes in various geomaterials, including bead-, soil- and sand-packs (Degueldre et al., 1996; Kulenkampff et al., 2008; Fernø et al., 2015b; Kulenkampff et al., 2015; Dogan et al., 2017;

Lippmann-Pipke et al., 2017), and sandstones (Ogilvie et al., 2001; Goethals et al., 2009; Fernø et al., 2015a; Pini and Madonna, 2016; Zahasky and Benson, 2018). A more comprehensive list of the PET works to date, and their corresponding core samples investigated for the dynamic imaging of solute transport is provided in Table 2.5. In general, these studies have been primarily qualitative, with the intention to demonstrate the capability of PET to visualise fluid flows inside opaque porous media. However, only recently have experimental studies been validated against predictions by numerical models (e.g. (Boutchko et al., 2012; Lippmann-Pipke et al., 2017)) and/or used for quantitative evaluations, such as to characterise local fluid saturations (Fernø et al., 2015a; Zahasky and Benson, 2016) or to quantify the dispersion in rocks (Pini and Madonna, 2016; Zahasky and Benson, 2018). As it can be seen in Table 2.5, a broad range of radiotracers are used; they have been mainly selected according to the time each experiment takes, making it a system dependent variable. In other words, the half-life of the chosen radiotracer should be long enough to carry out scans and to be detected to produce valuable imaging results. However, questions remain unanswered on how these radiotracers interact with the system (i.e. between the rock and the fluid). This is particularly important for rocks with high geochemical reactivity, such as carbonates, which have been rarely studied (see Table 2.5). Above all, to standardise the use of PET, efforts are needed to first test a range of rock samples and fluids to evaluate the potential of PET as a quantitative tool to study spreading and mixing in heterogeneous porous media, thereby, providing a complement to the information gathered from X-ray CT, which is inherently limited to static properties. A more detailed review of the PET imaging technique applied in the context of water resources research can be found in our recent publication in Zahasky et al. (2019).

Radioisotope	**Half-life**	**Scanner series**	**Sample**	**Reference**
^{11}C	20.3 mins	Siemens Biograph PET-CT	Berea sandstone	(Pini et al., 2016)
		Siemens Biograph PET-CT	Bentheimer sandstone	(Fernø et al., 2015b)
^{68}Ga	67.7 mins	custom-built	Crystalline rock	(Degueldre et al., 1996)
		custom-built	Granodiorite rock	(Maguire et al., 1997)
^{18}F	109.7 mins	Siemens ECAT PET	sandpacks	(Khalili et al., 1998; Boutchko et al., 2012)
		Siemens Biograph PET-CT	natural sediments	(Thorpe et al., 2019)
		Siemens Inveon MicroPET	Berea sandstone	(Zahasky and Benson, 2018; Vasco et al., 2018)
		Siemens ECAT PET	Granite fracture	(Kulenkampff et al., 2008)
		unclassified	Hopeman sandstone	(Ogilvie et al., 2001)
		Siemens ECAT PET	Ledian sandstone	(Goethals et al., 2009)
		Siemens ECAT PET	naturally fractured shale	(Maucec et al., 2013)
		Mediso nanoScan PET/CT	fractured Edwards Carbonate	(Brattekås et al., 2016; Brattekås and Seright, 2018)
		Siemens Inveon MicroPET	Vesicular basalt	(Zahasky et al., 2018)
		Siemens Inveon MicroPET	fractured Bentheimer sandstone	(Hu et al., 2017)
^{64}Cu	12.7 hrs	custom-built	porous building materials	(Hoff et al., 1996)
		Siemens ECAT PET	soil column	(Gründig et al., 2007)
		ClearPET (by Raytest)	soil column	(Kulenkampff et al., 2018)
		ClearPET (by Raytest)	soil column	(Kulenkampff et al., 2018)
^{99m}Tc	6.01 hrs	GE Millenium SPECT	sediment column	(Boutchko et al., 2012)
^{55}Co	17.53 hrs	Siemens ECAT PET	Ledian sandstone	(Goethals et al., 2009)
^{124}I	4.2 days	Siemens ECAT PET	Granite fracture	(Kulenkampff et al., 2008)
^{22}Na	2.6 yrs	Siemens Biograph PET-CT	Outcrop chalks	(Fernø et al., 2015a)
		Siemens Biograph PET-CT	Bentheimer Sandstone	(Fernø et al., 2015a)
		ClearPET (by Raytest)	Opalinus clay	(Kulenkampff et al., 2016; Lippmann-Pipke et al., 2017)

Figure 2.5: List of literatures that used PET to study miscible displacement in porous media

Chapter 3

Imaging Methods

- Some of the material covered in this chapter has been published in ***Kurotori, T.**, Zahasky, C., Hosseinzadeh Hejazi, S. A., Shah, S. M., Benson, S.M., Pini, R. Measuring, imaging and modelling solute transport in a microporous limestone, Chemical Engineering Science 196 (2019) 366-383.*
- The analysis performed in section 3.2.3 has been published in *Zahasky, C., **Kurotori, T.**, Pini, R., Benson, S.M. Positron emission tomography in water resources and subsurface energy resources engineering research, Advances in Water Resources 127 (2019) 39-52.*

3.1 Chapter summary

In this chapter, details of the imaging methods deployed as part of this PhD thesis are explained. To summarise, three different types of imaging techniques have been utilised, namely (i) micro X-ray Computed Tomography (CT), (ii) medical X-ray CT and (iii) Positron Emission Tomography (PET). These have been applied for the *in situ* characterisation of rock spatial properties at (i) pore- (μm) and (ii) subcore-scale (mm), and (iii) of the real-time evolution of tracer plume during pulse tracer tests. The working principles of each imaging technique is outlined, to provide a fundamental understanding of the capabilities and limitations of the methods proposed. The performance of the scanners in resolving the spatial distributions of the rock structural properties and the dynamic transport processes have been evaluated in terms of uncertainty analysis and

experiment reproducibility. The signal-to-noise (SNR) analysis between PET and X-ray CT has been carried out to highlight the complementarity of these two techniques, particularly in the context of imaging solute transport in porous media. Details of the scanners used, including the scanner parameters, reconstruction methods and image processing protocols are also discussed.

3.2 Multiscale imaging techniques

Image analysis and reconstruction have been carried out using AVIZO-9 (ThermoFisher Scientific) for the dataset acquired using micro-CT, while in-house MATLAB routines have been used for the image processing of PET and medical-CT scans.

3.2.1 X-ray CT imaging

X-ray CT is based on the attenuation of X-rays through a medium; a narrow beam of X-rays produced from a X-ray tube on one side of the sample is passed through the object and reaches the detector at the opposite side with less intensity as a result of X-ray attenuation. The latter is parametrised by means of a linear attenuation coefficient μ_I, as defined by the Beer-Lambert law (Pedrotti et al., 2007):

$$I_f/I_o = \exp(-\mu_I h) \tag{3.1}$$

where I_o is the initial intensity of the X-ray beam; I_f is the detected value after the beam passes through an homogenous sample of thickness h. For each attenuation event, the linear attenuation coefficient is measured in one volume element (voxel). By rotating either the sample (for a micro-CT scanner) or the X-ray source and the detector around the object (for a medical-CT scanner), multiple projections of the same 2-D slice are measured, that are combined to obtain the linear attenuation coefficients of each voxel within a 2-D slice. 2-D images of different slices are then stacked together to produce a 3-D reconstruction of the specimen. Typically, the CT attenuation value of each voxel is represented on the image projections as gray scale (Curry et al., 1990), which is a function of the average bulk density (electron density) and effective atomic number of the given voxel. For CT scanning (X-ray energies larger than 100 kV), where Compton scattering is the predominant interaction, linear attenuation coefficient can be assumed to be only linearly

dependent on the bulk density. However, for energies levels below 100 kV or materials with high atomic number, the contribution of photoelectric absorption increases rapidly and thus this assumption no longer holds (Akin and Kovscek, 2003). This is the case when dopants (e.g. a heavy salt, such as potassium iodine, KI) are used to enhance the attenuation contrast between two fluids in the CT scans. In such cases, a dedicated calibration may be required. Further details on the theories of X-ray CT in the context of petroleum engineering research can be found in Akin and Kovscek (2003).

Micro CT imaging

Tomographic images of dry cylindrical plugs with volume, $V_{\text{plug}} \approx 0.2$ cm^3, have been acquired for all the rock cores used in the pulse tracer tests (e.g. Bentheimer Sandstone, Ketton Limestone and Edwards Brown Carbonate). This was done with a Versa XRM-500 X-ray micro-CT scanner (ZEISS), with images taken at raw voxel resolutions of (4.3×4.3×4.3) μm^3 for Ketton Limestone, and (9.9×9.9×9.9) μm^3 for Bentheimer Sandstone and Edwards Brown Carbonate. For each system, two set of micro-CT scans are performed along the axial direction of the sample; these images are then stitched together to produce a complete imaging dataset, giving a total of $1000^3 - 2000^3$ voxels. The following scanning parameters have been applied: 80kV of voltage, 7W of power, and a total of 3000 projections being collected for each tomographic image. The micro-CT images have been reconstructed using the built-in algorithm provided by Zeiss, and are processed using AVIZO-9 software, so as to estimate properties, such as porosity and the rock grain size distributions (GSDs) presented in Section 5.2.

In this work, a general method is proposed to extract these properties, which involves the following key operations using AVIZO-9. First, the reconstructed cross-sectional greyscale images are segmented into two phases (i.e. zeros: the pore phase and ones: the solid phase) by applying the watershed algorithm; this involves defining a suitable threshold, which is relatively straightforward, due to the clear contrast between the two phases. Porosity can then be estimated by simply counting zeros and ones (Pini and Madonna, 2016). Next, each grain is differentiated using a Separation toolbox, i.e. *separate object*; this transforms the 2-D segmented images into individual 3-D particles. The last step of the analysis is "cleaning" of the imaging dataset. This involves (i) removing the incomplete grains around the edges of the images, and (ii) eliminating

the trace particles that are smaller than the equivalent diameter, $d_e = 40\mu$m. The latter step is performed because these small particles are considered to be imaging artefacts, as demonstrated in Menke et al. (2015). Data cleaning is achieved by implementing *border kill* and *remove small spots* operations in the software. The validity of the proposed method has been verified by using a well-defined porous medium, i.e. granular glass beads (SiLibeads®, supplied by VWR, UK) (see Chapter 5 for details).

Medical CT imaging

Tomographic images of dry and the water-saturated core samples were acquired with a Toshiba Aquilion 64 TSX-101A clinical X-ray CT scanner for Bentheimer Sandstone and Edwards Brown Carbonate, whereas the corresponding scans of beadpacks and Ketton Limestone were obtained using a Universal Systems HD-350 X-ray CT scanner. The distribution of the total (intra- and inter-granular) voxel porosity, ϕ_{T} can be computed as follows (Pini and Madonna, 2016):

$$\phi_{\mathrm{T}} = \frac{\overline{CT}_{\mathrm{wet}} - \overline{CT}_{\mathrm{dry}}}{CT_{\mathrm{water}} - CT_{\mathrm{air}}} \tag{3.2}$$

where CT refers to the CT number in Hounsfield units of the pure fluids (air, -1000 HU and water, 0 HU); $\overline{CT}$ is the value assigned to any given voxel in the system, which therefore includes contributions from the rock grains in addition to either air or water. The latter are obtained by taking CT scans with the rock saturated with dry air and water, respectively. The following set of imaging parameters has been applied, tube current: 200 mA, energy level of radiation: 120 kV, display field of view (FOV): (512×512) voxels, with voxel dimension of $(0.5 \times 0.5 \times 1)$ mm^3 for the Universal Systems scanner or $(0.1 \times 0.1 \times 1)$ mm^3 for the Toshiba scanner. The images have been reconstructed using the reconstruction filter "body", with standard kernel.

As described in Pini et al. (2012), the noise associated with medical X-ray CT scanning can be readily determined by following the standard rules of error propagation, using the expressions below:

1) For the CT noise:

$$\sigma_{\Delta_n} = \frac{\sqrt{2}\sigma_{\mathrm{vox}}}{\sqrt{n}} \tag{3.3}$$

2) For the porosity uncertainty:

$$\sigma_{\phi_n} = \frac{\sqrt{2}\sigma_{\text{vox}}}{\sqrt{n}(CT_{\text{water}} - CT_{\text{air}})} \approx \frac{\sigma_{\Delta_n}}{1000} \tag{3.4}$$

Where σ_{Δ_n} and σ_{ϕ_n} are the standard deviations obtained from subtracting two independent CT images that represent distribution of voxel CT and porosity values, respectively; σ_{vox} is the standard deviation associated to each voxel and n is the number of repeated scans. The assumption is done here that the measurements are affected by random errors, which is commonly the situation for X-ray CT scans, as explained in Pini et al. (2012); Pini and Madonna (2016). As an example of general validity, Figure 3.1 shows the CT noise (or the porosity uncertainty in the secondary y-axis), plotted as a function of number of inverse square root of repeated scans, $1/\sqrt{n}$, for the result obtained on a Ketton Limestone core. Three different reconstructions of voxel resolutions have been considered in the analysis, i.e. (0.5×0.5×1), (1×1×1) and (2×2×2) mm^3. The dash-dotted lines are the predictions using Eqs. 3.3 and 3.4 while the measurements of CT noise at one selected cross-sectional slice (corresponding the the centre of the core) are given as symbols. The shaded regions correspond to the uncertainties in the cross-sectional slices computed over the entire length of the core ($L = 10$ cm). As it can be seen in the figure, the CT noise yields a narrow span in the data at each $1/\sqrt{n}$, depending on the axial location of the core (given by width of the shaded regions). This is primarily due to the differences in the material density along the axial axis of the core (caused by spatial heterogeneity). For this reason, a slightly larger scatter is attained for more heterogeneous rocks, i.e. Edwards Brown Carbonate ($\Delta\sigma_{\Delta_n} \approx 3$ HU vs $\Delta\sigma_{\Delta_n} \approx 2$ HU, compared at $n = 1$ with voxel size of (0.5×0.5×1) mm^3). It is also indicated in the figure that the CT noise can be readily reduced by considering the following two scenarios: (i) by subtracting images over increased number of repeated scans, and/or by (ii) coarsening the voxel sizes. For quantitative analysis presented in this work, the raw CT images were resampled into voxels with a dimension of (2×2×2) mm^3, thus allowing the noise to be reduced to about 1.0% (or 10 HU). Notably, the predicted result gives an excellent match with the experimental dataset, thereby confirming the random nature of the uncertainty in the CT measurements.

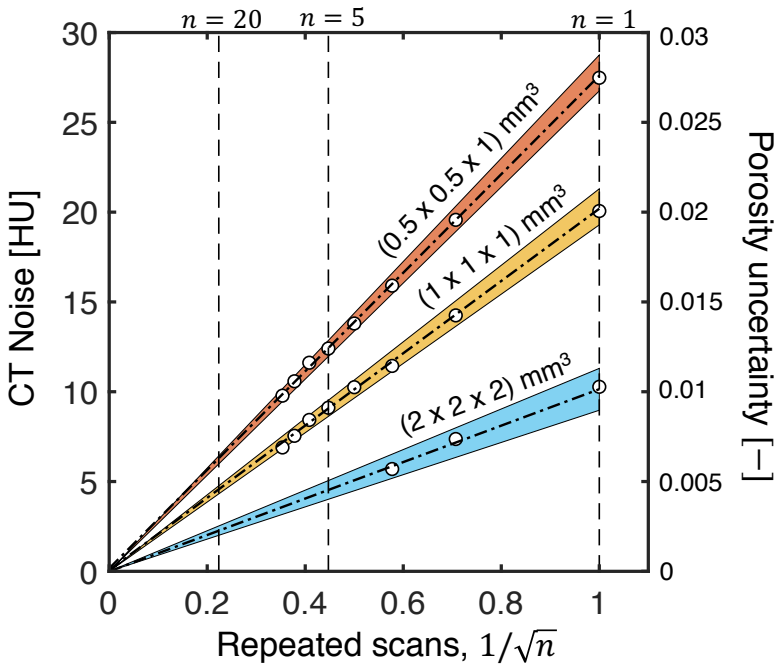

Figure 3.1: CT and porosity noise associated with X-ray CT scans on a Ketton Limestone core, plotted as a function of number of repeated scans, $1/\sqrt{n}$. Three different voxel resolutions have been considered in the analysis, namely (0.5×0.5×1), (1×1×1) and (2×2×2) mm^3. The circles are the experimental results obtained for one cross-sectional slice (in the x-y plane), while the shaded regions correspond to the uncertainty range computed from all the cross-sectional slices for the entire core. The lines are the predictions obtained from Eqs. 3.3 and 3.4.

3.2.2 PET imaging

Positron Emission Tomography (PET) is based on the injection of positron emitting radionuclides to image chemical and or biological processes. To explain the physics of PET scanning, we can consider three main processes (Bailey et al., 2005; Turkington, 2011):

Positron decay and annihilation

The very first stage of a PET scan is known as positron decay. It occurs when a positively charged positron (e^+) is emitted from an unstable nucleus (the radionuclide) to balance out the atomic charge. The emitted positron looses kinetic energy by exciting and ionising nearby atoms and will, eventually, interact with a single electron when all kinetic energies have been lost. This interaction is called annihilation and results in the emission of two 511 keV gamma photons (γ) in opposite directions. As an example of general validity, the decay of an $^{18}_{9}$F radionuclide (the

primary radioisotope used for tracer tests in this study) can be represented by:

$$^{18}_{9}\mathrm{F} \rightarrow {}^{18}_{8}\mathrm{O} + e^{+} + v_e + \text{energy} \tag{3.5a}$$

$$e^{+} + e^{-} \rightarrow \gamma + \gamma \tag{3.5b}$$

Coincidence detection

These pairs of high-energy photons are detected by a three-dimensional cylindrical array of ring detectors located along the axial field of view (FOV) of a PET scanner. These detectors make use of the concept that the two gamma photons (γ) detected within a very short time frame by two opposite detectors are likely to come from the same annihilation event (typically with a defined time threshold in the order of nanoseconds (Bailey et al., 2005)). This is known as "coincidence event" which is assumed to occur somewhere along the line connecting the two detectors, referred to as the line-of-response (LOR). However, because the ring detectors attached to a PET scanner have finite surface area, it is more appropriate to conceptualise these "lines" as three-dimensional parallelepiped surfaces, which can therefore be referred to as the volume-of-response (VOR) (Kinahan et al., 2004). Millions of these coincidence events are recorded in a PET scan as raw dataset, enabling the reconstruction of time-lapse images that present the spatial distribution of radioactivity within the specimen.

Image reconstruction

The following steps are required during image reconstruction: (i) random coincidences and dead-time corrections (ii) attenuation correction, and (iii) detector normalisation (Bailey et al., 2005). The spatial resolution of a PET image is limited to about 2.5 mm and 1 mm in clinical and pre-clinical instruments, respectively (Levin and Hoffman, 1999; Moses, 2011). While the spatial resolution is largely governed by the physical size of the detector element (Moses, 2011), it is also effectively limited by the fundamental physics of the positron annihilation and detection process; this includes the errors associated with non-collinearity, positron range, lost events, scattered coincidence and random coincidence events, as demonstrated in the conceptual diagram shown in Figure 3.2. Further details on the theory of PET are beyond the scope of this thesis, and can

be found in our recent publication (Zahasky et al., 2019).

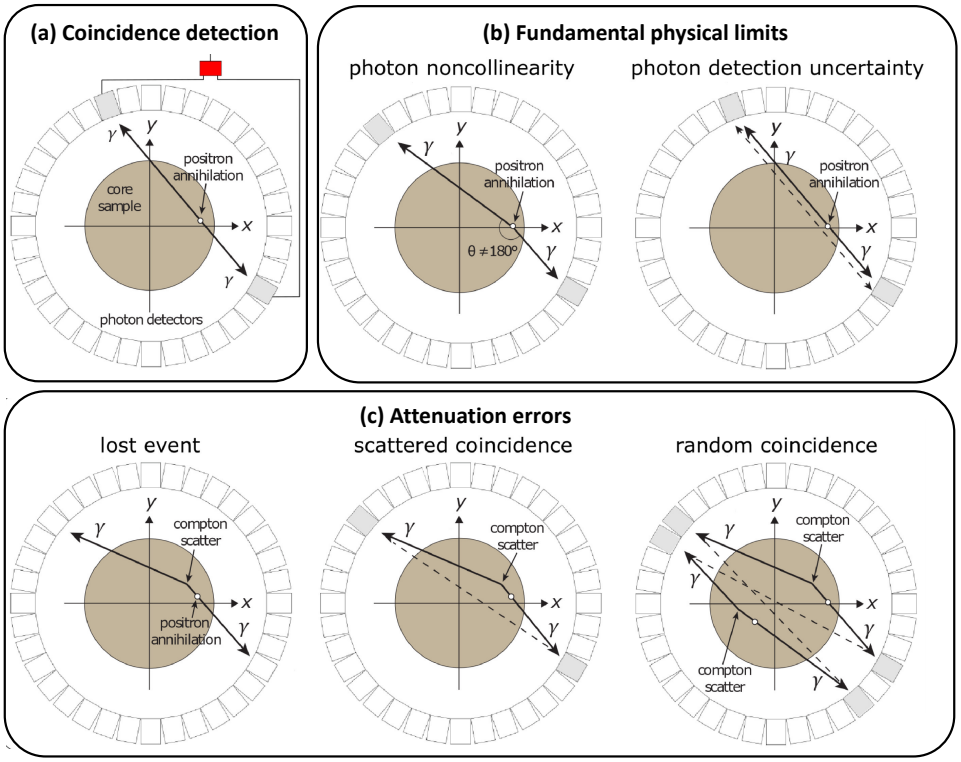

Figure 3.2: (a) Illustration of coincidence detection of positrons along the volume-of-response (VOR) (with struck detector highlighted in grey). (b) Illustration of photon noncollinearity, where $\theta \neq 180^{o}$. VOR calculations assume that $\theta = 180^{o}$. Also shown in figure (b) is the demonstration of photon detectors that can not distinguish between the two VOR as shown by the solid and dashed lines, due to the physical size limit of the detector element. (c) Conceptual diagrams of a lost event, a scattered coincidence and a random coincidence event. (left) Lost event occurs when the difference between photon detection times at the photon detectors is greater than the coincidence time threshold. (centre) The dashed line indicates the false line of response determined for a scattered coincidence event. (right) A random coincidence event occurs when two false VOR are registered from separate annihilation events. All of these sources of errors contribute towards the overall spatial resolution of a PET scanner. Figure adapted from Zahasky et al. (2019).

In this work, two different PET scanners have been used, namely the preclinical PET (Siemens INVEON DPET) and clinical PET (Siemens Biograph 64 PET/CT), for the experiments with consolidated and unconsolidated porous media, respectively. During a tracer test with radiotracer, the whole axial FOV of the PET scanner was imaged throughout the experiment without any physical movement of the sample. For a clinical scanner, this corresponds to a length of about 20 cm, while for the preclinical PET, the axial FOV is 12 cm. The PET scans have been reconstructed using the following algorithms: an iterative method based on a 3-D ordered subsets expectation maximisation (3-D OSEM-OP MAP, for the experiments with the preclinical PET) and an analytical method using filtered back projection (FBP, for the experiments with

the clinical PET). The obtained images have been coarsened to produce voxels with dimension (2.3×2.3×2.4) mm^3 (preclinical PET) and (1.4×1.4×2) mm^3 (clinical PET). These 3-D images are reconstructed further by (1) resampling into discrete time frames, (ii) applying for decay correction and (iii) converting the PET intensity distributions into radiotracer concentration. The methods used for these calculations are explained in Section 7.3.

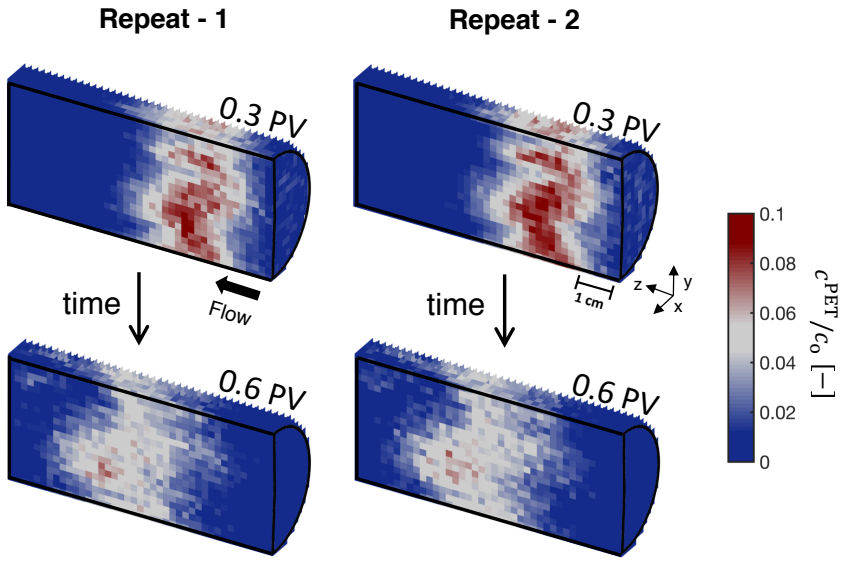

Figure 3.3: Comparison of the three-dimensional (3-D) internal concentration maps in Edwards Brown Carbonate (EB) for a repeated experiment carried out at $q = 15$ mL/min. The results are presented for two distinct time frames, corresponding to 0.3 and 0.6 pore volumes (PV) with an average of ±0.06 PV in each frame. To allow comparisons, the voxel concentration values are normalised by the feed concentration, c_o. The PET images have been reconstructed at a voxel resolution of (2.3×2.3×2.4) mm^3.

To highlight the good reproducibility of PET to image the temporal evolution of the solute plume, a set of repeated pulse-tracer experiment has been performed on a geologic porous medium, i.e. Edwards Brown Carbonate (diameter 5.1 cm, length 10.3 cm) under ambient conditions at the same flow rate, $q = 15$ mL/min. The results, following the injection of a tracer pulse ([^{18}F]FDG) is shown in Figure 3.3 at two different time intervals corresponding to the pore volumes of 0.3 and 0.6 PV. As indicated in the figure, the local distributions of the solute plume between the two independent experiments yield very similar behaviour. In the next section, both qualitative and quantitative evidences of how PET presents a more rigorous and accurate approach to image the spatial and temporal evolution of the full tracer plume are presented.

3.2.3 PET vs CT for *in situ* imaging of tracer transport

One of the primary motives for utilising PET for the *in situ* imaging of solute transport is because it gives a much higher sensitivity and signal-to-noise ratio (SNR) than is possible with X-ray CT tracers. The temporal resolution of PET scans is higher than all but the most advanced medical X-ray CT scanners, and the required radiotracers concentrations are so small ($\mathcal{O}\sim10^{-13}$ mol/mL) that changes in system fluid properties are negligible. The most commonly used tracers for X-ray CT imaging are iodide salts, such as potassium iodide (KI) or sodium iodide (NaI). The high electron density of iodide produces an enhanced X-ray attenuation, and enables it to be distinguished from other water or brine liquids in the sample. However, the drawback of using brine solutions is the change in fluid density that results from the addition of the quantities of salt required to obtain a strong SNR. The latter may introduce undesired buoyancy and density effects that would inherently affect the displacement behaviours.

To compare the signal-to-noise behaviour of medical X-ray CT and preclinical PET imaging, pulse injection experiments with both brine-tracer and radio-tracer were performed. Short (2 mL) pulses of tracer were injected into a Bentheimer sandstone sample (diameter 5.1 cm, length 10.3 cm) using the experimental procedure described in Chapter 7, and with the core-flooding system shown in Chapter 4. For X-ray CT imaging, aqueous solutions of KI (6.06 wt%) and KCl (7 wt%) were used as tracer and carrier fluid, respectively. X-ray CT scans were acquired every 2 minutes following tracer injection and the concentration of tracer was measured by subtracting baseline scans of the core fully saturated with KCl from scans with the KI pulse travelling through the core. For PET imaging, [^{18}F]FDG (with concentration, 0.51 mCi/mL) and tap water were used as tracer and carrier fluid, respectively. The PET scans were reconstructed with time-steps of 47 seconds. The experiments were conducted at flow rate, 4 mL/min. A qualitative comparison of three-dimensional normalised voxel intensity values is shown in Figure 3.4 after approximately 0.4 pore volumes of carrier fluid were injected into the sample. As shown, both the spatial structure of the tracer plume and the tracer distribution within the plume are more clearly resolved in the PET images as compared to those acquired with the X-ray CT scanner. Support to this observation is depicted in Figure 3.5, where a comparison of X-ray CT and PET 2-D cross-sectional images (sliced at the centre of the core) are shown on a more heterogeneous rock core (i.e. Ketton Limestone).

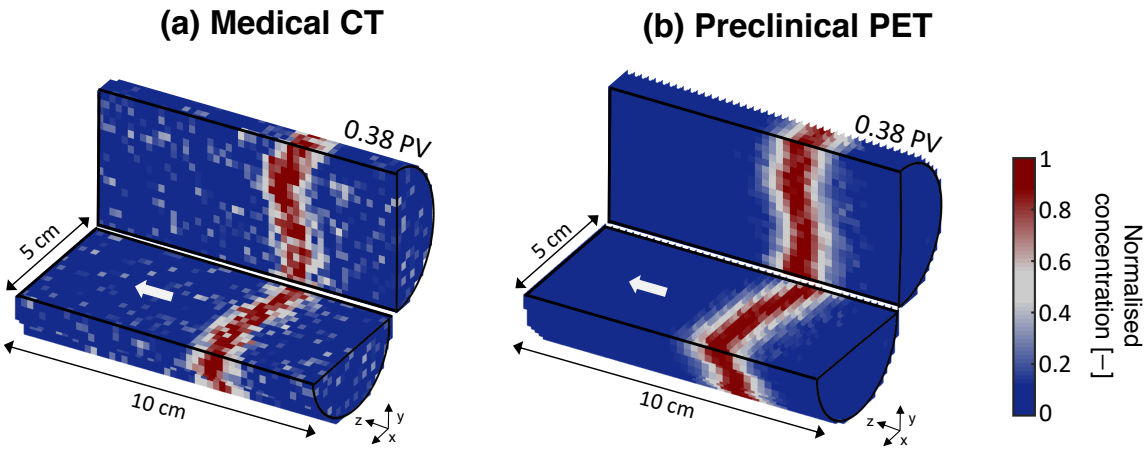

Figure 3.4: Comparison of the 3-D concentration maps of the tracer plume in a Bentheimer Sandstone acquired from (a) Medical CT (Toshiba Aquilion 64 TSX-101A clinical X-ray CT) and (b) PET (Siemens Inveon preclinical PET). These images have a voxel size of (2.5×2.5×2.0) mm^3 and (2.3×2.3×2.4) mm^3, respectively. The images correspond to scans taken at 0.38 pore volume. To allow comparisons, the voxel concentration values have been normalised by the maximum slice-averaged concentration from the first scan.

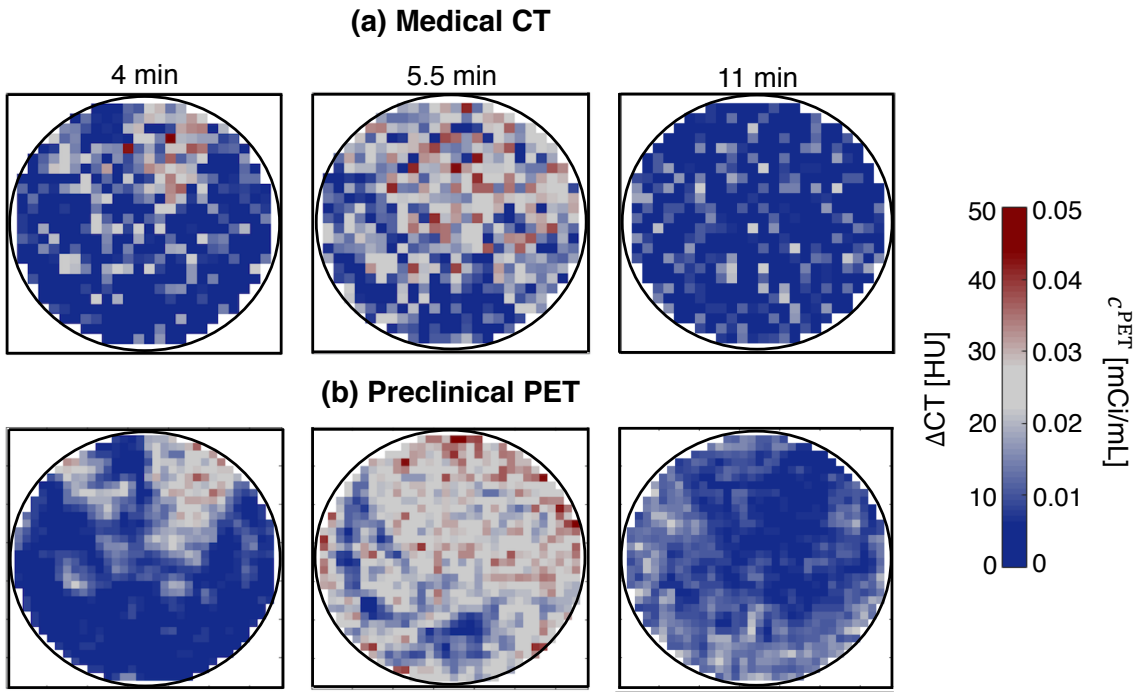

Figure 3.5: Comparison between medical CT and preclinical PET imaging of *in situ* tracer transport in the same Ketton Limestone core. The images are presented for the 2-D cross-sectional planes (x-y coordinate) at the center slice of the core, at three distinct times intervals after pulse injection: $t = 4$, 5.5 and 11 mins. The experiments were carried out at $q = 4$ mL/min. The PET and X-ray CT data have voxel size of (1.5×1.5) mm^2 and (1.9×1.9) mm^2, respectively. The colour maps of the 2-D images are given by radio-tracer concentration (c^{PET}) for PET, and absolute difference in the CT numbers between the scans of pulse tracer injection and the scans of the KCl saturated core (ΔCT) for X-ray CT.

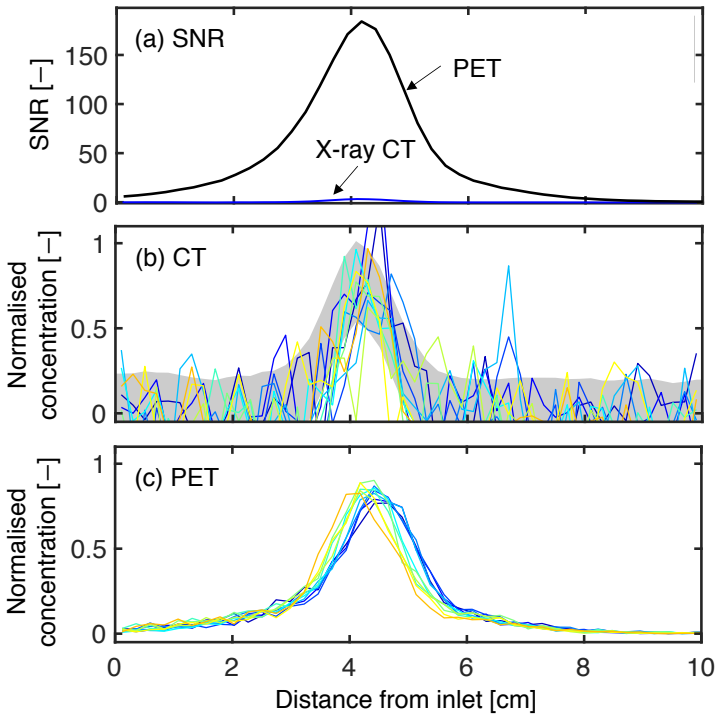

Figure 3.6: (a) Comparison of signal-to-noise ratio (SNR) obtained from X-ray CT and PET measurements following a pulse injection of tracer in the same Bentheimer Sandstone core. (b) Slice-averaged internal concentration profiles for 11 rows of voxels located along a horizontal slice of the core, measured with X-ray CT. Shaded grey region indicates measurement uncertainty as determined by the standard deviation of voxel concentrations containing no tracer. (c) Internal concentration profiles for 11 rows of voxels located along a horizontal slice through the centre of the core, imaged with PET. Standard deviation of voxel concentrations is thinner than coloured lines. Figure adapted from Zahasky et al. (2019).

A more quantitative comparison of the dataset acquired on a Bentheimer Sandstone is presented in Figure 3.6. The top plot illustrates the calculated SNR for PET and CT along the length of the sample. The maximum SNR in the PET profile is ∼180 while the maximum SNR obtained from the CT dataset is only about 3. In this case, the signal is the slice-averaged concentration and the noise is quantified by calculating the standard deviation of voxel concentration variation in all of the voxels in the regions of the core that contain no tracer. A region is determined to have no tracer if the slice-averaged concentration is less than 1% of the maximum slice-averaged concentration. The lower plots in Figure 3.6 show axis-parallel concentration profiles (colored lines) and the standard deviation of concentration measurements (indicated by width of grey regions) for X-ray CT (middle plot) and PET (lower plot). It is important to emphasise that CT SNR is a function of material (i.e. KI brine) electron density contrast relative to other fluid in pore space (i.e. KCl brine), and therefore is independent of scan time. The PET SNR is

a function of radioactivity concentration and to a lesser extent image time-step length (image quality was found to be consistent down time-steps as short as 10 seconds). Both the qualitative and quantitative comparison of the saline and radioactive tracers make it clear that the tracer imaged with PET has a higher sensitivity and a much higher SNR compared with X-ray CT imaging, making it well suited for studies on in-situ quantification of mixing and spreading.

Chapter 4

Experimental Apparatus

4.1 Introduction

Efforts have been made during initial phase of this PhD to design and develop a multi-functional core-flood system to conduct *in-situ* pulse tracer experiments. The latter is built in-house partially using commercially available components, which have been carefully selected based on functionality, cost, sensitivity and compactness. In particular, the following key specifications were considered in the design:

- Constant flow pulse tracer tests with brine- [$KI_{(aq.)}/KCl_{(aq.)}$] and radio-tacers [$^{11}C/^{18}F$]
- Ability to carry out X-ray CT and PET imaging
- Ability to transport system to PET facility centres
- Injection of fluids from both directions ("transmission" and "echo" technique)
- Instantaneous real-time data-logging of the connected instruments

In the section below, the details of the core-flooding experimental apparatus are discussed, including the core-holder, the operating modes, and the required calibrations (i.e. detectors and dead-volume analysis). The essential design considerations required to optimise the performance of laboratory core-flooding experiments using X-ray CT/PET technique are also discussed.

4.2 Experimental set-up

4.2.1 The core-holder

A Hassler type core-holder has been designed and commissioned for the experimental system; the corresponding 3-D CAD drawing is presented in Figure 4.1 (sketched using SolidWorks 2017, Innova Systems UK Ltd). The core-holder is made of aluminum (Al alloy, EN 573-3 Grade EN AW-6082), and has been hard-anodised to provide high resistance to corrosion from the use of brine solutions (coating standard DEF STAN 03-26, thickness $\sim$50 μm). The sample is positioned between two aluminum end-caps that incorporate three fluid ports each (1/16" NPT Tapped holes), corresponding to (i) the main loop for the flow of tracer and carrier fluids, (ii) confining pressure fluid, and (iii) up- or down-stream pressure measurements. The latter presents one unique feature of the design and enables direct measurements of pressure drop across a core sample with minimum disturbances caused by the inlet and outlet tubings. This eliminates errors associated with corrections needed to account for the additional resistance of the flow lines. To ensure homogeneous fluid distributions across the entire cross-section of the core, symmetric and regularly distributed grooves with a depth of 1 mm are milled on each face of the end-caps. The core-holder can accommodate a cylindrical core sample with a diameter of 5 cm, and variable lengths of $10 - 13$ cm. This is sufficient for the rock samples used in this study; however, longer or shorter cores can be accommodated by using barrels of different lengths. The design also contains two cylindrical disks (with 8 holes for M6 x 38 mm stainless steel screws) placed at each side of the core-holder to hold the end-caps in place. To prevent bypassing of fluids during experiments, each end-cap includes six nitrile o-rings (Barnwell UK Ltd) that provide tight annular seal between the outer cylindrical body or heat-shrink sleeve (used to separate the confining fluid from core samples) and the end-caps. The core-holder has been successfully tested with radial confining pressures up to 80 bars; this is well-beyond the pressure needed for the experiments considered in this study, i.e. $p_{\text{conf}} \approx 6 - 30$ bars. Two custom-made stainless steel stands are used to fix the core-holder horizontally on the bed of the scanning instrument.

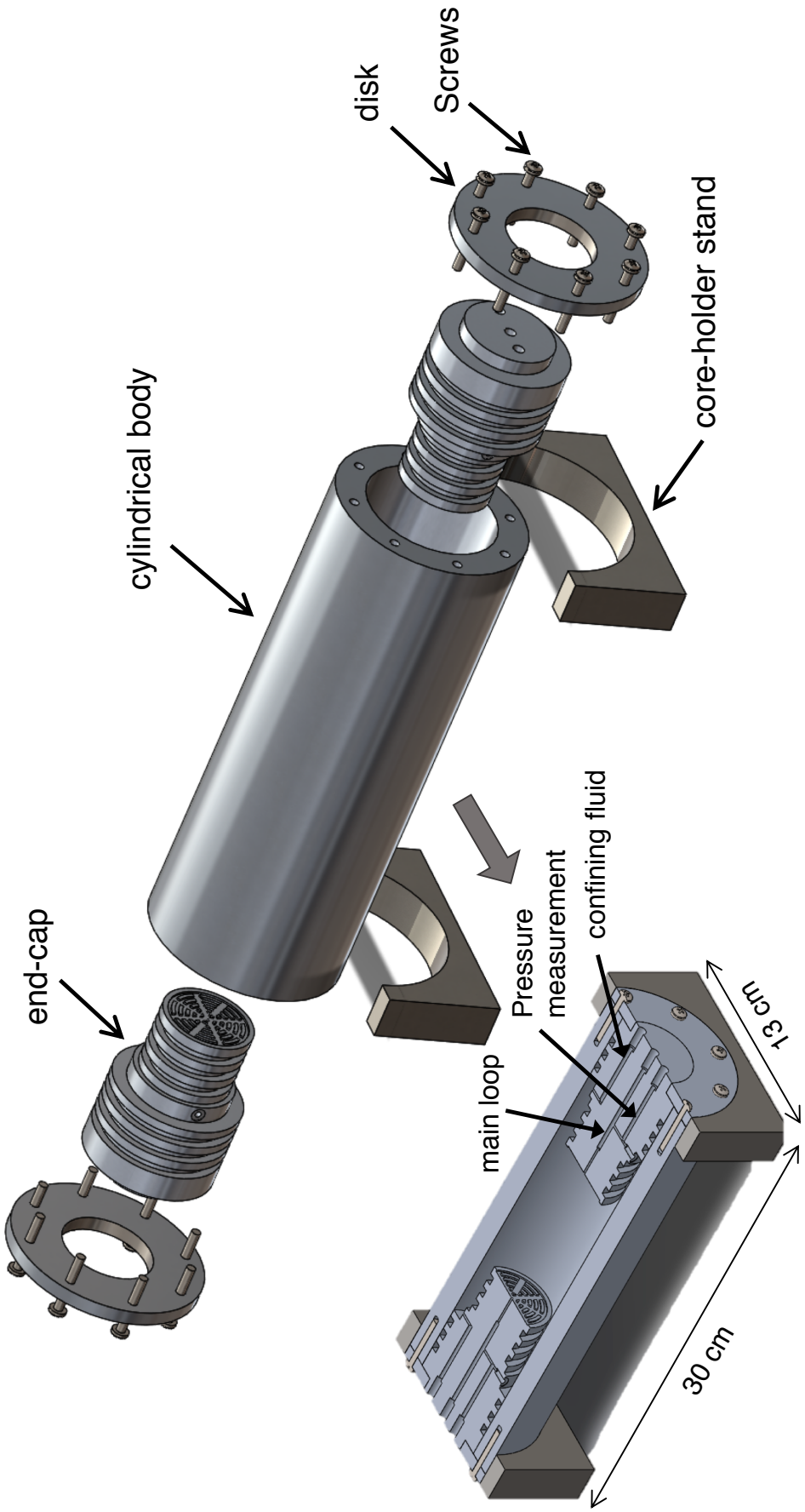

Figure 4.1: 3-D sketch of the core-holder designed in this work. The core-holder is made of aluminum and mainly consists of 2×end-caps with disks, 1×cylindrical body, 2×core-holder stands, 2×disks.

4.2.2 The core-flooding apparatus

The schematic diagram of the custom-built core-flooding apparatus is depicted in Figure 4.3. A constant, confining annular pressure between the jacketed sample and an outer aluminium tube is maintained by a high-pressure syringe pump (P2, Teledyne ISCO, model 1000D). Two conductivity micro flow cells (CI, Model 829, Amber Science, USA) are mounted up- and down-stream of the core-holder to measure the concentration of the inflow and outflow solution. These are connected to a multi-function conductivity meter (Model 8032, Amber Science, USA) that converts the measured resistance into conductivity (C1 and C2, accuracy: 2%rel.). For experiments involving the use of a radiotracer, two shielded radioactivity detectors are utilized (custom-built configuration, Carroll & Ramsey Associates, USA). Before the inlet sensors are the two dual-position six-port injection valves (Cheminert, HPLC 6 port injection valve, VICI, Thames Restek UK Ltd.) that have been used to (i) control the direction of fluid flows in the system (details discussed in the next section) and (ii) inject a tracer pulse. The valve uses an electric actuator to switch the direction of flow of the clean solvent stream to flush the sample loop (1 or 2 mL in this study) or to by-pass it (see inset of Figure 4.3). A piston-driven syringe pump (P1, Teledyne ISCO, model 1000D) is used for continuous injection of the carrier fluid through the sample at controlled flow rates, which are additionally measured through a liquid flow meter (FI, SLS-1500, Sensirion, Switzerland, accuracy: 5%rel.) that is mounted downstream of the effluent detector. The system features a differential pressure transducer (DPI, Keller UK, model PRD-33X, accuracy: 0.05%FS) connected through tubing ported directly to the inlet and outlet faces of the sample. For the experiments with consolidated rocks, an additional syringe pump (P3, Teledyne ISCO, model 1000D) was employed to maintain a back-pressure of $\sim$1 bar(g) on the outer face of the sample (dotted lines in Figure 4.3), thus by-passing the liquid flow meter. The various components of the system are connected by means of PEEK and PTFE tubing (OD 1/16”-1/8”). In order to ensure the operating pressure does not exceed the working pressure of the components, pressure relief values (Swagelok, SS-RL3S4 series) are installed at the inlet and outlet of the core-holder. They have been calibrated to a set point limit of 3 bars. Custom-made trolleys have also been built to allow easy transport of the experimental set-up between different facility centers. A digital photograph of the entire core-flooding apparatus is shown in Figure 4.2.

Figure 4.2: Digital photograph of the core-flooding set-up designed and commissioned in this work. The left figure is the experimental system (schematic presented in Figure 4.3) when packed in custom-built trolleys whereas the figure on the right corresponds to the entire set-up placed on the bed of a X-ray CT/PET scanner

The set-up has been used for the experiments involving three different scanning instruments: (i) Universal Systems HD-350 X-ray CT scanner at Imperial College London for preliminary tracer experiments and measuring structural properties of the rocks; (ii) Siemens INVEON DPET at Stanford University for PET experiments on consolidated rocks; (iii) Siemens Biograph 64 PET/CT at Imanova Ltd for PET/CT experiments on unconsolidated beadpacks.

4.2.3 Experimental technique and operation modes

The set-up allows conducting pulse-tracer tests by considering two experimental methods, namely the 'transmission' and 'echo' techniques. The former refers to the classical dispersion experiment, where a bolus of tracer is injected into a core and the effluent breakthrough profile is measured at the downstream (outlet) end of the system. The results obtained from this approach on various porous media are presented in Chapters 5, 7 and 8 of this thesis. The "echo" technique involves reverting the flow direction after the injected tracer has propagated for a given distance into a porous medium. In this case, the "effluent" curve is measured at the upstream (inlet) end of the system. It is worth mentioning that the latter present a very useful

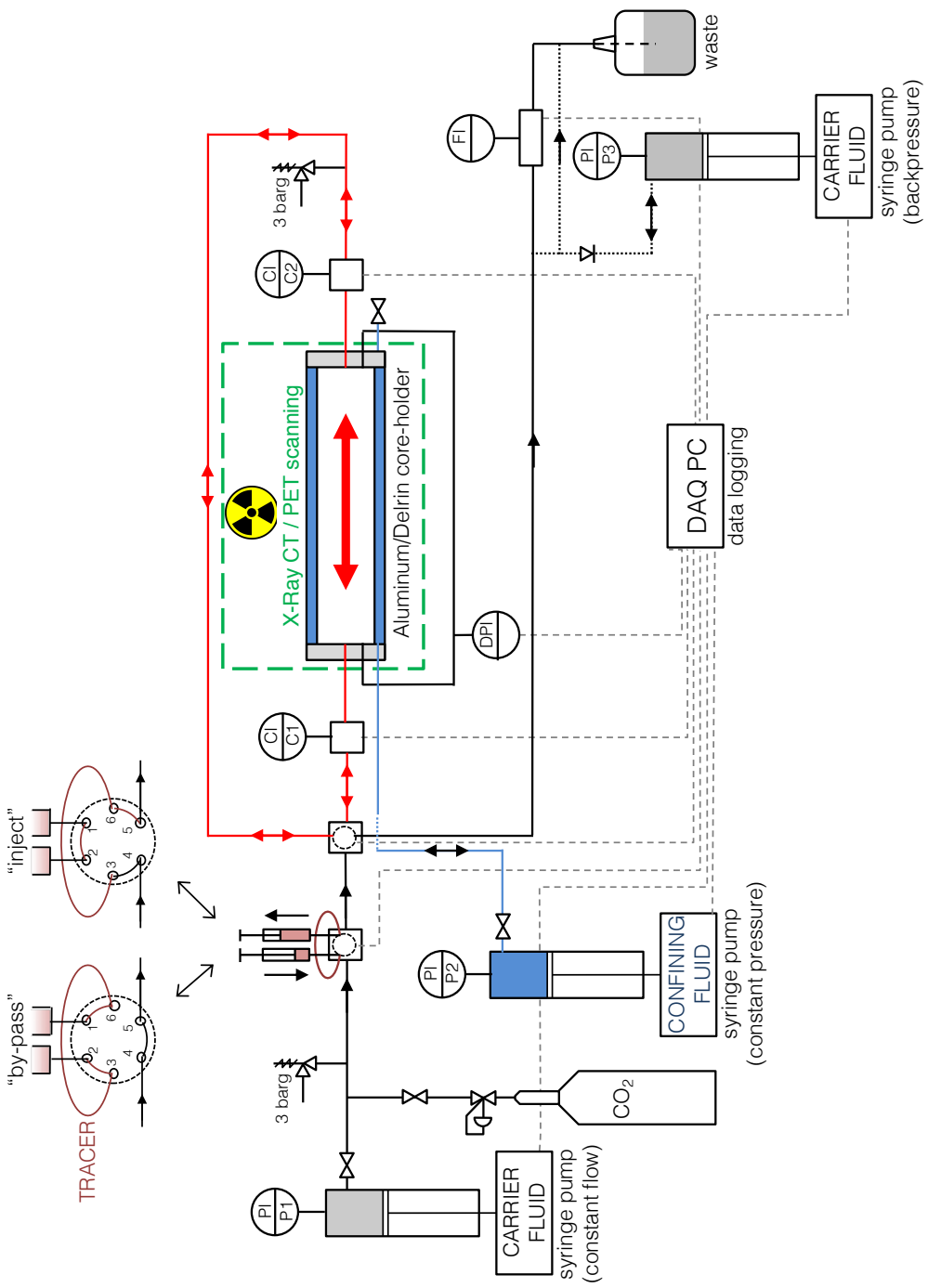

Figure 4.3: Schematic of the experimental core-flooding apparatus used to carry out pulse-tracer tests with simultaneous imaging by X-ray CT and PET. Dashed lines represent electrical connections to the data acquisition system, while the dotted lines refer to the modification adopted for the experiments with back-pressure. The concentration of the injected (C1) and effluent solution (C2) is measured through either conductivity or radioactivity detectors. Additional instrumentation includes two dual-position six-ports valves for (i) tracer loading/injection and changing flow direction, a differential pressure transducer (DPI), a flow meter (FI), as well as three syringe pumps for injection at constant flow rate (Q1), for maintaining a constant confining pressure (P2) and for regulating the back-pressure (P3). The red lines refers to the tubings that allow change in flow direction

approach to minimise the effect of plume spreading caused by subcore-scale heterogeneities; this is demonstrated in Chapter 10. To accommodate both flow modes, the system has been designed such that flow reversal can take place by a valve actuation, thereby minimising any disturbance to the flow fields (demonstrated in Section 4.2.5). Figure 4.4 illustrates how this is achieved in practice using the second dual-position six-port injection valve.

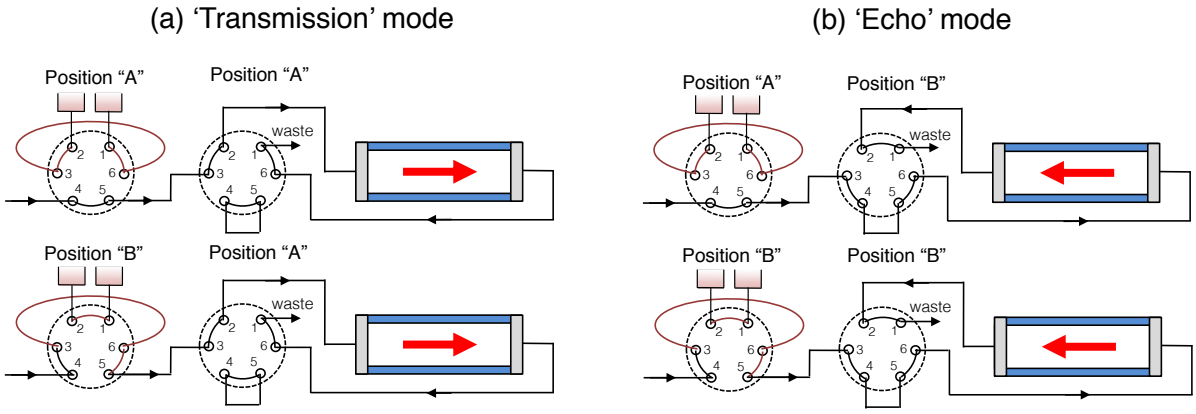

Figure 4.4: Schematic diagram illustrating the two modes of operation for the experimental set-up shown in Figure 4.3; (a) "transmission" (forward flow) and (b) "echo" (backward flow). For each mode, the top diagram refers to the injection of the solvent (carrier fluid), while the bottom diagram corresponds to the injection of the tracer.

4.2.4 Data-logging

Automatic, real-time data-logging of each component in the core-flooding system (radioactivity/conductivity, temperature, pressure, flow rate) is achieved by means of an in-house developed Graphical User Interface (GUI) in LabVIEW 2016 (National Instruments^{TM}). The control panel provides an easy-to-use interface where measurements can be recorded by simply specifying the file path and time intervals. The GUI also enables automatic injection of tracer and reversal of flow direction by means of functional buttons. A snapshot of the control panel is shown in Figure 4.5.

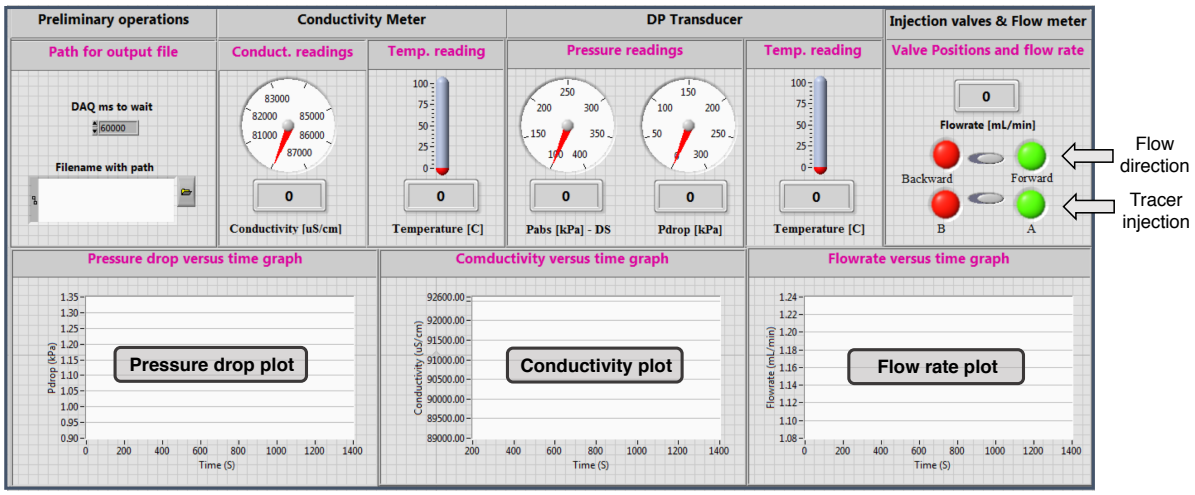

Figure 4.5: Snapshot of the Graphical User Interface (GUI) written in LabVIEW 2016. The control panel provides numerical and graphic interpretation of the dataset obtained from various components in the set-up, including up- and downstream pressures, temperature, tracer activity and flow rate. The injection valves (i.e. for tracer injection and change in flow direction) can also be controlled from the interface.

4.2.5 Experiment design

Choice of fluid pairs:

For the tracer experiments involving conductivity measurements, aqueous solutions of potassium iodide [$KI_{(aq)}$] and potassium chloride [$KCl_{(aq)}$] were used as tracer and carrier fluid, respectively. This solution pair has been selected such that minimal variations in the tracer diffusion coefficients (i.e. $D^0 = 19.6 - 20.3 \times 10^{-10}$ m^2/s at 25 °C; values collected from Lasaga (2014)) are expected. This ensures that electrostatic effects of the ionic specifies are minimised during tracer tests. The suitability of the solutions has been further validated by comparing the effluent profiles obtained from an independent set of observations involving radio-tracer measurements (results are presented in Chapter 5). It is worth noting that failure to account for the latter may affect dispersion measurements, as clearly demonstrated by both experimental and numerical work by Muniruzzaman et al. (2014); Muniruzzaman and Rolle (2017). The neutrally buoyant brine solutions used in this work have been prepared from pure $KCl_{(s)}$ (> 99%, Sigma Aldrich) and $KI_{(s)}$ (ReagentPlus®, 99%, Sigma Aldrich), for two different sets of concentrations, namely $KI_{(aq)}$ (2.0wt%)−$KCl_{(aq)}$ (2.3wt%) and $KI_{(aq)}$ (6.1wt%)−$KCl_{(aq)}$ (7.0wt%). The latter uses a high concentration of a doped-tracer to enhance the CT contrast between the two fluids during X-ray CT imaging (used to design and validate experimental protocols). The density of the so-

lutions have been measured using an oscillating U-tube density meter (DM5000 by Anton Paar) at 20 °C and 1 atm, to ensure that the density difference between tracer and carrier solution does not exceed 0.1%; this is very important as demonstrated in the next section.

The same (but more dilute) carrier solution ($KCl_{(aq)}$, $0-2.3$wt%) was used for the experiments involving a radiotracer; for the latter, two isotopes have been used, namely ^{11}C (half-life, $t_{1/2}$ = 20.3 min) and ^{18}F ($t_{1/2}$ = 109.7 min), which have been chemically processed to yield solutions of [^{18}F]FDG (Fluorodeoxyglucose) and [^{11}C]$NaHCO_3$ (sodium bicarbonate) in the carrier fluid (activity concentration varying between $0.3-1.1$ mCi/mL, corresponding to $A_{Bq} = 11-41 \times 10^6$ Bq/mL). In this case, the detected activity (concentration) of the solution, c_D^{out} (or c_D^{in}), is corrected to the radioactivity at the injection time, c^{out} (or c^{in}), by accounting for radioactive decay, e.g., for the outlet detector, $c^{out}(t) = c_D^{out}(t)e^{\lambda t}$, where $\lambda = \ln(2)/t_{1/2}$. The concentration of radiotracer in the solution injected into the porous sample can be readily calculated as,

$$c_0 = \frac{A_{Bq}}{N_A}\frac{t_{1/2}}{\ln(2)} \tag{4.1}$$

where $N_A = 6.022 \times 10^{23}$ mol^{-1} is the Avogadro constant; accordingly, $c_0 = 0.3-0.9 \times 10^{-13}$ mol/mL and $c_F = 2-7 \times 10^{-13}$ mol/mL were used for the tracer tests involving [^{11}C]$NaHCO_3$ and [^{18}F]FDG, respectively. In addition to ensuring that the tracer solutions are also neutrally buoyant, these very low concentration values highlight the high-sensitivity of PET for imaging tracer transport. Experiments with ^{18}F (reservoir core samples) were carried out at the Small Animal Imaging Facility of the Stanford Center for Innovation in In-Vivo Imaging (SCI3, Stanford University, USA), while those involving ^{11}C (beadpacks) were carried out at Imanova Limited (Invicro LLC, London, UK). Both facilities enable on-site production of the radiotracer solution. Details of the fluid properties used for the tracer tests in this thesis are summarised in Table 4.1.

To convert activity measurements (radioactivity or conductivity) into concentration, a constant correction factor has been applied for each experimental dataset based on a calibration performed on the fluid mixtures using the detectors in the experimental set-up. As an example of general validity, the calibration curve measured at multiple volume fractions of the mixture, $KI_{(aq)}$ (6.1wt%)$-KCl_{(aq)}$ (7.0wt%) is given in Figure 4.6, in which a clear linear relationship is observed.

Table 4.1: Properties of the fluid pairs used for the pulse-tracer tests. The viscosity values of the brine solutions were obtained from Goldsack and Franchetto (1977), and corrected for the concentration based on a linear interpolation between two nearest experimental points. The subscript '1' denotes for tracer and '2' corresponds to the carrier fluid. $\Delta\rho$ and ε are the absolute and relative density differences, respectively.

Tracer	Carrier fluid	μ_1 [pa·s]	μ_2 [Pa·s]	$\Delta\rho(\varepsilon)$ [kg/m^3]
KI (2.0wt%)	KCl (2.3wt%)	8.83×10^{-4}	8.88×10^{-4}	0.3(0.03%)
KI (6.1wt%)	KCl (7.0wt%)	8.68×10^{-4}	8.89×10^{-4}	0.8(0.08%)
[^{18}F]FDG	H_2O	8.90×10^{-4}	8.90×10^{-4}	$< 0.05\%$
[^{11}C]$NaHCO_3$	H_2O	8.90×10^{-4}	8.90×10^{-4}	$< 0.05\%$

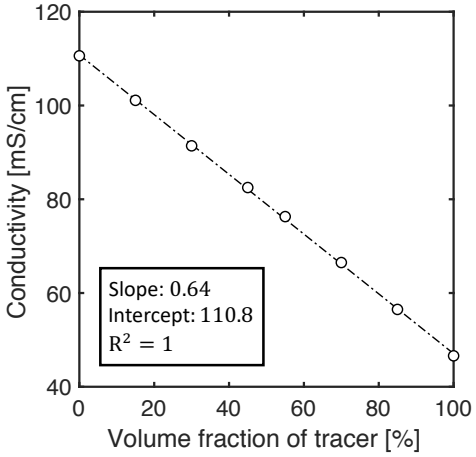

Figure 4.6: Example of a calibration curve for the fluid-mixture, $KI_{(aq)}$ (6.1wt%)−$KCl_{(aq)}$ (7.0wt%) obtained from the activity detector used in the core-flooding set-up. The latter was determined from measuring the conductivity values at eight different volume fractions of the fluid pair (symbols). The dashed line corresponds to the fitted linear regression line, with R-squared value, $R^2 = 1$ (slope: 0.64 and intercept: 110.8)

Gravitational and viscous effects:

The gravity number, G, is commonly used to provide a quantitative measure of extent of buoyancy effects during miscible displacements, and is defined as follows (Berg et al., 2010):

$$G = \frac{\Delta\rho g k L d}{\mu_1 q} \tag{4.2}$$

where $\Delta\rho$ is the density difference between the injected (ρ_1) and the displaced fluid (ρ_2); g is the gravitational acceleration (9.80665 m/s^2); μ_1 is the viscosity of the tracer solution; q is the volumetric flow rate of the fluid injected. k, L and d are the physical properties associated

with the porous medium, corresponding to permeability, length and diameter, respectively. The following ranges of G have been obtained for the tracer experiments involving rocks (shown in Chapter 7), i.e. $G = 0 - 2.4 \times 10^{-3}$ (Bentheimer Sandstone), $G = 0 - 2.6 \times 10^{-3}$ (Ketton Limestone) and $G = 0 - 1.9 \times 10^{-4}$ (Edwards Brown Carbonate) (details of the rock properties used for the calculations are provided in Chapter 6, Table 6.3); these values are well below the gravity-dominated regime, as suggested by Berg et al. (2010) ($G < 1.5 \times 10^{-2}$).

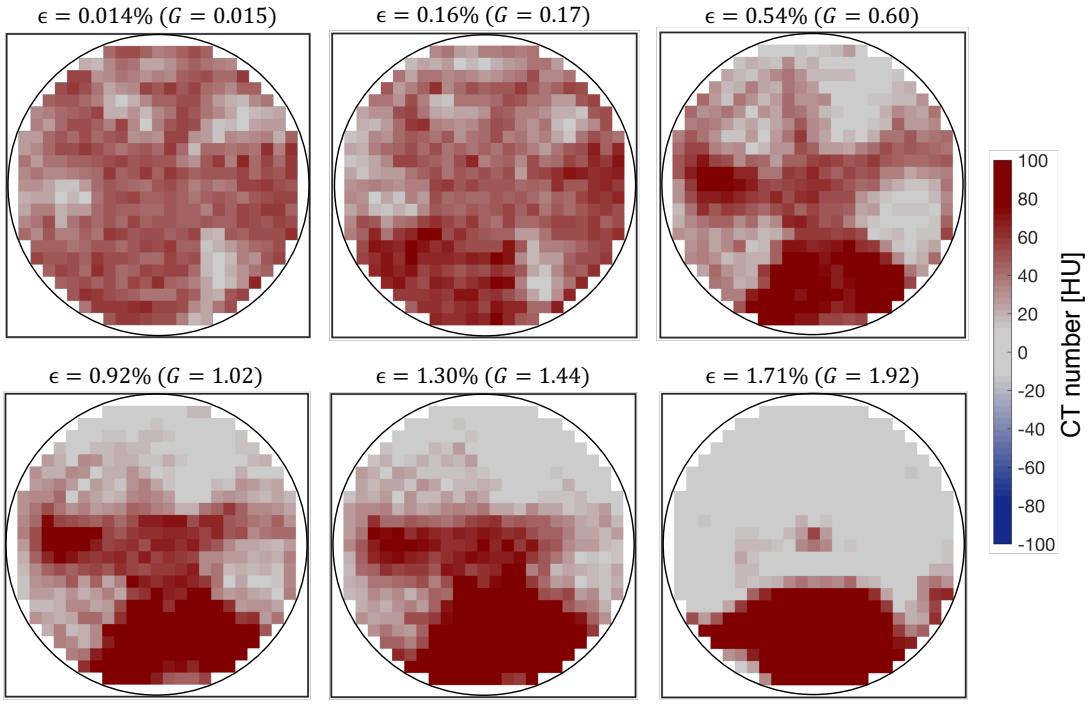

Figure 4.7: 2-D maps of a 1 mm-thick slice of the beadpack, as obtained from a reconstructed X-ray CT scans acquired at a distance of 2 cm from the inlet face of the core. The color scale corresponds to the CT numbers in Hounsfield units and the image is obtained by substracting the CT image obtained at the same location when the core was saturated with the NaCl (5wt%). Each image represents a different tracer concentration (4.75 – 7.0wt%), thus corresponding to a different relative density contrast between the fluids (ϵ). The experiments were carried out at $q = 5$ mL/min and the images were coarsened into a constant voxel size of (1.78×1.78) mm^2.

As described in the following, we provide additional evidence for this by directly imaging the tracer flow in the sample. An experimental campaign has been designed to determine the maximum allowable density difference, such that gravity effects are minimised (or completely avoided). To this aim, a series of tracer tests were carried out on a packed-bed of granular beadpacks ($d = 5$ cm, $L = 10$ cm, SiLibeads®, supplied by VWR, UK) by using 5wt% aqueous sodium chloride (NaCl) solution as the carrier fluid, together with a range of tracer solutions with potassium iodide (KI) content varying between 4.75 and 7.0wt%. During the experiments, X-ray

CT scans were taken simultaneously at a fixed distance from the inlet face of the beadpack. The corresponding 2-D maps acquired at a distance of 2 cm from the inlet face of the core are shown in Figure 4.7. It can be seen that a homogeneous distribution of the tracer is obtained when the relative density difference between the fluids is less than $\sim 0.2\%$ (corresponding to $G < 0.17$). This is more apparent when plotting the corresponding average CT values at every horizontal slice along the radial direction of the core (shown in Figure 4.8). In the plot, the average CT numbers have been normalised by their mean values of the first slice (top section of the core). As shown, we notice that the effect of gravity is much more pronounced for $G > 0.6$, with very large proportion of tracer present in the bottom half of the core. For all the experiments carried out in this study, the displacement processes is considered to be stable (therefore, no viscous fingering) because the tracer and carrier solution have very similar viscosities, i.e. the mobility ratio, $M_\mu = \mu_2/\mu_1 \approx 1$.

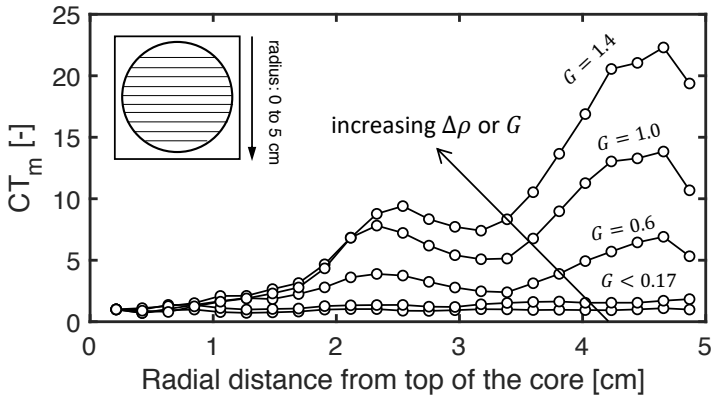

Figure 4.8: The average CT numbers plotted along the radial slice from the top of the core, for the 2-D maps shown in Figure 4.7. The mean CT numbers, i.e. $\mathrm{CT_m}$ are normalised by the corresponding values of the first slice (top slice). The results are shown for various gravity parameters, i.e. $G = 0.015$, 0.17, 0.60, 1.02 and 1.44.

Dead volume and excess dispersion:

The dead volume (V_D) of the experimental system has been estimated from conducting multi-rate pulse tracer tests without porous medium (the two end-caps are pressed against each other). Specifically, V_D is calculated from taking the difference between the mean residence time of the inlet and outlet curves. For the tracer tests carried out in this thesis, the estimated dead volume can vary in the range between $1.0 - 4.2$ mL (corresponding to approximately $1 - 8\%$ of the total pore volume of the core samples studied). This variation is attributed to the facility centres,

where the experiments were conducted, as the tubing lengths needed to be adjusted to cope with different scanning environment. The results from such test were also used to examine the extent of dispersion that occurs in the inlet and outlet tubing; the breakthrough profiles measured from a tracer test carried out without porous medium at $q = 2$ mL/min is presented in Figure 4.9. The fact that the inlet and effluent curves are practically unaltered confirm that mixing in the lines and injection ports is minimal.

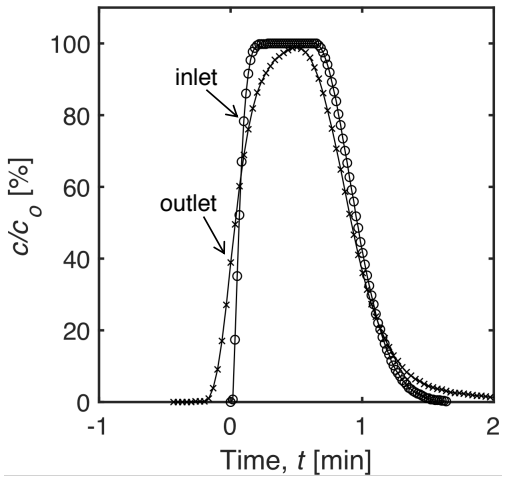

Figure 4.9: The inlet and outlet breakthrough curves obtained from the pulse-tracer test when the two end-caps are intact. The test is carried out at flow rate, $q = 2$ mL/min. The concentration values in the figure are normalised by the feed concentration, c_o and the outlet curve has been shifted to account for the time spent in the tubing.

Monitoring and evaluating changes in operating conditions:

An example of the temperature, pressure drop and flow rate recorded are shown in Figure 4.10 for a brine-tracer experiment carried out on a Ketton Limestone core at flow rate, $q = 8$ mL/min. These conditions have been closely monitored during all experimental runs to assess the general quality of the measured dataset. Very importantly, as it can be seen from the figure, the flow rate blip caused by the injection of a tracer pulse using the injection valve is relatively small ($\Delta q \sim 0.8$ mL/min), and can be recovered within ~ 1 min (corresponding to about 6% of the total experiment time). Accordingly, the average flow rate during the experimental time remains unaffected, i.e. $q = 7.95$ mL/min, which lies within the uncertainty of the liquid-flow sensor ($\pm 5\%$). We also observe that the pressure (e.g. $\Delta p \approx 3.6$ kPa) and temperature (e.g. T ≈ 20.4 ^{o}C) stay fairly constant throughout the injection period.

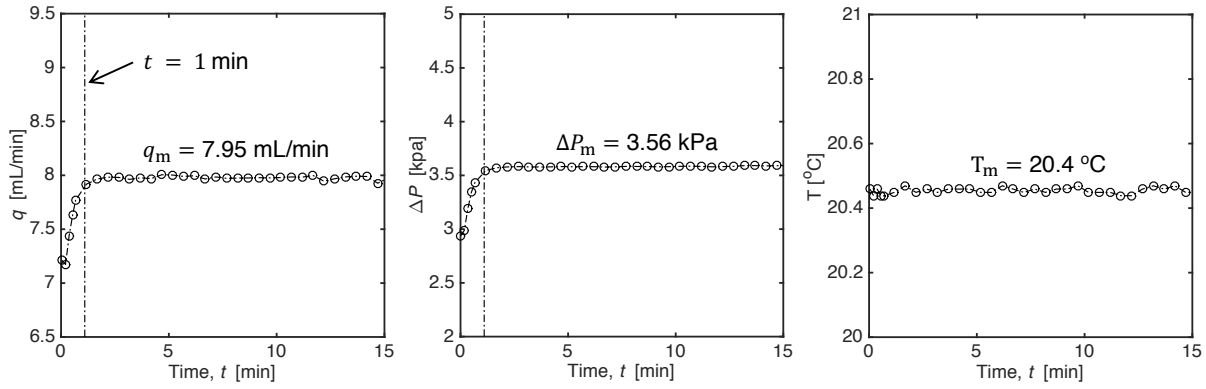

Figure 4.10: Examples of pressure, flow rate and temperature recordings during the entire duration of a pulse-tracer experiment conducted on a Ketton core at $q = 8$ mL/min.

4.3 Concluding remarks

A compact, multi-functional core-flooding system has been designed and commissioned to conduct pulse-tracer tests coupled with simultaneous imaging of flows by X-ray CT and PET. The system is automated in terms of pulse-tracer injection and controlling the flow direction, so as to increase experiment reproducibility. A series of validation tests have been performed with the set-up, in which we demonstrated that the effects of excess mixing in the tube lines, as well as flow interruptions caused by switching the injection valves are minimal. In order to optimise the sensitivity in the breakthrough measurements, fluid pairs have been carefully chosen to provide sufficient measurement sensitivity (radioactivity and conductivity) and CT contrast. The system enables using both radio- (labelled with $[^{18}F]$ or $[^{11}C]$) and brine-tracer ($KI_{(aq)}$), which have shown excellent agreement in addition to not being affected by unstable viscous fingering, compound specific dispersion or buoyancy effects during the displacement process. By ensuring the performance of the designed experimental set-up that allows integrating various imaging techniques (such as PET or X-ray CT), as well as different operational modes ("transmission" or "echo"), the ultimate goal is to produce an accurate 3-D dataset that provides quantitative insights into solute mixing and spreading in heterogeneous porous media.

Chapter 5

Control Experiments on Beadpacks

- Some of the contents in this chapter has been published in ***Kurotori, T.**, Zahasky, C., Hosseinzadeh Hejazi, S. A., Shah, S. M., Benson, S.M., Pini, R. Measuring, imaging and modelling solute transport in a microporous limestone, Chemical Engineering Science 196 (2019) 366-383.*
- The associated PET imaging dataset presented in this chapter can be obtained from the UKCCSRC data repository (dataset ID 13607385).

5.1 Introduction

To validate the experimental protocol that combines pulse-tracer tests with *in situ* imaging of flows by Positron Emission Tomography (PET), a series of control experiments have been carried out on a granular beadpack over the range of Péclet numbers, $25 < \mathrm{Pe} < 250$. The suitability of the radio-tracer used (i.e. $[^{11}\mathrm{C}]\mathrm{NaHCO_3}$) has been confirmed by comparing the observations with the corresponding results obtained from classic brine-tracer measurements. The effluent profiles obtained from the two independent measurement techniques have been systematically evaluated by means of experiment reproducibility, residence time distribution (RTD) analysis and comparisons with empirical correlation, as well as numerical models, such as the random-walk (RW) theory and the Advection Dispersion Equation (ADE). The capability of PET for quantitative evaluation of subcore-scale dispersion has been investigated by observing

the dynamic, multidimensional concentration profiles, and by computing the mixing measures (i.e. dilution index), which have been subsequently compared to their numerical counterpart.

One of the practical outcomes of this work is the generation of a dispersion dataset to be compared to the literature data that are somewhat scattered (details are discussed in Section 5.6.2). While many studies exist on experiments with beadpacks (e.g. (Hiby, 1962; Pfankuch, 1963; Perkins and Johnston, 1963; Dullien, 1992; Seymour and Callaghan, 1997; Kandhai et al., 2002; Guedes de Carvalho and Delgado, 2005)), only few have gathered a three-dimensional dataset (Zhao et al., 2011; Dogan et al., 2017). In that respect, the results presented in this chapter are very important to "calibrate" the system for sub-core scale (mm-scale) observations, in view of the inherent heterogeneity of rock sample at the same scale and noise that comes with images acquired from non-invasive techniques.

5.2 Materials

Cylindrical packed beds of glass beads (diameter, $d = 3 - 5$ cm, length, $L = 15$ cm, particle diameter, $d_\mathrm{p} = 0.4 - 0.6$ mm, SiLibeads®, supplied by VWR, UK) were used. Prior to the experiments, dry micro-CT scans were acquired on a small sample of the same glass beads (∼300 beads) to quantify the microstructural properties of the medium, including the grain size distribution (GSD). The estimated average grain diameter (d_p) is then used in the definition of Péclet number ($\mathrm{Pe} = vd_\mathrm{p}/\mathcal{D}$), and to evaluate the longitudinal dispersivity, α_L, where $\alpha_\mathrm{L} \approx d_\mathrm{p}/2$ (Gist et al., 1990). A snapshot of a 2-D cross-sectional slice of a grey-scale and the segmented tomograms, together with the corresponding 3-D reconstructed images are presented in Figure 5.1. These images were taken at a constant voxel resolution of $(3.8 \times 3.8 \times 3.8)$ $\mu\mathrm{m}^3$ using the micro-CT scanning parameters detailed in Section 3.2.1. The dataset is analysed using AVIZO-9 (ThermoFisher Scientific), by implementing the following operations in the toolbox, *watershed segmentation*, *separate object*; *border kill* and *remove small objects* (see Section 3.2.1). This yields an average particle diameter, $d_\mathrm{p} = 568$ μm, which lies well within the range provided by the supplier. A histogram showing the distribution of grain sizes is given in Figure 5.2.

As expected, the mercury intrusion curve (details of the measurement protocol described in Chapter 6) depicted in Figure 5.3b indicates that the beadpack is characterised by a very narrow

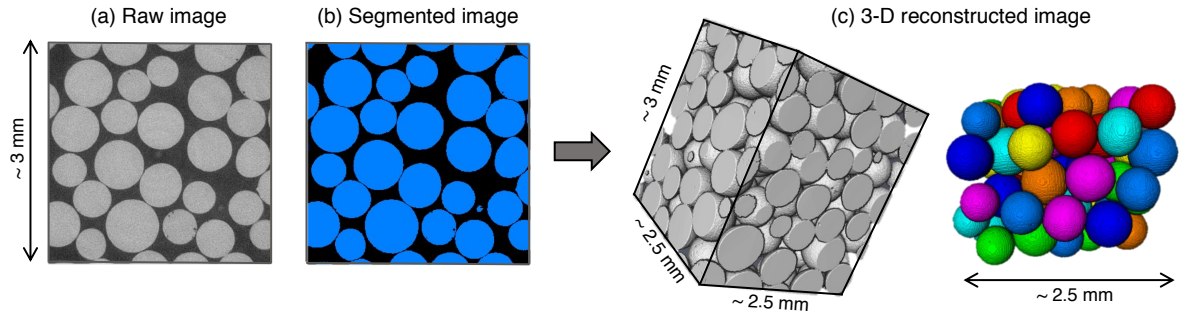

Figure 5.1: Micro-CT image analysis carried out on a small plug of dry unconsolidated beadpack with volume, $V_{\text{plug}} = 0.2$ cm^3). The results are shown for (a) a cross-sectional slice of a grey-scale tomogram (raw data obtained from Micro-CT scans), (b) a segmented 2-D image of (a), and (c) the reconstructed image that presents individual 3-D spherical grains in the beadpack. The analysis has been carried out using AVIZO 9.0. The micro-CT scans are acquired using a voxel size of $(3.8 \times 3.8 \times 3.8)$ μm^3.

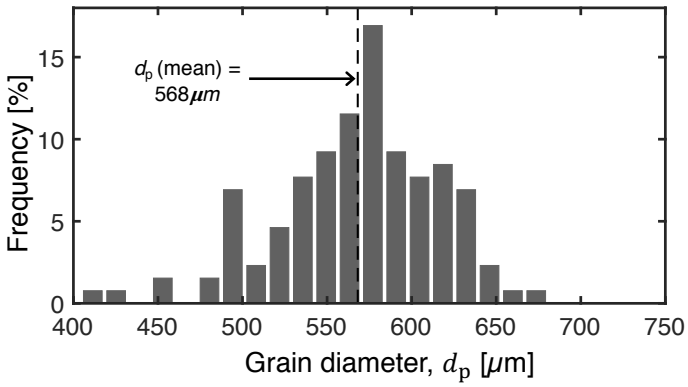

Figure 5.2: Histogram plot of the grain size distribution (GSD) of granular beadpacks. The latter has been analysed using AVIZO-9 following the protocol detailed in Chapter 3. The dashed line corresponds to the estimated average diameter, $d_{\text{p}}(\text{mean}) = 568$ μm. Approximately 250 glass beads were considered in the calculation.

pore-size distribution that possesses inter-granular porosity only. Also presented in Figure 5.3a are the one-dimensional slice-averaged porosity profiles that have been measured by X-ray CT on the large cylindrical samples that show minimal porosity variation along their length (deviations from the average $< 1.0\%$). The homogeneity of the packing is also confirmed by the 3-D porosity map presented in Figure 5.4a, which results in a narrow distribution of porosity with an average total porosity value of $\phi_{\text{T}} = 0.36 \pm 0.01$ (Figure 5.4b). The permeability of the beadpack was estimated from the Kozeny-Carman equation, i.e. $k = \phi_{\text{T}}^3 d_{\text{p},50}^2/(150(1-\phi_{\text{T}})^2) = 2.4 \times 10^{-10}$ m^2 (equivalent to 243 Darcy).

The radiotracer, [^{11}C]NaHCO$_3$ (sodium bicarbonate, half-life, $t_{1/2} = 20.3$ min) with an activity concentration, 0.22 mCi/mL (corresponding to 0.24×10^{-14} mol/mL) was used for the exper-

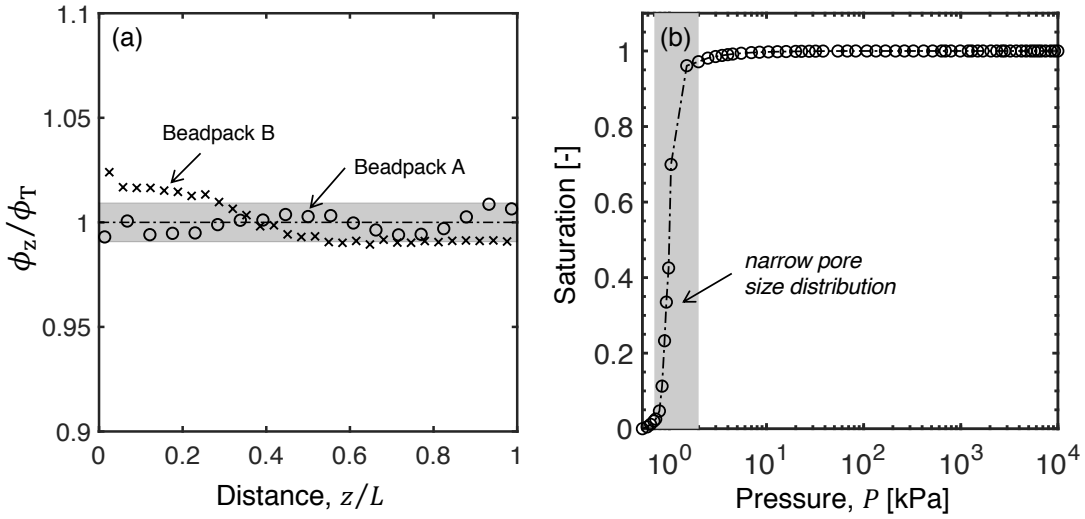

Figure 5.3: (a) Slice-averaged porosity profiles (ϕ_z) along the reduced sample length (z/L) for the beadpacks (L = 15 cm) obtained by X-ray CT. The results include the dataset for two porous systems, including beadpack A (for PET experiments) and beadpack B (for conductivity experiments). The plotted values are normalised with the mean porosity of the core, i.e. $\phi_T = 0.36$ and the shaded region represents 1.0% relative deviation from the mean. (b) The corresponding mercury intrusion curves that have been measured with a Micromeritics Autopore IV on a small sister sample ($V_{plug} \approx 0.3$ cm^3) in the pressure range from vacuum to 22.8 MPa.

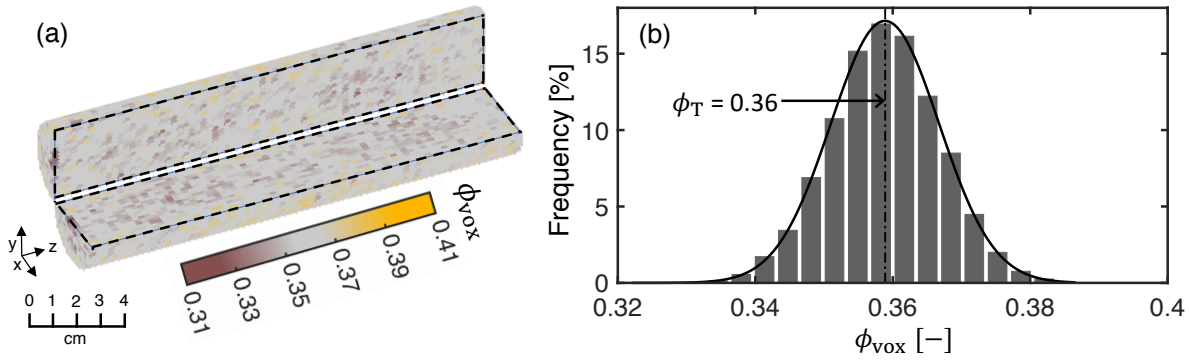

Figure 5.4: Left: 3-D porosity map of the granular beadpack (d = 3 cm, L = 15 cm, voxel dimension: (1.4×1.4×2) mm^3). Both vertical and horizontal cross-sections along the length of the sample are shown. Right: the corresponding histogram indicating the voxel-level porosity values (ϕ_{vox}) of the beadpack. The solid line is the best fit to the normal distribution for the histogram plot, giving an average porosity of 0.36.

iments with PET imaging. The latter was chemically produced at Imanova Limited (Invicro LLC, London, UK) using an aqueous base solution of $KI_{(aq)}$ (2.0wt%). In this case, $KCl_{(aq)}$ (2.3wt%) was used as the background carrier fluid (relative density difference $\sim$ 0.03%, corresponding to the Gravity numbers, $G = 0.019 - 0.18$, as described in Section 4.2.5). An equivalent, non-labelled fluid pair, $KCl_{(aq)}$ (2.3wt%) and $KI_{(aq)}$ (2.0wt%) were considered for the experiments involving conductivity measurements. The volume of tracer injected is 2 mL

for all the experiments.

5.3 Experimental procedure

The measurements reported in this study were performed in the core-flooding apparatus described in Chapter 4. Figure 5.5 shows the core-holder used for the tracer experiments which includes a thin aluminum tube (thickness 1.5 mm, internal diameter, 7 cm), two Delrin end-caps that are secured on each face of the beadpack with threaded nylon rods.

Prior to the experiment, the beads were dried for at least 4 days at 80 °C. Both faces of the two end-caps were covered with two aluminium meshes each (aperture size of 0.085 mm, Advent Research Materials Ltd, UK) and a heat-shrink FEP sleeve (50.8 mm bore, Polyflon Technology Ltd, UK) was slid on one of them. After that, the beads were carefully poured into the sleeve, while gently tapping the end-cap to achieve a random packing. The second end-cap was mounted on top of the pack and the sleeve was carefully heated to achieve a tight annular seal around the sample and the nitrile o-rings (Barnwell, UK) mounted on both end-caps. The confining aluminium tube was slid on the end-caps that were sealed by means of another set of nitrile o-rings, and that were subsequently pressed and secured against the sample by means of four nylon all-thread rods. The annular space was then filled with confining fluid (tap water), while maintaining the core-holder in vertical position, so as to ensure that air was removed from the system. The confining pressure was then increased gradually to the set value of 8 bar and the sample-holder was placed on the bed of the scanning instrument. The system was purged with gaseous CO_2 (purity $> 99\%$, BOC Ltd., UK), followed by the injection of the aqueous carrier solution that was circulated for at least 8 pore volumes (PV) to achieve complete liquid saturation of the pore space. X-ray CT scans of the sample were acquired prior and after injection of the aqueous solution to register its position and to compute porosity maps. The system was allowed to equilibrate at the given flow rate ($q = 2 - 19$ mL/min, see Table 5.1) to reach a stable pressure drop and the tracer solution (with or without radiolabeling) was loaded in the 2 mL sample loop. The experiment started by switching the injection valve and was continued for the time equivalent to the injection of 3 PV, while continuously monitoring the concentration of the solution entering and leaving the sample.

For comparison with results from transport models, the breakthrough profiles need to be corrected for the time spent by the tracer in the tubing between the detectors and the faces of the sample, $t_D = V_D/q$, where V_D is the measured dead volume (3.1 mL in this case) (see Section 4.2.5 for details of the measurement procedure). The linear calibration of the conductivity detectors was carried out on a regular basis by using the baseline and saturation readings of the inlet conductivity detector as reference.

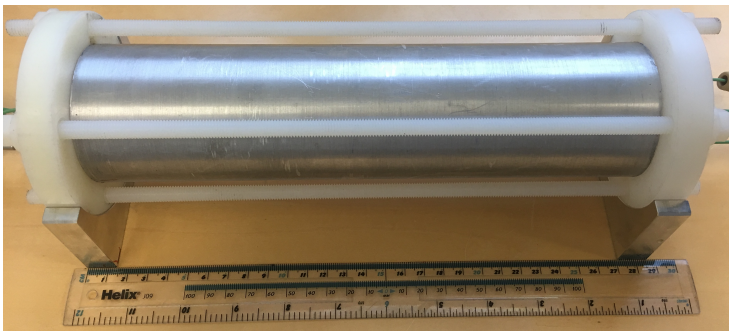

Figure 5.5: Snapshot of the core-holder used to conduct the experiments involving unconsolidated beadpacks. The design is similar to Figure 4.3 shown in Chapter 4, but has been adapted to minimise the deformation of the packed beads when sliding into the core-holder.

5.4 Modelling and data analysis

5.4.1 Modelling approach and parameter optimisation

The well-known one-dimensional Advection Dispersion Equation (ADE) is used to describe the transport of solute in the granular beadpack, i.e.

$$\phi_T \frac{\partial c}{\partial t} + u \frac{\partial c}{\partial z} = \phi_T D_L \frac{\partial^2 c}{\partial z^2} \tag{5.1}$$

where D_L is the longitudinal dispersion coefficient, c is the tracer concentration, u is the superficial fluid velocity, t and z are the time and space coordinates. The model is solved numerically by using a finite-difference approach with backwards and central differences for the spatial derivatives. The ordinary differential equations (ODEs) are solved using the `ode15s` solver in MATLAB, with the following specifications; total grid points of $N_g = 800$ (corresponding to a constant grid size, $\Delta x = 0.019$ cm); maximum time step of $\Delta t = 0.01$ minutes; relative (`RelTol`) and absolute error tolerances (`AbsTol`) have been set to 1×10^{-2} % and 1×10^{-4} mCi/mL or

$1 \times 10^{-2} \times c_{\mathrm{o}}$ g/mL, respectively. The initial and boundary conditions used for the ADE model follow the expressions given by Danckwerts (Fogler, 1999), which is given in Section 7.4.

For the range of Péclet numbers tested (Pe = 25 − 250), the transport is dominated by advection, and the following expression for dispersion coefficient applies: $D_{\mathrm{L}} = \alpha_{\mathrm{L}} v$ (Dullien, 1992), where v is the (pore) interstitial velocity ($v = u/\phi_{\mathrm{T}}$). In this work, the longitudinal dispersivity, α_{L} was treated as the sole fitting parameter for the entire experimental dataset (five flow rates and eight experiments in total, see Table 5.1).

Optimisation of the dispersivity is achieved by means of Genetic Algorithm solver II (GA) in the MATLAB global optimisation toolbox, while minimising the following objective function:

$$J = \sum_{i=1}^{N_{\mathrm{q}}} \sum_{j=1}^{N_{\mathrm{p}}} \frac{(\widetilde{c}_{i,j}^{\,\mathrm{out}} - c_{i,j}^{\,\mathrm{out}})^2}{c_{\mathrm{max},i}^{\mathrm{out}}} \tag{5.2}$$

where N_{q} is the number of flow rate; N_{p} is the number of experimental data points of each measured effluent profile; $\widetilde{c}^{\,\mathrm{out}}$ and $c^{\,\mathrm{out}}$ are the predicted, and the measured effluent concentration breakthrough curves (BTCs), respectively. In order to provide an equal weight to each curve, the least-squares objective function is normalised by the maximum measured concentration of each dataset, i. In the algorithm, the number of generations were set at 50, and population size at 24. The upper and lower bounds for the optimisation were taken as $\alpha_{\mathrm{L}} = [0.01,\ 0.1]$ cm. Further details of the genetic algorithm used in this work, including the advantages of the proposed optimisation approach can be found in Section 7.4.2.

5.4.2 Residence time distributions functions and dilution index

Experimental and modelling results have been additionally evaluated within the Residence Time Distribution (RTD) framework (Fogler, 1999). When applied to the computed effluent concentration, c^{out}, the *normalised* RTD function $E_{\Theta}(\Theta)$ is defined as follows,

$$E_{\Theta}(\Theta) = \tau_{\mathrm{exp}} E(t) \tag{5.3}$$

where $\Theta = t/\tau_{\text{exp}}$ is a reduced time that represents the number of pore volumes that have flowed through the sample up to time t, while $E(t)$ is the classic RTD function:

$$E(t) = \frac{c^{\text{out}}(t)}{\int_0^\infty c^{\text{out}}(t)dt} \tag{5.4}$$

As such, $E(t)$ provides a normalisation of the data that is required when comparing results from different experimental runs using tracers in different amounts and of different type (brine vs. radioisotopes); $E_\Theta(\Theta)$ also removes dependency on system size and average residence time. The mean residence time of the distribution is obtained by computing the first moment of the RTD function, i.e.

$$\tau^*_{\text{exp}} = \int_0^\infty tE(t)dt \tag{5.5}$$

where the subscript 'exp' is added here to distinguish the mean residence time obtained from the experiment from the theoretical counterpart, i.e. $\tau = \phi_{\text{T}}AL/q$, where A is the cross-sectional area of the core. As described in Section 5.3, the mean residence time obtained from the application of Eq. 5.5 to the experimental data needs to be corrected for the "dead" volume, V_{D}. An additional correction is applied to both numerical simulations and experiments to account for the mean residence time of the tracer input function, i.e. $\tau_{\text{exp}} = \tau^*_{\text{exp}} - \tau_{\text{inj}} - V_{\text{D}}/q$.

The material balance in both experiments and simulations is verified by quantifying the error $\varepsilon = 1 - M^{\text{out}}/M^{\text{in}}$, where the mass of tracer M is computed as,

$$M = q\int_0^\infty c(t)dt \tag{5.6}$$

which is thus applied to both the inlet ('in') and outlet ('out') tracer profiles. We note that for all numerical simulations reported in this study this error was always below 0.4%, while tracer recoveries in all the experiments were greater than 95%.

The extent of subcore-scale mixing within the homogeneous beadpack has been investigated by means of dilution index, Γ (Kitanidis, 1994), and can be obtained from,

$$\Gamma(t_i) = V_{\text{vox}} \exp\Big[-\sum_{j=1}^{N_{\text{v}}} P_j(t_i)\ln(P_j(t_i))\Big] \tag{5.7}$$

where $P_j(t_i) = M_j/M$ is the ratio of solute mass in voxel j to the total mass of tracer in the system; N_v is the number of voxels, V_{vox} is the voxel volume and t_i is the time frame over which the given PET image has been reconstructed. To make comparisons with results from the one-dimensional ADE, Γ is also calculated upon assuming complete mixing of the solute in the radial direction; in this case M_j is the observed slice-averaged solute mass, and V_{vox} and N_v are the slice volume and number of slices in the sample, respectively.

5.5 Results

As an example of general validity, Figure 5.6 presents a selection of tracer breakthrough curves for experiments conducted on glass beadpack ($q = 10$ mL/min). The curves are reported in terms of the normalized RTD function, E_Θ, as a function of the reduced time, $\Theta = t/\tau_{\text{exp}}$. In the figure, three sets of curves are plotted that represent repeats of the same experiment using brine and radioactive tracers. An excellent agreement is observed for the three independent curves, thus verifying (i) the reproducibility of the experiments, (ii) the validity of the measurement approach (conductivity vs. radioactivity) and (iii) the suitability of the selected tracers. As expected, the beadpack shows a narrow and symmetric profile centred around the expected mean residence time ($\Theta = 1$); this is characteristic of a very homogeneous material. In the following, the experimental results obtained over a range of flow rates (or Péclet number, Pe) are analysed by following a systematic approach that includes (i) verification of the material balance, (ii) residence time distribution (RTD) analysis and model validation, and (iii) investigation of the internal dynamic displacement of the tracer by PET.

5.5.1 Effluent breakthrough curves

Table 5.1 provides a summary of all the tracer tests conducted on glass beadpack covering the range of Péclet numbers, Pe $= 25-250$. We note that there is a very good agreement between the expected (τ) and the measured (τ_{exp}) mean residence time of the system, with deviations that are generally less than 1% for the range of flow rates studied. Similarly, a good mass recovery is generally observed ($M^{\text{out}}_{\text{exp}}/M^{\text{in}}_{\text{exp}} > 0.95$), confirming that the selected tracer ($\text{KI}_{(\text{aq})}$) can be regarded as conservative. As anticipated by the the excellent agreement shown in Figure 5.6,

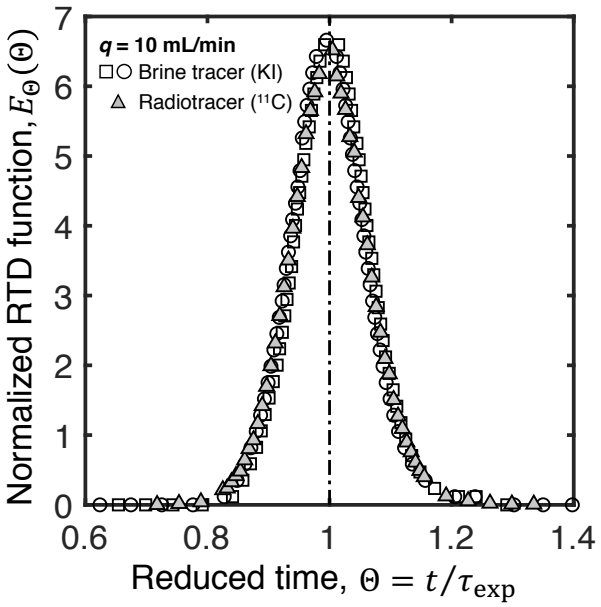

Figure 5.6: Normalised RTD function, E_Θ, as a function of the reduced time, $\Theta = t/\tau_{\text{exp}}$, for experiments carried out on beadpack ($q = 10$ mL/min) using a combination of tracers, namely $\text{KI}_{(\text{aq})}$ (for conductivity measurements) and the radio-isotope ^{11}C (for radioactivity measurements)

similar conclusions can be drawn for the experiment conducted with the ^{11}C radiotracer (last row in Table 5.1, corresponding to Pe = 130).

The tracer breakthrough concentration profiles measured at various flow rates are shown in Figure 5.7b for the experiments with $\text{KI}_{(\text{aq})}$ as tracer, together with a typical inlet pulse concentration profile (Figure 5.7a). In the figure, experimental data are given as symbols, while the solid lines refer to results obtained from the solution of the one-dimensional ADE model. The latter uses the longitudinal dispersivity as the sole fitting parameter for the whole dataset, yielding an optimum value of $\alpha_{\text{L}} = 0.029$ cm (with $J = 0.102$ g/mL after minimisation). The corresponding flow-rate dependent values of the longitudinal dispersion coefficient (D_{L}) are summarised in Table 5.1. The numerical simulations were run using a square function to describe the input pulse, while matching the experimentally injected mass of tracer ($M_{\text{exp}}^{\text{inj}}$). It can be seen that in 5.7b the model closely predicts the experimental outlet breakthrough profiles over the whole range of flow rates studied. The obtained dispersivity value is in close agreement with experimental observations reported in the literature for homogeneous bead- and sand-packs (Dullien, 1992), where $\alpha_{\text{L}} \approx 0.5 d_{\text{p}}$ (which correspond to $\alpha_{\text{L}} \approx 0.028$ cm for the beadpacks used in this study).

Table 5.1: Overview of the experiments conducted on glass beadpacks. Reported variables are: volumetric flow rate (q), average residence time ($\tau = \phi_T AL/q$), mean residence time of injected pulse (τ_{inj}), mean residence time of effluent (τ_{exp}, with the corresponding error $\varepsilon = 1 - \tau_{exp}/\tau$), recovered mass of tracer (M_{exp}^{out}, with the corresponding error $\varepsilon = 1 - M_{exp}^{out}/M_{exp}^{inj}$). A correction is applied to the computed mean residence time to account for the volume of the tubing between the outer faces of the sample and the conductivity cells (V_D = 3.1 mL); for the experiments with the radiotracer, V_D = 0 mL, because the inlet and outlet breakthrough profiles have been obtained directly from the PET images. The volume of tracer injected in each experiment is 2 mL.

q [mL/min]	τ [min]	τ_{inj} [min]	τ_{exp} [min]	M_{exp}^{out} [g]	D_L [cm^2/min]
2.0	52.90	0.68	53.22 (0.6%)	0.130 (1.5%)	0.009
5.0	21.16	0.25	21.32 (0.8%)	0.132 (-0.8%)	0.023
5.0	21.16	0.26	21.16 (0.0%)	0.132 (0.1%)	0.023
10.0	10.58	0.12	10.51 (0.7%)	0.139 (-4.5%)	0.045
10.0	10.58	0.12	10.59 (0.1%)	0.127 (3.8%)	0.045
15.0	7.05	0.10	7.12 (1.0%)	0.130 (0.8%)	0.068
19.0	5.57	0.08	5.64 (1.2%)	0.132 (1.5%)	0.086
q [mL/min]	τ [min]	τ_{inj} [min]	τ_{exp} [min]	M_{exp}^{out} [mCi]	D_L [cm^2/min]
10.0	10.94	0.11	11.03 (0.8%)	0.433 (–)	0.045

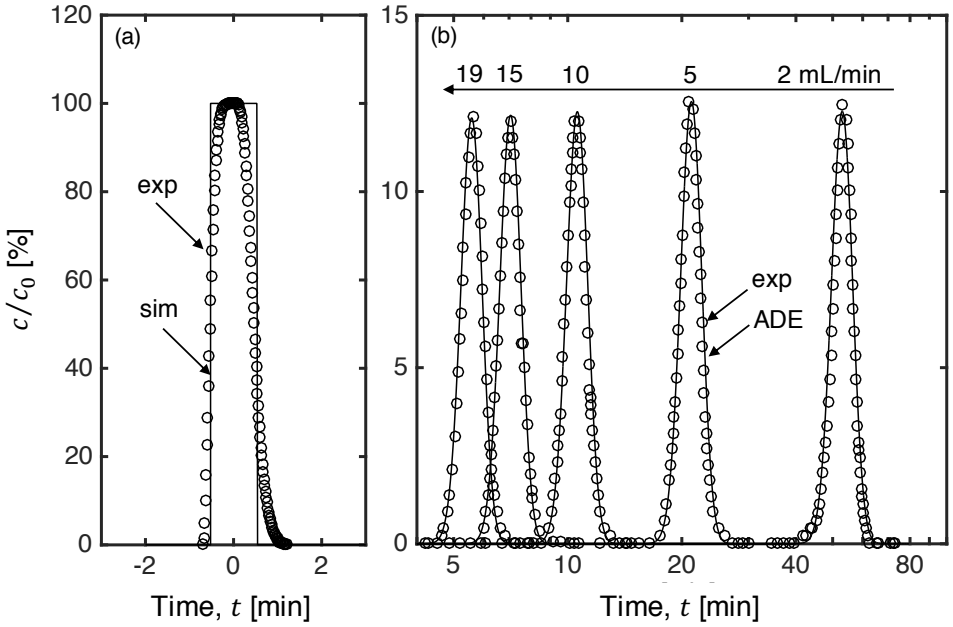

Figure 5.7: Results from the pulse-tracer experiments conducted on glass beadpack at flow rates q = 2 − 19 mL/min, corresponding to Pe =25, 65, 130, 195 and 247. Concentration profiles have been obtained from conductivity measurements at the (a) inlet (q = 2 mL/min shown as example) and (b) effluent side of the sample. The symbols represent experimental data, while solid lines refer to model results (ADE) using a fitted dispersivity, α_L = 0.029 cm. Concentration values are normalised by the feed concentration, c_0. Time in figure (b) is presented using a logarithmic scale.

5.5.2 Internal profiles

Figure 5.8 shows the internal concentration profiles at various times along the length of the sample for the experiment conducted at $q = 10$ mL/min using the radiotracer ^{11}C that was imaged using PET. Six profiles are shown in the figure, each of them representing a 20-second time frame. These profiles have been obtained from the reconstructed PET scan by averaging voxel concentration values within each 2 mm-thick slice. Results from application of the ADE are also shown in the figure (dashed lines) and confirm the excellent agreement observed above in the analysis of the tracer breakthrough profiles. We note that the model has been applied here in a fully predictive manner, i.e. by using the dispersivity value that was obtained from fitting the effluent breakthrough curves (brine tracer). The agreement between model and experiments confirms the well-known ability of the one-dimensional ADE to capture solute transport in homogeneous porous media, such as beadpacks. Most significantly, these results provide an important verification of the suitability of PET to enable dynamic measurement of the spatial distribution of the tracer concentration within an opaque porous medium non-invasively.

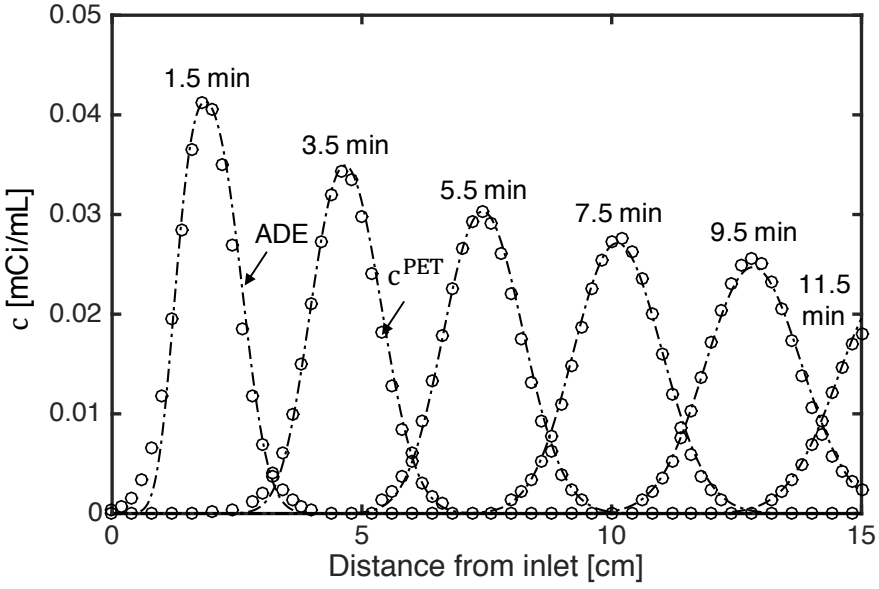

Figure 5.8: Slice-averaged internal concentration profiles along the length of the sample obtained from PET experiments on glass beadpack at various times (t =1.5, 3.5, 5.5, 7.5, 9.5 and 11.5 min). The experiment has been conducted at a volumetric flow rate $q = 10$ mL/min and each time represents a 20-second time frame, corresponding to about 0.15, 0.3, 0.5, 0.7, 0.9 and 1.1 PV injected). Experimental data are shown by symbols, while the dashed lines are predictions from the one-dimensional solution of the ADE ($\alpha_L = 0.029$ cm).

5.5.3 Three-dimensional imaging of solute transport

Three-dimensional images of the tracer activity in the uniform beadpack are shown in Figure 5.9 for the experiment carried out at $q = 10$ mL/min. On the left-hand side of the figure are shown experimental results corresponding to about 0.25, 0.5 and 0.75 PV injected. In the figure, both vertical and horizontal cross-sections along the sample are shown, which indicate that the displacement remains fairly uniform in all directions. We note that the tracer plume moves along the vertical plane at a slight (and constant) angle. This is most likely caused by core-holder inlet end-effects, which have distorted the injected tracer plume. Nevertheless, this effect is quite small, as confirmed by the close agreement between the experimental and model-predicted one-dimensional profiles discussed earlier. The corresponding three-dimensional reconstructions of the tracer plume obtained from the numerical solution of the one-dimensional ADE are shown on the right-hand side of Figure 5.9. As anticipated by the experimental observations, there is uniform mixing of the tracer plume as it moves through the sample. The growth of the mixing zone is evidenced by the slight discolouring of the solute plume with increasing distance travelled, which again reproduces quantitatively the behaviour captured by the PET scans. Support to this observation is provided by the value of dilution index that has been computed from Eq. 5.7 at the three times shown in the figure for both experiment and 1-D simulation. The obtained values (normalised by the volume of the sample, i.e. $\Pi = \Gamma / V_{\text{core}}$) are $\Pi_{\text{3D}}^{\text{exp}} = 0.18$, 0.20 and 0.23 for PV = 0.25, 0.5 and 0.75, respectively. As expected, the dilution index increases with distance travelled, as a result of the dispersion process. Most significantly, these estimates are in very good agreement with their numerical counterpart, i.e. $\Pi_{\text{1D}}^{\text{mod}} = 0.18$, 0.22 and 0.25, and with the corresponding experimental values computed using slice-averaged properties ($\Pi_{\text{1D}}^{\text{exp}} =$ 0.19, 0.22 and 0.25). These observations confirm the suitability of the one-dimensional ADE to describe subcore-scale mixing inside the beadpack.

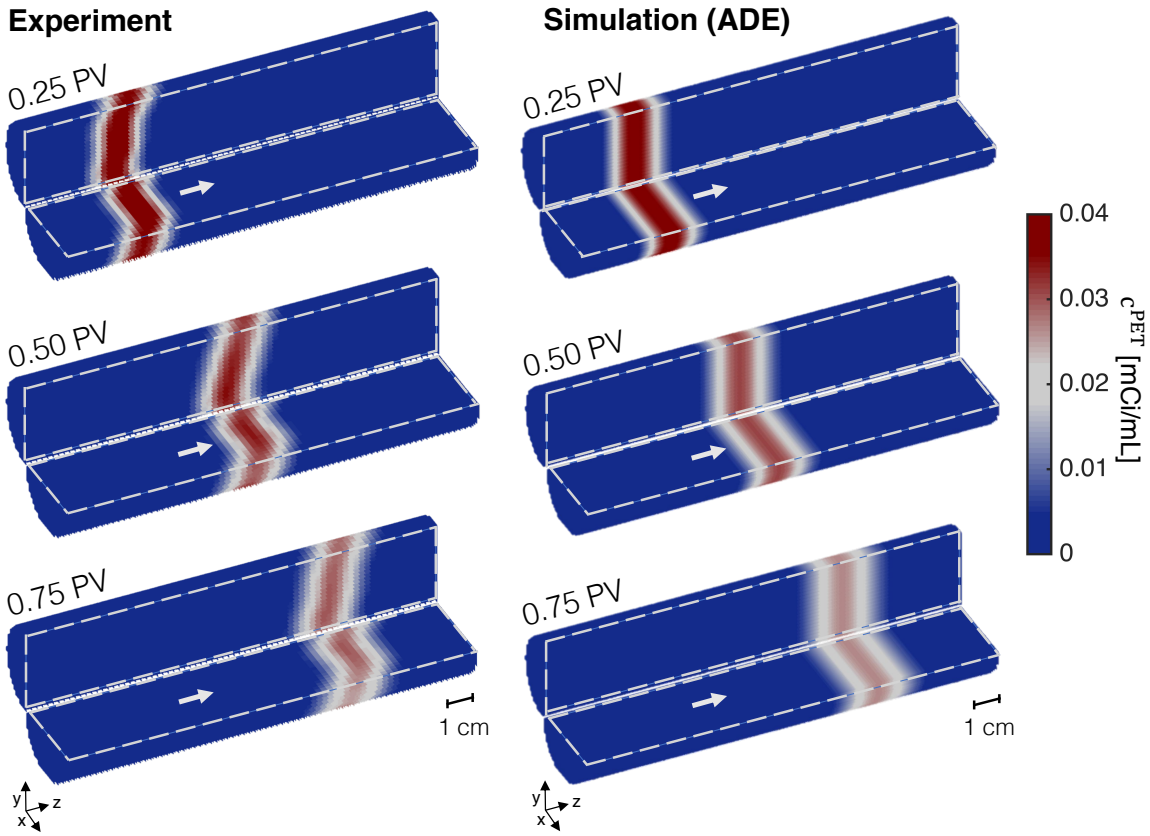

Figure 5.9: 3-D concentration maps of the tracer plume in glass beadpacks at distinct times, namely 2.7, 5.4, and 8.1 min (±0.16 min) and corresponding to the injection of 0.25, 0.50 and 0.75 PV. The experimental data (on the left) are obtained from the PET scans and are compared to the 3-D reconstructions of the numerical solution of the one-dimensional ADE (on the right). The experiment has been conducted at $q = 10$ mL/min. Voxel size: $(1.4{\times}1.4{\times}2)$ mm^3.

5.6 Discussion

5.6.1 Characteristic RTD functions

Normalised RTD functions $E_\Theta(\Theta)$ are reported in Figure 5.10 for the tracer experiments on beadpacks. The experimental dataset includes measurements obtained at all flow rates, with different tracers and upon injecting them in different amounts; nevertheless, all data gather around a single E_Θ curve, which can thus be interpreted as a characteristic function of the given system, irrespective of its size and average residence time (Fogler, 1999). In the figure, the solid line represents the corresponding prediction by the ADE, which treats mechanical dispersion as a Fickian process with a constant longitudinal dispersivity, α_L. The excellent agreement between experiments and model for $\mathrm{Pe} = 25 - 250$ supports the applicability of this approach and,

accordingly, the attainment of an asymptotic longitudinal dispersion coefficient, $D_{\mathrm{L}} \propto \mathrm{Pe}$. This last observation further indicates that transport behaviour has become Gaussian, in agreement with predictions based on the Continuous Time Random Walk (CTRW) formulation. In fact, for fairly homogeneous porous media (e.g., the sandpacks with $\beta > 1.6$ discussed in Berkowitz et al. (2006)) the timescale on which D_{L} approaches a constant value is given by the time needed to traverse a characteristic inter-pore layer distance l by diffusion, i.e. $t_{\mathrm{diff}} = l^2/2\mathcal{D}$; by further defining $t_{\mathrm{adv}} = l/v$ as the time for the solute to travel the same distance by advection, then $l^* = t_{\mathrm{diff}}/t_{\mathrm{adv}} = \mathrm{Pe}/2$ represents the required number of characteristic lengths l travelled to reach the asymptotic regime (Bijeljic et al., 2011) (note that $l^* = \tau_2$ in the CTRW formulation by Berkowitz et al. (2006)). For the beadpacks used in this study $l = d_{\mathrm{p}} \approx 0.5$ mm and $l^* = 13-125$ for $\mathrm{Pe} = 25 - 250$, corresponding to $6 - 63$ mm; this distance is indeed well below the length of the cylindrical pack ($L = 100 - 150$ mm).

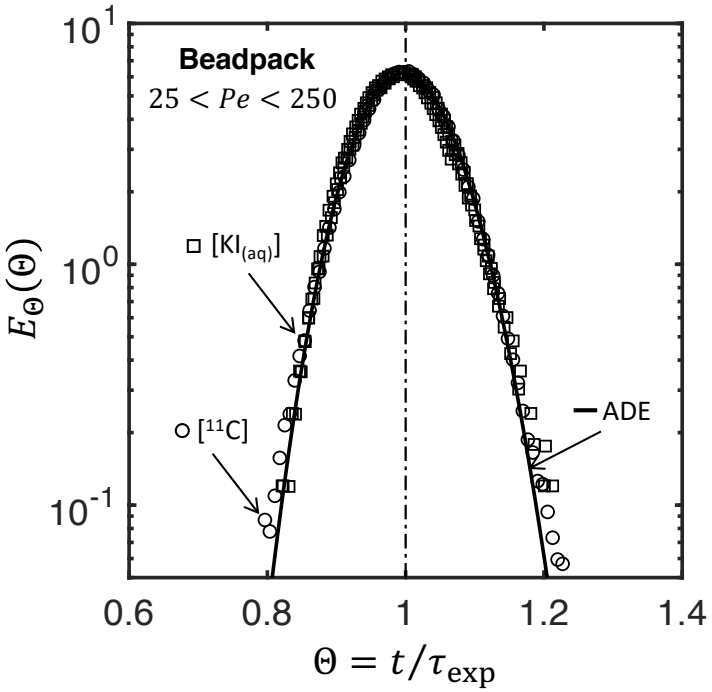

Figure 5.10: Normalised RTD function, E_Θ, as a function of the reduced time, $\Theta = t/\tau_{\mathrm{exp}}$, for all the experiments carried out in this study on uniform beadpack ($25 < \mathrm{Pe} < 250$, Table 5.1). The symbols correspond to the experimental data obtained from radio-tracer [^{11}C] (circles) and brine-tracer [$\mathrm{KI_{aq}}$] (squares). The solid lines refers to numerical solution of the ADE model.

5.6.2 Correlating longitudinal dispersion coefficients

The longitudinal dispersion coefficients obtained upon fitting the tracer breakthrough curves are shown in Figure 5.11 as a function of the Péclet number for the beadpacks investigated in this study. The results from this study (full symbols) are compared to literature data (empty symbols) and correlations reported in the literature. The latter take the following general form (Sahimi et al., 1986),

$$D_{\mathrm{L}}/\mathcal{D} = 1/\sqrt{2} + \sigma \mathrm{Pe}^{m} \tag{5.8}$$

where σ and m are constant parameters, associated with the porous medium and the flow regime, respectively. In particular, previous modelling work has convincingly shown that a sequence of two transport regimes exist when advection dominates over diffusion ($\mathrm{Pe} > 5$), namely the boundary-layer dispersion regime ($m \approx 1.2$) followed by the mechanical dispersion regime, where $m \approx 1$ (Saffman, 1959; Sahimi et al., 1986; Bijeljic et al., 2004). While the boundary between these two regions is not very clear (Salles et al., 1993), we also note that the departure of the power-law regime ($D_{\mathrm{L}}/\mathcal{D} \sim \mathrm{Pe}^{1.2}$) from a pure linear behaviour ($D_{\mathrm{L}}/\mathcal{D} \sim \mathrm{Pe}$) is rather modest and comparable to the (inherent) uncertainty that affects dispersion coefficients measured experimentally. In fact, published measurements on sand- and bead-packs show a significant scatter in the experimental data, and can only be correlated with the general relationship above when $\sigma \approx 0.5$ and $1 < m < 1.2$ for $\mathrm{Pe} \approx 5 - 300$ (for a collection of more than 150 data-points see Bear (1972)) or when $0.25 < \sigma < 2.5$ and $m = 1$ for $\mathrm{Pe} \approx 1 - 800$ (see Figure 5.11). Several factors were considered to be the reason for the deviation: such as differences in measuring technique, apparatus, packing materials and methods used and other aspects (e.g. wall effects) (Delgado, 2007). Accordingly, m has been set equal to unity in this study to be consistent with the use of the ADE formulation (Berkowitz et al., 2006); this further enables the definition of a constant dispersivity coefficient, $\alpha_{\mathrm{L}} = D_{\mathrm{L}}/v = \sigma d_{\mathrm{p}}$, which thus represents a characteristic property of the porous medium (and the sole fitting parameter in the ADE) (Steefel and Maher, 2009). Notably, our results on beadpacks ($d_{\mathrm{p}} = 568$ μm) closely follow the trend predicted by the correlation above when using (again) $\sigma = 0.5$, i.e. the longitudinal dispersivity in uniform beadpacks is $\alpha_{\mathrm{L}} \approx d_{\mathrm{p}}/2$, a result that is also consistent with predictions based on a random-walk model (Gist et al., 1990). By confirming the reliability of the estimated dispersion coefficients,

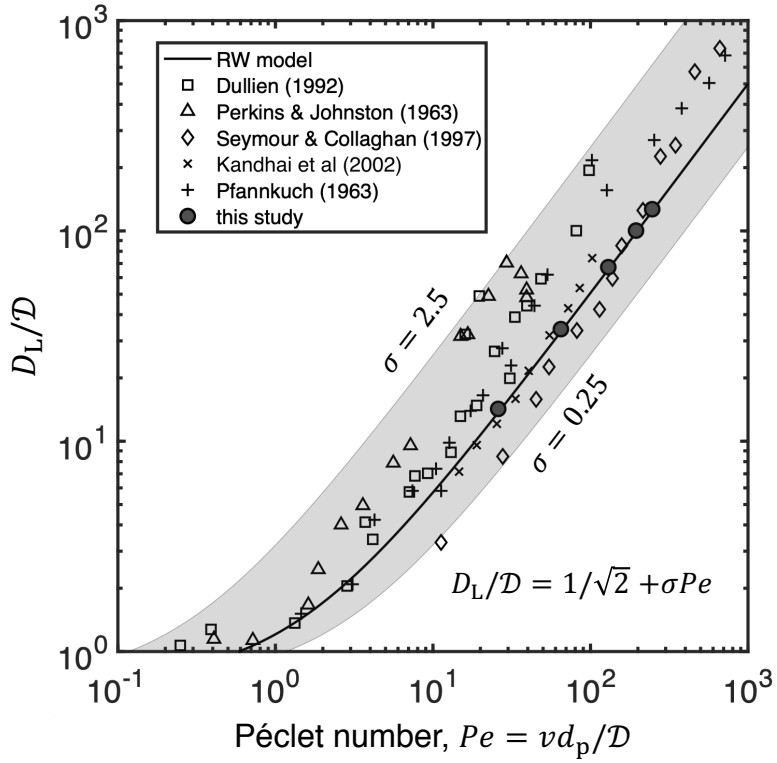

Figure 5.11: Dispersion dataset on sand/beadpacks plotted in terms of normalised longitudinal dispersion coefficient ($D_L/\mathcal{D}$) as a function of Péclet number, Pe. The results obtained from this study are shown as dark-filled symbols. The empty symbols are the literature data (that covers Péclet numbers, Pe $= 0.1 -$ 1000), collected from various sources, i.e. (Pfankuch, 1963; Perkins and Johnston, 1963; Dullien, 1992; Seymour and Callaghan, 1997; Kandhai et al., 2002). These experimental measurements are described by a widely used correlation for dispersion in porous media (Sahimi et al., 1986), i.e. $D_L/\mathcal{D} = 1/\sqrt{2} + \sigma$Pe, with $\sigma = 0.25 - 2.5$ (shaded region). The latter is reduced to Random Walk (RW) theory when $\sigma = 0.5$ (solid line) (Gist et al., 1990).

this result also supports the suitability of our experimental design and apparatus, where mixing in the tubing and from the porous sample is minimised.

5.7 Concluding remarks

We have undertaken a numerical and experimental study in which solute transport in uniform beadpacks has been investigated over a wide range of Péclet numbers (Pe $= 25 - 250$). Miscible displacements were conducted by combining classic pulse-tracer tests with the simultaneous imaging of the transport of radiotracer using PET. The experimental protocol was successfully validated by comparing results obtained from the corresponding brine-tracers. To appropriately describe the experimental observations, the well-known ADE model has been applied and thor-

oughly evaluated with both the tracer effluent history and the the internal concentration profiles measured by PET. Over the flow rates investigated in this study, we observe a linear dependence of the dispersion coefficient on the Péclet number ($D_{\mathrm{L}} \propto \mathrm{Pe}$), leading to a constant value of dispersivity, i.e. $\alpha_{\mathrm{L}} = 0.029$ cm. The latter represent an intrinsic parameter of the porous medium that is consistent with theory, as predicted by the random-walk model (i.e. $\alpha_{\mathrm{L}} = 0.5 d_{\mathrm{p}}$). In this context, this result provides a more consistent picture than the dispersion measurements reported in the literature on sand/beadpacks. As demonstrated by the close agreement with the ADE model for describing the experimental internal profiles, we show that PET allows for precise imaging of solute transport at a resolution of about 4 mm^3. This is further demonstrated by the very good agreement between the experimental dilution index and the values computed from the ADE over three discrete time intervals. Such observations confirm the ability of PET to provide quantitatively the highly-resolved spatial and temporal information on the fundamental mechanisms governing the dispersion process. This is a key to advance our understanding of anomalous transports in natural heterogeneous rocks because PET enables accurate and direct measurements of local spreading and mixing inside an opaque porous medium, as discussed in the next chapters of this thesis.

Chapter 6

Rock Samples Characterisation

6.1 Introduction

Rocks show heterogeneities over a wide range of length scales (from nanometers to kilometers), including complicated pore and grain structures, that form multiscale porosity, from micro- (submicron pores) to vuggy pores (with pore sizes that are much larger than the corresponding grains or crystals) (Lucia, 1983). This structural complexity has been shown to greatly affect fluid flows during both single (Pini et al., 2016; Walsh and Withjack, 1994) and multiphase displacements (Krause et al., 2009; Perrin and Benson, 2010). In particular, unexpected flow behaviours have been reported, such as an *apparent* dependence of the relative permeability on fluid flow rate (Reynolds and Krevor, 2015; Krause and Benson, 2015), and the so-called 'non-Fickian' transport as described in Chapter 2. However, due to insufficient information on the internal rock structure (such as local porosity, permeability and pore size distributions), the detailed connection between the physical characteristics of the rock and the dynamic behaviour of the fluid remain inconclusive in the open literature. The term 'anomalous' transport is hence introduced to describe solute transport in these complex rocks (Dentz et al., 2017). In this chapter, we present an experimental framework for the multidimensional characterisation of rock petrophysical properties. We deploy a combination of multiscale imaging techniques, including micro- and medical X-ray Computed Tomography (CT) to provide three-dimensional structural details of the rock sample both at the pore- (μm) and core-scale (mm-cm). A combination of Helium pyconometry and Mercury intrusion porosimetry were applied to obtain pore

size distributions. This information will be used in the subsequent chapters to improve the fundamental understanding of dynamic mixing and dispersion processes in rock cores, including both sandstones and carbonates.

6.2 Materials and Methods

6.2.1 Rock samples

In this study, we perform the comprehensive analysis on three cylindrical rock cores (diameter: $d = 51$ mm, lengths: $L = 100-103$ mm), namely Bentheimer Sandstone (BS, Kocurek Industries INC, Caldwell, TX, USA), Edwards Brown Carbonate (EB, Kocurek Industries INC, Caldwell, TX, USA) and Ketton Limestone (KL, Ketton Quarry, Rutland, UK). It was observed that these rock cores possess very different characteristic features, such as complicated pore and grain structures (BS, EB), significant proportion of microporosity (EB and KL) as well as macroscopic porosity vugs (EB). BS is a relatively homogeneous sample comprised of angular grains that are dominated by quartz (95%) with tracer amount of clay and feldspar minerals (Andrew et al., 2014). The carbonate cores present a more heterogeneous environment, with EB consisting dominant proportion of $CaMg(CO_3)_2$ (dolomite) and $CaCO_3$ (calcite), and KL that contains $CaCO_3$ of approximately 98% (Lai et al., 2015).

6.2.2 Methodology

A flow chart of the material characterisation techniques applied in this chapter is given in Figure 6.1. To characterise the heterogeneity of the samples, up to six small cylindrical plugs (diameter 8 mm, length 10 mm) were drilled from the main core of each rock type. The core-plugs were prepared using a Scheppach Top Pillar DP16SL bench drill (Figure 6.1) with a 1 cm diameter drill bit. Measurements of skeleton density were performed by Helium pycnometry using a Micromeritics AccuPyc II 1340. With the latter, a sample of known mass is first placed in the compartment of a known volume, followed by purging Helium into the chamber at a set temperature and pressure of 25 ^{o}C and 135 kPa, respectively. The system is then allowed to equilibrate, and the *apparent* density measured based on Boyle's Law. This is followed by the

acquisition of capillary pressure curve by mercury intrusion porosimetry (MIP) in the pressure range from vacuum to 22.8 MPa using a Micromeritics Autopore IV 9500. The experiment was carried out at room temperature (~23 ^{o}C) and a penetrometer (Micrometritics, 3 mL sample volume, 0.39 mL intrusion volume) was used for this purpose. Details of the micro- and medical CT instruments used, including the scanning parameters for data acquisition are described in Chapter 3.

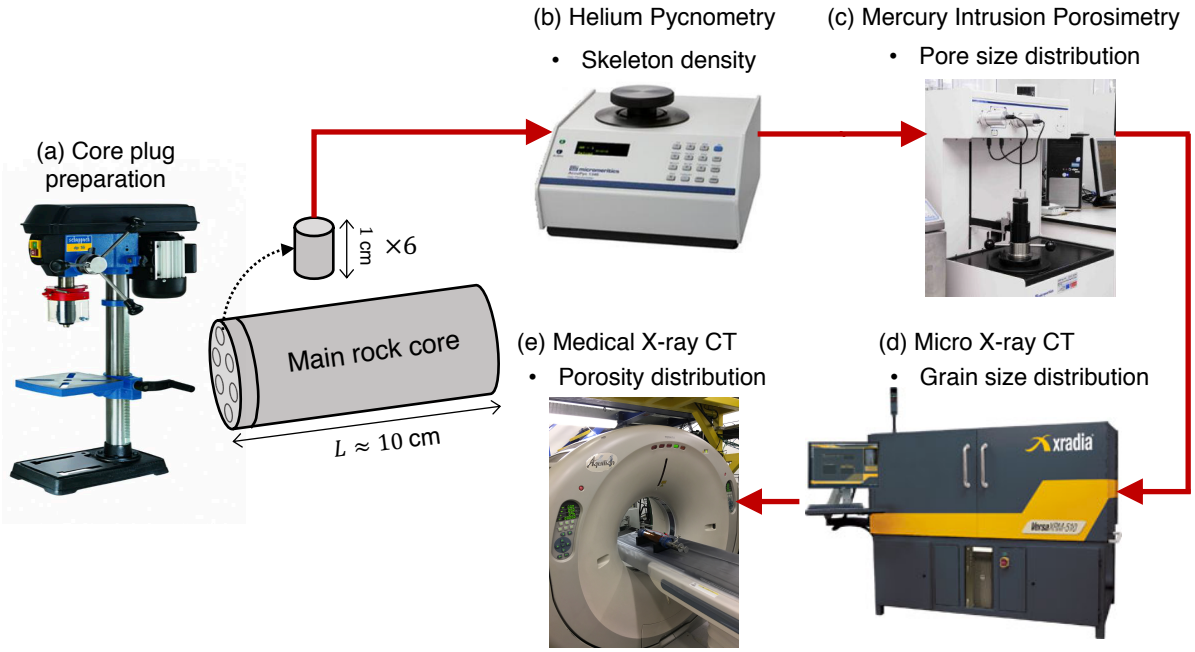

Figure 6.1: Flow chart of the material characterisation techniques considered in this chapter.

6.3 Helium pycnometry and Mercury intrusion capillary pressure measurements

As described in Pini and Benson (2013), Helium pycnometry is needed to correct the MIP curve for unresolved pore space to obtain a reliable estimate of the total sample porosity, $\phi_{\mathrm{T}} = 1 - \rho_{\mathrm{env}}/\rho_{\mathrm{sk}}$. The corresponding values of the skeletal (ρ_{sk}) and envelope (bulk) density (ρ_{env}) of the three rocks are reported in Table 6.1.

Figure 6.2 presents the capillary pressure curves measured for the three rock types. The results are shown in terms of saturation (i.e. cumulative intrusion normalised by the total intruded

Table 6.1: Petrophysical properties of the rock samples obtained from Helium pycnometry and Mercury intrusion porosimetry.

Property	**Bentheimer S**	**Ketton L**	**Edwards B**
Skeletal density, ρ_{sk} [g cm^{-3}]	2.64	2.77	2.85
Bulk density, ρ_{env} [g cm^{-3}]	2.01	2.01	1.55
Total porosity, ϕ_T [–]	0.24	0.28	0.46

volume) over elevated pressures from vacuum up to 22.8 MPa. The capillary pressure, P_c, is translated into an equivalent pore throat radius, r_p, via the Young-Laplace equation:

$$r_p = 2\gamma_{surf}\cos(\theta)/P_c \tag{6.1}$$

where $\gamma_{surf} = 485$ mN/m is the surface tension for mercury/air and $\theta = 2.4435$ rad is the contact angle. The pore throat size distribution is obtained from the measured change in the mercury saturation, S_{nw}, i.e.

$$f(r_p) = dS_w(P_c)/dr_p \tag{6.2}$$

where $S_w(P_c) = 1 - S_{nw}(P_c)$ is the wetting phase saturation. In Figure 6.3 are shown the pore-throat size distribution curves obtained for BS, EB and KL. These are composite curves that have been obtained upon combining the curves measured on the mm-plugs for each rock sample and are therefore representative of a sample with volume of about $1 - 2$ cm^3. Note that in the figure the distributions have been weighted by the radius, $r_p f(r_p)$, so that the incremental area under the curve is proportional to the fractional volume of the pores associated with that r_p.

The pore entry size distribution of the BS (Figure 6.3a) is largely unimodal with a single distinct peak at about 15 μm. It is also shown that a very small fraction of intra-particle pores are present at $r_p \approx 0.01$ μm,. This can be attributed to the presence of modest proportion of clay minerals (∼3% (Peksa et al., 2017)) where significant degree of intra-granular porosity is typically observed (Aylmore and Quirk, 1967). In contrast, the two carbonate samples (EB and KL, Figure 6.3b and c) exhibit a distinct bimodal distribution. For EB, the peak at large radii is found at about 10 μm and is quite broad ($0.1 - 20$ μm); a non-negligible fraction (∼10%) of much smaller pores is clearly visible with a mean value of the distribution of 0.01 μm. For KL, the peak at large radii (40 μm) is attributed to inter-particle pores, while the peak at small r_p is attributed to intra-particle pores ($0.01 - 0.1$ μm). It is worth noting that the latter

occupy a significant fraction ($\sim 30 - 40\%$) of the total porosity in KL. This is comparable to the experimental measured values reported in the literature, i.e. 40% of total pore space below 10^{-1} μm (Lai et al., 2015).

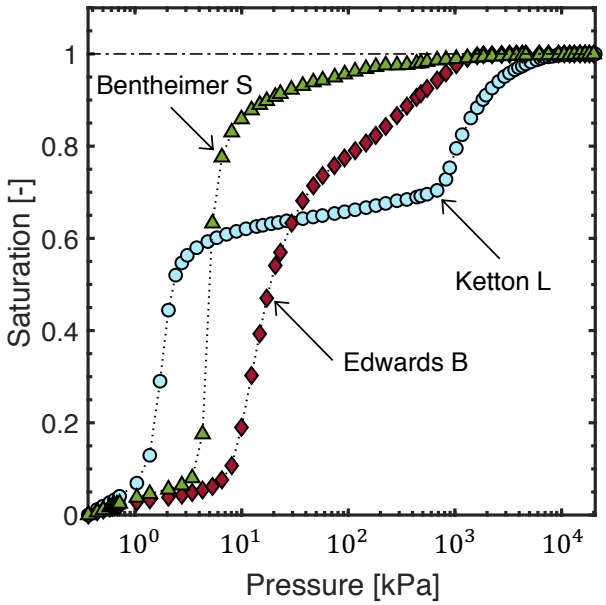

Figure 6.2: MIP curves measured on a small plug of volume, $V_{\text{plug}} \approx 0.2$ cm^3, for the three rock types, i.e. BS, KL and EB. The experiments were carried out using a Micromeritics Autopore IV for the pressure range, $p = 0.001 - 22.8$ MPa. The saturation values were obtained from normalising the cumulative intrusion by the total intruded volume (corresponding to 0.124, 0.125 and 0.250 mL/g for BS, KL and EB, respectively)

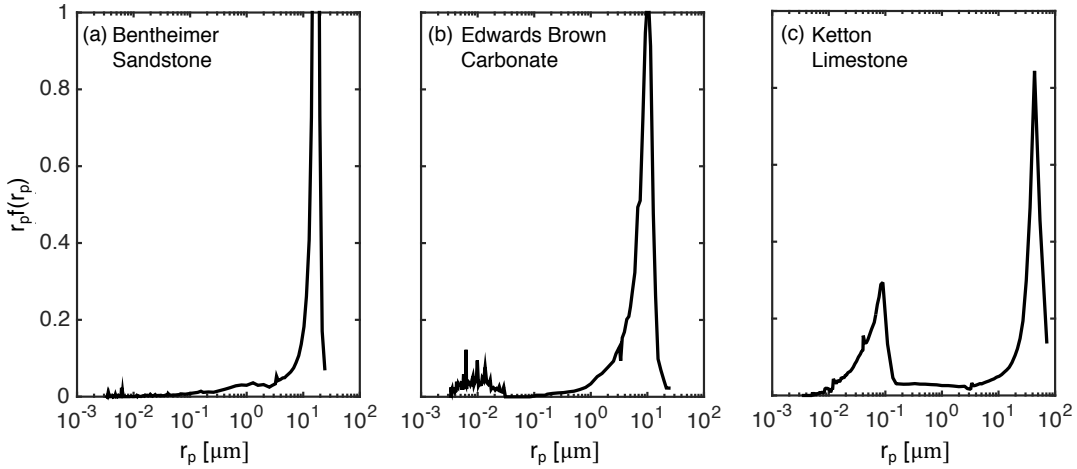

Figure 6.3: Pore-throat size distribution, $r_{\text{p}} f(r_{\text{p}})$ (Eqs. 6.1 and 6.2, as determined from mercury injection capillary pressure measurements for (a) BS, (b) EB and (c) KL.

6.4 Microscopic properties from micro-CT imaging

Histograms of the grain size distribution of the three rock samples are given in Figure 6.4. In the figure, the values are presented in terms of volume-equivalent diameter, d_e, which is defined as the diameter of a sphere that has the same volume as a rock grain, i.e.

$$d_e = \left(\frac{6}{\pi} V_p\right)^{\frac{1}{3}} \tag{6.3}$$

where V_p is the volume of a particle that is obtained from analysis of the micro-CT imaging dataset acquired on a small cylindrical sub-plug with volume, $V_{\text{plug}} \approx 0.2$ cm^3, using AVIZO (details of the image processing protocol is described in Section 3.2). This gives a total of about 1000 particles for KL, and 4000 particles for the analysis involving BS and EB. Note that the equivalent diameters, d_e, have been log-transformed to produce normal probability density functions (given by the solid lines in Figure 6.4). The histogram charts for BS and EB give distinct normal distribution curves with an average equivalent diameter $d_{\text{e}}(\text{mean}) =$ 257 and 391 μm, respectively. On the contrary, KL exhibits a clear bimodal distribution with two peaks that are centred at around mean equivalent diameters of $d_{\text{e}}(\text{mean}) \approx 400$ μm and $d_{\text{e}}(\text{mean}) \approx 610$ μm. Notably, 30% of the particles belong to the first peak, resulting in an overall average diameter $d_{\text{e}}(\text{mean}) = 541$ μm. The obtained grain size distributions are comparable to the results reported in the literature, i.e. the mean equivalent diameter obtained in this study, i.e. $d_{\text{e}} = 257$ μm (BS) and $d_{\text{e}} = 541$ μm (KL) are in good agreement with the data found in other sources, such as $d_{\text{p}} = 227$ μm (BS) (Andrew and Matthew, 2015), and $d_{\text{p}} = 500 - 650$ μm (KL) (Menke et al., 2015; Bailey et al., 2007).

Figure 6.5 presents 2-D and 3-D images obtained from micro-CT for the three rock samples (A detail of the arrangement of individual grains is also provided. We clearly observe distinct grain scale features for the three rock types; well-sorted round grains for KL and more disordered angular grains for BS and EB. As evidenced by the high-resolution 2-D images, we also notice a large proportion of well-developed vuggy pores that are present in EB, in alignment with the literature observations (Maclay and Land, 1988).

To further characterise the nature of the rock grains, the degree to which the the 3-D particle

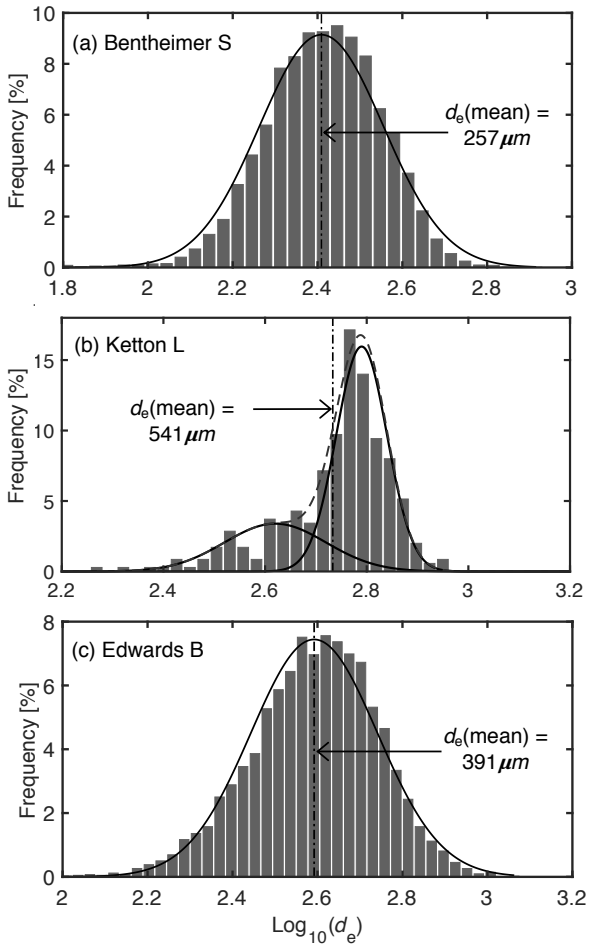

Figure 6.4: Histogram plots of the grain size distributions together with the corresponding normal distribution probability density function of (a) BS, (b) KL and (c) EB. The values of the location (mean, s) and scale (standard deviation, σ) parameters are as follows: $s = 2.41$ and $\sigma = 0.146$ (BS), $s_1 = 2.61$, $s_2 = 2.79$, $\sigma_1 = 0.100$ and $\sigma_2 = 0.05$ (KL), $s = 2.59$ and $\sigma = 0.149$ (EB). The dataset were obtained from micro-CT scans acquired on a small plug of volume, $V_{\mathrm{plug}} \approx 0.2$ cm^3 and processed using AVIZO-9 software. The values are reported in equivalent spherical diameter, d_e that has been obtained from Eq. 6.3.

shape deviates from a perfectly round sphere is evaluated by means of a sphericity index, Ψ, and is calculated by using the following equation (Wadell, 1935):

$$\Psi = \frac{\pi^{\frac{1}{3}}(6V_p)^{\frac{2}{3}}}{A_p} \tag{6.4}$$

where A_p is the surface area of a particle. Ψ takes a value of unity for a completely round object, and lower values indicate a particle being less spherical. A summary of the sphericity index determined for the three rock core samples, together with a control material, i.e. granular beadpack (BP) are provided in Table 6.2. As evidenced in the table, the extent of non-sphericity

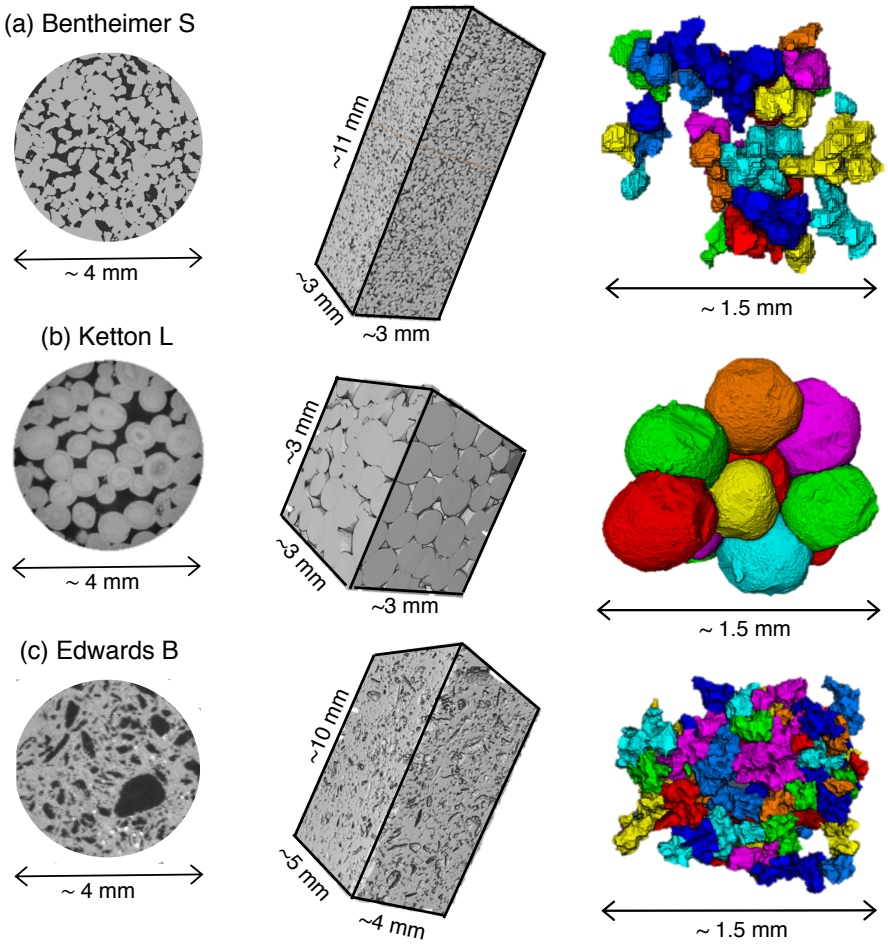

Figure 6.5: Left: snapshots of high-resolution 2-D grey-scale tomograms acquired using micro-CT imaging technique as detailed in Chapter 3. Right: 3-D volume images of sub-sections of the micro-CT scans. Each colour represents individual grain with an average equivalent diameter of 257 μm, 541 μm and 391 μm for BS, KL and EB respectively.

increases in the order BP<KL<BS<EB. We note that the value of the beadpacks is indeed very close to 1 (i.e. $\Psi = 0.97$).

Table 6.2: Summary of the rock grain properties obtained from micro-CT image analysis. Depending on the rock sample, about $1000 - 4000$ particles were considered in the analysis.

	Beadpack	**Bentheimer S**	**Ketton L**	**Edwards B**
Surface area, A_p [mm^2]	1.07	0.42	1.32	1.24
Volume, V_p [mm^3]	0.099	0.013	0.105	0.051
Sphericity index, Ψ [$-$]	0.97	0.63	0.82	0.53

6.5 Structural properties from medical CT imaging

Characterisation of these rock samples have also been made at the core-scale (mm-cm). Figure 6.6 presents the slice-average (1-D) porosity profiles along the longitudinal direction of the samples of (a) BS, (b) KL and (c) EB. These have been obtained from the 3-D porosity maps measured using X-ray CT imaging technique, as detailed in Section 3.2.1. The three rock samples exhibit variable porosities, with the strength of heterogeneity that increases in the order BS<KL<ED (with standard deviations corresponding to $\sigma_z = 0.22, 0.34$ and 0.55%, respectively). The total sample porosity, ϕ_{T}, is computed from averaging all the voxel porosity values and yield = 0.25, 0.23 and 0.41, for BS, KL and EB, respectively. On the right hand side of Figure 6.6 are shown the corresponding porosity histograms for voxel size $(1{\times}1{\times}1\ \mathrm{mm})^3$. In this case, we obtain larger variations in porosity; in particular, very similar voxel absolute porosity deviations are seen for BS ($\sigma_{\mathrm{vox}} = 2.1\%$) and KL ($\sigma_{\mathrm{vox}} = 2.3\%$), with a much higher variations observed in EB ($\sigma_{\mathrm{vox}} = 4.4\%$). In the figure, the relative voxel porosity values are presented (normalised by the total porosity, i.e. $\phi_{\mathrm{vox}}/\phi_{\mathrm{T}}$) and the solid lines refer to the best fitted probability distribution functions. We notice that the distinction in porosity contrast between the three samples becomes less apparent when the values are normalised by the total porosity, i.e. $\overline{\sigma}_{\mathrm{vox}} = 0.082$, 0.096 and 0.074 for BS, KL and EB, respectively.

The localised spatial heterogeneity is illustrated in Figure 6.7 by the three-dimensional porosity maps with a voxel size of about 8 mm^3 (top), together with a snapshot of each sample (bottom). To allow comparisons, the color scale of each map is fixed to ± 0.05 of the average total porosity, ϕ_{T}. Notably, the distribution of porosity values at the subcore-scale is very wide for EB, thus confirming the presence of vuggy pores (contributing to high porous regions) and dense crystals (contributing towards low porosity regions). This is also clearly visible from the digital photograph of the rock core, given at the bottom of the figure. For BS, such local variation is minimal, and is comparable to the 3-D porosity map of granular beadpacks (see Figure 5.4). The uncertainty associated with the porosity measurements is about 0.01 (at voxel size of 8 mm^3) for the X-ray CT scanner considered in work (details of this analysis given in Section 3.2.1).

To evaluate the characteristic behaviour of the correlation structure for the rock cores studied, the empirical semi-variograms of the voxel porosity values are computed in the x, y and z

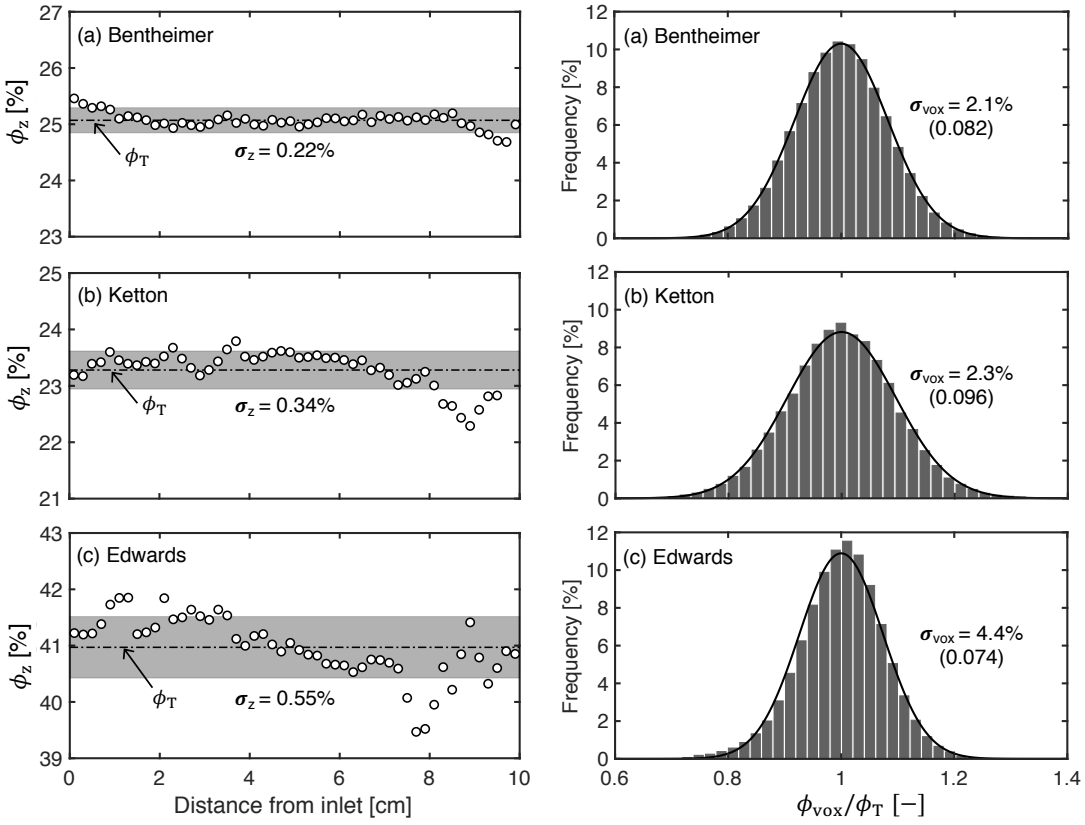

Figure 6.6: Left: Slice-average internal porosity profile along the axial direction of the core (a) BS, (b) KL and (c) EB. The plotted values have been obtained from averaging 1 mm thickness cross-sectional slices of the 3-D X-ray CT porosity maps. The shaded regions denote the standard deviation of the mean porosity value of each system. Right: Histogram plots of voxel porosity values. The solid lines correspond to the best fit normal distribution curves. The porosity values are normalised by the mean porosity of each system (ϕ_T = 25, 23 and 41%, respectively)

directions, by using the following expression (Pini et al., 2016):

$$\gamma_i(h) = \frac{1}{2N(h)} \sum_{N(h)=1}^{N} (w_j - w_k)^2 \tag{6.5}$$

where i is the direction (x, y or z) in which the semi-variogram is calculated; h is the 'distance-lag' separating two voxels (i.e. $h = j - k$), thus giving a total of N sets of distance pairs; w_j and w_k are the spatial quantities at position j and k, respectively. The experimental observations can then be described by applying an exponential model (Sarma, 2009), i.e.

$$\gamma_i(h) = (C_i - \gamma_i^0)[1 - \exp(-3h/a_i)] + \gamma_i^0 \tag{6.6}$$

where C is the 'sill' parameter in which a plateau is reached (corresponding to the limiting value

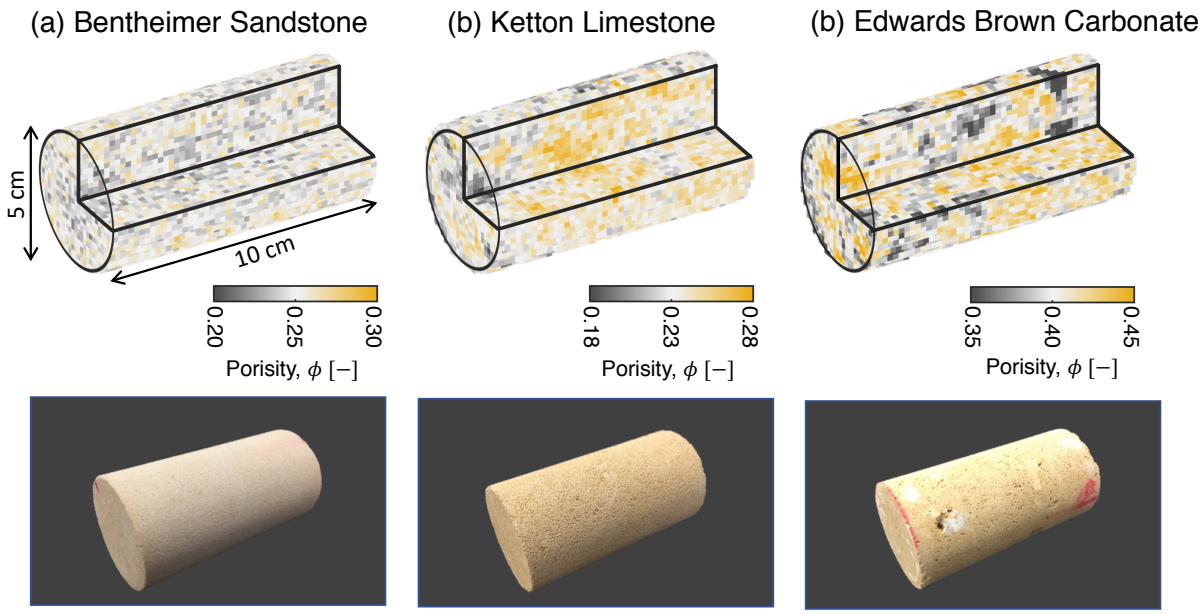

Figure 6.7: Top: 3-D porosity maps of the rock samples used in the pulse-tracer experiments presented in the later chapters. The tomographic images were acquired from a medical CT instrument, using the experimental protocol and scanner parameters detailed in Chapter 3. The raw images have been coarsened to a constant voxel size of about (2×2×2) mm^3. Bottom: digital photographs of the rock cores.

of the semivariogram); a is the range parameter (correlation length) that indicates the distance-lag at the 'sill' (e.g. the distance at which the data are no longer correlated). The so-called 'nugget effect' is also introduced in the model, i.e. $\gamma_i^0 = \gamma(h = 0)$, to account for any errors associated with the measurement technique and/or environmental variability that causes the values to deviate from the origin. The results, that present the semi-variograms in the direction parallel (circles) and perpendicular (triangles) to the flow are shown in Figure 6.8 for the three rock core samples. For better interpretation, the values have been normalised by the variance of the voxel porosity distributions of each dataset. In the figure, the experimental data are presented for the result computed for x/y- (triangles) and z- (circles) directions. The shaded area corresponds to the ranges of the exponential fits that have been obtained for 5 different spatial planes in each direction. First, we note that the 'nugget effect' is minimal for all cases (i.e. $\gamma_x^0 = \gamma_y^0 = \gamma_z^0 \approx 0$) and that the sill values are approximately equal to the variance of the spatial data, thus confirming that the porosity variations are normally distributed. As anticipated in the figure, we observe distinct correlation structure of the porosity field. For (a) BS and (b) KL, the range parameters are generally consistent in all directions, i.e. $a_{\mathrm{x}} \approx a_{\mathrm{y}} \approx a_{\mathrm{z}}$, suggesting that

these cores are distinguished by relatively low anisotropy. Moreover, we show that the sill value is reached at relatively short distance-lags for both systems, that take the maximum value of $a_z = 2.5$ and 3.5 mm for BS and KL, respectively (calculated from 10 cross-section planes); this accounts for about $2 - 4\%$ of the total length of the core samples used in this study. As seen in Figure 6.8, for EB, the distance-lag at the sill computed in the direction perpendicular to flow (empty triangles) is larger than the corresponding value obtained in the direction parallel to flow (circles). Interestingly, we note that the obtained values of correlation lengths can be very different depending on the cross-sectional planes. As an example of general validity, the porosity semi-variograms at two different cross-sectional planes in the direction perpendicular to flow are shown in Figure 6.8c (empty and filled triangles), in which very different values are obtained: $a_{x,1} = 4.9$ mm (filled triangles) and $a_{x,2} = 12.7$ mm (empty triangles). The variations in the correlation lengths may be manifested by the existence of vuggy porosity in EB, that introduces a significant larger value at the planes where vuggy pores are found, as compared to the sections where no large pores are present. Based on the discussions above, the correlation length increases in the order BS<KL<EB. However, these systems are far from a highly correlated structure, such as the one presented in (Pini et al., 2016), i.e. a Berea sandstone core, having a correlation length comparable to the length of the sample, i.e. $L = 10$ cm.

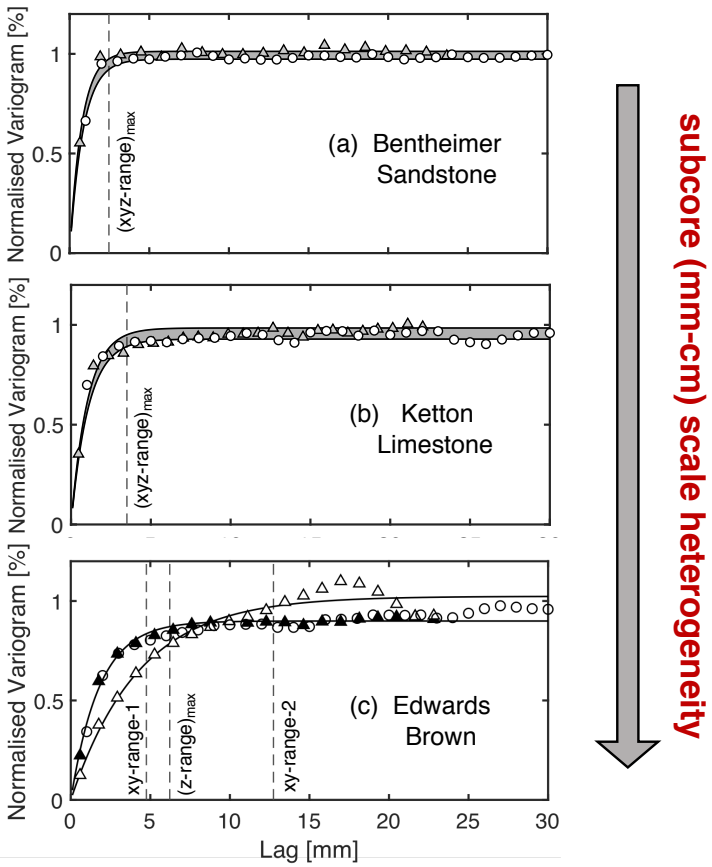

Figure 6.8: Semi-variograms of voxel porosity values for (a) BS, (b) KL and (c) EB. The symbols refer to the result obtained using Eq. 6.5, and is computed over x/y- (triangles) and z-directions (circles). The shaded regions are the best fits to an exponential model that has been obtained over 5 different cross-sectional planes. The values of the fitted range parameters are: $a_{\mathrm{x}} = a_{\mathrm{y}} = a_{\mathrm{z}} \approx 2.5$ mm (BS), $a_{\mathrm{x}} = a_{\mathrm{y}} = a_{\mathrm{z}} \approx 3.5$ mm (KL), $a_{\mathrm{x,max}} = 12.74$ mm, $a_{\mathrm{z,max}} = 6.22$ mm (ED). In figure (c), the semi-variograms obtained from three different cross-sectional planes are shown to highlight the spatial dependency in the obtained curves.

6.6 Permeability measurements

A series of multi-rate core-flooding experiments have been performed to measure the permeability (k) of the core samples. The latter was achieved by measuring pressure drops (ΔP) across each sample during steady-state water injection at various flow rates. The results are shown in Figure 6.9 for $5-6$ experimental flow rates (depending on the sample tested) that range between $q = 2 - 19$ mL/min. The gradient of the slope fitted to each curve, i.e. $S = \overline{\Delta P/q}$ (having an r-squared value of about 0.99) was then used in the Darcy's equation to provide an estimate of k,

$$k = -\frac{\mu L}{SA} \tag{6.7}$$

where μ is the viscosity of water that takes a value of 8.90×10^{-4} Pa·s, L and A are the length and cross-sectional area of the rock core, respectively. The following values of k were determined, BS: $k = 1.7 \ \pm 0.1 \times 10^{-12}$, KL: $1.9 \ \pm 0.1 \times 10^{-12}$ and EB: $0.13 \ \pm 0.01 \times 10^{-12}$ m^2.

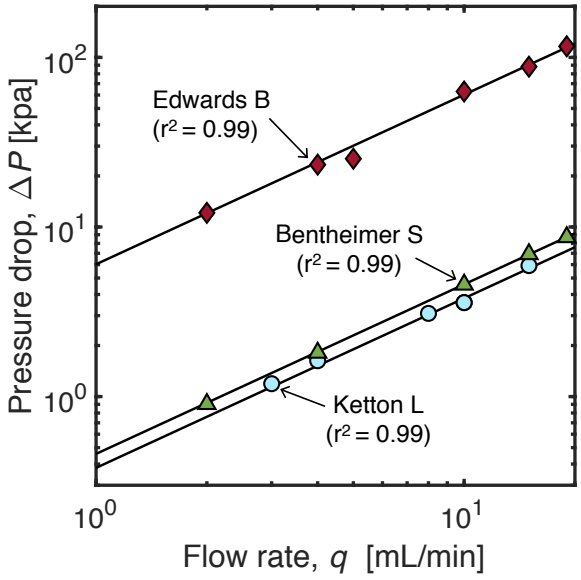

Figure 6.9: Pressure drops across the core samples during multi-rate water injection tests, at flow rates ranging between $q = 2 - 19$ mL/min. Measurements are reported over an average of 5 minutes after the pressure drop is stabilised. The symbols correspond to the experimental data and the solid lines are the best linear fits to the experimental measurements, with R-squared values of 0.99 obtained for all systems. This is used in the Darcy's equation to estimate permeability (k) of the samples. Viscosity, $\mu = 8.90 \times 10^{-4}$ Pa·s is used in the calculation. The figure is presented in double-logarithmic scale for better visualisation.

6.7 Concluding remarks

In this chapter, we have presented an integrated experimental approach that allows three-dimensional characterisation of structural heterogeneity of rock sample over length-scales from μm to cm. The experimental protocol has been applied on three rocks, including Bentheimer Sandstone, Ketton Limestone and Edwards Brown Carbonate. First, helium pycnometry, mercury intrusion porosimetry and micro-CT image analysis were applied on small sub-sets (up to plugs) of each rock samples to provide a distribution of baseline microscopic properties, such as pore- and grain-size distribution. We indicate the selected rock cores have very distinct features at the pore-scale; while Ketton is characterised by well-rounded grain structure with significant proportion of microporosity, we observe highly angular particles within Bentheimer

and Edwards. Notably, the latter also contains considerable amount of vuggy pore space that contributes significantly towards the overall spatial heterogeneity of the system. This is reflected from the analysis of the core scale properties performed with the medical-CT imaging dataset, where we show that Edwards has a large variability in the correlation structure that is much more pronounced than Bentheimer or Ketton. Bentheimer is characterised by a very uniform porosity distribution at the subcore-scale, as evidenced by the 3-D porosity map presented. The latter is comparable to the corresponding results for a homogeneous system, i.e. granular beadpacks that are given in the previous chapter. A summary of the key physical properties characterised for the three rock samples in this chapter is presented in 6.3. Direct measurements and quantifications of local structural heterogeneity is essential to advance our understanding of 'anomalous' transport because these properties have a great impact on the microscopic controls on mixing and spreading.

Table 6.3: Summary of the key petrophysical properties characterised for the rock core samples used in this study. The mean equivalent diameter (d_e), the sphericity index (Ψ), the total porosity (ϕ_T) and the correlation length (a) were obtained from analysis performed on the micro- and medical-CT images; the permeability was calculated from Darcy's law with pressure drops obtained from carrying out multi-rate water injection tests. The fraction of microporosity (ϕ_p/ϕ_T) was estimated from helium pycnometry and mercury intrusion porosimetry measurements

	Bentheimer S	**Ketton L**	**Edwards B**
Diameter, d [mm]	50.8	51.6	50.8
Length, L [mm]	103	100	103
Porosity, ϕ_T [%]	25.1	23.3	41.3
Microporosity ratio, ϕ_p/ϕ_T [vol.%]	~ 0	~ 35	~ 10
Pore volume, PV [mL]	52.4	48.7	85.6
Permeability, k [$\times 10^{-12}$ m^2]	1.7	1.9	0.13
Equivalent particle diameter, d_e [μm]	257	541	391
Sphericity index, Ψ [–]	0.63	0.82	0.53
Correlation length, a [cm]	0.3	0.4	1.3

Chapter 7

Tracer Tests on Rock Cores

In this chapter, we report on a detailed investigation of solute transport in three rock samples by combining experimental observations from pulse-tracer tests with models based on the advection dispersion approach. The results presented on Ketton Limestone have been published in *Kurotori et al. Measuring, imaging and modelling solute transport in a microporous limestone, Chemical Engineering Science 196 (2019) 366-383.* The imaging dataset associated with the publication may be obtained from the UKCCSRC data repository (dataset ID 13607385). Portions of the analysis on the other two rocks (i.e. Bentheimer Sandstone and Edwards Brown Carbonate) is published in *Kurotori et al. Three-Dimensional Imaging of Solute Transport in Reservoir Rocks by Positron Emission Tomography. 14th Greenhouse Gas Control Technologies Conference, Melbourne 21-26 October 2018 (GHGT-14).*

7.1 Introduction

As demonstrated in the previous chapter, the rock cores investigated in this thesis, namely Bentheimer Sandstone (BS), Ketton Limestone (KL) and Edwards Brown Carbonate (EB) are characterised by the following distinct features: (i) irregular grain structures (BS and EB); (ii) large proportion of microporosity (KL and EB); (iii) subcore-scale porosity heterogeneity (with strength increasing in the order BS<KL<EB); (iv) vuggy porosity (EB). The aim of this chapter is to investigate how these properties and their spatial variability affect the transport of solutes through the pore space of the rock. To this aim, pulse-tracer experiments have been carried out

covering a wide range of Péclet numbers, Pe $\approx 15 - 500$. A unique feature of the study is the use of Positron Emission Tomography (PET) to image the evolution of solute plume during the experiment. While a detailed analysis of these images will be presented in Chapter 9, the focus of this Chapter is on the quantitative evaluation of the breakthrough curves and the residence time distribution (RTD) functions. A workflow is described to extract key transport parameters, such as the mass transfer coefficient and dispersivity, and to evaluate their dependency on the Péclet number. To this aim, the experimental observations are interpreted by using two classic transport models, i.e. (i) the Advection Dispersion Equation (ADE) and (ii) the Multi-rate Mass Transfer (MRMT), where hydrodynamic dispersion is treated as a Fickian process.

7.2 Experimental

Pulse-tracer experiments were carried out using two experimental approaches. The first approach uses brine as the tracer and involves measuring breakthrough curves (BTCs) using a conductivity flow-cell mounted downstream of the sample. The second approach uses a radiotracer that is measured using radioactivity probes and imaged by PET. While the former serves as a useful comparison to validate observations on radiotracers, the latter have been used in this work to obtain multidimensional maps of the temporal and spatial evolution of the full tracer plume within the rock samples. All experiments have been carried out at room temperature and ambient pressure conditions.

7.2.1 Materials and fluids

Full details of the rock cores used for the pulse-tracer tests can be found in Chapter 6. [^{18}F]FDG (Fludeoxyglucose, half-life, $t_{1/2} = 109.7$ min) with variable concentrations, $0.3 - 1.1$ mCi/mL (corresponding to $c_{\mathrm{o}} = 2 - 7 \times 10^{-13}$ mol/mL) was used as the tracer for the experiments that involve PET imaging. This tracer is labelled with radioisotope, ^{18}F-fluoride ($^{18}\mathrm{F}^{-}$) that has been chemically produced on-site at the PET facility centre in Stanford Centre for Innovation in In-Vivo Imaging. The measured activity values of the tracer are decay-corrected using the following expression:

$$c(t) = c_{\mathrm{D}}(t)e^{\lambda t} \tag{7.1}$$

where $\lambda = \ln(2)/t_{1/2}$, c and c_D are the decay-corrected and detected activity concentration, respectively. Tap water was used as background carrier solution. For the control experiments that utilised conductivity-based tracer measurements, aqueous solutions of Potassium Iodide and Potassium Chloride (both supplied by Sigma Aldrich, purity > 99%) were used for the tracer and the carrier fluid, respectively (with concentration varying between $2.0 - 7.0$ wt.%, depending on the sample considered). Prior to the experiments, the density of the solutions was measured using an oscillating U-tube density meter (Anton Paar, DM5000) to verify that neutrally buoyant conditions were achieved (relative difference ~ 0.05 %). A summary of the fluids and key experimental parameters considered for the tracer tests is provided in Table 7.1. Details of the physical properties of the rock cores can be found in Table 6.3.

7.2.2 Experimental apparatus & procedure

A full description of the experimental set-up considered for the core-flooding experiments carried out in this work is explained in Chapter 4. Briefly, the in-flow detectors, including radioactivity (Custom-built, Carroll & Ramsey Associates, USA) and conductivity detectors (Model 8032, Amber Science, USA) were used for the measurements of up- and downstream tracer break-through curves. The set-up consists of three high-pressure syringe pumps (Teledyne ISCO, model 1000D) that have been applied for (i) continuous delivery of tracer and carrier fluids, (ii) maintaining a constant confining pressure, as well as (iii) back-pressure regulation of about 1 bar. An in-house developed GUI in LabVIEW platform (National Instruments) is used for real-time logging of data (1 second interval).

The core samples were dried for about 100 hours (at 60 °C) and then mounted into the custom-built aluminum core-holder (Figure 4.1). An incompressible fluid (tap water) is then introduced into the annular space between the core (jacketed with a double-layered heat-shrink FEB tube (50.8 mm bore, Polyflon Technology Ltd, UK)) and the core-holder. To prevent fluid bypassing, the water is pressurised and the pressure is maintained to a constant level throughout the experiment (8 bar for KL and 27 bar for BS and EB). The sample-holder is then placed on the scanner bed of the preclinical PET instrument (Siemens INVEON DPET). Prior to the tracer experiment, gaseous CO_2 (purity > 99%) is purged through the core sample, which is then displaced by the injection of the carrier solution for at least 8 pore volumes (PVs) to ensure

complete saturation of the core. The flow rate of the carrier solution is then set to the desired value, followed by the injection of a tracer pulse ($1-2$ mL depending on the experiment, see caption of Table 7.3). The latter is achieved by means of an injection valve (Cheminert, HPLC 6 port injection valve, VICI, Thames Restek UK Ltd). Each experiment lasted for about $3-4$ PVs.

Table 7.1: Details of the fluids and experimental parameters considered for the pulse-tracer tests.

	Bentheimer S	**Ketton L**	**Edwards B**
Flow rate, q [mL/min]	[2, 4, 10, 15, 19]	[2, 3, 4, 8, 10, 15, 19]	[2, 4, 10, 15, 19]
Péclet number, Pe [–]	$17-163$	$53-507$	$19-182$
Pore volume, PV [mL]	52.4	48.7	85.6
Confining pressure [bar]	27	7	27
PET fluid pair	[^{18}F]FDG/H_2O	[^{18}F]FDG/H_2O	[^{18}F]FDG/H_2O
Control fluid pair	KI/KCl (2.0/2.3)wt%	KI/KCl (6.1/7.0)wt%	–

7.3 PET imaging

The preclinical PET scanner produces 3-D volume images along the scanner field of view, (10×10×120) mm^3 at a voxel resolution of (0.78×0.78×0.80) mm^3. In this work, the PET scans have been reconstructed using a 3-D ordered subsets expectation maximisation (3-D OP-OSEM MAP (Hudson and Larkin, 1994)). The reconstructed images are then coarsened to produce a constant voxel size of (2.3×2.3×2.4) mm^3. The dataset was subsequently resampled into an (arbitrary) number of constant time frames $\Delta t = t_2 - t_1$ (with time corresponding to about ±0.07 PVs for each system). The average tracer activity detected in each voxel j, $c_j^{\mathrm{PET}}(t)$, is corrected for radioactive decay using the following expression (Pini et al., 2016):

$$c_j^{\mathrm{PET}}(t_i) = \frac{e^{\lambda t_i}}{\Delta t} \int_{t_1}^{t_2} c_{D,j}^{\mathrm{PET}}(t)dt \tag{7.2}$$

where $t_1 = t_i - \Delta t/2$, $t_2 = t_i + \Delta t/2$ and $t_i = (t_1 + t_2)/2$. The subscript j denotes the voxel-level quantities, where $c_j^{\mathrm{PET}}(t_i)$ is the voxel tracer intensity at t_i over the time interval Δt. As intensity values correlate linearly with radioactivity concentration (Zahasky et al., 2019), the following equation can be applied for conversion:

$$K_{\mathrm{corr}} = \frac{M_{\mathrm{exp}}^{\mathrm{inj}}}{\sum_{j=1}^{N_{\mathrm{vox}}} c_j^{\mathrm{PET}}(t_i) V_{\mathrm{vox}}} \tag{7.3}$$

where K_{corr} is the intensity-concentration correction factor; V_{vox} is the voxel volume; N_{vox} is the total number of voxels in the core. In this work, Eq. 7.3 has been computed for three discrete time intervals (corresponding to 0.4, 0.5 and 0.6 PVs) and an average quantity has been used for the conversion. This approach was further validated by performing this calculation for each slice in the core, where the observed variations in total tracer activity were systematically less than 1.5%.

7.4 Modelling

The Multi-rate Mass Transfer (MRMT) model (Coats et al., 1964) (also referred to as the "capacitance" (Baker, 1977; Bretz and Orr, 1987), the Mobile Immobile Model (MIM) (Honari et al., 2015), or the Dual-domain Mass Transfer (DDMT) model (Muniruzzaman and Rolle, 2017)) describes transport using a similar formulation as the ADE, but also accounts for additional resistance to mass transfer due to the transport through the micro-pores within the grains. While BS possesses minimal amount of micro-pores due to the existence of clay contents, microporosity is largely present in carbonate rocks, as demonstrated in the previous chapter. The one-dimensional form of the MRMT, in the absence of chemical reaction, reads as follows (Haggerty and Gorelick, 1995);

$$\phi\frac{\partial c}{\partial t} + (1-\phi)\phi_{\text{p}}\sum_{j=1}^{N_j} f_j\frac{\partial c_{\text{p},j}}{\partial t} + u\frac{\partial c}{\partial z} = \phi D_{\text{L}}\frac{\partial^2 c}{\partial z^2} \tag{7.4}$$

where u is the superficial fluid velocity, ϕ and ϕ_{p} denote the inter- and intra-granular porosity, which are associated with solute concentration c and c_{p}, respectively. The total porosity is thus obtained as $\phi_{\text{T}} = \phi + (1-\phi)\phi_{\text{p}}$ and, accordingly, the Péclet number uses the inter-granular porosity, i.e. $\text{Pe} = ud_{\text{p}}/(\phi\mathcal{D})$, where $\mathcal{D}$ is the molecular diffusion coefficient. t and z correspond to the coordinate variables assigned to time and space, respectively. Eq. 7.4 is written for a system composed of N_j grain classes, where f_j is the fraction of micropore volume in grain class j per unit of micropore volume (i.e. $f_j = \phi_{\text{p},j}/\phi_{\text{p}}$). The total mass transfer resistance is then obtained from summing all the individual contributions over entire grain classes, N_j. The latter

is commonly described using a first order rate expression:

$$(1-\phi)\phi_{\mathrm{p}} f_j \frac{\partial c_{\mathrm{p},j}}{\partial t} = k_{\mathrm{o}}(c - c_{\mathrm{p},j}) \quad \text{for } j = 1, ..., N_j \tag{7.5}$$

where k_{o} is the overall mass transfer coefficient, and is related to the effective (intrinsic) mass transfer coefficient, k_{m} by $k_{\mathrm{o}} = k_{\mathrm{m}} a_j$, where a_j is the specific surface area of grain class j. For spherical grains, such as those observed in oolitic limestones, it can be readily shown that $a_j = 6/d_{\mathrm{e},j}$, where $d_{\mathrm{e},j}$ is the equivalent particle diameter of the given grain class j. For rocks with more complicated geometries, such as BS or EB, the former can be approximated by $a_j = 6/(\Psi d_{\mathrm{e},j})$, where Ψ is the sphericity index (Eq. 6.4 given in Chapter 6). When no microporosity is present (i.e. $\phi_{\mathrm{p}} = 0$), Eq. 7.4 is simply reduced to the classical ADE formulation. For the range of Péclet numbers considered in this work (i.e. Pe > 15), hydrodynamic dispersion is assumed to be linearly related to v (Dullien, 1992): $D_{\mathrm{L}} = \alpha_{\mathrm{L}} v$, where v is the interstitial (pore) velocity ($v = u/\phi$) and α_{L} is the so-called longitudinal dispersivity. The latter is a measure of the heterogeneity of the pore space and represents therefore a characteristic property of the porous medium. In this study, transverse dispersivity (α_{T}) is considered to be negligible, as it is about one order of magnitude smaller than the corresponding value in the longitudinal direction, according to the results reported in the literature (Perkins and Johnston, 1963). For example, Ketton Limestone: $\alpha_{\mathrm{L}} = 0.16$ cm Honari et al. (2015) vs. $\alpha_{\mathrm{T}} = 0.013$ cm (Boon et al., 2017). We also note that the Fickian treatment of dispersion in the ADE or MRMT formulations implies that the injected tracer pulse has evolved into a Gaussian plume on a length-scale that is smaller than the length of the rock sample. Under such circumstances the dispersion coefficient approaches its asymptotic value (Neuman and Tartakovsky, 2009). The validity of the ADE and MRMT formulations to describe the experiments conducted in this study will be demonstrated throughout the Results and Discussion sections.

Tracer concentrations computed within the sample are binned over a given time interval to allow for a direct comparison with the dynamic image frames generated from the PET scanner (Section 7.3), i.e.

$$C(z, t_i) = \frac{1}{\Delta t} \int_{t_1}^{t_2} \overline{c}(z, t) dt \quad \text{for} \quad 0 \leq z \leq L \tag{7.6}$$

with $\Delta t = t_2 - t_1$ and where internal solute concentration is $\overline{c} = [\phi c + (1-\phi)\phi_{\mathrm{p}} c_{\mathrm{p}}]/\phi_{\mathrm{T}}$.

7.4.1 Numerical solution procedure

Since the tracer tests are initiated with the core being saturated with carrier solution, the following initial conditions is used:

$$\text{for } t = 0 \text{ and } 0 \leq z \leq L: \; c = c_{\mathrm{p},j} = 0 \;\; \text{for } j = 1, ..., N_j \tag{7.7}$$

Boundary conditions at the core inlet ($z = 0$) and outlet ($z = L$) follow the expressions given by Danckwerts (Fogler, 1999):

$$\text{for } z = 0: \; c(z = 0) = c_0 + \frac{\phi D_{\mathrm{L}}}{u} \left.\frac{\partial c}{\partial z}\right|_{z=0} \tag{7.8a}$$

$$\text{for } z = L: 0 = \left.\frac{\partial c}{\partial z}\right|_{z=L} \tag{7.8b}$$

where c_0 is the concentration of tracer just before entering the sample. The latter is measured by the inlet conductivity (or radioactivity) detector and is reproduced in the numerical code by means of interpolation through the experimental points. The partial differential equations, Eqs. 7.4 and 7.5, are discretised in space using the finite-difference method (FDM) with various sets of grid points, N_{g} (i.e. $N_{\mathrm{g}} = 200$ for the carbonate cores and $N_{\mathrm{g}} = 600$ for the relatively homogeneous sandstone), corresponding to grid sizes, $\Delta x = 0.017 - 0.050$ cm. The space derivatives are approximated using the central difference operator for each internal node and the backward difference operator for the first and last node. The resulting set of ordinary differential equations is solved simultaneously in time using the `ode15s` solver in MATLAB, with a maximum allowed time step, $\Delta t = 0.5$ sec. For each experimental dataset, the following relative (`RelTol`) and absolute error tolerances (`AbsTol`) have been set, i.e. KL: `RelTol` $= 1 \times 10^{-3}$ %, `AbsTol` $= 1 \times 10^{-4}$ mCi/mL, or for BS and EB: `RelTol` $= 1 \times 10^{-6}$ %, `AbsTol` $= 1 \times 10^{-6}$ mCi/mL. The input parameters used to solve the numerical model include the sample properties described in the previous chapter, as well as feed concentration, flow rates and volume of tracer injected, which are adjusted depending on the experimental conditions (see Tables 7.1 and 7.3). As explained in the next section, various model scenarios have been evaluated, where the remaining set of parameters has been found by fitting the model to the tracer breakthrough curves.

7.4.2 Modelling approach & optimisation procedure

The datasets from multi-rate pulse-tracer tests were first interpreted by using the ADE. The latter is solved for the experiments on the relatively homogeneous core samples, i.e. BS and KL, in which the longitudinal dispersivity, α_{L} has been treated as the sole fitting parameter for each experimental BTC. Two scenarios have been considered in the MRMT framework: in MRMT-1, the longitudinal dispersivity (α_{L}) and intra-granular porosity (ϕ_{p}) have been taken as global fitting parameters, while letting the mass transfer coefficient (k_{o}) depends on the flow rate; MRMT-2 takes the optimum model parameters attained from MRMT-1, i.e. k_{o} and ϕ_{p} as fixed model inputs, while fitting α_{L} to each flow rate. With the latter, the goal is to evaluate the potential non-linear dependency of the dispersion coefficient on fluid velocity, i.e. $D_{\mathrm{L}} \propto v^m$, that has shown a notable discrepancies in the literature, with $m = 1.0 - 1.4$ over the range of Péclet numbers considered in this study ($\mathrm{Pe} \approx 20 - 500$) (Bear, 1988; Honari et al., 2015; Blunt et al., 2013; Berkowitz et al., 2006).

In the case of BS and EB, only one grain class (i.e. $N_j = 1$) is used in the model, as suggested by the measured grain size distributions (mean grain size, $d_{\mathrm{e}} \approx 260$ μm (BS) and $d_{\mathrm{e}} \approx 390$ μm (EB)) (see Chapter 6). With the latter, the overall mass transfer coefficient (k_{o}) is fitted, rather than k_{m} due to the non-spherical nature of the system (sphericity index, $\Psi < 0.7$, see Table 6.3). For KL, two classes of spherical grains ($d_{\mathrm{p},1} = 220$ μm and $d_{\mathrm{p},2} = 660$ μm) are considered ($\Psi = 0.8$, see Table 6.3), based on the bimodal peak observed in the grain size distributions. To this end, an additional global fitting parameter, f_1 (proportion of grain class 1, where $f_1 + f_2 = 1$) is deployed. A flow chart illustrating the modelling scenarios applied in this work is shown in Figure 7.1. For each model scenario, the following objective function was minimised to reproduce the experimentally obtained tracer effluent profiles:

$$J = \sum_{i=1}^{N_{\mathrm{q}}} \sum_{j=1}^{N_{\mathrm{p}}} \frac{(\widetilde{c}_{i,j}^{\,\mathrm{out}} - c_{i,j}^{\,\mathrm{out}})^2}{c_{\mathrm{max},i}^{\mathrm{out}}} \tag{7.9}$$

where N_{q} and N_{p} are the number of flow rates and of experimental points in each tracer effluent curve; $\widetilde{c}^{\,\mathrm{out}}$ and $c^{\,\mathrm{out}}$ are the effluent concentration values predicted by the model and measured experimentally, respectively. The denominator in Eq. 7.9 is the maximum value of effluent tracer concentration and ensures that similar weight is given to the various flow rates. The non-

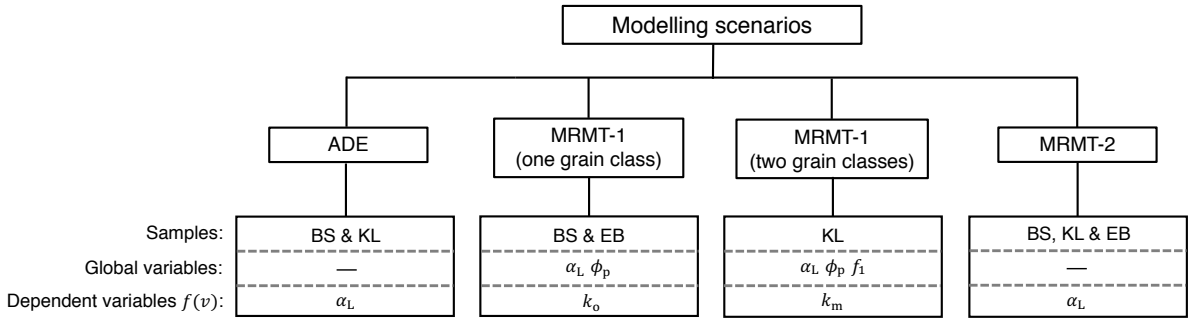

Figure 7.1: Schematic digram illustrating the modelling approaches proposed to best describe the experimental breakthrough curves. Depending on the scenario, the number of fitting parameters varies between $1-10$: $[\phi_p, \alpha_L, f_1, k_o$ or $k_m]$.

dominated sorting genetic algorithm II (GA) in the MATLAB global optimization toolbox was used to identify the optimal model parameters. This approach extends conventional optimisation routines by considering elitism, in addition to stochasticity. This has the dual benefit of reducing computation time and avoiding entrapments within local minima (Rajagopalan et al., 2016; Hosseinzadeh Hejazi et al., 2017). Briefly, the algorithm starts with random sets of the initial population of decision variables (parents) and calculates the objective function for each set independently. In the next stage, a new generation of population (children) is created both by random mutation as well as crossover between the parents from the previous generation with better fitness value. This procedure is repeated until the optimal set of parameters is achieved with the lowest value of the objective function. In this study, the population size was fixed at 24 times the number of decision variables and the number of generations was limited to 50. Depending on the model scenario considered, the total number of parameters that were simultaneously fit varied. One parameter was used in the ADE-based scenarios, while up to ten fitting parameters were considered in the MRMT-based scenarios. The lower and upper bounds imposed for the optimiser are provided in Table 7.2.

Table 7.2: The lower and upper bounds of the fitting parameters used in the optimisation routines.

	α_L [cm]	ϕ_p [–]	k_m [mm/min]	k_o [min^{-1}]	f_1 [–]
Bentheimer S	$0.02-0.10$	$0.00-0.20$	–	$0.00-1.82$	–
Ketton L	$0.10-0.20$	$0.04-0.11$	$0.01-0.20$	–	$0.0-0.5$
Edwards B	$0.05-0.25$	$0.01-0.35$	–	$0.09-2.73$	–

7.5 Results

In this section, the results obtained from pulse-tracer tests over a range of flow rates (or Péclet number, Pe) are analysed for the three rocks. First, we present a comparison of the experimental effluent profiles obtained from radio- and brine-tracers, together with a quantitative assessment on the sensitivity of each measurement approach. The experiment and modelling results are then studied for each porous system independently by following a similar approach that includes (i) evaluation of the proposed modelling approaches, (ii) BTC analysis, and (iii) investigation of the internal dynamic displacement of the tracer by PET. To allow comparisons, the obtained BTCs are also presented in terms of Residence Time Distribution (RTD) function (E_Θ) over normalised time ($\Theta = t/\tau_{\text{exp}}$), as described in Section 5.4.2. A summary of all the pulse-tracer tests conducted in this chapter is provided in Table 7.3.

7.5.1 Sensitivity & reproducibility of the measurement techniques

Figure 7.2 presents the normalised RTD curves obtained from the two independent techniques, namely radioactivity for radio-tracer (^{18}F), and conductivity for brine-tracer (KI) measurements. The results are shown for two characteristic rock cores: BS (figure a) and KL (figure b) for the experiment carried out at $q = 10$ mL/min. In the figure, we observe an excellent agreement between the different sets of curves, thus verifying the validity of using the selected radio-tracer ([^{18}F]FDG) for the study of solute transport in both sandstone and carbonate rocks. This is also confirmed from the good mass recovery i.e. $M^{\text{out}}_{\text{exp}}/M^{\text{in}}_{\text{exp}} > 97.8\%$ obtained for the pulse-tracer experiments involving radioactivity measurements (summarised in Table 7.3). We note that the radioactivity technique presents a more precise measurement approach, as evidenced by the zoomed in section of the low concentration tails given in the inset of Figure 7.2(a) and (b). This is quantitatively confirmed by computing the signal-to-noise ratio, SNR $= s/\sigma_{\text{std}}$, where s is the mean tracer concentration of a measured BTC. To compute s, a threshold of 1% of the peak concentration has been set. σ_{std} is the standard deviation of the baseline readings when there is no tracer (carrier fluid only). The latter is determined from a dataset recorded over 60 seconds (corresponding to 60 measurement points). Consequently, we obtain SNR for a radio-tracer BTC that is about 20 times larger than the corresponding conductivity curves

Table 7.3: Overview of the brine- and radio- tracer experiments carried out in this work. Reported variables are: volumetric flow rate (q), average residence time ($\tau = \phi AL/q$), mean residence time of injected pulse (τ_{inj}), mean residence time of effluent (τ_{exp}, with the corresponding error $\varepsilon = 1 - \tau_{\text{exp}}/\tau$), recovered mass of tracer ($M^{\text{out}}_{\text{exp}}$, with the corresponding error $\varepsilon = 1 - M^{\text{out}}_{\text{exp}}/M^{\text{inj}}_{\text{exp}}$). A correction is applied to the computed mean residence time to account for the volume of the tubing between the outer faces of the sample and the conductivity cells; this corresponds to 4.2 mL for KL, and 4.0 mL for the PET experiments on BS and EB. The dead volume for the conductivity tracer tests was 3.1 mL. The volume of tracer injected is 1 mL for the experiments with KL, and 2mL for BS and EB.

Bentheimer Sandstone

q [mL/min]	τ [min]	τ_{inj} [min]	τ_{exp} [min]	$M^{\text{out}}_{\text{exp}}$ [mCi]
2.0	26.20	0.59	26.22 (-0.1%)	1.027 (0.58%)
4.0	13.10	0.31	13.14 (-0.3%)	1.339 (0.03%)
10.0	5.24	0.12	5.25 (-0.1%)	1.607 (0.58%)
15.0	3.49	0.08	3.50 (-0.1%)	1.734 (0.01%)
19.0	2.76	0.06	2.76 (-0.1%)	1.858 (0.02%)

q [mL/min]	τ [min]	τ_{inj} [min]	τ_{exp} [min]	$M^{\text{out}}_{\text{exp}}$ [g]
10.0	5.24	0.12	5.21 (0.5%)	0.038 (4.4%)

Ketton Limestone

q [mL/min]	τ [min]	τ_{inj} [min]	τ_{exp} [min]	$M^{\text{out}}_{\text{exp}}$ [mCi]
2.0	24.33	0.37	24.16 (0.7%)	0.251 (–)
3.0	16.22	0.26	16.32 (0.6%)	0.418 (–)
4.0	12.17	0.21	12.11 (0.5%)	0.556 (–)
4.0	12.17	0.20	12.24 (0.6%)	0.756 (–)
8.0	6.09	0.15	5.86 (3.8%)	0.779 (–)
10.0	4.87	0.12	4.66 (4.4%)	0.879 (–)
15.0	3.25	0.08	3.02 (7.0%)	0.953 (–)
19.0	2.56	0.06	2.36 (7.8%)	1.106 (–)
19.0	2.56	0.06	2.39 (6.8%)	1.302 (–)

q [mL/min]	τ [min]	τ_{inj} [min]	τ_{exp} [min]	$M^{\text{out}}_{\text{exp}}$ [g]
8.0	6.09	0.16	5.98 (1.9%)	0.130 (2.3%)
10.0	4.87	0.13	4.71 (3.2%)	0.129 (5.0%)
15.0	3.25	0.08	3.13 (3.6%)	0.130 (-0.1%)
19.0	2.56	0.08	2.46 (4.1%)	0.134 (-2.2%)

Edwards Brown Carbonate

q [mL/min]	τ [min]	τ_{inj} [min]	τ_{exp} [min]	$M^{\text{out}}_{\text{exp}}$ [mCi]
2.0	43.11	0.58	43.51 (-0.9%)	1.028 (2.13%)
4.0	21.55	0.31	21.69 (-0.6%)	1.835 (0.92%)
10.0	8.62	0.12	8.65 (-0.4%)	1.389 (0.61%)
15.0	5.75	0.08	5.69 (1.0%)	2.027 (0.49%)
15.0	5.75	0.08	5.65 (1.7%)	1.688 (0.11%)
19.0	4.54	0.07	4.51 (0.6%)	2.196 (0.02%)

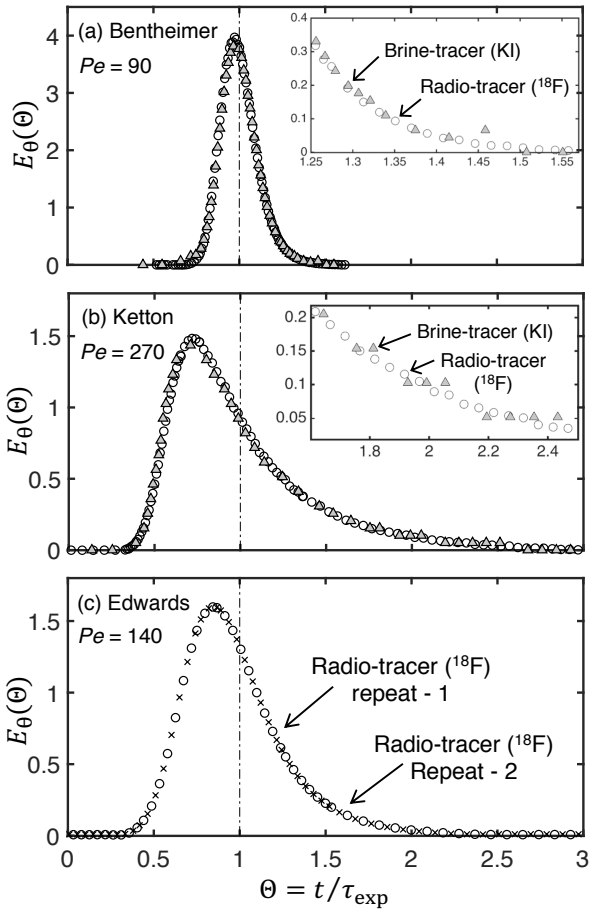

Figure 7.2: Comparisons of Residence Time Distribution breakthrough curves measured using the brine(KI)- (triangles) and radio(^{18}F)-tracers (circles) for (a) BS (b) KL. A zoomed in section of the BTC tails are shown in the inset of each plot to highlight the sensitivity of the measurement techniques. (c) presents the BTCs measured from radio(18F)-tracer for a repeated experiment carried out on EB. The values are shown in a normalised RTD function, E_Θ as a function of reduced time, $\Theta = t/\tau_{\text{exp}}$. The experiments were performed at $q = 10$ mL/min for (a) and (b), and $q = 15$ mL/min for (c).

($\text{SNR}_{^{18}\text{F}}/\text{SNR}_{\text{KI}} \approx 20$). Although the actual sensitivity of each measurement technique can be optimised by accounting for several factors, such as the model of detectors used, the concentration and choice of fluid-pairs, the analysis carried out here highlights the excellent sensitivity of radio-tracers in measuring BTCs, given that only a very small quantity of solute is needed ($\mathcal{O} \sim 10^{-13}$ mol/mL). Such measurement approach also indicates an excellent reproducibility, as can be seen in Figure 7.2 (c) for a repeated test carried out on the Edwards Brown core at $q = 15$ mL/min.

7.5.2 Bentheimer Sandstone

For Bentheimer Sandstone (BS), as anticipated from Table 7.3, a good agreement is achieved between the theoretical residence time (τ) and the experimental residence time (τ_{exp}) over the entire ranges of flow rate investigated (with relative error, $\epsilon < 0.5\%$). With these experiments, asymptotic regime has already been fully established, and therefore the Fickain treatment of dispersion using the transport models (i.e. ADE or MRMT) is valid. This can be confirmed using the same analogy to the discussion presented in Section 5.6.1, where the characteristic length-(or time-) scale required for the dispersion coefficient to reach an asymptotic value is given by $l^* = t_{\text{diff}}/t_{\text{adv}} = \text{Pe}/2$ (Bijeljic et al., 2011). For the range of Péclet number considered here, $l^* = 9-90$ and $l = d_{\text{e}} \approx 0.26$. This gives the required characteristic lengths, $l^* \times d_{\text{e}} \approx 2-25$ mm, which lie well below the length of the sample used ($L = 103$ mm). A summary of the optimum model parameters obtained from the different modelling scenarios discussed in Section 7.4 is shown in Table 7.4. As expected, the MRMT-based scenarios provide a better fit to the experimental effluent profiles compared to ADE. This is apparent by a smaller value of objective function obtained (numerical values shown in the caption of Table 7.3). However, we also note that the J value for MRMT-1 ($J = 0.059$ mCi/mL) is much higher than that of MRMT-2 ($J = 0.024$ mCi/mL). The latter produces a narrow range of dispersivity, α_{L}, that show a general increase over system flow rate. An analysis of the correlation between velocity and dispersion coefficients is provided later in Section 7.6.

Table 7.4: Optimum model parameters obtained from fitting experimental breakthrough curves on Bentheimer Sandstone (BS) using two transport models, namely ADE and MRMT. Details of the modelling approaches applied are summarised in Section 7.4. The optimum values obtained for the global fitting variables are: $\alpha_{\text{L}} = 0.051$ cm and $\phi_{\text{p}} = 0.006$ (MRMT-1). The following value of objective function were attained for each modelling scenario, i.e. ADE: $J = 0.068$ mCi/mL, MRMT-1: $J = 0.059$ mCi/mL, MRMT2: $J = 0.024$ mCi/mL.

	ADE		**MRMT-1**		**MRMT-2**	
q	D_{L}	α_{L}	k_{o}	D_{L}	D_{L}	α_{L}
[mL/min]	[cm^2/min]	[cm]	[min^{-1}]	[cm^2/min]	[cm^2/min]	[cm]
2.0	0.019	0.048	0.030	0.020	0.018	0.044
4.0	0.038	0.048	0.762	0.041	0.033	0.041
10.0	0.104	0.053	0.998	0.101	0.097	0.048
15.0	0.182	0.062	1.489	0.152	0.162	0.054
19.0	0.240	0.064	1.169	0.193	0.214	0.056

The BTCs measured on the BS core are shown in Figure 7.3, for the flow rates ranging be-

tween $2 - 19$ mL/min (corresponding to Péclet numbers, $17 \leq \text{Pe} \leq 163$). In the figure, the plotted values are normalised by the feed concentration, c_o. The symbols are the experimental measurements collected from radio-tracer injections while the solid lines are the corresponding predictions obtained for the optimum model scenario (i.e. MRMT-2). In general, we observe that the selected modelling approach provides a good description of the measured BTCs over all the flow rates. The model yields a narrow span in the asymptotic dispersivity ($\alpha_{\text{L}} = 0.041 - 0.056$ cm), giving an average of about $\alpha_{\text{L}} = 0.049$ cm. In this case, the model takes the optimum parameter obtained from MRMT-1, giving a single value of intra-granular porosity for the entire dataset, i.e. $\phi_{\text{p}} = 0.006$, that corresponds to about 2% of the total pore space in the BS core. This indeed provides a verification on the existence of modest microporous clay minerals ($\sim 3\%$, as explained in Section 6.3) that contribute towards only a small proportion of the total porosity. This consistency suggests that the proposed MRMT approach can correctly capture the influence of the small-scale microporosity from the experimental measurements of 1-D breakthrough curves; this does not only confirm the rigorousness of the proposed experimental and modelling approach (which involves fitting the effluent profiles for the entire dataset covering a wide range of Péclet numbers), but also proves the high sensitivity of the measurement technique for resolving the modest features. Nevertheless, small discrepancies still persist between the experiment and model predictions particularly in the concentration tails at late times, as highlighted in the double-logarithmic plot of the BTCs presented in Figure 7.3(b). Interestingly, we note that introducing a very small amount of microporosity does not have a pronounced impact on the dispersivity value obtained ($\alpha_{\text{L}} = 0.049$ cm), as the latter is similar to the corresponding ADE dispersivity (i.e. $\alpha_{\text{L}} \approx 0.055$ cm) and the value found in the open literature, i.e. $\alpha_{\text{L}} = 0.048$ cm (measured using NMR techniques) (Singer et al., 2016) where no microporosity was assumed. These dispersivity values are generally smaller than that measured on more structurally correlated sandstones, such as Berea ($\alpha_{\text{L}} = 0.04 - 0.4$ cm) (Pini and Krevor, 2019),

In Figure 7.3 are shown the 1-D internal concentration profiles plotted along the axial direction of the BS core. The results are presented for three representative flow rates, i.e. $q = 4$, 10 and 19 mL/min (corresponding to Pe = 34, 86 and 163), with 6 distinct time intervals in each sub-plot that represent an average of ± 0.06 PVs. The symbols are the experimental data measured by PET, that has been computed from averaging the voxel concentration values in

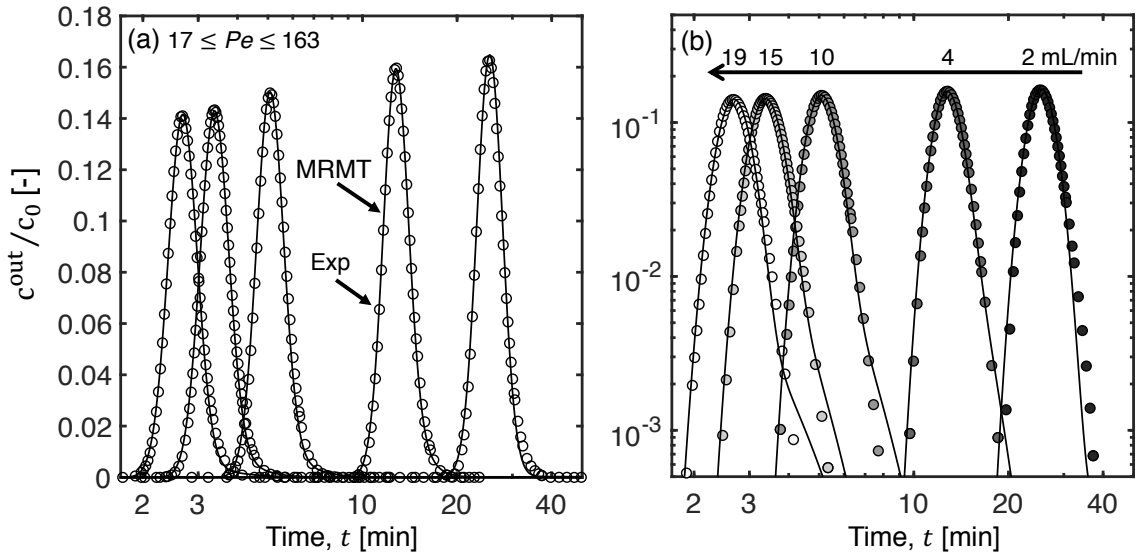

Figure 7.3: (a) BTCs obtained from the PET experiments for BS at flow rates $q = 2, 4, 10, 15, 19$ mL/min (corresponding to Pe $= 17, 34, 86, 129, 163$). The symbols represent radio-tracer measurements, while the solid lines refer to the optimum MRMT fits (MRMT-2, fitted values reported in Table 7.4). The values of concentration are normalised by feed concentration, c_0. (b) log-log plot of (a) to emphasise the concentration tails of the BTCs.

each cross-sectional slice (0.8 mm thickness) over the entire length of the core. The dashed lines correspond to the fully predicted concentration plumes produced by using the optimum model parameters obtained from fitting the effluent curves using MRMT-2. As can be seen in the figure, the model provides an accurate description on the migration of tracer plume over all time intervals at each flow rate. The observation is also consistent for all the flow rates tested. Similar to the dynamic profiles observed within a homogeneous beadpack (presented in Chapter 5), we indicate that the BS is characterised by a small degree of mixing, as evidenced by the modest change in the concentration peak over distance travelled. The inlet effect is persistent in the results with BS, and is proved to be insignificant, as the early tailing diminishes when the tracer plume propagates over the core sample at later times.

7.5.3 Ketton Limestone

A summary of all tests conducted on KL is given in Table 7.3. The dataset includes nine pulse-tracer tests with the radiotracer ([^{18}F]FDG) and four control test conducted with the brine tracer (KI). The results from the latter ($q = 8, 10, 15, 19$ mL/min) are shown in Figure 7.5 alongside the curves measured with the radiotracer and show an excellent agreement. Interestingly, we

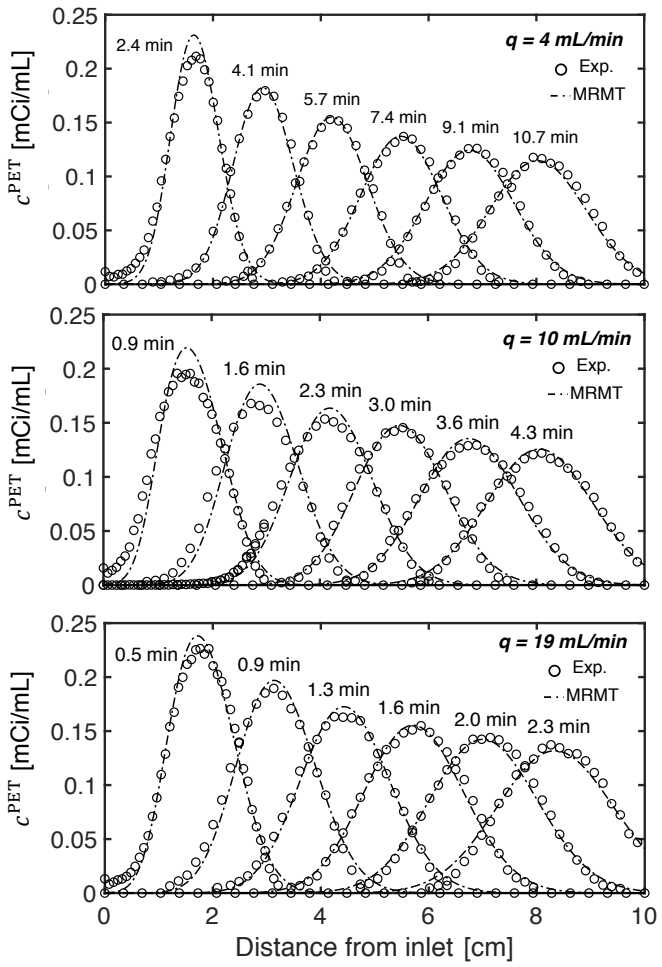

Figure 7.4: Slice-averaged (1-D) internal concentration profiles plotted along the longitudinal direction of the BS core. The curves are shown for six distinct time frames. The experimental results for three flow rates are shown, i.e. $q = 4$, 10 and 19 mL/min (corresponding to Péclet numbers, $\mathrm{Pe} = 34, 86, 163$). The symbols are the experimental data obtained from PET and the solid lines are the corresponding MRMT-2 model predictions. The experimental profiles have been computed from averaging 0.8 mm thickness cross-sectional (x-y plane) slices of the 3-D PET dataset and each curve represents an average of ± 0.06 PVs

observe a systematic increase in the difference between the expected (τ) and the measured (τ_{exp}) mean residence time of the system with increasing Pe, reaching relative deviations of up to $\sim 8\%$. While deviations are generally less than 1% for $\mathrm{Pe} < 80$ (corresponding to $q < 4$ mL/min), in all the other cases $\tau_{\mathrm{exp}} < \tau$. This suggests that there is an apparent and increased inaccessibility of some of the pore space with increasing Pe. This behaviour can, in principle, be reproduced by the MRMT model, by using the fraction of stagnant pore space as a fitting parameter (in addition to the dispersivity and the mass transfer coefficient) and by letting it be dependent on the flow rate. The obtained values of this base case are reported in Table 7.5 (case MRMT-0 with one

grain class, $J = 49 \times 10^{-4}$ mCi/mL, $\phi_p = 9.0 - 7.7\%$, $\alpha_L = 0.134 - 0.178$ cm). This approach has been applied systematically in the literature when fitting tracer curves measured on carbonate rocks (Baker, 1977; Batycky et al., 1982; Bretz and Orr, 1987; Honari et al., 2015). We contend that it lacks of physical significance and that this *apparent* decrease in the microporosity reflects the presence of a distribution of grain sizes in KL, as demonstrated in the following section.

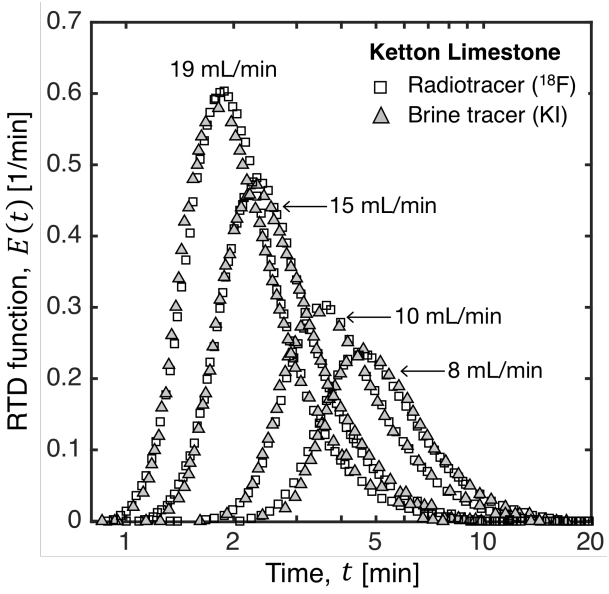

Figure 7.5: Measured RTD function, $E(t)$ for experiments carried out on KL at flow rates q = 8, 10, 15, 19 mL/min, corresponding to Pe = 214, 267, 401, 507. At each flow rate, measurements have been carried out using both brine(KI)- (triangles) and radio(^{18}F)-tracers (squares). Time is presented using a logarithmic scale.

BTCs measured on KL are shown in Figure 7.6 for the range of Péclet numbers, Pe $= 50 - 500$, by using a linear (Figure 7.6(a)) and a logarithmic scale (Figure 7.6(b)) for the concentration. For the sake of clearer representation, only the data acquired with the radiotracer are given. We note that when using radiotracers, we can measure concentrations up to four orders of magnitude smaller than the inlet concentration, i.e. $c/c_0 \approx 1 \times 10^{-4}$, as shown in Figure 7.6(b). This concentration range is comparable, if not wider than values reported in the literature for BTCs measured experimentally (Berkowitz et al., 2006; Vogler et al., 2018). While radiotracers provide a higher sensitivity to low concentrations as compared to conductivity measurements (as also demonstrated in 7.5.1), other tracers (e.g., Uranine (Gouze et al., 2008a)) allow extending this range even further and resolving concentration tails at late times, which can be extremely important for rocks containing microporosity (Gjetvaj et al., 2015).

Table 7.5: Optimum model parameters obtained upon fitting the ADE and the MRMT models to the tracer breakthrough profiles measured on KL. For the ADE model, the longitudinal dispersivity, α_L, has been set as flow-rate dependent. For model MRMT-0 (one grain class), α_L, ϕ_p and k_m have been fitted to each flow rate independently ($J = 1 \times 10^{-4} - 24 \times 10^{-4}$ mCi/mL, depending on the flow rate). For model MRMT-1 (two grain classes), α_L, ϕ_p and f_1 (volumetric fraction of one grain class) are treated as global fitting parameters (fitted values: $\alpha_L = 0.15$ cm, $\phi_{im} = 0.085$, $f_1 = 0.22$), while k_m is fitted to each flow-rate ($J = 51.4 \times 10^{-4}$ mCi/mL). MRMT-2 takes k_m, ϕ_{im} and f_1 from MRMT-1 and fit α_L to each flow rate independently ($J = 43.0 \times 10^{-4}$ mCi/mL).

	ADE	**MRMT-0**			**MRMT-1**		**MRMT-2**	
q	D_L	k_m	D_L	ϕ_p	k_m	D_L	D_L	α_L
[mL/min]	[cm^2/min]	[mm/min]	[cm^2/min]	[–]	[mm/min]	[cm^2/min]	[cm^2/min]	[cm]
2.0	0.17	0.047	0.082	0.090	0.049	0.089	0.088	0.148
3.0	0.30	0.048	0.121	0.088	0.050	0.133	0.149	0.168
4.0	0.44	0.054	0.193	0.082	0.054	0.177	0.197	0.165
8.0	0.96	0.089	0.348	0.081	0.084	0.355	0.353	0.148
10.0	1.25	0.101	0.454	0.080	0.100	0.443	0.431	0.145
15.0	2.04	0.107	0.775	0.074	0.122	0.665	0.643	0.144
19.0	2.62	0.136	0.897	0.077	0.149	0.842	0.795	0.141

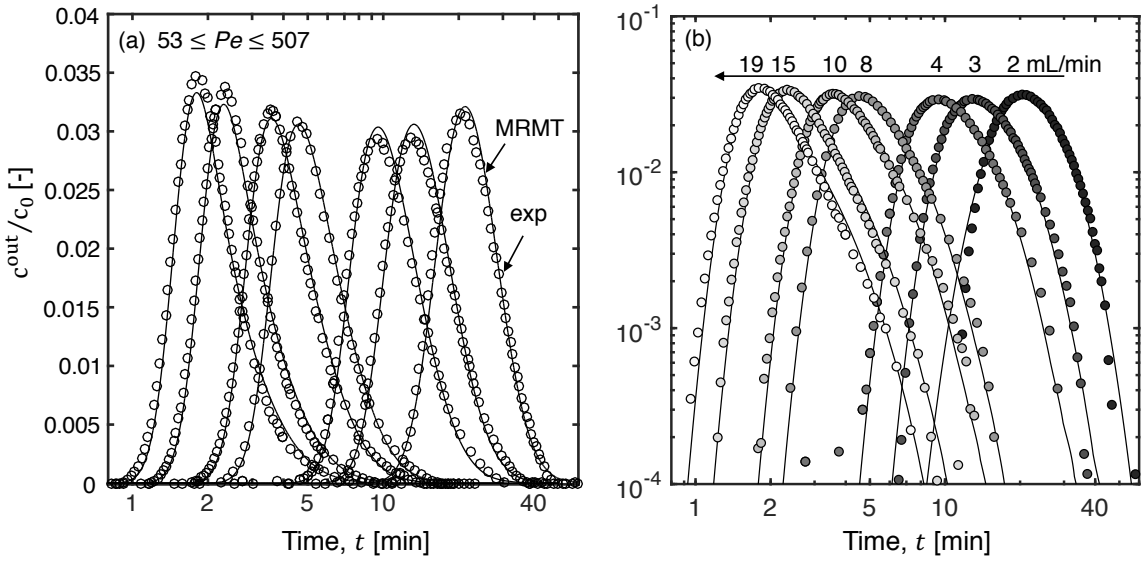

Figure 7.6: Effluent concentration breakthrough curves obtained from the PET experiments on Ketton Limestone for the flow rates ranging between 2 mL/min and 19 mL/min (corresponding to Pe = 53, 80, 107, 214, 267, 401 and 507, respectively). Figure (a) is presented using a linear scale (for the concentration), while (b) shows the same curves plotted on a double logarithmic scale. The symbols represent experimental data, while solid lines refer to model results (MRMT-1, fitted values reported in Table 7.5).

In Figure 7.6, it can be seen that experimental (symbols) and model results (solid lines, case MRMT-1) are in very good agreement. The latter have been obtained upon solving the one-dimensional MRMT model, by considering two characteristic grain sizes and by treating (i) the volume fraction of one grain class (f_1), (ii) the intragranular porosity (ϕ_p) and (iii) the longitudinal dispersivity (α_L) as global fitting parameters, in addition to fitting the flow-rate dependent mass transfer coefficient, k_m. The values of all fitted parameters are summarised in Table 7.5 (case MRMT-1, $J = 51 \times 10^{-4}$ mCi/mL). The fitted longitudinal dispersivity ($\alpha_\mathrm{L} = 0.15$ cm) is roughly one order of magnitude larger than the measured transverse dispersivity in KL (Boon et al., 2017), and compares favourably with estimates reported in the literature for carbonate rocks, such as Indiana Limestone ($\alpha_\mathrm{L} = 0.38$ cm) (Gist et al., 1990) and, most significantly, KL ($\alpha_\mathrm{L} = 0.16$ cm) (Honari et al., 2015).

It can be demonstrated that in these experiments, the time- (or length-) scale has been established for the dispersion coefficient to reach its asymptotic value. In fact, solute transport in KL has been shown to be characterised by a rather narrow spread of pore velocities (Bijeljic et al., 2013), thus resembling the behaviour observed in rocks with a highly connected pore space and with only moderate heterogeneities. For the experiments on Ketton Limestone, $l^* = \mathrm{Pe}/2$,

where $l \approx 0.320$ mm (Bijeljic et al., 2013) and $\mathrm{Pe} = vl/\mathcal{D}$. The dispersion coefficient reaches therefore an asymptotic value after the solute travels an average distance of $5 - 50$ mm for $\mathrm{Pe} = 30 - 300$, which is again below the length of the sample used ($L = 100$ mm). The model uses a constant value of intra-granular porosity, which accounts for roughly 30% of the total pore space in Ketton. This value is in excellent agreement with the independent estimate by mercury intrusion porosimetry (see Chapter 6). Most significantly, the mass transport resistance that is introduced by the presence of microporosity no longer needs to be compensated by an apparent decrease in its volume fraction; rather, access to this porosity is controlled by the mass transfer coefficient, which in the MRMT-1 model takes a different value depending on the grain class considered, i.e. $6k_{\mathrm{m}}/d_{\mathrm{e},j}$. The obtained fractions of the two representative grain classes ($f_1 = 0.22$ for $d_{\mathrm{e}} = 220$ μm and $f_2 = 1 - f_1 = 0.78$ for $d_{\mathrm{e}} = 660$ μm) compare favourably with our analysis performed on the micro-CT scans acquired on a smaller sister plug. This is demonstrated in Figure 7.7, where the two binned bar plot illustrating the proportion of the selected two grain classes are shown ($f_1 \approx 0.19$ and $f_2 \approx 0.81$).

We note that the MRMT-1 model provides a fit to the experimental data that is as good as the MRMT-0 approach, despite the significant reduction in the number of fitted parameters ($F_{11,479} = 1.78$, $p > .05$). Moreover, the application of MRMT-1 model with only one grain class ($f_1 = 1$) resulted in a significantly larger value of the objective function ($J = 160 \times 10^{-4}$ mCi/mL), emphasising the importance of capturing heterogeneities associated with the grain size distribution of rocks. However, we also show that introducing additional flexibility in fitting the measured profiles by considering α_{L} that depend on the flow rate (case MRMT-2, in Figure 7.1) does not provide a marked improvement in describing the experimental data (MRMT-1: $J = 51 \times 10^{-4}$ mCi/mL, MRMT-2: $J = 43 \times 10^{-4}$ mCi/mL, with fitting values reported in Table 7.5).

To better emphasise the inadequacy of the ADE to describe solute transport in KL, simulations were also run using this model and a longitudinal dispersivity that depends on the flow rate, in an attempt to capture the additional transport mechanism between inter- and intra-granular pore space. The parameter values obtained from this fitting exercise are also reported in Table 7.5 (case ADE) and the results are depicted in Figure 7.8 in terms of absolute deviations normalised by the tracer concentration in the feed as a function of the reduced time. In general, we

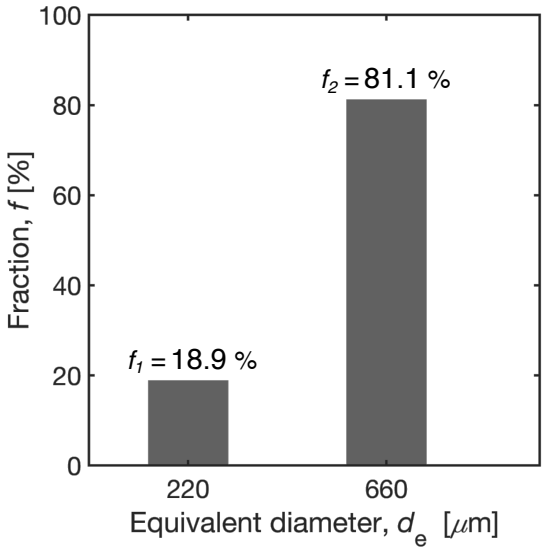

Figure 7.7: Histogram illustrating the proportion of two grain classes, $d_{\mathrm{p},1} = 220$ μm and $d_{\mathrm{p},2} = 660$ μm in KL. The dataset was obtained from the grain size distribution analysed in Figure 6.4b, by considering 2 bins with a defined threshold of $d_{\mathrm{e}} = 440$ μm.

notice that the application of the ADE results in a much larger dispersivity ($\alpha_{\mathrm{L}} \approx 0.4 - 0.7$ cm) as compared to the value obtained from a model of the form of the MRMT equation ($\alpha_{\mathrm{L}} = 0.15$ cm). Most significantly, the ADE produces a much poorer description of the measured effluent profiles. As shown in Figure 7.8, the two models perform comparatively well at low flow rates ($q = 2$ mL/min). At larger flow rates, the fit of the ADE deteriorates, i.e. it misses both the early breakthrough of the tracer and the long-time tailing, with deviations as large as 40% relative to the actual measured values. On the contrary, the agreement between the MRMT model predictions and the experimental data is consistently good over the whole range of flow rates.

One-dimensional concentration profiles along the length of the Ketton core are shown in Figure 7.9 for each flow rate tested at four distinct times. The latter correspond to the time at which 0.15, 0.3, 0.5 and 0.75 PV have been injected into the sample. In the plots, symbols refer to measurements that have been obtained from the reconstructed PET scans by averaging voxel concentration values within each 2.3 mm-thick slice and over a given time frame, which has been chosen so as to always represent $t/\tau_{\mathrm{exp}} = 0.16$ PV. Simulation results are given by the dashed lines and represent predictions by the MRMT-1 model. It can be seen that the latter is able to capture the temporal evolution of the solute plume as it moves through the rock at all flow rates. The overall agreement between experiment and model predictions is satisfactory,

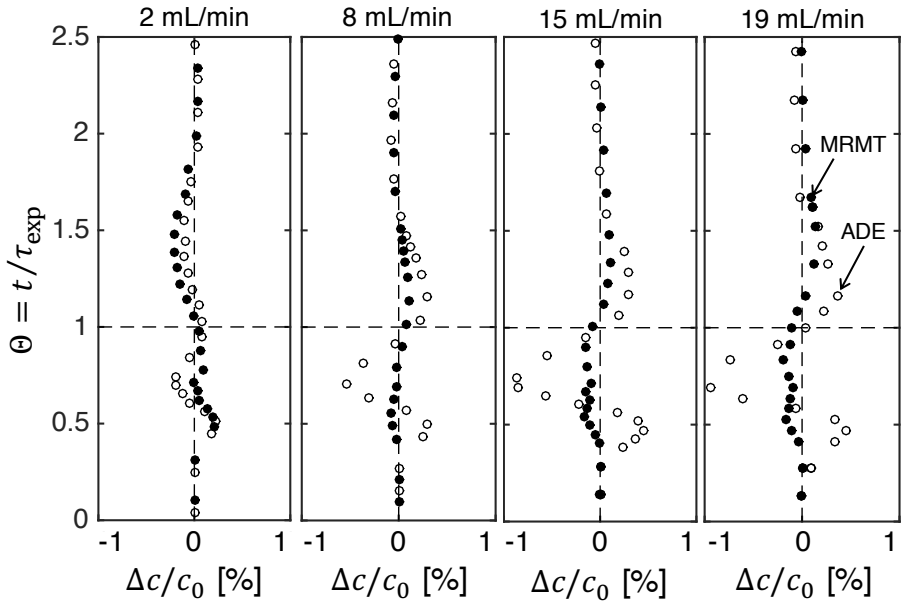

Figure 7.8: Deviations between measured tracer concentrations at the effluent and predictions by the ADE (empty circles) and MRMT-1 (filled circles) models for the experiments with KL. The deviation is computed as $\Delta c = (c^{\text{exp}} - c^{\text{mod}})/c_0$, where c_0 is the feed concentration, and is plotted as a function of the reduced time, $\Theta = t/\tau_{\text{exp}}$.

considering that the model is applied here in a fully predictive manner and the wide range of flow rates tested ($53 < \text{Pe} < 507$). Nevertheless, discrepancies exist, particularly at early times, that may reflect a systematic flaw in the adopted modelling approach. In particular, we note that the model predictions are less dilute than the experimental data. As discussed further in Chapter 9, the solute plume in the rock sample is significantly spread out by the presence of small-scale (mm) heterogeneities and has limited uniformity in the solute concentration. Accordingly, the numerical averaging of the experimental concentration values to produce the 1-D profiles shown in Figure 7.9 leads to an overestimation of the actual extent of mixing (dilution).

7.5.4 Edwards Brown Carbonate

As indicated in Table 7.3, the experiments with EB reveal a notable difference in the residence time between the experimental value (τ_{exp}) and the theoretical counterpart (τ). Similar to that shown in KL, we generally observe a larger deviation with increasing flow rate, that varied between -0.9 and 1.7%. This apparent dependency of flow rate on the total pore space of the flow field can again be attributed to the mass transfer limitations in the micropores. As compared to KL, we note that such characteristic behaviour is weaker (see Table 7.3), primarily because

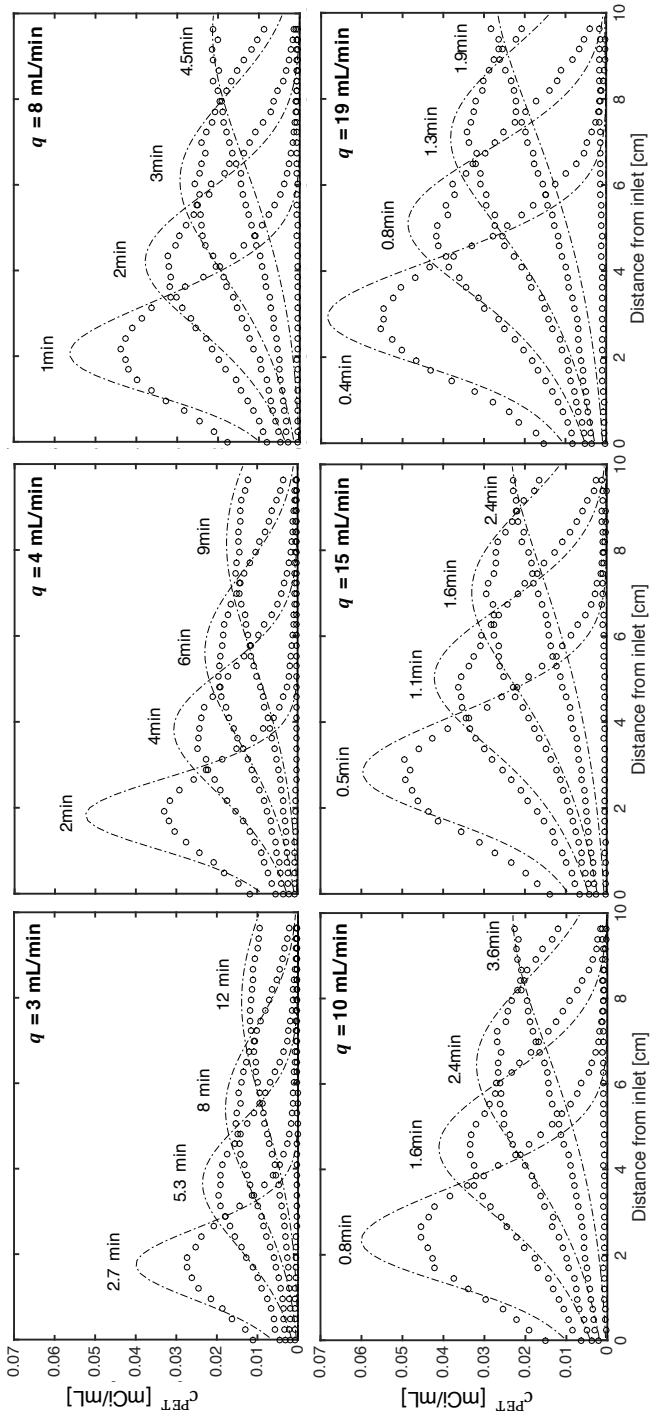

Figure 7.9: Slice-averaged internal concentration profiles along the length of the sample obtained from the PET experiments on KL at various flow rates (q = 3, 4, 8, 10, 15 and 19 mL/min) and at different times, corresponding to the injection of 0.15, 0.3, 0.5 and 0.75 PV. The symbols are experimental data, while the dashed lines are simulation results obtained from the MRMT-1 model. Because PET scans are reconstructed over discrete time intervals, each profile plotted represents a time frame of about ± 0.08 PV (arbitrarily chosen).

the volume fraction occupied by the intra-granular pore space (i.e. ∼10%, as demonstrated in Chapter 6) is significantly less than KL.

Table 7.6: Optimum model parameters obtained from fitting MRMT to the BTCs measured on EB (model results plotted in Figure 7.10). Details of the modelling scenarios considered in this work can be found in Section 7.4. MRMT-1 produces a single set of following variables: $\alpha_L = 0.225$ cm and $\phi_p = 0.118$. The following values of objective function were obtained for each scenario, i.e. $J = 0.0146$ mCi/mL (MRMT-1) and $J = 0.0134$ mCi/mL (MRMT-2).

	MRMT-1		**MRMT-2**	
q	k_o	D_L	D_L	α_L
[mL/min]	[min^{-1}]	[cm^2/min]	[cm^2/min]	[cm]
2.0	0.583	0.067	0.067	0.228
4.0	0.837	0.134	0.140	0.237
10.0	1.303	0.333	0.338	0.229
15.0	1.429	0.499	0.469	0.211
19.0	1.753	0.632	0.595	0.212

The BTCs measured for the EB core are presented in Figure 7.10 again using (a) a linear-scale for the concentration and (b) double-logarithmic scale to highlight the concentration tails. Also plotted in the figure are the corresponding model predictions (solid lines) that were obtained from fitting the measured curves using the MRMT-1 approach; the latter closely predicts the experimental BTCs over the entire dataset ($q = 2 - 19$ mL/min). In figure(b), we show that the model is also capable at capturing the tailings of the BTCs. The model yields a single value of dispersivity, i.e. $\alpha_L = 0.225$ cm that is significantly larger than the corresponding values obtained for KL ($\alpha_L = 0.15$ cm) and BS ($\alpha_L \approx 0.05$ cm), thus reflecting the pronounced effects of heterogeneous features observed in EB, such as vuggy porosity, complicated grain/pore structures and subcore-scale porosity heterogeneity. Again, the obtained dispersivity coefficient in this system corresponds to an asymptotic value as the length of the core used (i.e. $L = 103$ mm) is significantly larger than the characteristic length scale required to evolve into a "Fickian" regime (i.e. $l^* \times d_e \approx 4 - 40$ mm, with $d_e \approx 0.39$ mm). The output of the MRMT-1 model gives an intra-granular porosity, $\phi_p = 0.118$, which corresponds to about 28% of the total pore space. While this is consistent with the reported values in the literature, i.e. $\phi_p = 0.10$ (Lai et al., 2015), it is noticeably higher than our independent MIP estimates ($\phi_p/\phi_T \approx 10\%$). For EB, we show that letting dispersivity depends on the flow rate is unnecessary due to the small differences in the objective function between MRMT-1 ($J = 0.0146$ mCi/mL) and MRMT-2 ($J = 0.0134$ mCi/mL). Accordingly the presented results provide more consistency because the

proposed modelling approach minimises the use of fitting parameters. The optimum model parameters obtained for the different fitting approaches proposed are summarised in Table 7.6.

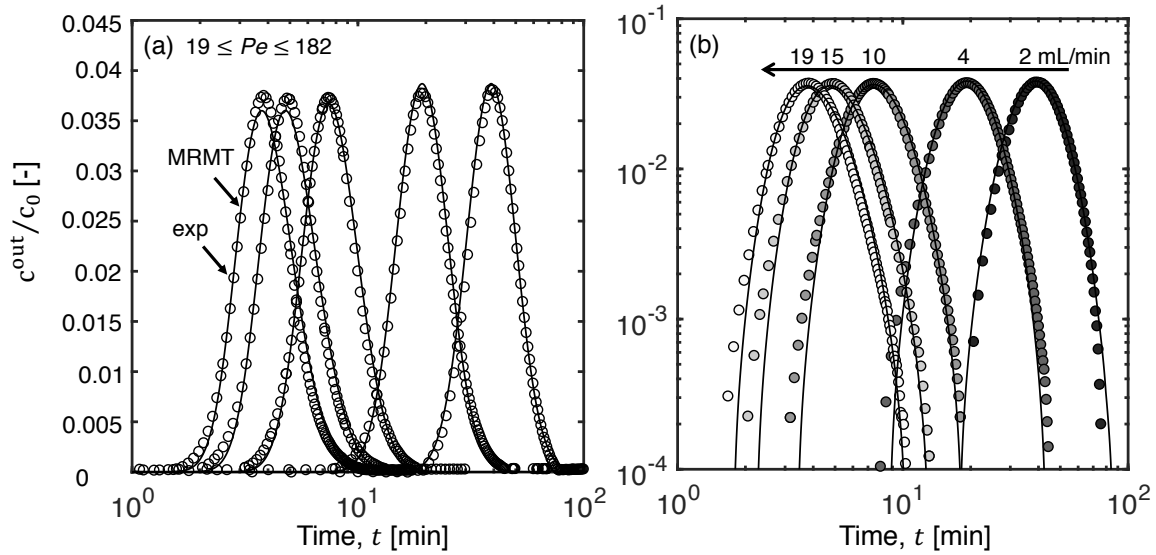

Figure 7.10: BTCs obtained from the radioactivity measurements on EB for $q = 2 - 19$ mL/min (corresponding to Pe = 19, 38, 96, 144 and 182, respectively). Figure (a) is presented on a semi-logarithmic scale, while (b) shows the same curves plotted on a log-log plot. The symbols are experimental measurements, while solid lines refer to the corresponding model fits (i.e. MRMT-1, model parameters reported in Table 7.6).

To evaluate the predictive capability of the MRMT-based models to describe the dynamic behaviour of the displacement process within the rock core, the 1-D internal concentration profiles obtained from the PET dataset are plotted along with the MRMT-1 model predictions (shown in Figure 7.10). The results are presented for five time frames (with each time frame corresponding to an average of about 0.12 PVs) at three distinct flow rates, $q = 4, 10$ and 19 mL/min. In general, we notice that the internal dispersion behaviour is similar to that presented in KL. First, we observe that the displacement of the tracer plume is characterised by a significant mixing, as demonstrated by the rapid broadening of the concentration profiles over time. In the figure, we notice that the deviations between experiment and model are much larger when the tracer is first entered into the core, and is gradually reduced over time/length scales. This observation in fact highlights the establishment of Fickian regime as the solute plume propagates along the core.

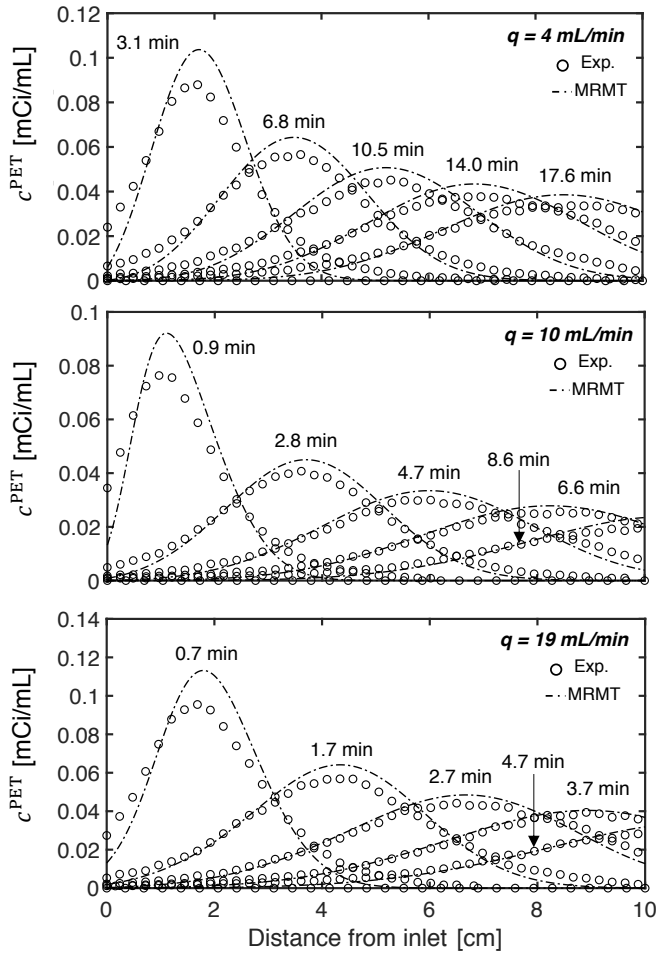

Figure 7.11: Internal concentration profiles plotted along the axial direction of the EB core. The curves at four distinct time frames are shown, with each represent an average of ±0.06 PVs. The symbols are the PET data and the solid lines are the corresponding MRMT-1 model predictions. The results are presented for the experiments carried out at three distinct flow rates; $q = 4, 10$ and 19 mL/min. This corresponds to Péclet numbers, $\mathrm{Pe} = 38, 96$ and 182, respectively

7.6 Discussions

7.6.1 Dependency of dispersion coefficients on fluid velocity

To examine the suitability of a power law correlation ($D_\mathrm{L} \propto v^m$) to describe hydrodynamic dispersion for the range of Péclet number considered ($\mathrm{Pe} = 20 - 500$), the obtained longitudinal dispersion coefficients, D_L are plotted as a function of the (pore) velocity, v, in Figure 7.12. The dataset is presented on a double-logarithmic scale in each sub-plot, and the obtained values of D_L are shown for the two modelling approaches tested, namely MRMT-1 (empty circles, no dependency) and MRMT-2 (filled triangles, dependency). The lines correspond to the best-fitted

curves for measured dataset that have been regressed to a power law function. As expected, for MRMT-1, we obtain a pure linear dependence of dispersion coefficient on fluid velocity (i.e. $m = 1$). Notably, small deviations in the exponents, $m = 0.95 - 1.12$ (depending on the porous media) are observed when α_{L} is fitted to each experimental flow rate (case MRMT-2). Recalling that even homogeneous bead- and sand-packs produces a large discrepancy in the exponent $m \approx 1 - 1.2$ (discussed in Chapter 5), we contend that this narrow span in the exponent can easily lie within the experimental uncertainties of dispersion measurements. In fact, when the dispersion dataset obtained from MRMT-2 is correlated using a linear regression (i.e. by forcing $m = 1$), an excellent fit is also obtained (shown in the inset of Figure 7.12), with an average R-squared value of $R^2 \approx 0.997$. Based on the analysis carried out in this section, we note that the obtained experimental dispersion complies with the theoretical definition of dispersion coefficient, $D_{\mathrm{L}} = \alpha_{\mathrm{L}} v$ (for Pe > 15) (Dullien, 1992), leading to an intrinsic dispersivity value characteristic of a porous medium.

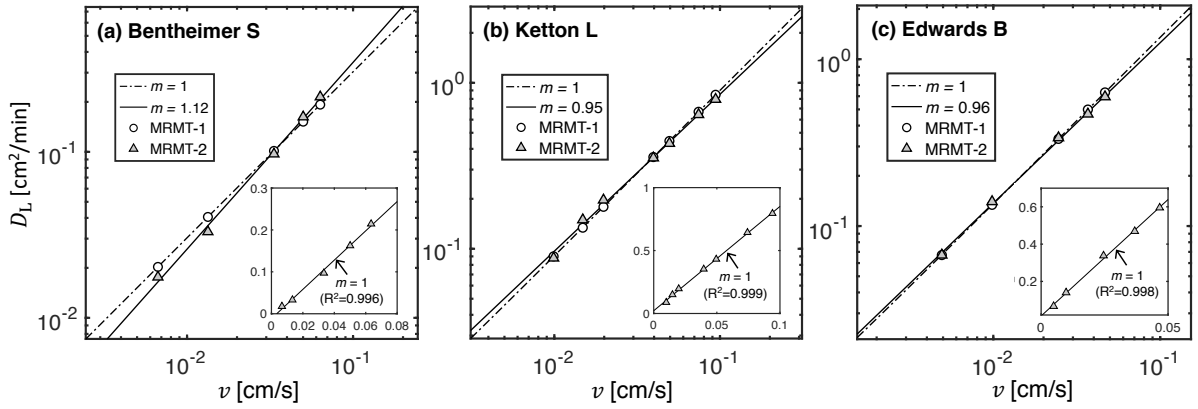

Figure 7.12: Comparisons of the power law correlation between interstitial velocity and longitudinal dispersion coefficient, i.e. $D_{\mathrm{L}} \propto v^m$. The circles are the results from MRMT-1, whereas the corresponding dataset obtained from MRMT-2 is given as triangles. The solid lines are the best-fit to each dataset with a power-law function. In the inset of each sub-plot is presented the MRMT-2 dispersion data that has been regressed to a linear function.

7.6.2 Correlating longitudinal dispersion coefficients

Figure 7.13(a) presents an updated dispersion plot (compared to the one presented in Chapter 5), that includes experimental dataset measured on four porous media, including beadpacks (BP, squares), Bentheimer Sandstone (BS, triangles), Ketton Limestone (KL, circles), and Edwards Brown Carbonate (EB, diamonds). The results are shown in terms of $D_{\mathrm{L}}/\mathcal{D}$ as a function of

Péclet number ($\mathrm{Pe} = vd_\mathrm{e}/\mathcal{D}$) on a double logarithmic scale, so as to cover a wide range of dataset measured. Again, the empirical correlation proposed by Sahimi et al. (1986) is applied here to describe our experimental measurements on geologic core samples;

$$D_\mathrm{L}/\mathcal{D} = 1/\sqrt{2} + \sigma \mathrm{Pe}^m \tag{7.10}$$

where σ and m are the constant and exponent used to describe inhomogeneity of a porous medium. In this study, $m = 1$ applies to all the cases, as demonstrated in the previous section. Since the experiments carried out here lie in the advective-dominated regime ($\mathrm{Pe} > 15$), the diffusive term in Eq. 7.10 (i.e. $1/\sqrt{2}$) can be neglected. Combining Eq. 7.10 with the definition of dispersivity, i.e. $\alpha_\mathrm{L} = vD_\mathrm{L}$, it can be shown that $\alpha_\mathrm{L} = \sigma d_\mathrm{e}$. The strength of heterogeneity, as measured from the σ parameter (sometimes referred to as the "inhomogeneity factor" (Perkins and Johnston, 1963)), can be related to the transport property obtained from pulse-tracer tests (α_L) and the microscopic property of a porous medium, d_e. The results obtained from Eq. 7.10 are indicated by the solid lines in Figure 7.13. For a homogeneous medium, such as granular sand- and bead-packs, the inhomogeneity factor takes a smallest value $\sigma = 0.5$ (i.e. $\alpha_\mathrm{L} = 0.5 \times d_\mathrm{p}$), as suggested by the Random-Walk theory (Gist et al., 1990) (dashed line). As evidenced in the figure, the inhomogeneity factor for rocks takes much larger values than uniform beadpacks, even for a relatively homogeneous system, such as BS. The latter gives σ that is almost four times larger, i.e. $\sigma = 1.9$. For the core samples considered in this work, the heterogeneity increases in the order BP (0.5) < BS (1.9) < KL (2.8) < EB (5.8). Remarkably, this sequence follows nicely with the structural heterogeneity of the core samples, as indicated in Chapter 6. The agreement provided here presents an independent verification that transport properties can be used to quantify the strength of heterogeneity of the rock. Results from Honari et al. (2015) are also plotted in Figure 7.13 as empty symbols alongside the dataset from this study, and confirm the excellent agreement with Eq. 7.10 for $0.1 < \mathrm{Pe} < 1000$ and over a range of dispersion coefficients that span four orders of magnitude. It is worth noting again that our modelling approach uses $m = 1$ in Eq. 7.10 and that we don't observe here the weak nonlinear dependence of the dispersion coefficient on the Péclet number ($D_\mathrm{L}/\mathcal{D} \sim \mathrm{Pe}^{1.2-1.4}$) that has been reported in previous studies on carbonate rocks, including Ketton Limestone (Bijeljic et al., 2011; Honari et al., 2015).

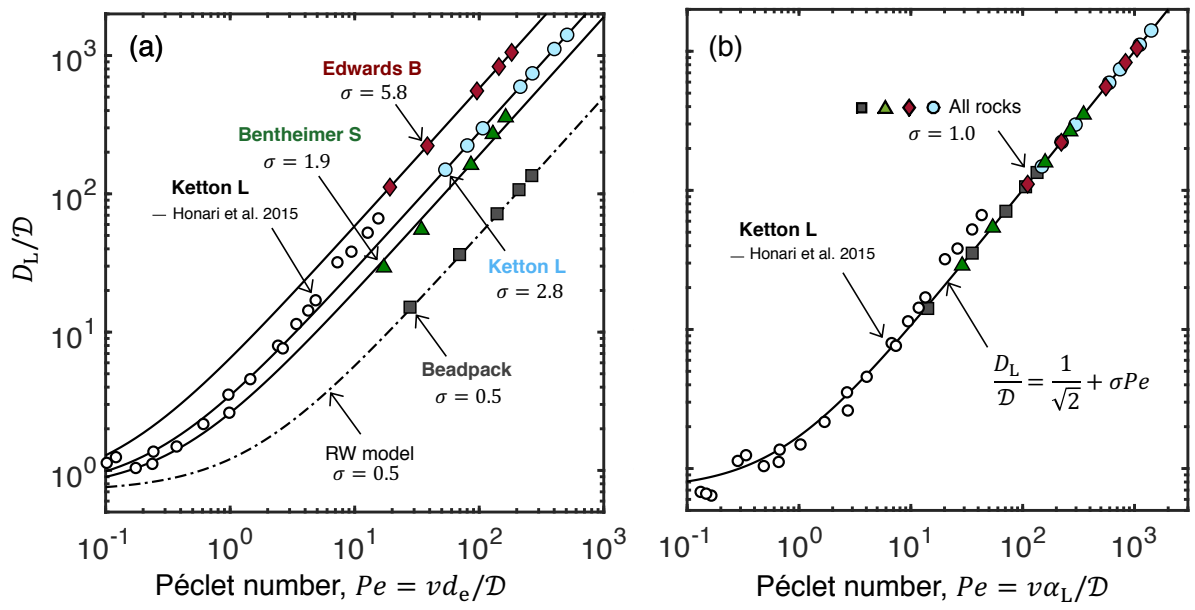

Figure 7.13: Normalised longitudinal dispersion coefficient, $D_L/\mathcal{D}$ plotted as a function of Péclet number. The filled symbols are the experimental data obtained from this work, namely BS (triangles), KL (circles), EB (diamonds) and BP (squares); the empty circles are the available literature data found on KL (Honari et al., 2015), and the solid lines are the commonly used empirical correlation (Sahimi et al., 1986), i.e. $D_L/\mathcal{D} = 1/\sqrt{2} + \sigma \mathrm{Pe}^m$, with σ and m being the inhomogeneity coefficients. In Figure (a), the equivalent diameter, d_e was used as characteristic length scale in the Péclet number definition ($\mathrm{Pe} = vd_e/\mathcal{D}$), whereas the longitudinal dispersivity, α_L ($\mathrm{Pe}_\alpha = v\alpha_L/\mathcal{D}$) were used in Figure (b).

In order to better interpret the correlation between dispersion and Péclet number amongst porous media, our dispersion data is also evaluated by means of defining the Péclet number as $\mathrm{Pe}_\alpha = v\alpha_L/\mathcal{D}$, therefore using α_L as the characteristic length scale l (results presented in Figure 7.13b). We observe that the dispersion measurements follow one single curve (with $\sigma = 1$), irrespective of the rock sample. The inhomogeneity factor, i.e. σ determined in this Chapter is summarised in Table 7.7.

7.6.3 Characteristic RTD functions

Figure 7.14 presents the normalised RTD function $E_\Theta(\Theta)$ plotted over reduced time ($\Theta = t/\tau_{exp}$) for all the tracer experiments carried out in this study. As a reference, the result obtained for beadpacks (BP) is also shown in the figure. As indicated in the figure, while we observe a symmetric (with peak of the curves at $\Theta = 1$) and single characteristic RTD curve in the case of BP (irrespective of the system size and flow rate), the profiles measured on rocks are characterised by the typical features of anomalous ('non-Fickian') transport, namely an early

breakthrough and a long-time tailing. This is evident, as the peak of the curves deviate from $\Theta = 1$. For BS, this deviation is quite small, and the RTD functions are characterised by a very narrow distribution ($\Theta \approx 0.7 - 1.4$) that approaches a single reference BTC. On the contrary, the BTCs for the carbonate cores are much more dispersed and are characterized by a significant early breakthrough, $\Theta \approx 0.4$, followed by a much more pronounced tailing at later times (up to $\Theta \approx 2.0 - 3.0$). Despite of being a more heterogeneous rock core, we note that EB produces a curve that is more 'Fickian' than KL, which is apparent by the sharper decay in the BTC tailing. This highlights the relative importance of microporosity on controlling the anomalous behaviour observed, particularly towards the long-time tailing of the BTCs. Interestingly, for the two carbonate rocks, both experimental data (symbols) and model predictions (solid lines) no longer collapse into a single characteristic $E_\Theta(\Theta)$ curve. Instead, they indicate a clear trend with the late-time tailing of the breakthrough curve becoming more pronounced with increasing Pe. We note that in this study this behaviour has been observed irrespectively of the tracer used (see Figure 7.5), taking the order of EB<KL. As discussed in the next section, this characteristic flow-rate effect is to be traced back to the intra-granular transport processes in the microporous rocks.

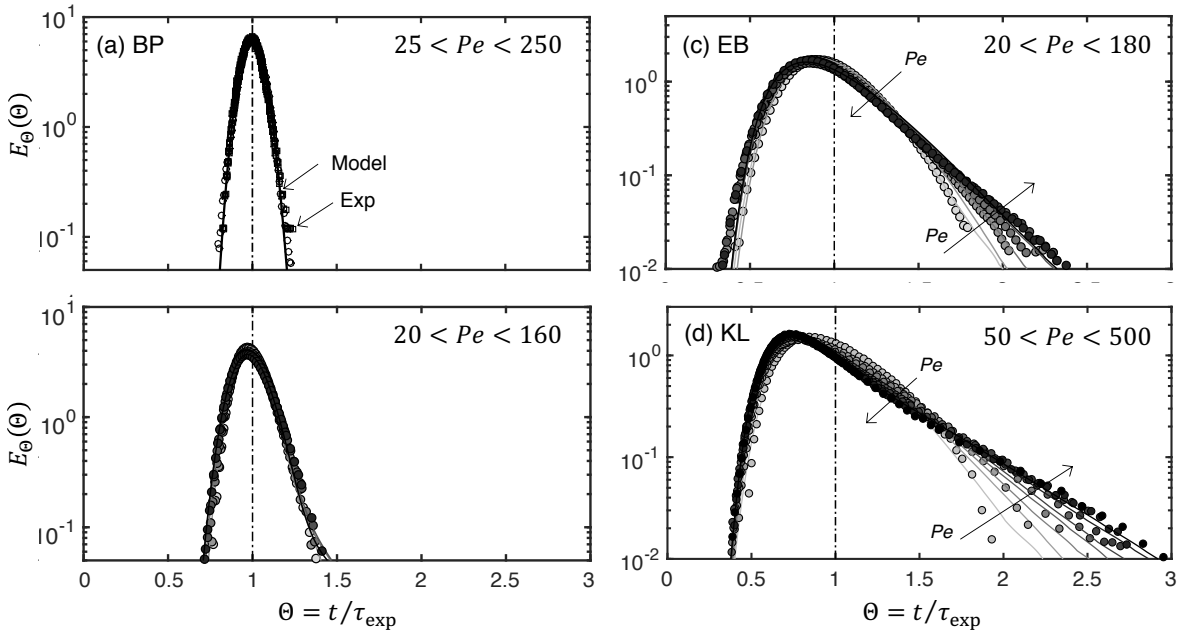

Figure 7.14: Normalised RTD function, E_Θ, as a function of the reduced time, $\Theta = t/\tau_{exp}$, for all the experiments carried out in this study on (a) BP ($25 < \text{Pe} < 250$, taken from Chapter 5), (b) BS ($20 < \text{Pe} < 160$), (c) EB ($20 < \text{Pe} < 180$) and (d) KL ($50 < \text{Pe} < 500$). The symbols correspond to the experimental data, while the solid lines refers to the numerical solution of the ADE (BP) and MRMT models (MRMT-1 for EB and KL, MRMT-2 for BS).

7.6.4 Mass transfer limitations in microporous rocks

A key distinctive feature of carbonate rocks is the presence of a significant amount of intra-granular porosity, which in KL and EB, can account for about $10 - 30\%$ of the total pore volume. To access this microporosity in a regime dominated by advective flow, the solute particles need to diffuse through the boundary layer that surrounds the rock grains and whose thickness ultimately depends on the hydrodynamic conditions. This external fluid film resistance is often described using a simple linear rate expression of the form of Eq. 7.5 with an overall mass transfer coefficient, k_o. For the experiments with KL, the latter can be transformed to the intrinsic mass transfer coefficient by assuming spherical particles, i.e. $k_\mathrm{m} \approx k_\mathrm{o} d_\mathrm{e}/6$. This conversion is corrected by the sphericity index ($\Psi = 0.53$) for EB, i.e. $k_\mathrm{m} = k_\mathrm{o}/a \approx \Psi k_\mathrm{o} d_\mathrm{e}/6$ (where the specific surface area, $a \approx 6/(\Psi d_\mathrm{e})$), to account for the non-spherical nature of the grains. In Figure 7.15 the mass transfer coefficient obtained from fitting the tracer breakthrough curves in terms of the Sherwood number, $\mathrm{Sh} = k_\mathrm{m} d_\mathrm{e}/\phi\mathcal{D}$, is plotted as a function of the Reynolds number, $\mathrm{Re} = \rho u d_\mathrm{e}/\mu$ for the result obtained on KL (filled circles) and EB (empty circles). In the inset of the figure, the same data are plotted, but in terms of k_m as a function of the Péclet number, $\mathrm{Pe} = v d_\mathrm{e}/\mathcal{D}$. As expected, the Sherwood number increases with increasing Re (or Pe), which reflects the thinning of the boundary layer with increasing flow rate. Notably, the observed variation of the mass transfer coefficient for KL closely follows the widely applied empirical correlation for packed beds (Wakao and Funazkri, 1978):

$$\mathrm{Sh} = 2 + 1.1\mathrm{Sc}^{1/3}\mathrm{Re}^{0.6} \tag{7.11}$$

where the Schmidt number is defined as $\mathrm{Sc} = \mu/(\rho\phi\mathcal{D})$ and, accordingly, $\mathrm{Re} = \mathrm{Pe}/\mathrm{Sc}$. For EB, the mass transfer data falls somewhat below the correlation curve and instead, it can be described by imposing the lower limit of the Eq. 7.11 with 0.5, rather than 2 (dashed line in Figure 7.15). Such deviation can be attributed to the geometric complexity of the EB core, in contrast to an ideal system, e.g. a uniformly packed bed. In fact, literature data reveals a significant scatter in the experimental measurements even on packed beds, where $\mathrm{Sh} < 2$ is generally observed at low Re (Ruthven, 1984). As anticipated in the previous section, the interaction between the two transport mechanisms, (i) mechanical dispersion through inter-granular

pores and (ii) molecular diffusion through the intra-granual (micro)pores, is quite complex and produces a characteristic flow-rate effect in the E_Θ plot. In fact, the two transport parameters both increase with increasing Péclet number, albeit with a different strength: $D_\mathrm{L} \propto \mathrm{Pe}$ and $k_\mathrm{m} \propto \mathrm{Pe}^{0.6}$. At low Péclet numbers, the boundary layer surrounding the rock grains is large, to the extent that diffusive mass transfer across inter- and intra-granular pores enables achieving a more uniform transport of solute. With increasing Péclet number, the diffusive boundary layer becomes thinner, corresponding to a larger value of k_m that enables the solute to still probe the intra-granular pore space of the rock. However, the difference between the rates of the two transport mechanisms is now much larger and the delayed diffusion of the solute from the micropores causes long-tailing in the elution profiles and, accordingly, anomalous transport.

We also note from Eq. 7.11 that for $\mathrm{Re} \to 0$, the mass transfer coefficient approaches the limiting values $k_\mathrm{m} = 0.0032$ cm/min (KL) and $k_\mathrm{m} = 0.0026$ cm/min (EB), which can be related to an *effective* diffusion coefficient in the porous medium:

$$\text{for KL} : \mathcal{D}_\mathrm{eff} = k_\mathrm{m}\frac{d_\mathrm{e}}{2} \approx 1 \times 10^{-4}\ \mathrm{cm}^2/\mathrm{min} \tag{7.12a}$$

$$\text{for EB} : \mathcal{D}_\mathrm{eff} = k_\mathrm{m}\frac{d_\mathrm{e}}{0.5} \approx 2 \times 10^{-4}\ \mathrm{cm}^2/\mathrm{min} \tag{7.12b}$$

The common perception is that in a porous medium $\mathcal{D}_\mathrm{eff} = \mathcal{D}/X$, where X is a correction factor that accounts for the obstructions presented to diffusion in a tortuous pore space (Dullien, 1992). Because of the definition of the Sherwood number given above, in this study $\mathcal{D}_\mathrm{eff} = \phi\mathcal{D}$, which corresponds to $X \approx 6.2$ (KL) and $X \approx 3.0$ (EB). Notably, this value is much larger than the typical estimate for well-sorted sand ($X \approx \sqrt{2}$ (Sahimi et al., 1986)) and more comparable to the value reported for rocks with a fractional volume of micropores similar to the samples studied in this work ($X \approx 4.7$ for Bandera Sandstone with 34% microporosity (Dullien, 1992)). Accordingly, when *total* porosity is used in the definition of the *effective* diffusion coefficient, $\mathcal{D}_\mathrm{eff} = \phi_\mathrm{T}\mathcal{D}/b$, a tortuosity coefficient is recovered for both KL and EB, that takes the value $b = 1.4$ and 1.2, respectively.

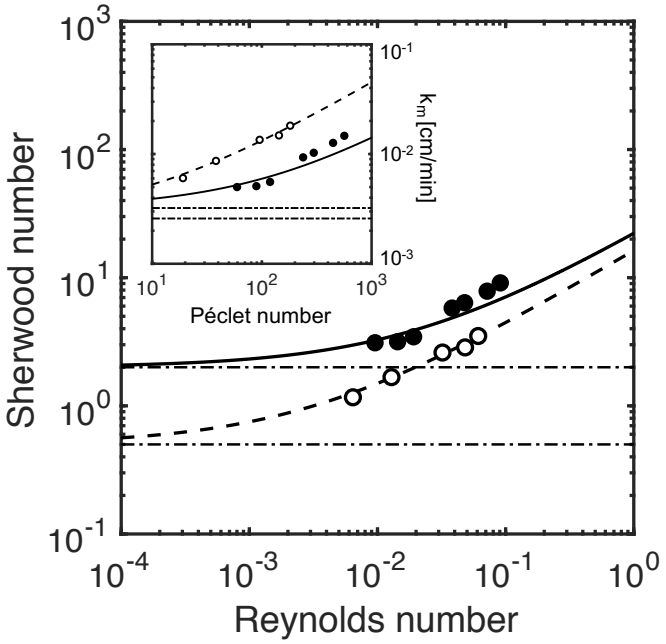

Figure 7.15: Mass transfer data for KL and EB plotted as Sherwood number, $\mathrm{Sh} = k_\mathrm{m} d_\mathrm{e}/(\phi\mathcal{D})$, as a function of the Reynolds number, $\mathrm{Re} = \rho u d_\mathrm{e}/\mu$, where k_m is the intrinsic mass transfer coefficient, d_e is the equivalent grain diameter, ϕ is the inter-particle porosity, $\mathcal{D}$ is the molecular (bulk) diffusion coefficient, ρ and μ are the fluid density and viscosity, respectively. Symbols corresponds to values of k_m obtained upon fitting the MRMT-1 model to the experimental tracer breakthrough curves for KL (filled circles) and EB (empty circles). The solid line represents a widely used correlation for mass transfer packed beds Wakao and Funazkri (1978), i.e. $\mathrm{Sh} = 2 + 1.1\mathrm{Sc}^{1/3}\mathrm{Re}^{0.6}$, where $\mathrm{Sc} = \mu/(\rho\phi\mathcal{D})$. The dashed line is the correlation plotted when the limiting value is 0.5. In the inset, the same data are plotted in terms of k_m vs. Péclet number, $\mathrm{Pe} = v d_\mathrm{e}/\mathcal{D}$, where v is the interstitial velocity ($v = u/\phi$). Constant parameter values: $\rho = 1000$ kg/m^3, $\mu = 0.001$ Pa.s and $\mathcal{D} = 1 \times 10^{-9}$ m^2/s.

7.7 Concluding remarks

We have undertaken a study in which solute transport in three rocks has been investigated over a wide range of Péclet numbers ($\mathrm{Pe} \approx 15 - 500$). Miscible displacements were conducted by combining classic pulse-tracer tests with the simultaneous imaging of the transport of radiotracers using PET. The experimental protocol is validated by comparing results obtained with brine- and radio-tracers. The signal-to noise ratio (SNR) analysis indicates that radio-tracer measurements provides a much higher sensitivity as compared to the classical measurement technique involving conductivity measurements. The former presents a promising technique for the study of solute transport in heterogeneous porous media due to its ability to quantitatively obtain the dynamic evolution of entire tracer plume. Two transport models, the Advection Dispersion Equation (ADE) and the Multi-Rate Mass Transfer (MRMT) model, have been thoroughly evaluated with both the tracer effluent history and the internal concentration profiles measured

by PET.

In all the systems, we observe a linear dependence of the dispersion coefficient on the Péclet number ($D_L \propto Pe$) over the range of flow rates investigated. The analysis of the residence time distribution functions reveal mass transport limitations in the microporous carbonate rocks in the form of a characteristic flow-rate effect, which was not present in Bentheimer Sandstone. The MRMT model has been successfully applied to describe the breakthrough curve measurements on the rock samples by considering various classes of grain sizes (depending on the sample), and by using single dispersivity and intra-granular pore space that is independent of the fluid velocity. In this study, the extent of heterogeneity was quantified from dispersivity measurements in terms of "inhomogeneity factor", which increases in a order that is consistent with the geometric heterogeneity of the rocks, as characterised in Chapter 6 (BS < KL < EB). By comparing the results obtained from the ADE with MRMT models, we demonstrate the use of MRMT is essential particularly for highly microporous rocks (i.e. EB and KL). This is not only because the latter provides a better description of the effluent profiles, but also gives much smaller dispersion coefficients, as a consequence of decoupling the effects of microporosity from "Fickian" dispersion. Mass transfer between the flowing fluid and the porous particles is well described using an external fluid film resistance model and the obtained mass transfer coefficients scale favourably against a widely used correlation for packed beds ($k_m \propto Pe^{0.6}$). These results provide a more consistent picture than what the current literature may suggest regarding the use of the MRMT model to carbonate rocks.

Table 7.7: A comparison between equivalent grain diameter, d_e, longitudinal dispersivity, α_L and inhomogeneity factor, σ measured in this study. The latter was obtained from ($\sigma = \alpha_L/d_e$. α_L for BS corresponds to an average value obtained from the MRMT-2, over the Péclet numbers studied.

	d_e [mm]	α_L [mm]	σ [–]
Beadpack	0.570	0.29	0.52
Bentheimer S	0.257	0.49	1.90
Ketton L	0.541	1.53	2.83
Edwards B	0.391	2.25	5.75

Chapter 8

Modelling Anomalous Transport Using CTRW Framework

8.1 Introduction

While the MRMT approach provides an insightful perception of anomalous transport by introducing microscopic mass transfer due to the presence of dual-porosity (i.e. intra- and intergranular porosity), it does not explicitly consider the influence of spatial heterogeneity. In this chapter, the same breakthrough curve (BTC) dataset on the three core samples analysed in the previous chapter is re-evaluated by implementing the continuous time random walk (CTRW) theory. By using a stochastic formulation, the latter accounts for the presence of small-scale heterogeneities in the porous medium (Cortis and Berkowitz, 2004; Berkowitz et al., 2006), thereby enabling the quantitative description of a broad range of anomalous behaviours observed in the effluent profiles (Kosakowski et al., 2001). The objective of this study is therefore two fold; first, the CTRW theory is applied for the first time to the analysis of measurements on laboratory carbonate samples. Secondly, by analysing different rock samples, the aim is to achieve a better understanding of the obtained model parameters and their variation with flow rate. In addition to comparing the suitability of the CTRW model to describe the measured BTCs, the obtained parameters are compared to those estimated using the MRMT model.

8.2 Modelling

The transport equation of the one-dimensional CTRW model, in its general form, is written as follows (Berkowitz et al., 2006; Heidari and Li, 2014):

$$\frac{\partial \overline{c}(z,t)}{\partial t} = -\int_0^t M(t_i)\left[v_\psi \frac{\partial \overline{c}(z,t')}{\partial z} - D_\psi \frac{\partial^2 \overline{c}(z,t')}{\partial z^2}\right] dt' \tag{8.1}$$

where $\overline{c}$ is the concentration normalised by the feed, c_o. v_ψ and D_ψ are the 'transport velocity' and '*generalised* dispersion coefficient' in the CTRW framework, respectively. The model considers the movement of solute particles as a stochastic (random) process that can be described from a series of transition events with displacements z and time steps $t_i = t - t'$. The displacement events are governed by a memory function, $M(t_i)$ (Berkowitz et al., 2006). The latter plays a central role in the CTRW model to capture anomalous transport, because it accounts for the unresolved heterogeneities at the subcore-scale (Cortis and Berkowitz, 2005). In the mathematical formulation of the CTRW theory, the Laplace transform of the memory function, $\tilde{M}(\omega)$ is often used:

$$\tilde{M}(\omega) = t_1 \omega \frac{\tilde{\psi}(\omega)}{1 - \tilde{\psi}(\omega)} \tag{8.2}$$

where t_1 is the mean transit time of solute particles to traverse between two sizes, z and z'. $\mathcal{L}[\psi(z,t)] = \tilde{\psi}(\omega)$ is the probability density function (PDF) that determines the distribution of tracer transition times. Various definitions of $\tilde{\psi}(\omega)$ are provided in the open literature to better describe 'anomalous' behaviour observed in the BTC measurements. In this study, we apply one of the most common types of density function, the so-called "truncated power law" (TPL):

$$\psi(t) = \left[t_1 \tau_2^{-\beta} \exp(\tau_2^{-1}) \Gamma(-\beta, \tau_2^{-1})\right]^{-1} \frac{\exp(-t/t_2)}{(1 + t/t_1)^{1+\beta}} \quad \text{for} \quad 0 < \beta < 2 \tag{8.3}$$

where t_2 is the "cutoff" time that corresponds to the the time when power-law (anomalous) behaviour ends (Heidari and Li, 2014). $\tau_2 = t_2/t_1$ and Γ is the incomplete gamma function (Abramowitz and Stegun, 1970). The extent of non-Fickian behaviour is measured by β ($0 < \beta < 2$), with larger values referring to more homogeneous systems. The applications of the TPL-based CTRW framework has been successfully demonstrated in various experimental works on well-defined porous media, including (both homogeneous and heterogeneous) bead-/sand-packs,

as well as soil columns (Berkowitz et al., 2000; Cortis and Berkowitz, 2004; Bijeljic and Blunt, 2006; Deng et al., 2008; Berkowitz and Scher, 2009; Heidari and Li, 2014; Muniruzzaman and Rolle, 2017). On the contrary, very limited studies are reported where the CTRW has been applied to describe observations in rocks: Berea sandstone (Cortis and Berkowitz, 2004; Bijeljic et al., 2011) (Berea sandstone), Portland limestone (Bijeljic et al., 2011) and fractured till (Kosakowski et al., 2001).

To account for the presence of microporosity, an alternative model, known as the CTRW sorption model (Cortis et al., 2006) has been used. This model treats the microscopic diffusion of solute particles by a series of adsorption and desorption events through the use of an additional density function $\gamma(\omega)$,

$$\gamma(\omega) = \omega + \Lambda - \Lambda\tilde{\varphi}(\omega) \tag{8.4}$$

such that the overall PDF of a single particle transition in Laplace space becomes:

$$\tilde{\psi}(\omega) = \tilde{\psi}_0(\gamma(\omega)) \tag{8.5}$$

where Λ is the average sorption ('sticking') rate. $\tilde{\varphi}(\omega)$ is the probability function of 'sticking' time in the Laplace domain and $\tilde{\psi}_0$ is the distribution function associated with the heterogeneity of the pore space. As the rock samples considered in this study show a great extent of geometric heterogeneity at the pore scale (see Chapter 6), the TPL model (Eq. 8.3) has been used in $\tilde{\psi}_0$ to account for the microscopic complexities. Cortis et al. (2006) proposed a combination of two expressions to represent the PDF of 'sticking' times of a solute particle; this consists of a power-law tailing (with exponent n), and a uniform distribution function, given by the following expression:

$$\tilde{\varphi}(\omega) = W\frac{1}{1+\omega^n} + (1-W)\frac{1}{T\omega} \tag{8.6}$$

where W is the weight fraction given to each function, T is the truncation time for the distribution. For our dataset, as the tailings of the BTCs do not indicate a power-law behaviour (as seen in Chapter 7), Eq. 8.6 can can be simplified to $\tilde{\varphi}(\omega) = 1/1+\omega$, with $W = 1$, $n = 1$. This is equivalent to the classical ADE for the sorbing tracer transport.

Similar to the MRMT model, the Danckwerts boundary condition can be applied at the inlet

(also referred to as Robin inlet condition) and outlet (also known as Neumann exit condition) face of the core to solve Eq. 8.1:

$$\begin{cases} \text{for } z = 0: \ \bar{c}_o = M\big(\bar{c} - \frac{D_\psi}{u_\psi}\frac{\partial \bar{c}}{\partial z}\big)\Big|_{z=0} \\ \text{for } z = L: \ 0 = \dfrac{\partial \bar{c}}{\partial z}\Big|_{z=L} \end{cases} \tag{8.7}$$

where $\bar{c}_o$ is the normalised solute concentration just before it enters the inlet face of the core. The latter is described by a square input function fitted to the experimental concentration curve measured by the inlet detector.

The transport equation of the CTRW model (Eq. 8.1) is solved in the Laplace domain using the MATLAB toolbox provided by Cortis and Berkowitz (2005) and the concentration profiles are then converted numerically to the time domain using the inversion algorithm (de Hoog et al., 1982).

8.2.1 Modelling methods & optimisation protocol

In this work, a 2-step fitting approach is proposed to obtain the CTRW parameters. In the first fitting cycle, the transport parameters [v_ψ, D_ψ], the TPL parameters [β, t_1, t_2] and the sticking rate, Γ (if needed) were taken as the adjustable variables. Hereby, these parameters are fitted independently to each experimental flow rate to give the best match between the measured and predicted BTCs. The 'theoretical' intrinsic parameters of the medium, i.e. β, α_ψ and t_2 (as indicated in Berkowitz and Scher (2009)), averaged over the entire dataset are then taken as the model input for fitting cycle 2 where the following parameter are fitted to each BTC: [t_1, v_ψ] (CTRW-TPL) and [t_1, v_ψ, Λ] (CTRW-sorption). For all cases, the following objective function, J is minimised:

$$J = \sum_{j=1}^{N_\mathrm{p}} \left(\frac{\overline{C}_j^{\,\mathrm{mod}} - \overline{C}_j^{\,\mathrm{exp}}}{\overline{C}_j^{\,\mathrm{exp}}} \right)^2 \tag{8.8}$$

where N_p is the total number of experimental points in each BTC. $\overline{C}_j^{\,\mathrm{mod}}$ and $\overline{C}_j^{\,\mathrm{exp}}$ are the converted concentration values obtained from experiment and model prediction at each experimental point j, respectively (where $\overline{C}_j = 1 - \bar{c}_j$). The objective function takes least-squared regression of the relative difference in the concentration values to ensure equal weight is assigned to each

measured point in a breakthrough curve. Accordingly, the conversion ($\overline{C}_j = 1 - \bar{c}_j$) is applied to avoid dividing 0 (baseline) values in the objective function. The Single-Objective Genetic Algorithm, `ga` solver in MATLAB global optimisation toolbox has been used in the optimiser. The population size has been set to 100 times the number of adjustable parameters, with a total of 100 generations. The following range of constraints were imposed for the model parameters: $v_\psi(\mathrm{cm/min}) = [v \times 0.5, v \times 2.0]$ (where v is the interstitial velocity), $v_\psi/D_\psi(\mathrm{cm}^{-1}) = [2, 70]$, $\beta = [1.1, 1.7]$, $\log_{10}(t_1) = [-3, -0.1]$, $\log_{10}(t_2) = [0.1, 1.5]$ and $\Lambda = [0.0, 0.3]$. In this study, the CTRW-TPL model is applied to capture the experimental BTCs on all the rock cores, whereas CTRW-sorption model is evaluated for the microporous rocks only, i.e. EB and KL. A schematic diagram illustrating the proposed modelling approach is presented in Figure 8.1.

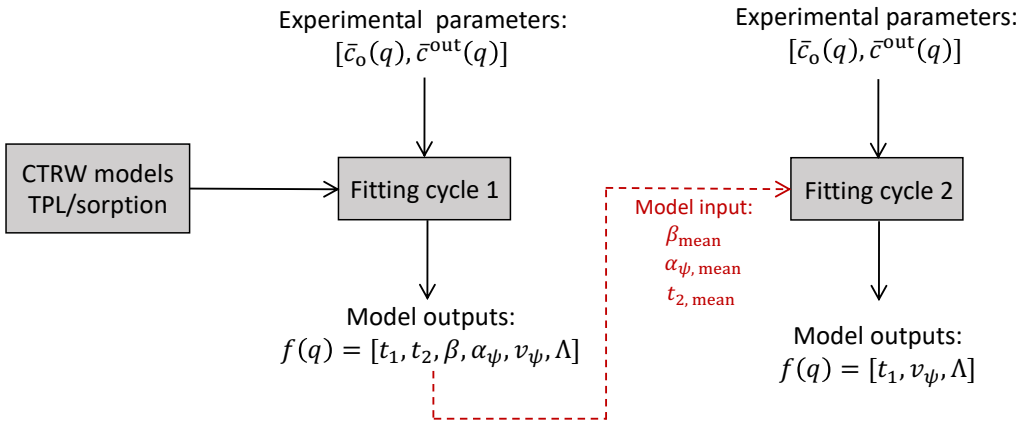

Figure 8.1: Fitting scenarios considered for the CTRW-based models. The proposed method considers an integrated approach where the measured BTCs are first fitted for each experimental flow rate independently (fitting cycle 1). The averaged model parameters (i.e. β_{mean}, $\alpha_{\psi,\mathrm{mean}}$, $t_{2,\mathrm{mean}}$) obtained in cycle 1 are then taken as model inputs for fitting cycle 2. With the latter, t_1, v_ψ and Λ are fitted to each flow rate.

8.3 Results

8.3.1 Evaluation of different CTRW approaches

A summary of the optimum parameters obtained upon application of the CTRW model with the sorption and TPL functions are given in Tables 8.1 and 8.2, respectively. The values of objective function (corresponding to the sum of all the individual values of J over the entire experimental flow rates of each porous media) are reported in the captions of Tables 8.1 and 8.2. The results represent the output values from fitting cycle 2. For Edwards Brown (EB), it can be seen that

the use of sorption model does not provide a better description of the measured breakthrough profiles, as evidenced by the small difference in the objective function (CTRW-sorption: $J = 9.99 \times 10^{-5}$ and CTRW-TPL: $J = 7.80 \times 10^{-5}$). As noted in Chapter 6, while the proportion of sub-micron size pores is not negligible, their size is very small (~ 0.01 μm) and the extent of diffusion may therefore be limited, as compared to advection. Accordingly, the observation of anomalous transport in EB is largely due to the presence of sub-core scale heterogeneities. On the contrary, in the case of Ketton Limestone (KL), the fit is significantly improved by going from the TPL model ($J = 9.73 \times 10^{-4}$) to the sorption model ($J = 3.76 \times 10^{-4}$). This observation confirms the need to account for the influence of intra-particle pores on transport. Notably, the model requires only a small value of 'sticking rate' to describe the experimental observations. This is because the measured profile for KL does not exhibit a strong power-law behaviour, but rather decays like an exponential tail (shown in Figure 7.6).

Table 8.1: Optimum model parameters obtained from fitting radio-tracer breakthrough profiles using CTRW-sorption model for the experiments with Ketton Limestone (KL) and Edwards Brown Carbonate (EB). The reported values correspond to the model outputs from fitting cycle 2, as demonstrated in Figure 8.1. For each system, the model takes the following TPL variables: $\beta = 1.53$, $\alpha_\psi = D_\psi/v_\psi = 0.068$ cm, $t_2 = 10^{1.30}$ (19.7) min (KL, $J = 3.76 \times 10^{-4}$), $\beta = 1.44$, $\alpha_\psi = 0.21$ cm, $t_2 = 10^{0.89}$ (7.8) min (EB, $J = 9.99 \times 10^{-5}$). The values of objective function correspond to sum of all the flow rates.

	Ketton L				**Edwards B**			
q [mL/min]	v_ψ [cm/min]	D_ψ [cm^2/min]	$\log_{10}(t_1)$ [−]	Λ [−]	v_ψ [cm/min]	D_ψ [cm^2/min]	$\log_{10}(t_1)$ [−]	Λ [−]
2.0	0.607	0.041	-0.377	0.050	0.423	0.087	-1.139	0.009
3.0	0.925	0.063	-0.462	0.034	–	–	–	–
4.0	1.316	0.089	-0.658	0.027	0.885	0.182	-1.313	0.005
8.0	2.903	0.196	-1.118	0.010	–	–	–	–
10.0	3.893	0.264	-1.356	0.032	2.469	0.508	-1.840	0.000
15.0	6.212	0.420	-1.662	0.038	3.857	0.794	-2.079	0.005
19.0	8.104	0.549	-1.830	0.054	5.034	1.037	-2.283	0.009

8.3.2 Analysis of effluent breakthrough curves (BTCs)

This section compares the measured effluent curves and the corresponding description obtained upon application of the CTRW model using the values reported in Tables 8.1 and 8.2. The results are presented in Figure 8.2 for the three rock samples and for all the flow rates tested (Péclet numbers, Pe $= 15 - 500$). The model predictions are plotted for the best scenario that have been chosen based on the evaluation performed in the previous section (TPL model for BS and EB, sorption model for KL). It can be seen that, an excellent agreement is obtained for

Table 8.2: Optimum model parameters obtained from fitting experimental breakthrough curves on the three rock cores using the CTRW-TPL model. The values are reported for fitting cycle 2, as explained in Figure 8.1. For each system, the model takes a consistent value of the following parameters (obtained from fitting cycle 1): $\beta = 1.61$, $\alpha_\psi = 0.021$ cm, $t_2 = 10^{0.45}$ (2.8) min (BS, $J = 1.27 \times 10^{-3}$), $\beta = 1.51$, $\alpha_\psi = 0.070$ cm, $t_2 = 10^{1.06}$ (11.5) min (KL, $J = 9.73 \times 10^{-4}$), $\beta = 1.42$, $\alpha_\psi = 0.19$ cm, $t_2 = 10^{0.85}$ (7.1) min (EB, $J = 7.80 \times 10^{-5}$). The values of the objective function reported correspond to the sum of all the flow rates.

	Bentheimer S			**Ketton L**			**Edwards B**		
q [mL/min]	v_ψ [cm/min]	D_ψ [cm^2/min]	$\log_{10}(t_1)$ [−]	v_ψ [cm/min]	D_ψ [cm^2/min]	$\log_{10}(t_1)$ [−]	v_ψ [cm/min]	D_ψ [cm^2/min]	$\log_{10}(t_1)$ [−]
2.0	0.591	0.013	-1.948	0.572	0.040	-0.437	0.391	0.074	-0.885
3.0	–	–	–	0.933	0.065	-0.616	–	–	–
4.0	1.228	0.026	-2.396	1.120	0.078	-0.394	0.842	0.159	-1.084
8.0	–	–	–	2.801	0.196	-1.026	–	–	–
10.0	3.128	0.067	-2.780	3.717	0.260	-1.225	2.519	0.476	-1.775
15.0	4.716	0.100	-2.896	6.091	0.426	-1.578	3.948	0.747	-2.018
19.0	5.985	0.127	-2.981	7.951	0.557	-1.736	5.126	0.969	-2.189

all the experimental measurements. In general, we observe an improvement in capturing the overall extent of the solute plume as compared to the MRMT model for more heterogeneous core samples (i.e. KL and EB), particularly at the peak of the BTCs. Remarkably, for all the rock cores investigated in this study, the anomalous behaviour of the solute plume under varying flow conditions can be well-described by using a single set of model parameters: t_2, α_ψ and β. The values of β decrease in the order from BS (1.62) < KL (1.53) < EB (1.42), which is in agreement with the measured extent of spatial heterogeneity, as characterised in Chapter 6 (in terms of correlation length) and in Chapter 7 (in terms of inhomogeneity factor). The obtained value for BS ($\beta = 1.62$) is only slightly lower than the reported value for a homogeneous sandpack, i.e. $\beta = 1.66$ (Berkowitz and Scher, 2009), thus confirming the relatively 'Fickian' nature of the flow field. Nevertheless, the differences in β amongst these geologic core samples are quite small, and are comparable to a "homogeneous" core measured in the literature, i.e. Berea sandstone, $\beta = 1.59$ (Cortis and Berkowitz, 2004). This implies that our systems are only weakly to moderately heterogeneous and thereby, supports the argument about the asymptotic behaviour discussed in the previous chapter. In fact, these β values are much higher than the fractured media obtained from field-scale tracer tests, for instance, a fractured till yields $\beta < 0.7$ (Kosakowski et al., 2001). In this work, the 'cut-off' time, t_2 increases from BS, EB to KL, taking up the value of 2.8, 7.1 and 19.7 mins, respectively. This order is in accordance with the amount of intra-particles pores present in each system. The value of t_2 is the time at which the power-law tail ends, and therefore ensures the transport evolves into a fast decaying Fickian behaviour. This further suggests that the power-law tailings in the BTCs are strongly controlled by the presence of micropores.

Figures 8.3, 8.4 and 8.5 present a more detailed comparison of the experimental BTCs (symbols) and the corresponding model predictions obtained from different theoretical frameworks (i.e. ADE: dash-dotted lines, MRMT: dash-lines and CTRW: solid lines) for BS, EB and KL, respectively. The results are shown for three flow rates (i.e. $q = 4$, 10 and 19 mL/min) and the concentration values are plotted on a logarithmic scale (to highlight the concentration tails) over normalised time ($\Theta = t/\tau_{\text{exp}}$). For BS, it can be seen that the ADE under-predicts the long-tailing in the BTCs, while the MRMT model results in its over-prediction. The results from CTRW-TPL model lies somewhere in between the two predicted profiles and provide the best

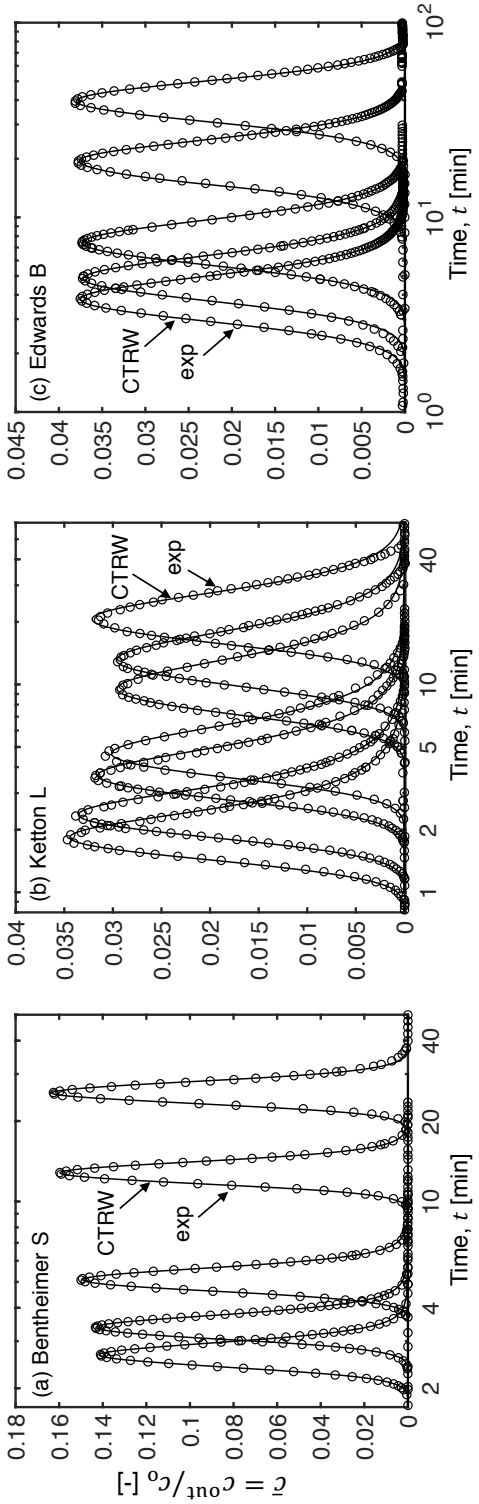

Figure 8.2: Effluent BTCs for (a) BS, (b) KL and (c) EB for the flow rates ranging between $q = 2 - 19$ mL/min (corresponding to Péclet numbers, $\mathrm{Pe}(vd_p/\mathcal{D}) = 15 - 500$). The symbols are the experimental data while the solid lines are the CTRW model predictions: CTRW-TPL model for BS and EB (model parameters reported in Table 8.2) and CTRW-sorption model for KL (model parameters reported in Table 8.3).

description of the experimental observations. This is evidenced by the plots presented on top of Figure 8.3, where the absolute deviations ($\Delta\overline{c} = \overline{c}^{\mathrm{exp}} - \overline{c}^{\mathrm{mod}}$) are shown over reduced time for the three models. Hereby, the average standard deviation obtained for the three representative flow rates for the CTRW model, i.e. 0.08 %, is significantly smaller than the corresponding vales for ADE: 0.41 % and for MRMT: 0.26 %. On the contrary, for the microporous rocks (i.e. EB and KL), we observe that both the CTRW and the MRMT models provide a good description of the experimental dataset. While the CTRW model produces a slightly better fit, the absolute deviations between the predicted (CTRW or MRMT) and the measured concentration values are comparable; this is shown in the upper sections of Figures 8.4 (for EB) and 8.5 (for KL).

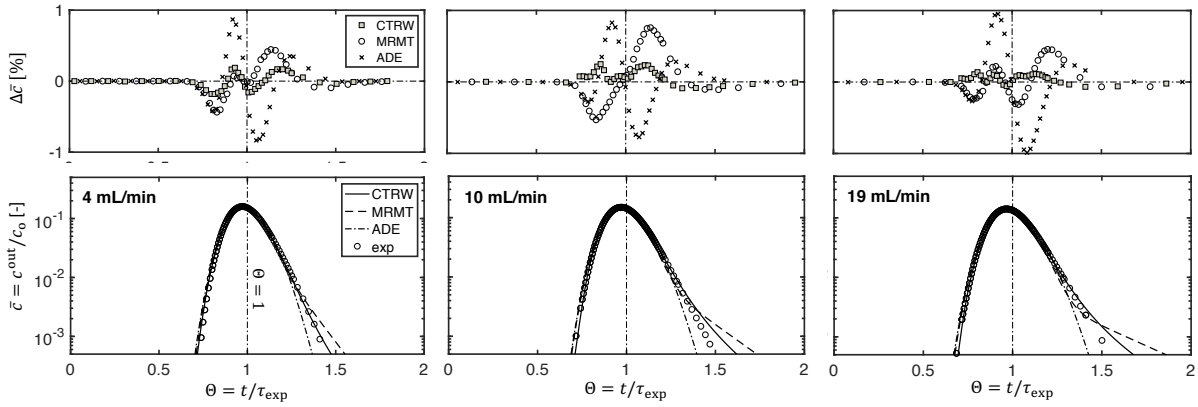

Figure 8.3: Comparisons of measured BTCs (symbols) and the predictions obtained from the three different transport models, namely ADE: dash-dotted line, MRMT: dash-line and CTRW(TPL): solid line. The results are shown for EB at three flow rates, 4, 10 and 19 mL/min (corresponding to Pe = 34, 85 and 162). The figure is presented on a semi-logarithmic scale to emphasise the BTC tails. The deviations between measured and the predicted tracer concentration (i.e. $\Delta c = (\overline{c}^{\mathrm{exp}} - \overline{c}^{\mathrm{mod}})$) are given on the top of the figure. The results are presented in a normalised concentration, $\overline{c} = c^{\mathrm{out}}/c_{\mathrm{o}}$ as a function of reduced time, $\Theta = t/\tau_{\mathrm{exp}}$.

8.4 Discussions

8.4.1 Correlating transit time, t_1 in the TPL

Figure 8.6 presents the transit time, t_1 plotted over the transport velocity, v_ψ for the three rock samples. The solid lines correspond to the best fit of the data points to a power-law function, i.e. $y = ax^b$. As demonstrated in the figure, a strong correlation persists for all the porous media. In particular, we observe that t_1 is inversely proportional to v_ψ, in accordance with the observations indicated in the literature (Berkowitz and Scher, 2009, 2010). According to

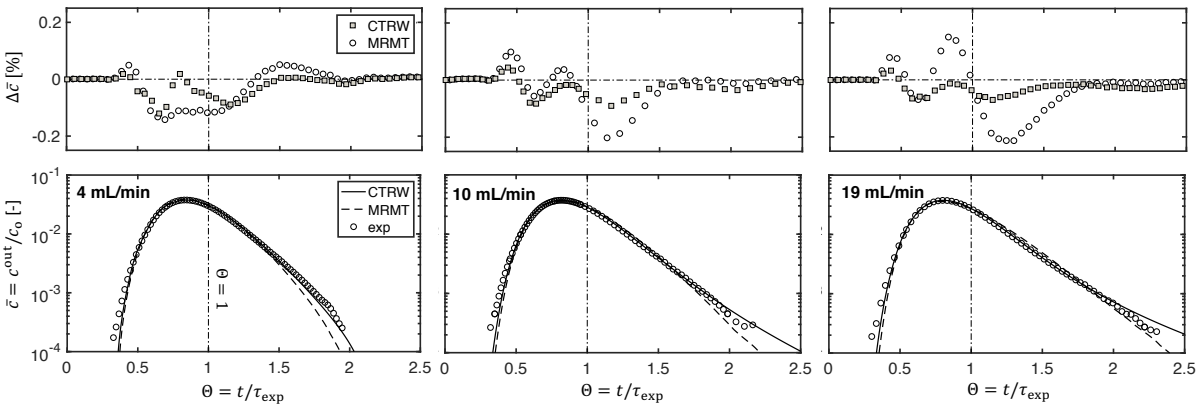

Figure 8.4: Comparisons of experimental BTCs (symbols) and the model predictions obtained from MRMT: dash-line and CTRW (TPL): solid line for EB at q = 4, 10 and 19 mL/min (Pe =38, 96 and 182).

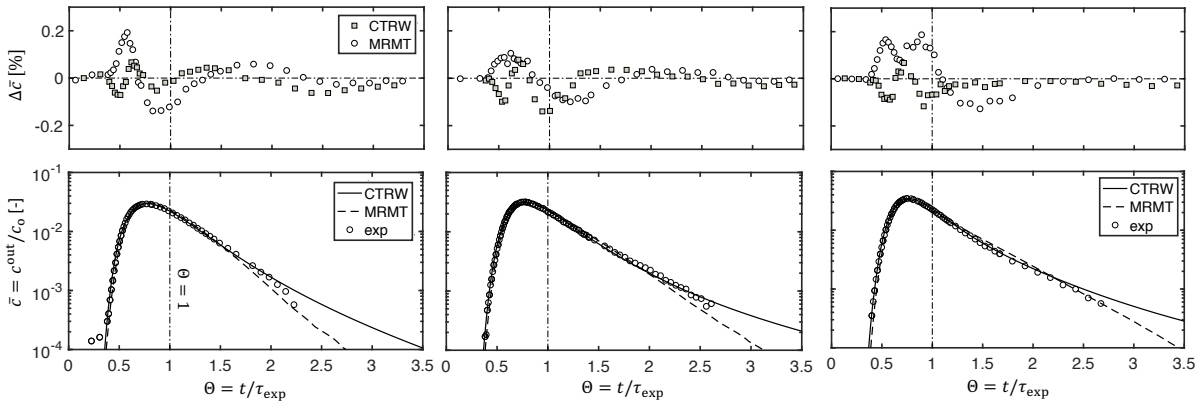

Figure 8.5: Comparisons of experimental BTCs (symbols) and the model predictions obtained from MRMT: dash-line and CTRW (sorption): solid line for KL at q = 4, 10 and 19 mL/min (Pe = 107, 267 and 508).

these literatures, the value of t_1 can be associated with the 'transport velocity', v_ψ, by means of $t_1 = \overline{s}/v_\psi$, where $\overline{s}$ is the characteristic displacement factor, which can be related for instance to the the average grain sizes, d_p. For BS, we find that t_1 is directly proportional to the inverse of v_ψ (i.e. $b \approx -1$), with the constant, $\overline{s} = 0.0058$ cm (corresponding to about 23% of the average grain diameter). This is comparable to the the reported values for sandpacks, that gives about $15 - 38$ % of grain size, depending on the system heterogeneity (Berkowitz and Scher, 2009). Interestingly, for the microporous rocks, we observe a power-law correlation, with the exponent, $b = -1.2$ (EB) and $b = -1.4$ (KL). This is somewhat different from that has been observed by (Berkowitz and Scher, 2009, 2010), where $t_1 \propto v_\psi^{-1}$. However, it should also be noted that the latter were interpreted from three measurement points, and the relationship may be applicable only to relatively uniformly distributed pore spaces (Berkowitz and Scher, 2009).

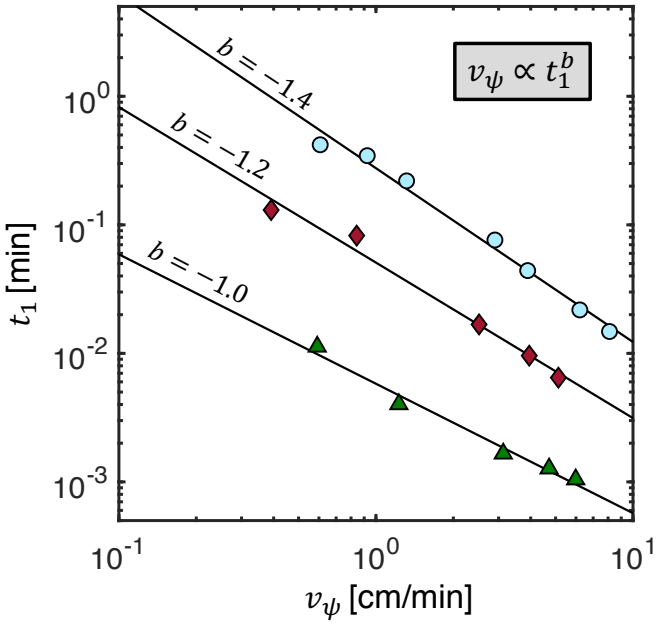

Figure 8.6: Relationship between CTRW transition time (t_1) and velocity (v_ψ) for BS (triangles), KL (circles) and EB (diamonds). The symbols correspond to the optimum values obtained from fitting the experimental BTCs using the CTRW model (i.e. CTRW-sorption for KL, CTRW-TPL for BS and EB). The dashed lines are the best fitted power-law functions with the following constants, m and exponents: b: $m = 0.006$, $b = -1.0$ (BS), $m = 0.276$, $b = -1.4$ (KL) and $m = 0.051$, $b = -1.2$ (EB).

8.4.2 Correlating CTRW dispersivity coefficients

As noted in the Results section, a constant value of 'dispersivity' ($\alpha_\psi = v_\psi/D_\psi$) has been attained for each rock core studied. This parameter can be regarded as an intrinsic rock property. In particular, the value of α_ψ increases in the same direction as subcore-scale heterogeneity, i.e. BS (0.21 mm) < KL (0.68 mm) < EB (1.89 mm). In Figure 8.7 is presented the dispersion dataset (symbols) determined from the CTRW theory for the three rock cores. The results are plotted for the *generalised* dispersion coefficient normalised by the molecular diffusion coefficient ($D_\psi/\mathcal{D}$), over Péclet number (defined as $\mathrm{Pe}_\psi = v_\psi d_\mathrm{e}/\mathcal{D}$, where d_e is the equivalent grain diameter). Again, the well-known empirical correlation, $D_\psi/\mathcal{D} = 1/\sqrt{2}+\sigma_\psi \mathrm{Pe}_\psi$ (Sahimi et al., 1986) is used here to describe the experimental dataset. The latter has been modified by accounting for the transport parameters defined in the CTRW framework, where σ_ψ is the inhomogeneity factor. As a reference, the results obtained for the granular beadpacks (squares) are also shown in the figure. The latter corresponds to the simplex case where the CTRW transport parameters are reduced to the classical ADE framework, i.e. $v_\psi = v$ and $D_\psi = D_\mathrm{L}$, and thus $\sigma = \sigma_\psi = 0.5$ applies (dashed line). As given by the solid lines in the figure, the generalised dispersion coefficients determined

for each rock core can be well-described by a single parameter σ_ψ, that takes a value of 0.8, 1.3 and 4.8 for BS, KL and EB, respectively. The obtained inhomogeneity factor in the CTRW framework can be directly linked to the correlation length, a measured for each system (see Chapter 6, Table 6.3). For all the rocks investigated, it can be readily shown that $\sigma_\psi/a \approx 0.35$ mm^{-1}. It is important highlighting that although both quantities (i.e. σ_ψ and a) provide a measure of the extent of heterogeneity associated with a porous medium, they were obtained independently. The σ_ψ is determined from the analysis carried out on the BTCs, and therefore can be referred to as a transport property. On the other hand, a is the physical property that has been characterised directly from the structural information of the porous medium.

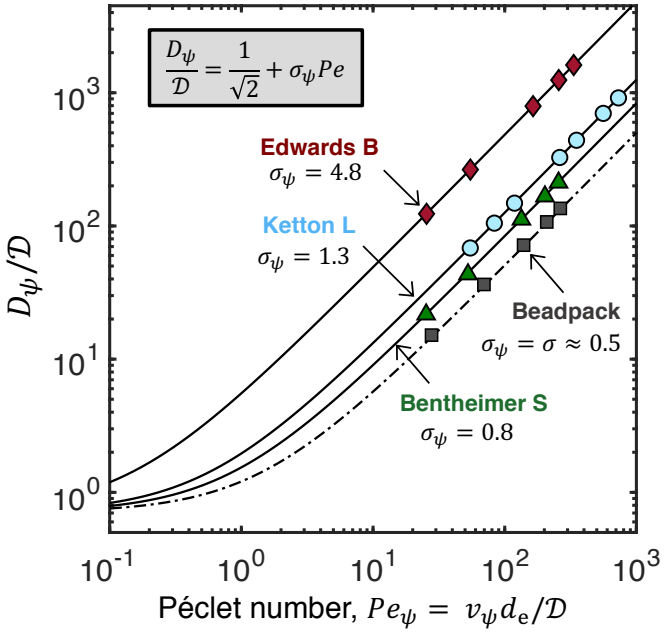

Figure 8.7: Dispersion data plotted in terms of normalised "dispersion coefficient" ($D_\psi/\mathcal{D}$) as a function of Péclet number ($\mathrm{Pe}_\psi = v_\psi d_e/\mathcal{D}$). The results obtained from CTRW models are shown as filled symbols while solid lines are the widely used empirical correlation by Sahimi et al. (1986), with the numerical formulation given in the plot. The following values of inhomogeneity factors (σ_ψ) were obtained for each system, i.e. BS: $\sigma_\psi = 0.8$, KL: $\sigma_\psi = 1.3$, EB: $\sigma_\psi = 4.8$. As a reference, the results for beadpacks are also presented (where $\sigma_\psi = \sigma = 0.5$).

8.4.3 Interpreting CTRW transport parameters

While extensive numerical studies exist in the literature, the experimental interpretation of solute transport using the CTRW framework is very scarce as compared to the classical modelling approaches (i.e. ADE or MRMT). Accordingly, this limits the current understanding of the CTRW transport parameters. In this section, efforts have been made to correlate the 'gener-

alised' transport parameters, i.e. v_ψ and α_ψ to the 'classical' fluid (pore) velocity, v and the longitudinal dispersivity coefficient, α_L. Figure 8.8 compares the inhomogeneity factors determined from the two numerical models, namely MRMT and CTRW for the three rock cores studied. In the inset of the figure are shown the corresponding intrinsic dispersivity values. Again, the dataset for beadpack (squares) together with the 1:1 line (where $\sigma_\psi = \sigma$) is given in the figure as a reference. In this work, we find that $\sigma_\psi < \sigma$ (or $\alpha_\psi < \alpha_\mathrm{L}$) for all three systems. We argue that this is a result of decoupling the pore-level heterogeneities from the "CTRW" dispersivity α_ψ by means of introducing the β parameter, in the TPL model.

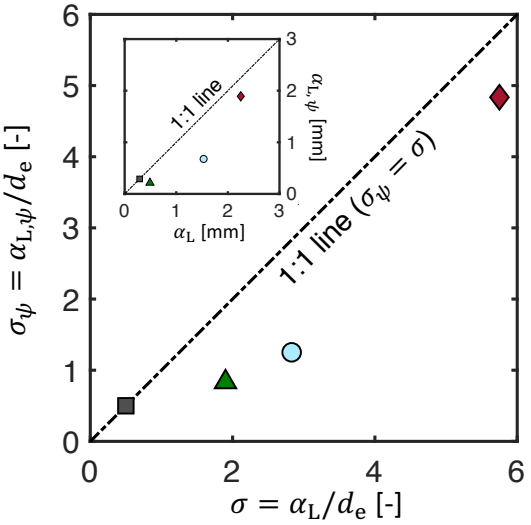

Figure 8.8: Comparison of inhomogeneity factors calculated from the MRMT (σ) and CTRW (σ_ψ) models. The symbols are the values obtained from for four porous media, thus including beadpacks (square), BS (triangle), KL (circle) and EB (diamond). The dashed line refers to the 1:1 line. The corresponding plot of dispersivity is given in the inset of the figure.

A comparison of CTRW transport velocity, v_ψ and the interstitial fluid velocity, $v(= q/(A\phi))$ is presented in Figure 8.9 for all the flow rates carried out in this work. As shown, $v_\psi > v$ applies to all cases; this is consistent with the results presented by Berkowitz and Scher (2009). In the CTRW framework, a higher value is attained for v_ψ because the latter corresponds to the average particle velocity, and thus accounts for the added small-range spatial variability in the microscopic flow field (Berkowitz et al., 2006). As indicated by the linear regression lines in the figure (dash-dotted lines), the measurements reported in this work follows a linear correlation between v_ψ and v, with the slope increases by the order KL (1.4) < BS (1.6) < EB (1.9). Our results on different systems give a consistent picture where the deviation $(v_\psi - v)$ becomes

smaller at lower flow rates, which will eventually lead to $v_\psi = v$ at no flow condition. This is evident by the constant b of the regressed slopes ≈ 0. Remarkably, the size of the characteristic slope determined in each system is in alignment with the 'geometric' heterogeneity observed at the pore-scale (shown in Chapter 6). Accordingly, the deviation between the two velocity values is expected to be larger with increasing complexity of the pore/grain structures in a porous medium.

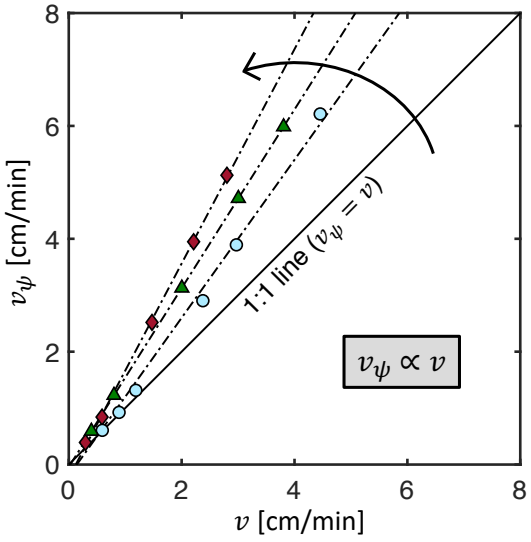

Figure 8.9: Correlation between 'transport velocity' (v_ψ) and pore velocity (v) for the three rock cores, BS (triangles), KL (circles) and EB (diamonds). The dashed lines correspond to the linear regression line for each dataset whereas the solid line is the 1:1 reference line. The values of the slopes are, $m = 1.4, 1.6, 1.9$ for KL, BS and EB, respectively. The intercept for all the lines are ~ 0.

8.5 Concluding remarks

In this work, we applied for the first time, the CTRW model to interpret the rich dataset obtained from the pulse-tracer tests on three rocks samples and over a wide range of Péclet numbers (Pe $= 15 - 500$). To generalise the use of CTRW model, we propose an integrated fitting approach that enables describing the entire set of experimental effluent profiles at varying flow conditions using a single set of model parameters, i.e. t_2, α_ψ and β. The numerical values of the characteristic model parameters obtained for the three rock cores investigated in this thesis are summarised in Table 8.3. These properties correspond to the transport parameters intrinsic to a medium and accordingly, would lead to a more consistent picture of the characteristic 'non-Fickian' behaviours observed in the breakthrough curves. We contend that generalisation

of the model parameters presented above also provide physical and predictive consistency in the flow-rate dependent variables, such as the transit time (t_1), the transport velocity (v_ψ) and the *generalised* dispersion coefficient (D_ψ). In this work, it was observed that the proposed CTRW modelling approach does not only correctly describe the different strengths of long-tailing indicated by the three characteristic rocks, but it also represents the best model for describing the breakthrough curves, as compared to the classical transport models (e.g. ADE or MRMT). However, it should be noted that a better fit to the experimental dataset is achieved at a cost of introducing more adjustable parameters in the CTRW model. As emphasised in the work by Kitanidis (2017), the application of Fickian models, such as ADE, to describe tracer transport in heterogeneous media can be significantly improved by accounting for the geometry at finer scales. An example of such application is given in Pini et al. (2016), where a streamtube formulation of the ADE correctly described tracer transport in a sandstone with a highly-correlated permeability field. In this context, advancing the use of Fickian models can indeed provide strong physical basis in understanding the nature of anomalous transport (Kitanidis, 2017).

Table 8.3: Summary of the characteristic transport parameters obtained from CTRW and MRMT models for the three rock cores.

	Bentheimer S	Ketton L	Edwards B
α_L [mm]	0.49	1.53	2.25
α_ψ [mm]	0.21	0.68	1.89
β [–]	1.62	1.53	1.42
t_2 [min]	2.8	19.7	7.1

To better understand the underlying mechanisms that influence anomalous transport in the context of CTRW theory, the optimum model parameters were examined by relating them to the structural heterogeneity of the rocks. Irrespective of the porous medium, a linear dependence of the *generalised* dispersion coefficient (D_ψ) over Péclet number (Pe_ψ) was observed. It was also shown that the 'CTRW' inhomogeneity factor, σ_ψ is directly proportional to the correlation length of the core samples (i.e. $\sigma_\psi/a \approx 0.35$ mm^{-1}). Over the range of flow rates investigated, the transit time t_1 is proportional to the inverse of transport velocity ($t_1 \propto v_\psi^{-b}$). Such proportionality is linear for the relatively homogeneous Bentheimer ($b = 1$), while a slight power-law correlation is observed for the microporous rocks (i.e. $b = 1.2$ for Edwards and $b = 1.4$ for

Ketton). In alignment with the theoretical interpretations, we obtain the values of v_ψ being higher than v for all the systems. Specifically, the deviations become larger for systems with stronger geometric heterogeneity at the pore-scale (i.e. Ketton $<$ Bentheimer $<$ Edwards).

Chapter 9

Uncovering the Spatial Structure of the Concentration Field in Rocks During Solute Transport

9.1 Introduction

Although hydrodynamic dispersion represents a useful parameter to quantify mixing during transport of solute in porous media (Dullien, 1992; Sahimi, 2011), as highlighted in Chapter 2, its practicability for the characterisation of heterogeneous systems has often been questioned. Hydrodynamic dispersion originates from the combined action of molecular diffusion (resulting from concentration gradients) and advection (resulting from velocity variations at the pore scale). The concepts of 'spreading' and 'dilution' have been introduced to describe the resulting mixing process: while the former alters spatial extent of the solute plume, the latter increases the total volume of the solute occupied by the plume (Kitanidis, 1994; Le Borgne et al., 2010). For a homogeneous system, spreading and mixing can be lumped together because the solute uniformly occupies the plume to its "full spatial extent"; this was clearly shown in Chapter 5. However, the distinction between these two mechanisms is necessary in porous rocks and natural systems in general. In fact, the presence of multi-scale heterogeneous features in these environments contributes strongly to the non-uniform spreading of the solute plume, thereby

introducing a key control on transport (Steefel and Maher, 2009). Examples of such heterogeneities are the characteristic laminations of sedimentary rocks (Murphy et al., 1984) or the microporous facies that are often encountered in limestones (Bijeljic et al., 2013). Understanding the interplay between spreading and dilution is important, because while they both provide the driving force for physical interactions between the fluids and the rocks (e.g., adsorption and chemical reactions), they do so over distinct time- (or length-) scales (Le Borgne et al., 2015).

Quantifying the distinction between spreading and dilution in heterogeneous porous media remains a scientific and technical challenge, because these mechanisms act simultaneously, giving rise to anomalous phenomena in the breakthrough curves (BTCs), as demonstrated in Chapters 7 and 8. One of the main contributions to the current uncertainty in the analysis of miscible displacements in laboratory core-floods is the lack of direct observations of the processes of spreading and dilution. By limiting the analysis to the interpretation of BTCs, the dispersion mechanisms cannot be unambiguously identified and the validity of the adopted modelling approach cannot be fully verified.

In this study, we deployed PET to observe the spatial and temporal evolution of the full tracer plume, thus providing the tools to investigate microscopic controls on mixing and spreading in three dimensions. While X-ray Computed Tomography has been applied in this thesis to characterise structural heterogeneity from micrometre to centimetre scale (see Chapter 6), in this chapter, we demonstrate how the use of PET enables uncovering the complex flow and transport processes observed at the subcore-scale, caused by the heterogeneities. A schematic diagram that illustrates the experimental workflow presented in this study is given in Figure 9.1. As indicated in the figure, the combined imaging techniques allow resolving both structural and dynamic features of the solute plume that would be otherwise not possible using classic pulse-tracer tests. We argue that the ability to directly visualise tracer concentration with such level of observational detail is key to advance our understanding of solute transport in rocks, and to account for heterogeneity in numerical models deterministically, that would ultimately lead to better estimation of the so-called “anomalous” transport.

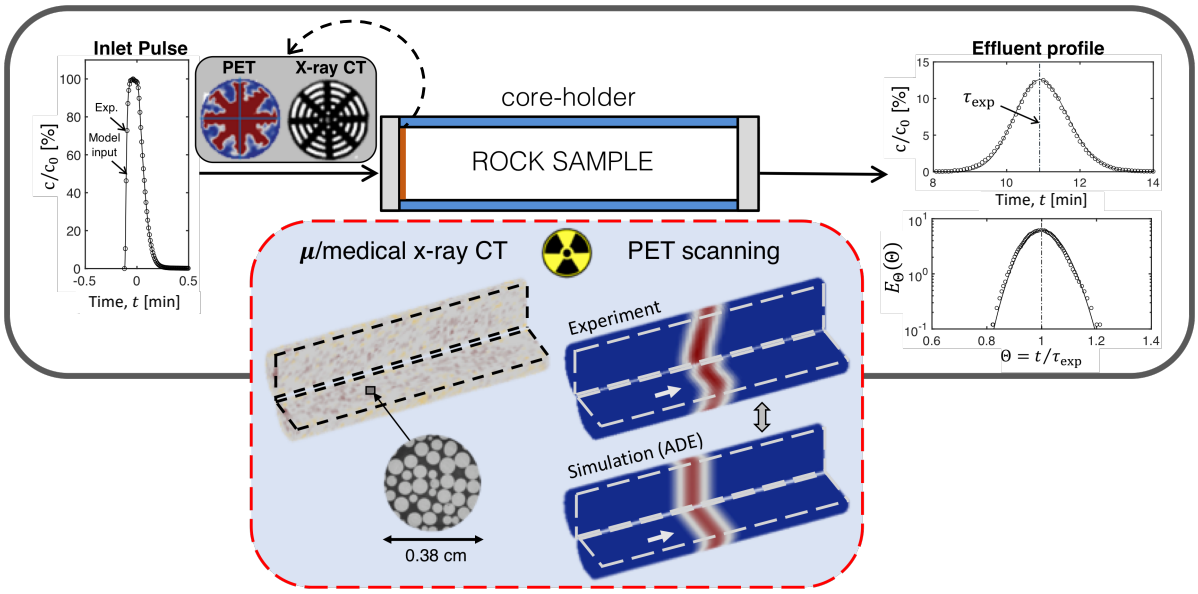

Figure 9.1: Schematic diagram that highlights the unique advantages of the proposed experimental protocol that involves integrating 3-D PET imaging to the conventional pulse-tracer tests.

9.2 Methods

The reconstructed PET scans acquired during pulse-tracer tests produce a temporal and spatial distribution of concentration values (at voxel resolutions of $4 - 12$ mm^3 depending on the scanner used) within a rock sample. This 3-D dataset is utilised in this chapter to quantify various measures of mixing and spreading; herewith, investigating the relationship between the two fundamental measures of solute dispersion in the context of 'non-Fickian' transport. In the following section, the mathematical expressions used to characterise the extent of solute mixing and spreading are presented. Where appropriate, these quantities are also determined for the three-dimensional reconstruction of the 'Fickian-based' transport models (i.e. ADE/MRMT), so as to directly evaluate the application of the 1-D models to predict the spatial and temporal behaviour of mixing at the sub-core level, in both homogeneous (i.e. BP and BS) and heterogeneous cores (i.e. KL and EB).

9.2.1 Mixing measures

Two global metrics of mixing is considered in this study. The first measure is known as the dilution index, Γ, initially proposed by Kitanidis (1994):

$$\Gamma(t_i) = V_{\text{vox}} \exp\Big[-\sum_{j=1}^{N_{\text{v}}} P_j(\underline{x}, t_i) \ln(P_j(\underline{x}, t_i)) \Big] \tag{9.1}$$

where N_v is the total number of voxels; V_{vox} is the voxel volume; $\underline{x}$ is the space coordinate, $\underline{x} = (x, y, z)$; t_i is the average time frame over which a given PET image has been reconstructed. P_j is the probability distribution function of the solute mass, given by the following expression:

$$P_j(\underline{x}, t_i) = \frac{c^{\text{PET}}(\underline{x}, t_i)}{\int_V c^{\text{PET}}(\underline{x}, t_i)\ dV} \tag{9.2}$$

where c^{PET} is the solute concentration per unit voxel volume. In this study, the integral was approximated using a trapezoidal method. The zero concentration values of the PET dataset are given an 'artificial' value of very small concentration (i.e. 1×10^{-5} mCi/mL) to avoid passing zero values to the natural logarithm in Eq. 9.1. The suitability of these assumptions were confirmed by performing a synthetic case of a known dilution index, which results in the relative errors of less than 0.2%. It is worth noting that $\Gamma(t_i)$ carries a unit of volume and the obtained value is therefore a function of the system size. To eliminate this dependency, $\Gamma(t_i)$ is normalised by the theoretical maximum value of dilution index, Γ_{max}. This corresponds to the volume of the core, $V_{\text{core}} = N_{\text{v}} V_{\text{vox}}$ (Kitanidis, 1994), i.e.

$$\Pi(t_i) = \frac{\Gamma(t_i)}{\Gamma_{\text{max}}} = \frac{\Gamma(t_i)}{N_{\text{v}} V_{\text{vox}}} \quad \text{with } \Pi \in [0, 1] \tag{9.3}$$

Π is referred to as the reactor ratio. By measuring the "reactor" volume occupied by the tracer, this parameter determines the global state of mixing. In this work, the comparisons between different systems were made by correcting the experimental values of $\Pi(t_i)$ by the volume of tracer injected, V_{inj} ($\Pi(t_i) = \Pi_{\text{exp}}(t_i) - V_{\text{inj}}/(\text{PV})$, where PV is the pore volume of the core). In a porous domain, the effect of porosity can be accounted by simply scaling the reactor ratio by the total porosity, ϕ_{T} i.e.

$$\widetilde{\Pi}(t_i) = \Pi(t_i)\phi_{\text{T}} \tag{9.4}$$

In the literature, various modifications to the classical definition of dilution index have been proposed, depending on a number of variables, such as the system configuration, the heterogeneity of the porous medium and the conditions of the experiments performed. Some of the commonly referred quantities are the flux-related dilution index (Rolle et al., 2009) and the mass-weighted dilution index (Boon et al., 2017). While the former has been readily applied for continuous injection processes under steady state flow conditions (Chiogna et al., 2011b; Rolle et al., 2012; Chiogna et al., 2012; Rolle et al., 2013), the latter is typically used on a one-dimensional transport problem (Boon et al., 2017). In this study, the dilution index is evaluated by using the classical formulation (i.e. Eq. 9.1).

An alternative way to characterise the global state of mixing is to consider the second moment of concentration (i.e. the concentration variance), ς^2, defined as the intensity of segregation, $I(t_i)$, originally proposed by Danckwerts (1952):

$$I(t_i) = \frac{\varsigma^2}{\varsigma^2_{\max}} \quad \text{with } I \in [0,1] \tag{9.5}$$

where

$$\varsigma^2 = \langle c^{\mathrm{PET}}(\underline{x}, t_i)^2 \rangle - \langle c^{\mathrm{PET}}(\underline{x}, t_i) \rangle^2 \tag{9.6}$$

where the angle bracket denotes the average concentration of all the voxel values at time frame t_i (corresponding to the first moment of concentration). Note that Eq. 9.6 takes the concentration that are normalised by the feed, c_o so that the resultant values yield a range between 0 and 1. For a binary system such as that considered in this work (tracer and carrier fluid), the maximum variance is defined by $\varsigma^2_{\max} = \langle c^{\mathrm{PET}}(\underline{x}, t_i) \rangle (1 - \langle c^{\mathrm{PET}}(\underline{x}, t_i) \rangle)$ (Kukukova et al., 2009). The intensity of segregation decreases over time as a consequence of mixing, and measures the deviation from concentration homogeneity. Accordingly, $I = 0$ corresponds to the system that has evolved into a concentration equilibrium (i.e. concentration values are same everywhere in the system).

9.2.2 Spreading measures

While the different mixing measures presented in the previous section determines the temporal variations in the global mixing state, they do not provide direct information on the spatial extent

of the plume. Le Borgne et al. (2010) proposes that the extent of spreading can be quantified by the spreading length scale, K, which can be computed from the standard deviation of the spatial distribution of concentrations:

$$K^2(t_i) = \frac{1}{L}\int_0^L [z(t_i) - \langle z(t_i)\rangle]^2 c^{\mathrm{PET}}(z, t_i)dz \tag{9.7}$$

where $\langle z(t_i)\rangle$ is the first moment (centre of mass), aligned with the direction of flow, i.e.

$$\langle z(t_i)\rangle = \int_0^L zP(z, t_i)dz \tag{9.8}$$

where z is the space variable in the longitudinal direction; $P(z, t_i)$ is the concentration distribution function along the core length, L, and can be determined from Eq. 9.2.

In this study, we evaluate an additional quantitative measure to characterise the extent of spreading; this approach is based on the classical expression of dilution index (Eq. 9.1), in which the following formulation is proposed:

$$\Delta\widetilde{\Pi} = \widetilde{\Pi}_{1\mathrm{D}} - \widetilde{\Pi}_{3\mathrm{D}} \tag{9.9}$$

where $\widetilde{\Pi}_{3\mathrm{D}}$ is the dilution index computed from the mass distribution function (i.e. Eq. 9.2) based on a 3-D volume while $\widetilde{\Pi}_{1\mathrm{D}}$ is computed using slice-averaged properties (by assuming complete mixing of the tracer plume in the radial direction). We note that both $\widetilde{\Pi}_{3\mathrm{D}}$ and $\widetilde{\Pi}_{1\mathrm{D}}$ are normalised by the volume and the length of the core, respectively, so as to obtain the same units. Accordingly, the extent of 'anomalous' spreading can be quantified by taking the difference between the two variables, i.e. $\Delta\widetilde{\Pi}$. The application of this measure will be evaluated by means of correlating it with other transport parameters that carry information on heterogeneity. To this aim, the inhomogeneity factor is compared, which has been obtained from independent analysis of breakthrough curve measurements; the result is presented in Section 9.3.4.

9.3 Results and discussions

9.3.1 Three-dimensional imaging of solute transport

The dynamic PET data acquired during pulse-tracer tests are provided in Figure 9.2, for the three rock cores, namely (a) Bentheimer Sandstone (BS), (b) Edwards Brown Carbonate (EB) and (c) Ketton Limestone (KL). These are presented in the form of three-dimensional tracer concentration maps at two distinct times, corresponding to the injection of 0.3 and 0.7 pore volumes (i.e. $t = 0.3\tau_{\text{exp}}$ and $0.7\tau_{\text{exp}}$). The results are given for the PET experiments conducted at $q = 4$mL/min and present the injection of a radio-tracer pulse (i.e. [^{18}F]FDG) into the cores saturated with (non-labelled) water (details of the experimental procedures are given in Chapter 7). In the bottom panel, predictions by the Fickian-based model representing the same time frames are also shown, which have been obtained upon reconstructing the solutions of the one-dimensional MRMT equation in three-dimensional domains. Specifically, the displacement profiles were computed by taking the optimum model parameters obtained upon fitting the effluent breakthrough profiles presented in Chapter 7. As anticipated by the experimental results, the displacement of tracer plume in the homogeneous BS is rather uniform, with a minor contribution from spreading. The rock is also characterized by a comparatively small degree of mixing; this is evidenced by the limited extent of the discoloration zone of the tracer plume. The agreement between the experiment and MRMT confirms the application of using core-scale properties to predict solute dispersion at the subcore-scale for the homogeneous BS. For the carbonate rocks, the images from the PET experiments clearly show that the tracer plume is significantly distorted through the action of preferential flow pathways, which are likely to originate from the subcore-scale heterogeneities described in Chapter 6. The images also show that the effects of these preferential flow pathways persist over time and enhance concentration contrasts between fluid parcels. The results presented in this study are the first direct demonstration that both mechanisms (spreading and dilution) are present in carbonate rocks. Interestingly, we observe that tracer mixing is much more pronounced in KL, despite of being a less heterogeneous system than the EB core (see Chapter 6). This is primarily because, while the concentration contrasts generated as a result of advective spreading lead to an enhanced mixing (Le Borgne et al., 2011), the effects of microporosity contribute more significantly to the

overall mixing process; this will be discussed further with the help of different mixing measures in later sections.

Based on a comparison between the PET data and the 3-D representation of the 1-D MRMT model, we also note that, the homogeneous model distributes the mass of tracer over a larger volume of water within the plume, this being the consequence of lumping mixing *and* spreading into a single parameter (Pini et al., 2016). The influence of subcore-scale heterogeneity is more apparent when the PET images are reconstructed on a 2-D plane, as presented in Figure 9.3 for X-Z plane sliced at the centre of the core and the X-Y cross-sectional slices at three different positions of the tracer plume. In the figure, we can clearly see that the existence of solute spreading, which gives rise to the so-called 'incomplete mixing' in the radial direction even for the relatively homogeneous system (i.e. BS). This suggests that characterising the dynamic process using an averaged quantity (i.e. concentration) may lead to erroneous conclusion as such approach does not reflect the full spectrum of transport mechanisms (Cushman and Tartakovsky, 2016). In fact, this was clearly demonstrated by the mismatch in the slice-averaged internal concentration profiles between the experiments and the 1-D transport models for the carbonate rocks, as shown in Chapter 7.

9.3.2 Characteristic behaviour in the concentration probability density functions

Figure 9.4 presents the temporal evolution of the concentration probability density functions (PDFs) for the three rock cores, together with the results obtained on the granular beadpack (BP). The PDFs have been computed for three distinct time intervals (corresponding to $t = 0.4\tau_{\text{exp}}$, $0.5\tau_{\text{exp}}$ and $0.6\tau_{\text{exp}}$) and the plots are presented on a semi-logarithimc scale to emphasise the tailing behaviour in the low concentration regions. The dataset is shown for the experiments conducted at $q = 10$ mL/min for BP and $q = 4$ mL/min for the rock samples. Details associated with the computation of the distribution functions are explained in the captions of Figure 9.4. As anticipated in the figure, we observe that the bulk concentration of the tracer (which corresponds to the maximum concentration values) decreases as a result of dilution process, as the solute plume invades the porous medium. We also note that the large concentration behaviour in the PDFs are characterised by an exponential decay for all the porous media. This observation

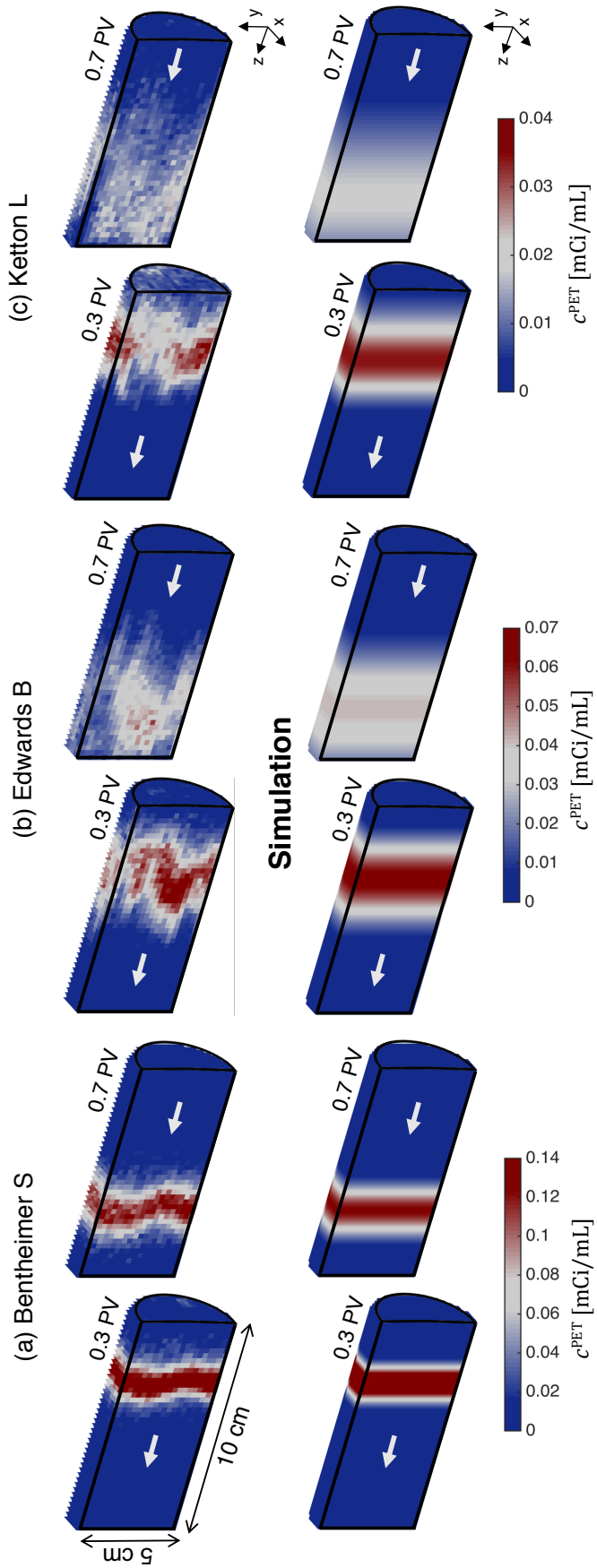

Figure 9.2: 3-D concentration maps showing the tracer plume migration in (a) Bentheimer Sandstone (BS), (b) Edwards Brown Carbonate (EB) and (c) Ketton Limestone (KL) at two distinct time frames, i.e. $\Theta = 0.3$ PV and 0.7 PV. The experimental data are obtained from PET scans at $q = 4$ mL/min and represent reconstructions over the constant time frames, i.e. $\Theta = \pm 0.08$ PV for KL and ± 0.06 for BS and EB. The corresponding predictions by the MRMT model (MRMT-1 for KL and EB, MRMT-2 for BS, as explained in Section 7.4.2) are also shown at the bottom of the figure. The latter have been obtained upon three-dimensional (3-D) reconstruction of the one-dimensional (1-D) MRMT equation. Voxel sizes for the experiment and simulation data are $(2.3\times2.3\times2.4)$ mm^3 and $(2.3\times2.3\times0.05)$ mm^3, respectively.

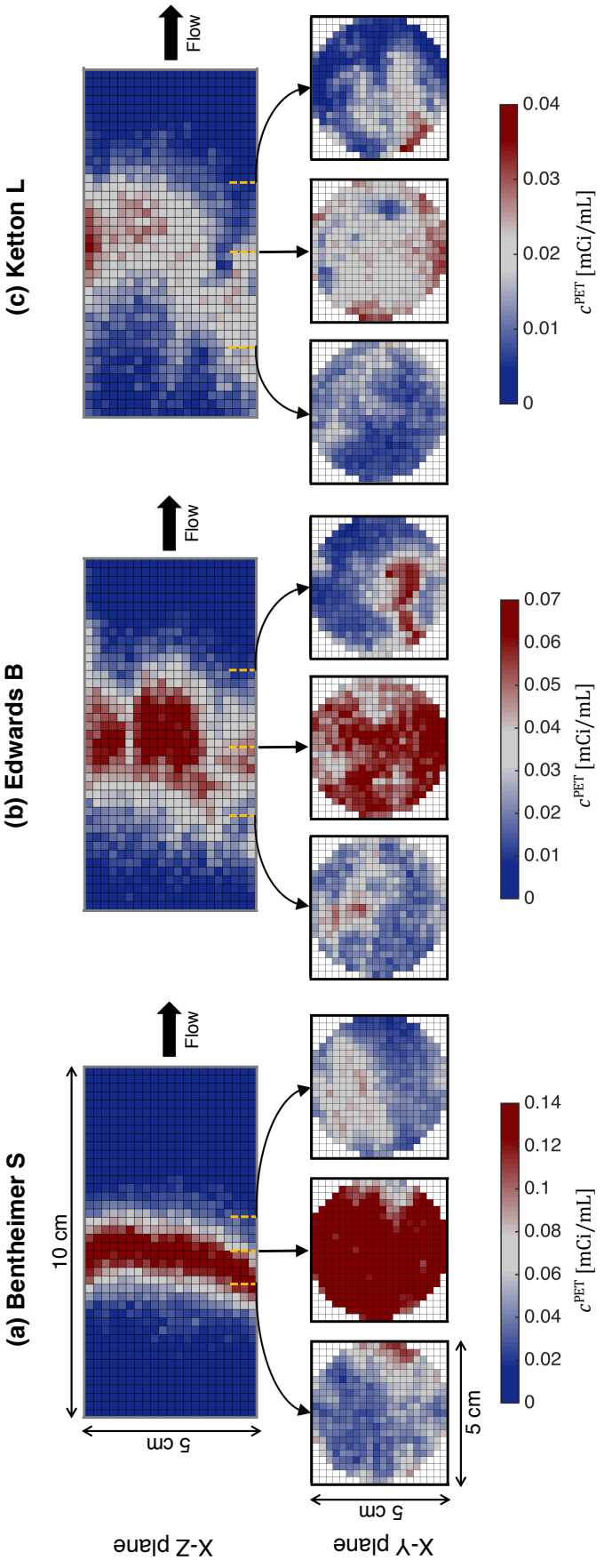

Figure 9.3: 2-D internal concentration profiles in (a) BS, (b) EB and (c) KL at $\Theta = 0.5$. The datasets have been reconstructed at constant time frame of about ± 0.07 PV. The experiments have been carried out at $q = 4$ mL/min. The images on the top are shown the 2-D central cross-sections (X-Z plane) whereas the cutting planes perpendicular to the flow direction is given at the bottom. To highlight incomplete mixing of the tracer plume, the latter is presented at three different radial cross-sections, including the solute front (right), the bulk (middle) and the tail (left). The PET data has a consistent voxel size of (2.3×2.3) mm^2.

is in agreement with the numerical studies presented in Le Borgne et al. (2015), in which the transport of solute was simulated in different strength of permeability fields. Interestingly, characteristic behaviours in the concentration PDF are observed for the four porous systems investigated. Specifically, the concentration distributions for BP are characterised by rather a 'convex' function, with the local minimum at around the mean concentration. This implies that the system contains a large proportion of voxel concentration values at $c \sim 0$ (where there is no tracer) and $c \sim c_{\max}$ (tracer bulk). Indeed, this behaviour is expected for a system with little dispersion where there is a clear distinction between tracer and background fluid. While this behaviour is still apparent in the homogeneous BS (but represent a more diluted case), the results for the carbonate rocks yield significant probabilities of concentration around the mean, i.e. $c \sim c_{\mathrm{m}}$. As a consequence, the proportion of high and low concentration levels are significantly reduced. This behaviour is characteristic of a medium that undergoes significant mixing, primarily due to the strong action of smoothing out of the concentration gradients. This highlights the pronounced effects of dilution caused by the characteristic feature of the carbonate rocks, such as the presence of spatial heterogeneity and microporosity.

When the concentration PDF are compared at the same pore volume injected (i.e. $\Theta = 0.5$), the differences in the concentration levels between the four porous media become even clearer. This is depicted in Figure 9.5, where we observe that the high concentration level reveals a span of almost one order of magnitude between the four core samples. Such deviation in the concentration is a direct manifestation of the structural complexities and reflects the consequence of the mixing mechanism that occur in each system. This implies that, while BP still has a large probability of high concentration solute to be diluted to the low concentration regime, the mixture in KL has already evolved into much closer to uniformity (concentration equilibrium) at $\Theta = 0.5$, with majority of the voxel quantities having similar values as the mean, c_{m}. The experimental results presented in this work yield a scaling of $1/c$ for the low concentration region, which is characteristic of profiles dominated by diffusion (Le Borgne et al., 2015). The corresponding reconstruction of the PDF using the 1-D ADE model shows an excellent prediction of the experimental distribution curve for the homogeneous BP, as can be seen in the inset of Figure 9.5. This verifies the reliability of PET to enable quantitative analysis of mixing during solute transport in porous media. Note that the the concentration PDFs in the figure are weighted by

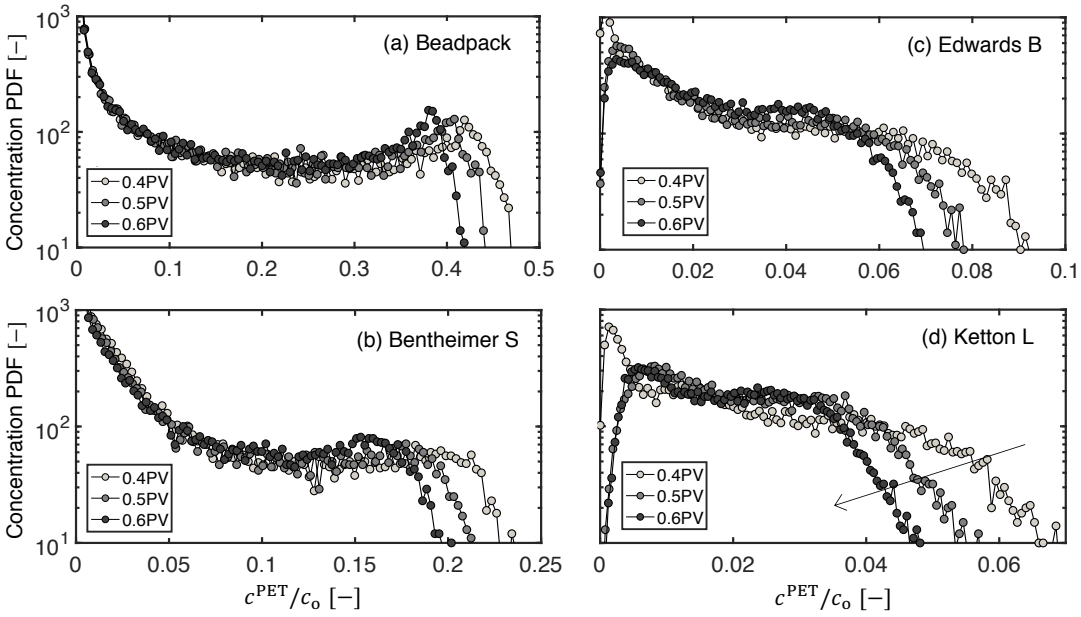

Figure 9.4: Temporal evolution of the concentration probability density functions (PDF) for (a) BP, (b) BS, (c) EB and (d) KL, represented with a logarithmic scale on the y-axis. For each system, three distinct time intervals are shown: $t = 0.4\tau_{exp}$, $0.5\tau_{exp}$ and $0.6\tau_{exp}$. The PDFs have been obtained from computing the histogram of voxel concentration values (bin size: 100) obtained from 3-D PET dataset, with reconstructed voxel size: 2.3×2.3×2.4 mm^3 (preclinical PET) and 1.4×1.4×2 mm^3 (clinical PET), giving a total of about 20,000 voxels for each calculation. The voxel values have been normalised by the feed concentration, i.e. c^{PET}/c_o. The results are presented for the experiments carried out at $q = 10$ mL/min for BP and $q = 4$ mL/min for the rock samples.

the total number of voxels (reported as concentration frequency) to allow comparisons between the dataset with different number of counts.

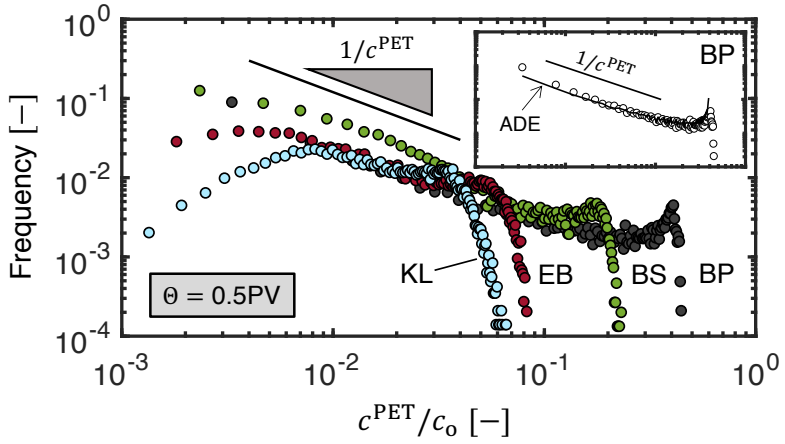

Figure 9.5: Log-log plot of concentration PDFs for the four porous media at time interval corresponding to $t = 0.5\tau_{exp}$. To allow comparisons, the PDFs have been normalised by the total number of voxels in each system. The inset shows the experimental dataset for BP (circles) together with prediction obtained from the one-dimensional ADE (solid line, using $\alpha_L = 0.029$ cm) for the same scale.

9.3.3 Insights from mixing measures

Figure 9.6 shows the evolution of the *normalised* dilution index (Π, Eq. 9.3) plotted as a function of the square root of the reduced time (Θ) for the four porous media. The experimental data for each system is denoted by different symbols in the plot and represent the time intervals when the total amount of injected tracer is in the system. Also shown in the figure are the values of dilution index predicted from the corresponding 1-D transport models (lines). The solid and dashed lines represent the regions where the full solute plume is in the core and entering/exiting the system, respectively. As expected, we observe that dilution index increases over time for all the systems until breakthrough, as a result of the dispersion process. At the times when all the tracer is in the sample, we also observe that the dilution index varies linearly with $t^{1/2}$ (or $\Theta^{1/2}$). This scaling behaviour is consistent with the numerical estimates (solid lines) obtained using the Fickian-based models (i.e. ADE or MRMT), as well as the analytical expressions derived in the literatures (e.g. (Kitanidis, 1994; Boon et al., 2017)). The close match between the experimental and the theoretical prediction of the dilution index suggests that the solute plume has (quickly) evolved into a Fickian behaviour on a length-scale $\mathcal{O}(l) \sim 10$ cm (corresponding to the length of the samples used) in all the core samples investigated in this work. While the latter is expected for the homogeneous systems (such as BP and BS), this behaviour is less intuitive for the heterogeneous carbonates. Although these rock cores exhibit heterogeneous environment at the subcore-scale, as can be clearly seen by the considerable development of plume spreading depicted in the 3-D PET images (Figure 9.2), they possess relatively short correlation lengths (in the range between $0.2 - 1.2$ cm, as characterised in Chapter 6). In other words, these rocks cores ($L \approx 10$ cm) are long enough for the spatial heterogeneity to be considered randomly distributed in space. In that respect, the results presented in this study suggest that the timescale to reach Fickian behaviour is governed primarily by the extent of structural correlations of the spatial heterogeneity, rather than the strength of the heterogeneity itself (which is rather weak). Moreover, the presence of microporosity in carbonates plays a significant role in 'homogenising' the effects of spreading (see Figure 9.2), thus acting as a catalyst to speed up the time scale to reach asymptotic (Fickian) regime. In this study, we demonstrate that the 1-D Fickian models provide a reasonable estimate of the global mixing process at the subcore-scale as long as the correlation length of heterogeneity is less than the

experimental observation scale. It is worth noting that the scaling of the experimental dilution index obtained in this study, i.e. $t^{1/2}$ does not show the expected dimensionality effect indicated by the numerical work presented in the literature, i.e. $\Pi \propto t^{n/2}$ where n is the dimension of the domain (Kitanidis, 1994). A possible explanation for this is that the boundary condition adopted in these column experiments limits any effect arising from transverse dispersion, making the experiments effectively one-dimensional. A potential modification of our experimental set up and protocol will be presented in Section 10.2.4. In the figure, we also notice that each medium is characterised by different slopes, which in turn allows us to understand the different rates of dilution in these systems. To quantify this, we take the derivative of dilution index ($\Pi = b\Theta^{0.5}$) over reduced time, giving the following expression:

$$\frac{\partial \Pi}{\partial \Theta} = 0.5 b \Theta^{-0.5} \tag{9.10}$$

where b is the power-law constant (corresponding to the slope of Figure 9.6, with the values reported in the captions of the figure). From Eq. 9.10, it can be deduced that, while the dilution rate gives a decay with the scaling $\Theta^{-0.5}$ for all the systems that satisfies the Fickian scale behaviour, the dilution rate between the systems can be significantly different, that varies with the constant $0.5a$. For the experiments conducted in this study, the dilution rate increases in the order BP(0.08)<BS(0.19)<EB(0.54)<KL(0.70), giving a span of about one order of magnitude.

The temporal evolution of the intensity of segregation, I, plotted over reduced time, Θ is presented in Figure 9.7. The symbols are the experimental results computed from PET whereas the dashed-lines are again the corresponding Fickian-model estimates. Unlike the dilution index, the value of intensity of segregation decrease over time, due to the reduction in the local concentration variances caused by solute mixing. For the results on BP and BS, the experimental measurements closely follow the numerical counterpart, thus confirming the application of the Fickian models in predicting the temporal behaviour of global mixing in homogeneous systems. For the heterogeneous carbonates, the discrepancy between experiment and simulation increases. Specifically, we note that the measured intensity of segregation gives a steeper decay than the theoretical prediction. This is mostly because heterogeneity, which is not considered in the 1-D model increases the concentration contrast due to plume deformation, which in turn enhances mixing (Le Borgne et al., 2014). Such deviation is less noticeable in the dilution index because

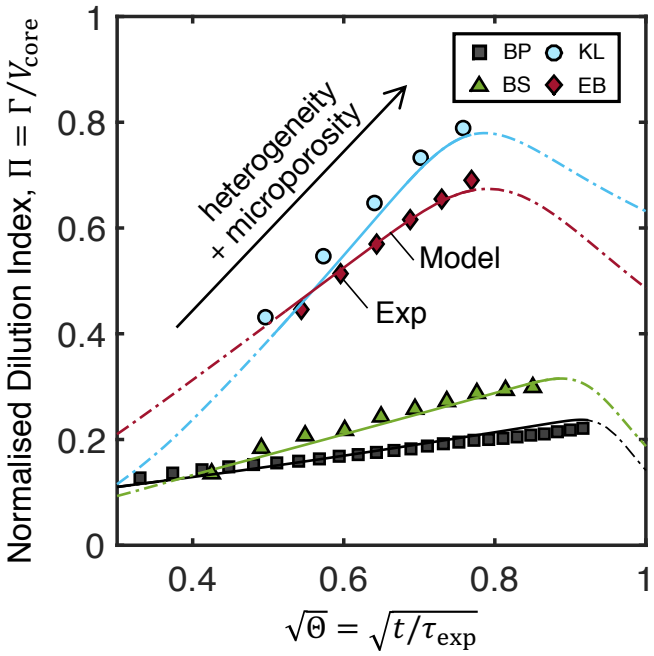

Figure 9.6: (a) Normalised dilution index (reactor ratio), Π plotted over square root of reduced time, $\sqrt{\Theta}$ for the four porous media: BP (squares), BS (triangles), EB (diamonds) and KL (circles). The solid lines are the corresponding 3-D reconstructions of the numerical solution of the 1-D transport models, namely ADE for BP and MRMT for the rock cores. The model parameters used correspond to the optimum values obtained upon fitting the effluent profiles (details can be found in Chapter 7). The dashed-lines refer to the times when tracer distribution is not conservative (i.e. tracer is either entering or leaving the core). The experiments were conducted at $q = 10$ mL/min for BP and $q = 4$ mL/min for the other samples. A linear fit to each experimental dataset in the plot yields the following constants variables: 0.16 (BP), 0.37 (BS), 1.08 (EB) and 1.39 (KL). These were used to estimate the dilution rate in each system.

the 1-D transport models used to compute the mixing measures indeed carries information on rock property heterogeneity by distributing the solute mass over a larger volume of water. Dilution index utilises the same concept (Chiogna et al., 2011a; Rolle and Kitanidis, 2014) and hence provides a good description of the experimental values as long as Gaussian regime has established. On the other hand, we contend that the intensity of segregation is more sensitive to local heterogeneity variations because it measures the degree of mixing by means of spatial difference in the concentration gradients. Accordingly, the homogeneous models under-predict intensity of segregation in systems that are characterised by significant spatial heterogeneity, which are the cases for KL and EB.

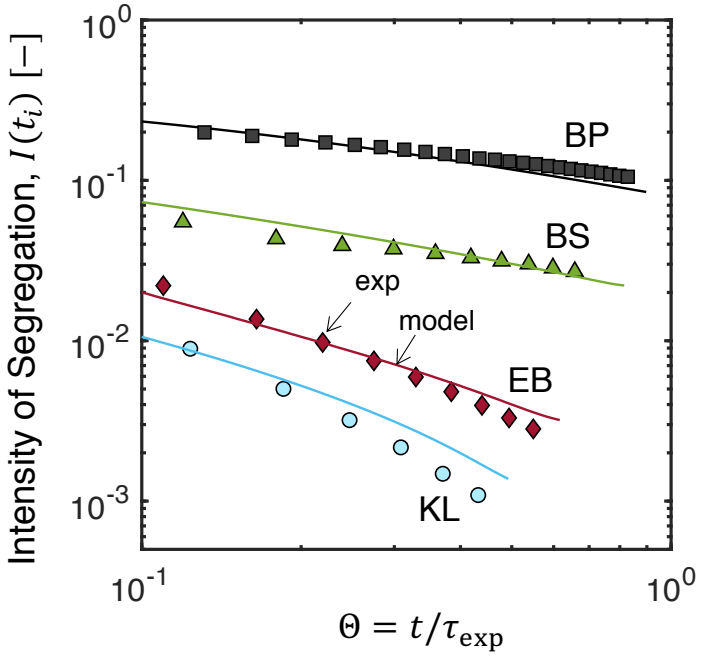

Figure 9.7: Log-log plot of intensity of segregation, $I(t)$ over reduced time, Θ for the four core samples. The symbols are the measured data whereas the dashed lines are the corresponding model reconstructions of $I(t)$. Details of the models used can be found in the captions of Figure 9.6.

9.3.4 Insights from spreading metrics

Figure 9.8 presents the experimental dilution index deviation ($\Delta\widetilde{\Pi}$, Eq. 9.9) plotted as a function of time ($\Theta = t/\tau_{\text{exp}}$), when more than 95% of the tracer injected is still conserved in the system. We note that a Fickian-based model should yield $\Delta\widetilde{\Pi} = 0$, because it assumes complete mixing in the radial direction. When the experiments are considered, a systematic difference between $\widetilde{\Pi}_{1D}$ and $\widetilde{\Pi}_{3D}$ is observed. Specifically, we show that the experimental values computed using slice-averaged properties are higher, thus reflecting the artificial ("numerical") mixing of the solute plume that has been significantly distorted by the presence of subcore-scale permeability heterogeneity. The sensitivity of this spreading measure is clearly demonstrated from the analysis carried out on the BP, where we notice that even the experiment with a homogeneous core yields a slight (but constant) deviation between the two computed quantities, i.e. $\Delta\widetilde{\Pi} \approx 0.005$. As explained in Chapter 5, the subtle inhomogeneity is introduced at the core entrance. In contrast, the results from the rock cores are characterised by a systematic increase in the $\Delta\widetilde{\Pi}$ over solute travel times, indicating the continuous development of plume deformation along the cores. As expected, we observe that the extent of plume spreading increases in the order BS<KL<EB, which is in accordance with the inherent heterogeneity of the core samples. We also show that

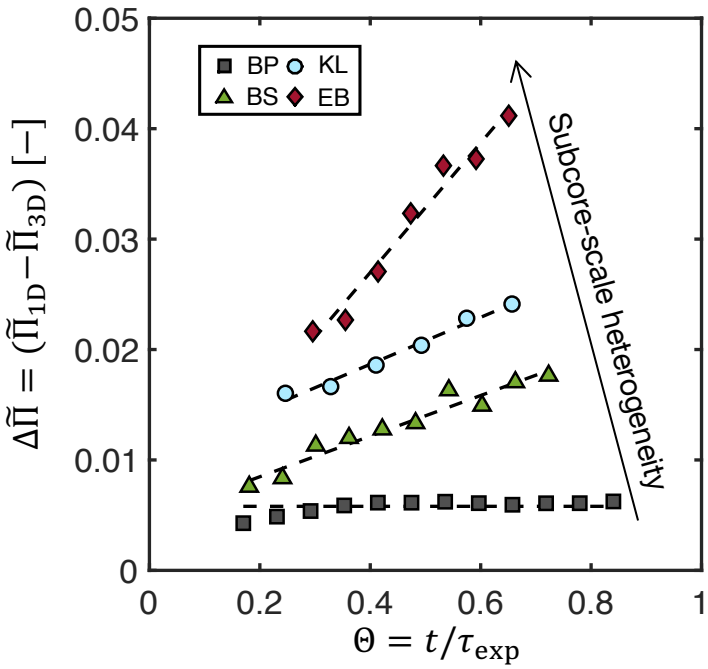

Figure 9.8: Experimental deviation of dilution index ($\Delta\widetilde{\Pi}$) plotted over reduced time (Θ) for the four porous systems. The values of $\Delta\widetilde{\Pi}$ are computed as the difference between dilution index obtained on a 3-D voxel basis ($\widetilde{\Pi}_{3D}$) and the 1-D counterpart (Eq. 9.9). The dashed-lines refer to the best fitted linear function with the following slopes: ~ 0 (BP), 0.018 (BS), 0.021 (KL) and 0.059 (EB).

the rate of plume deformation is constant over time, as given by the linear increase of the dilution index deviation. The following slopes are obtained from a linear regression to the experimental dataset: 0.018 (BS), 0.021 (KL) and 0.059 (EB). Interestingly, we observe that the rate of plume deformation of BS and KL are comparable, as evidenced by the similar slopes in the figure. This is most likely caused by the pronounced mixing in the KL, due to the presence of microporosity, which occupies about 30% of the total pore space. This helps to smooth-out the preferential flow paths in the flow field. As a result, the rate of plume deformation can be largely moderated by the enhanced action of mixing.

In order to verify the application of this spreading measure, we provide a connection between the experimental dilution index deviation ($\Delta\widetilde{\Pi}$) with intrinsic heterogeneity of the core samples. For the latter, we consider the inhomogeneity factor (σ) that has been obtained from macroscopic measurements of transport, i.e. by means of effluent breakthrough curve analysis (see Section 7.6.4 for details). Recalling that the inhomogeneity factor, defined as $\sigma = \alpha_{\mathrm{L}}/d_{\mathrm{e}}$ (where α_L is the longitudinal dispersivity and d_{e} is the equivalent grain diameter) determines the strength of heterogeneity in a porous medium and therefore should in principle control the deformation

of solute plume that is quantified from $\Delta\widetilde{\Pi}$. The results are plotted in Figure 9.9 for the four distinct types porous media at a fixed time interval, $t = 0.5\tau_{\text{exp}}$ (corresponding to $\Theta = 0.5$). As shown in the figure, we obtain a linear relationship between the inhomogeneity factor and the dilution index deviation; this is verified by the R-squared value: $\text{R}^2 = 0.99$. To further validate this relationship, $\Delta\widetilde{\Pi}$ is also calculated at other pore volumes where dilution index can be computed (i.e. at $\Theta = 0.4$ and 0.6). As a result, a linear correlation with consistent R-squared values of $\text{R}^2 \approx 0.98 - 0.99$ is attained (for the sake of clear presentation, only $\Delta\widetilde{\Pi}$ computed at 0.5 PV is shown in the figure). This result reflects the fact that the spreading of the tracer plume (measured by $\Delta\widetilde{\Pi}$) is directly proportional to the intrinsic heterogeneity of a porous medium, with the latter being determined by means of inhomogeneity factor, σ. Most importantly, the direct link between the two metrics provides an opportunity to better estimate the behaviour of incomplete mixing from core-scale dispersivity measurements.

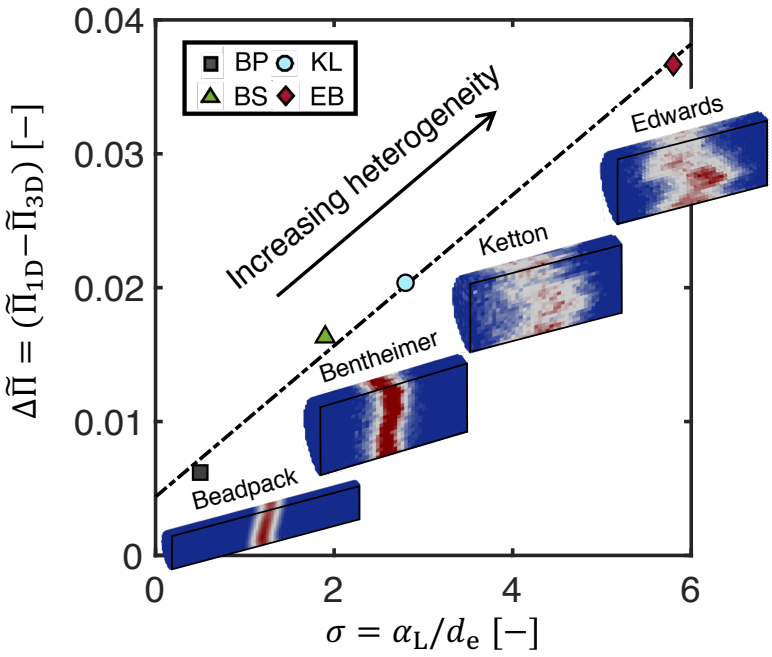

Figure 9.9: Correlation between inhomogeneity factor (σ) and dilution index deviation ($\Delta\widetilde{\Pi}$). The latter is obtained from PET imaging dataset (snapshots also shown in the plot) at a constant time interval, $t = 0.5 \times \tau_{\text{exp}}$, for the experiments at flow rates, $q = 10$ mL/min (BP) and $q = 4$ mL/min (BS, KL, EB). The inhomogeneity factors are calculated from $\sigma = \alpha_L/d_p$, with dispersivities obtained from ADE for BP, or MRMT models for other systems (numerical values are summarised in Table 7.7).

To correctly describe the anomalous behaviour of solute transport in natural systems, it is very important to appropriately evaluate how quickly the plume has evolved into asymptotic "Fickian" regime. The latter presents an essential means in characterising anomalous trans-

port because it determines the critical time (or length-) scales at which the attained transport parameter reaches an asymptotic constant value (Dentz et al., 2011). While this has been approximated by interpreting Continuous Time Random Walk theory based on solute transit times (Dentz et al., 2004; Bijeljic and Blunt, 2006) in the previous chapters, we now evaluate this from direct experimental observations using PET. With the latter, this can be studied directly by means of computing the temporal evolution of spreading length scale, K, given in Eq. 9.7. The results are plotted in Figure 9.10 over square root of reduced time, $\sqrt{\Theta}$. As evidenced in the figure, the time behaviour of the K plotted against $\sqrt{\Theta}$ generally follows a linear function over majority of the temporal range investigated in this study. The latter indeed corresponds to a characteristic spreading length of a Fickian plume (Le Borgne et al., 2010), implying that the plume size of the core samples presented in this work evolved into asymptotic condition quickly after the tracer has entered into the core. This observation indeed agrees well with the analysis carried out on the dilution index as discussed in the previous section. In the figure, it is shown that the result obtained with the BP core is initially non-Fickian, and translates into Fickian scaling after about $\Theta = 0.2$ (or $\sqrt{\Theta} = 0.45$). This is again caused by the inlet effects, in which the Fickian plume is then slowly established after propagating the homogeneous beadpack over a certain distance. The clear distinction between inhomogeneity (at the inlet) and the homogeneous beadpack makes the transport of tracer in a way that is more "correlated" than the rocks considered in this work, and thus requires slightly longer time to evolve into Fickian plume. Nevertheless, this time scale, i.e. $\Theta = 0.2$ is still very short as compared to the systems with strong permeability fields (Le Borgne et al., 2015).

9.4 Conclusion

In this study, we have produced for the first time, experimental observations of the temporal behaviour of mixing and spreading during the dynamic injection of a tracer pulse in four different core samples, including granular beadpack (BP), Bentheimer Sandstone (BS), Ketton Limestone (KL) and Edwards Brown Carbonate (EB). The method presented here utilises the 3-D concentration maps acquired from PET imaging, which serve as proxies for the independent characterisation of subcore-scale mixing and spreading.

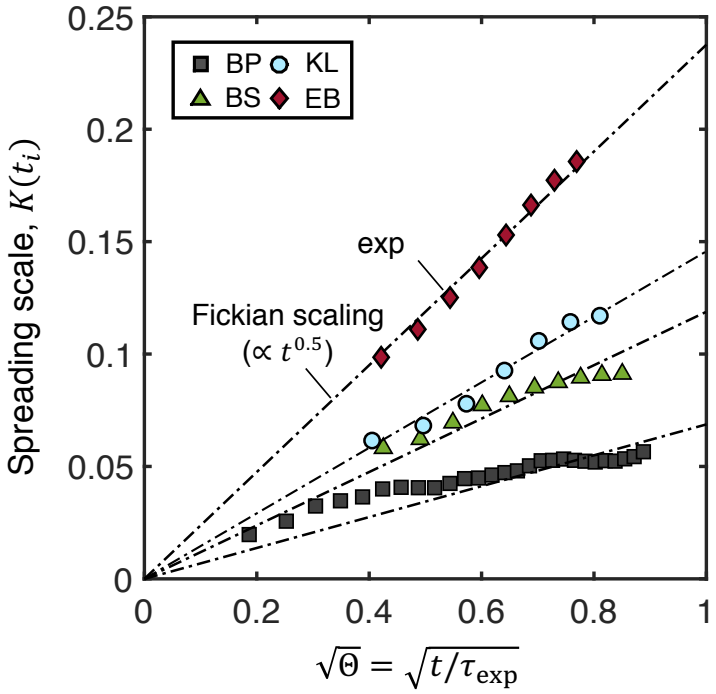

Figure 9.10: Spreading length scale, $K(t_i)$ plotted over square root of reduced time, $\sqrt{\Theta}$ for the four core samples. The symbols are the experimental data obtained from PET whereas the dashed lines correspond to the 'Fickian' scaling ($\propto t^{0.5}$) as reported in the literature: Le Borgne et al. (2010).

For each porous system, the 3-D concentration maps of the tracer plume reveal distinct flow behaviours, thus reflecting the intrinsic physical characteristics of the core samples. While BS shows a uniform distribution of tracer plume along the core length, the PET images provide direct evidence of macrodispersive spreading caused by the presence of subcore-scale heterogeneities in the carbonate rocks. With the latter, we demonstrate that the presence of microporosity contribute significantly towards the overall mixing of the system. As a direct consequence, this reduces the concentration gradients by introducing additional mass transfer within the solute plume. To describe the spatial and temporal evolution of the plume, we utilise various metrics, including the dilution index, the intensity of segregation and the spreading length scale.

It was observed that the dilution index and the spreading length scale increase with solute travel time with a Fickian scaling for all the samples studied. This implies that the degree of heterogeneity in these cores are rather moderate and that the advancement of advective spreading is minimised by the presence of microporosity. The intensity of segregation advances in the opposite direction, as a result of the smoothing of local concentration fluctuations. In this work, all the measures indicate that the mixing in the carbonate rocks is much more predominant. This

is because of the additional mass-transfer resistance that arises due to the intra-granular pore space, in addition to the Fickian diffusion. These mixing mechanisms are further intensified by the presence of advective spreading in the heterogeneous carbonates. The development of Fickian behaviour in the experimental observations of mixing has been verified by the reasonable agreement with the corresponding numerical predictions based on the conventional Fickian transport models (i.e. ADE/MRMT).

To investigate the time behaviour of incomplete mixing, we propose a new metric, namely the dilution index deviation, $\Delta\widetilde{\Pi}$. While the homogeneous models predicts $\Delta\widetilde{\Pi} = 0$, analysis from experiments showed that inhomogeneity persists in all the core samples (where $\Delta\widetilde{\Pi} > 0$). While this is negligible in the uniform beadpack, the temporal extent of advective spreading shows a linear increase in the rock cores, with the degree of incomplete mixing increasing in the order BS<KL<EB. We successfully verified the application of this measure by correlating it with the inhomogeneity factor, σ that was obtained from independent analysis carried out on the breakthrough curve measurements.

In summary, we have presented a novel experimental approach where the time behaviour of solute plume can be directly studied by means of mixing and spreading independently. The methodology has been successfully demonstrated in four porous media with distinct physical features. By incorporating different quantitative measures of mixing, we provide a detailed observational basis to advance our understanding of miscible displacements in complex porous media, thus providing a complement to the knowledge gained from 1-D breakthrough curve analysis. While the study has been carried out here to investigate the time evolution of the global mixing and spreading measures between different core samples at a selected flow rate, the analysis will be extended over the entire flow range of the experiments (i.e. flow rate, $q = 2 - 19$ mL/min) to examine the flow rate dependency of these metrics.

Chapter 10

Conclusions and Future Work

10.1 Conclusions

The presence of multi-scale heterogeneity in natural rocks results in a large variability of fluid velocities and ultimately leads to the observation of the so-called 'anomalous' transport. This limits our ability to accurately predict fluid transport in the subsurface and represents a major challenge for the advancement of various large-scale technologies. Some examples include: (i) the quantification of solubility trapping during geologic carbon sequestration applications in deep saline aquifers, which relies on the mixing between CO_2-saturated brine and the resident fresh brine; (ii) the estimation of the extent of the mixing-zone during enhanced oil recovery applications where a fully miscible solvent is used to displace hydrocarbons; (iii) the modelling of the natural gas-CO_2 displacement process in enhanced gas recovery operations. While laboratory studies on this subject have been reported in the literature, most of them have focused on a macroscopic description of transport (e.g., by means of analysing the one-dimensional tracer breakthrough curves). Yet, limited knowledge exists on the role played by the inherent subcore-scale structural heterogeneity of rocks on fluid spreading and mixing.

In this thesis, we have successfully demonstrated a new laboratory workflow to characterise dispersion, spreading and mixing during solute transport in rocks. The core of the workflow relies on the use of Positron Emission Tomography (PET) to observe in real-time the distribution of a tracer plume in three-dimensions. Because static properties, such as porosity, and their distri-

bution can nowadays be readily measured by X-ray Computed Tomography, this novel ability to image a solute plume in an opaque porous medium represents the missing link to validate numerical models of transport in heterogeneous porous media. A compact core-flooding system has been designed and commissioned to allow unidirectional flow pulse-tracer experiments coupled with simultaneous *in situ* imaging. The validity of the proposed experimental approach was confirmed by means of a set of control tests carried out on an unconsolidated beadpack (BP) over the range of Péclet numbers, $25 < \mathrm{Pe} < 250$. To this aim, the breakthrough curves measured using a radio-tracer ($[^{11}\mathrm{C}]\mathrm{NaHCO_3}$) were compared against brine-tracer (KI) measurements. An excellent agreement was observed between the experimental PET data and predictions from the Advection Dispersion Equation (ADE) in terms of both 1-D and 3-D internal concentration profiles. Over the range of flow rates tested, the dispersion coefficient scales linearly with the Péclet number, the estimated longitudinal dispersivity is constant and takes a value that is consistent with theoretical predictions (i.e. $\alpha_\mathrm{L} = d_\mathrm{p}/2 \approx 0.029$ cm). This observation further demonstrates the reliability of the measurement technique presented in this work for the characterisation of solute transport during miscible displacements.

For the study of solute transport in rocks, three samples were considered, namely Bentheimer Sandstone (BS), Ketton Limestone (KL) and Edward Brown Carbonate (EB). The three rocks have been characterised using a range of analytical and imaging methods, including helium pycnometry, mercury intrusion prorosimetry (MIP) and X-ray CT (micro- and medical-instruments), to provide a distribution of baseline microscopic properties, such as skeletal density, porosity, pore- and grain size distribution. Notably, the selected rock samples possess distinct strength of sub-core scale heterogeneity (BS<KL<EB) and present characteristic features, such as complicated grain structures and multiscale porosity. In addition to provide guidelines in the identification of characteristic length-scales for the selected rocks, this information is also used in the selection of the most appropriate model to describe transport in each system.

Unidirectional pulse-tracer tests were carried out on each rock core (diameter: 5 cm; length: 15 cm) over a range of Péclet numbers ($\mathrm{Pe} \approx 15 - 500$) and by simultaneously imaging the spatial and temporal evolution of the full tracer plume at a resolution of approximately 8 mm^3. The measured solute concentration profiles are evaluated using three transport models: the Advec-

tion Dispersion Equation (ADE), the Multi-Rate Mass Transfer (MRMT), and the Continuous Time Random Walk (CTRW) model. While the ADE model fails at capturing the anomalous behaviour manifested in the effluent profiles, both MRMT and CTRW models provide excellent fits to the experimental measurements for all the systems and over the entire range of flow rates studied.

The two modelling approaches provide consistent and complementary insight into the transport properties of the three rocks. Using the MRMT model, a linear correlation between Péclet number and the dispersion coefficient is observed over the range of flow rates and for the three rocks ($D_{\mathrm{L}} \propto Pe$). For the microporous carbonates (KL and EB), the additional mass transfer between the 'flowing' fluid (present in the intergranular pore space) and the 'stagnant' fluid (intragranular pore space) is captured using a first order rate expression, with the mass transfer coefficient scales with the Péclet number as $k_{\mathrm{m}} \propto Pe^{0.6}$. Accordingly, the characteristic flow rate dependency observed in the residence time distribution curves of the carbonate rocks can be traced back to the relative strengths of these two transport mechanisms. It is worth noting that the MRMT model is applied in this study by considering the dispersivity and the microporosity as global fitting parameters, rather than introducing an arbitrary flow-rate dependency as in previous studies.

A major outcome of the CTRW theory is the determination of the characteristic length scale to reach the asymptotic (Fickian) regime, which is below the length of the cylindrical core samples used in this study. This result is important and supports the application of the Fickian-based models (e.g. MRMT) with a constant dispersion coefficient. Also in this case, the CTRW model is applied by considering a set of global parameters (i.e. t_2, α_ψ and β) which depend on the rock, but are independent of the flow rate. In this context, we provide what are, to our knowledge, the first direct evaluation of the CTRW theory on the effluent tracer curves measured on (i) various consolidated rock cores and over a (ii) wide range of flow rates.

The three-dimensional dataset obtained from the PET images on the three rocks has been used to investigate mixing and spreading patterns in both space and time. These images provide direct evidence for the impacts of subcore-scale heterogeneities on the transport of solute, including incomplete mixing. The latter describes any behaviour that cannot be captured by the 1-D transport models. The extent of mixing has been further quantified by means of dilution index

and intensity of segregation, with both measures indicating that the mixing in the carbonate rocks are much stronger than in the sandstone. Notably, the time evolution of both dilution index and spreading scale follow a Fickian behaviour for all the three rocks. This further suggests the strength of heterogeneity in these rocks are moderate and that the presence of microporosity limits the degree of incomplete mixing. A new spreading measure based on the concept of dilution index has been proposed in this work to quantify the temporal extent of incomplete mixing. The latter increases in the order BP<BS<KL<EB, which is in alignment with the observed spatial heterogeneity in the porosity of the core samples.

In summary, the analysis presented in this thesis provides a first demonstration that PET can provide precise temporal and spatial concentration measurements in opaque porous media that can be further used to quantify mixing and transport properties in complex systems, such as rocks. The methods presented here represent a solid point of departure for studying more complex transport processes, such as those associated with chemical reactions and multiphase systems.

10.2 Suggestions for future work

As shown in Chapter 9, the degree of dispersion in the microporous carbonates is significant; this limits the analysis carried out on the different measures of mixing and spreading, because these metrics are applicable only when the entire plume is in the system. Accordingly, only few data points could be extracted for the results obtained on the carbonate cores. This problem can be effectively resolved by (i) considering longer core samples (e.g. 20 cm to fit within the axial field of view of the PET scanner), and/or (ii) injecting a shorter pulse of tracer into the system. The work presented in this thesis can be extended to investigate the following topics:

10.2.1 Subcore-scale heterogeneity and solute dispersivity

While the micro-CT images between the distribution of grains in the oolitic Ketton Limestone (see Chapter 6) and the dense random packing of glass beads (see Chapter 5) reveal significant similarity, we demonstrated that the dispersivity obtained for the limestone ($\alpha_L = 0.15$ cm) is about five times larger than for the uniform beadpack ($\alpha_L = 0.029$ cm). This discrepancy is

the direct consequence of the presence of sub-core heterogeneities, as indicated by the three-dimensional porosity maps presented in Chapter 6. In the context of solute transport, the terms 'spreading' (Kitanidis, 1994; Le Borgne et al., 2010) and 'macrodispersion' (Steefel and Maher, 2009) are used to emphasise that there is a differential advection process associated with these heterogeneities, which affects the degree of mixing. This effect is clearly visible in the 3-D concentration maps presented in Chapter 9. The larger dispersivity values obtained for the Ketton Limestone and for the other rock samples, originate from lumping into a single coefficient both effects of (Fickian) mixing and macrodispersive spreading, the latter being absent in uniform beadpacks. It was shown that for a sample of Berea Sandstone, the estimated longitudinal dispersivity decreased to $50-70\%$ of the original value upon using a streamtube formulation in the numerical transport model to account for subcore-scale permeability heterogeneity (Pini et al., 2016).

Inspired by the seminal work by Hulin and Plona (1989) on the reversibility of hydrodynamic dispersion, we carried out a preliminary experiment using the so-called "echo" technique, in which a tracer-pulse was injected into the sample and the flow was reversed after a finite time (just prior to tracer breakthrough). The result of this experiment is shown in Figure 10.1 for a test conducted at $q = 4$ mL/min on the same sample of Ketton Limestone. Qualitatively, we note that the breakthrough curve looks more symmetric and the characteristic long-time tailing has significantly reduced. This observation is supported by the comparison with predictions from the numerical model (MRMT). In the figure, the dashed line refers to the solution produced by using the same parameters obtained from the classic "transmission" experiments ($\alpha_{\mathrm{L}}^{\mathrm{T}} = 0.15$ cm and $k_{\mathrm{m}}^{\mathrm{T}} = 0.054$ mm/min, see Chapter 7 for details), while the solid line results from fitting the same model to match the echo curve ($\alpha_{\mathrm{L}}^{\mathrm{E}} = 0.09$ cm and $k_{\mathrm{m}}^{\mathrm{E}} = 0.14$ mm/min). In agreement with our hypothesis, the dispersivity value required by the model is now significantly reduced ($\alpha_{\mathrm{L}}^{\mathrm{E}}/\alpha_{\mathrm{L}}^{\mathrm{T}} \approx 0.6$), while the mass transfer coefficient has increased ($k_{\mathrm{m}}^{\mathrm{E}}/k_{\mathrm{m}}^{\mathrm{T}} \approx 2.5$). We attribute this behaviour to the cancellation, upon flow reversal, of the distortion of the solute plume caused by the presence of permeability heterogeneity. This distortion cannot be smoothed out by the effect of transverse dispersion alone, because the latter is still limited in Ketton ($\alpha_{\mathrm{T}}/\alpha_{\mathrm{L}} \approx 0.1$ Boon et al. (2017)). A large portion of these 'spreading' effects can however be eliminated by reversing the flow direction and the echo breakthrough curve appears therefore more diffusive. To validate

this further, the next step should consider coupling the "echo" approach with simultaneous *in situ* imaging by PET, thereby providing a direct evidence on the recovery of the plume spreading due to subcore-scale heterogeneities. If this holds true, future efforts should look into measuring hydrodynamic dispersion in laboratory core samples using the "echo" technique, because such experimental approach enables decoupling the "macrodispersion" effects from Fickian dispersion. This in turn allows estimating a dispersion coefficient that is more representative of a given rock-type, rather than being a sample specific, and hence is better suited for up-scaling.

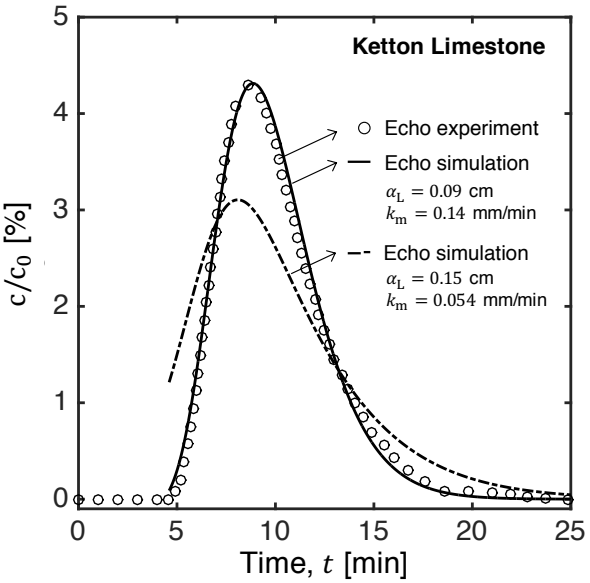

Figure 10.1: Concentration breakthrough curve obtained from an 'echo' test on Ketton Limestone at a flow rate $q = 4$ mL/min and by injecting a 1 mL pulse of the brine tracer (flow reversal was initiated at about 4.5 min). Symbols represent conductivity readings, while the lines are numerical solutions of the MRMT model: the dashed line is for a model that uses the parameters obtained from the classic "transmission" experiments ($\alpha_L^T = 0.15$ cm and $k_m^T = 0.054$ mm/min), while the solid line is obtained by newly fitting the model to match the echo curve ($\alpha_L^E = 0.09$ cm and $k_m^E = 0.14$ mm/min). Concentration values are normalised by the feed concentration, c_0. Figure taken from Kurotori et al. (2019).

10.2.2 Solute mixing and spreading in fractured rocks

Fractures are often found in the subsurface and are the result of tectonic movement (Berre et al., 2018). The ability to transport fluids through a network of natural (pre-existing) or induced fractures underlies many reservoir engineering technologies, including oil and gas extraction, geothermal energy utilization and nuclear waste disposal. More recently, driven by the rapid advancement of shale gas development, fractured rocks has shown an increasing interest in the

oil and gas industry primary because the exploration process is readily governed by the technology, known as "hydraulic fracturing", in order to improve the recovery rate of hydrocarbons (Curtis, 2002). However, the fundamental understanding of solute transport within fractured porous media is far from being well-characterised. This is primarily because the flow process is additionally complicated by the (i) tracer diffusion from the fracture matrix into the surrounding pore space of the rocks (Zhu et al., 2007), and (ii) the strong preferential flow paths of solute through the very high permeable fractured zones (Chuang et al., 2016). Understanding of the coupling between fracture and matrix flow requires direct characterisation of the spatial distribution of the rock's structural features at the subcore-scale, subject to different subsurface stress conditions. While 3-D imaging techniques such as X-ray CT has been used to measure the geometry of fractures (e.g. (Montemagno and Pyrak-Nolte, 1999; Deng et al., 2016)) and to investigate saturation, porosity and permeability distributions (e.g. (Zhu et al., 2007; Lai et al., 2017)), only few of them have experimentally investigated the corresponding flow behaviours that result from these complex physical characteristics of the fractured media (Hirono et al., 2003; Kulenkampff et al., 2008; Brattekås et al., 2016) (which are mainly associated with qualitative observations).

To fill this knowledge gap, the experimental workflow presented in this thesis can be extended to fractured porous media. This can be systematically done by first considering a single fracture matrix on a Ketton Limestone, as indicated in Figure 10.2. This work is currently ongoing, lead by a PDRA in the research group.

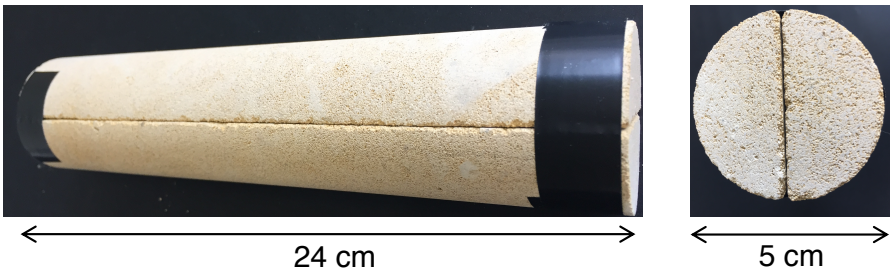

Figure 10.2: Snapshots of a fractured Ketton Limestone

10.2.3 Mixing and spreading at "realistic" subsurface conditions

Although, in this study, we applied and successfully demonstrated a new experimental approach to study solute transport in heterogeneous and microporous porous media, the analysis was limited to single-phase miscible displacements at ambient conditions. While subsurface solute transport can be subject to different miscible displacement processes in a number of situations, such as the flooding of CO_2 into natural gas and crude oil reservoirs at pressures above Minimum Miscibility Pressure (MMP), and the displacement of dissolved CO_2 into saline aquifers (Dullien, 1992; Bear, 1972), the real geological applications can be far more complicated.

First, most of the geological transport processes occur under reservoir conditions, with temperature and pressure in the range typically higher than ~ 50 °C and 10 MPa (Menke et al., 2015). An example of this can be the covenctive dissolution of supercritical CO_2 in the host brine. Under these conditions, the properties of the fluids can behave very differently, which would ultimately impact the mixing and spreading behaviour within a given system. To better represent the conditions in the subsurface, experiments should be extended to reservoir conditions. This would not present a limitation in the PET scans because the detection signal is temperature and pressure independent (Fernø et al., 2015a).

Another aspect that can be considered is the presence of a second, immiscible phase, as mixing in geological processes typically occur during multiphase flows. In the recent works by Honari et al. (2016); Zecca et al. (2017), it has been shown that the dispersivity measured during immiscible displacement is higher than the corresponding single-phase dispersivity and that it increases with saturations. While a higher value suggests an increased heterogeneity, questions remain unanswered on how the presence of second phase alters the small-scale heterogeneities of the system and more importantly, how these changes would consequently contribute to mixing and spreading. As demonstrated in this thesis, 3-D imaging techniques, such as X-ray CT and PET can provide answers to this.

As explained in Chapter 2, during solute transport in heterogeneous rocks, incomplete mixing can also occur at the pore-scale. However, the spatial resolution of PET is in the order of few mm^3, which is significantly larger than the typical size of a rock grain. This limits the PET observations of mixing and spreading processes to the core- and subcore-scale. The latter is done

by averaging the local velocity variations at the pore scale within each voxel (i.e. by assuming complete mixing in each voxel). To overcome this issue, we can scale-up the system such that the size of the particles of the porous media is larger than the spatial resolution of the PET scanner, as demonstrated in Figure 10.3. Depending on the geometry of the porous media considered, the impacts of heterogeneity can be investigated by means of direct microscopic (pore-scale) observations of mixing and spreading.

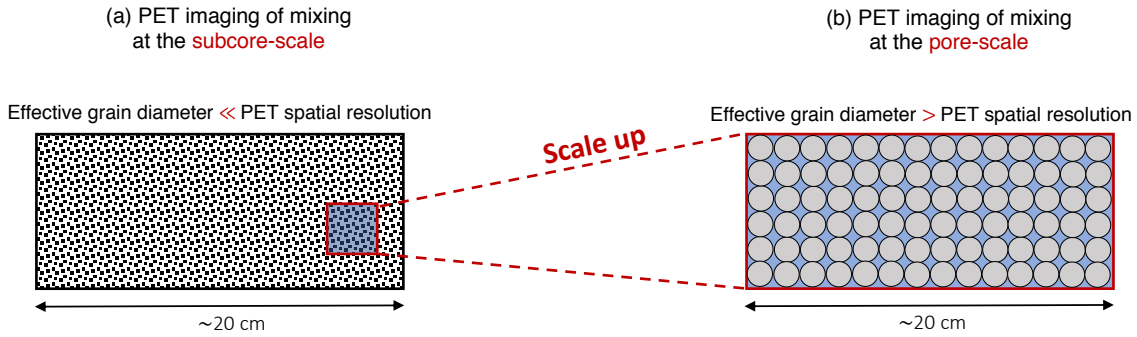

Figure 10.3: Conceptual diagram illustrating how PET imaging of solute transport can be extended to observations at the pore-scale

10.2.4 The effects of dimensionality on mixing in rocks

The classic approach of conducting breakthrough column experiments involves the injection of the tracer across the entire inlet face of the sample. This protocol was also used in this study, thereby minimizing any effect arising from transverse dispersion. Accordingly, the associated macroscopic measures of mixing, such as the dilution index, may not reproduce the expected dimensionaliy effect, even when computed from three-dimensional imagery. By agreeing with predictions from the one-dimensional models, the experimental results presented in Section 9.3.3 confirm these expectation. To address this problem, experimental protocols have been proposed in the literature where the tracer is injected only through the centre of the core inlet (e.g. as point injection), while simultaneously injecting the carrier fluid from the surrounding fluid ports (Ye et al., 2015). As illustrated by the schematic diagram of the solute plume following a point injection (shown in Figure 10.4), such technique enables to maximise the multidimensional transport of solute and therefore can be regarded as a true three-dimensional system. While previous work has focused on investigations after establishing steady state transport conditions (e.g. (Ye et al., 2015; Boon et al., 2017; Rolle et al., 2018)), these studies can be extended

using PET imaging technique to provide insights into the dynamic behaviour of 3-D mixing and spreading of a 3-D tracer plume.

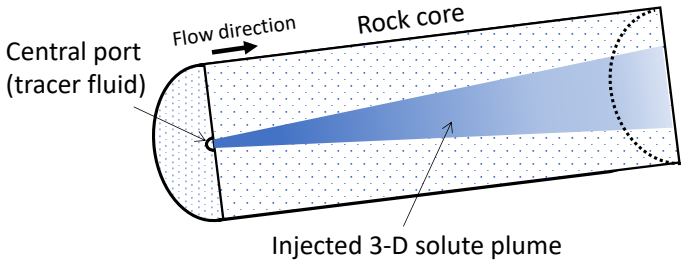

Figure 10.4: Schematic diagram of the three-dimensional solute plume within a porous medium following a point injection of the tracer fluid.

Bibliography

Abramowitz, M., Stegun, I. A., 1970. Handbook of mathematical functions. Dover Publications.

Adams, E. E., Gelhar, L. W., 1992. Field study of dispersion in a heterogeneous aquifer: 2. Spatial moments analysis. Water Resources Research 28 (12), 3293–3307.

Akin, S., Kovscek, A. R., 2003. Computed tomography in petroleum engineering research. Geological Society, London, Special Publications 215 (1), 23–38.

Andrew, M., Bijeljic, B., Blunt, M. J., 2014. Pore-scale imaging of trapped supercritical carbon dioxide in sandstones and carbonates. International Journal of Greenhouse Gas Control 22, 1–14.

Andrew, M., Matthew, 2015. Reservoir Condition Pore Scale Imaging of Multiphase Flow using X-Ray Microtomography. Ph.D. thesis, Imperial College London.

Aylmore, L. A. G., Quirk, J. P., 1967. The micropore size distributions of clay mineral systems. Journal of Soil Science 18 (1), 1–17.

Bailey, D. L., Townsend, D. W., Valk, P. E., Maisey, M. N., 2005. Positron emission tomography. Springer.

Bailey, L., Boek, E., Jacques, S., Boassen, T., Selle, O., Argillier, J., Longeron, D., 2007. Particulate invasion from drilling fluids. Society of Petroleum Engineers Journal 5 (04), 412–419.

Baker, L., 1977. Effects of Dispersion and Dead-End Pore Volume in Miscible Flooding. Society of Petroleum Engineers Journal 17 (03), 219–227.

Battiato, I., Tartakovsky, D., Tartakovsky, A., Scheibe, T., 2009. On breakdown of macroscopic models of mixing-controlled heterogeneous reactions in porous media. Advances in Water Resources 32 (11), 1664–1673.

Batycky, J., Maini, B., Fisher, D., 1982. Simulation of miscible displacement in full-diameter carbonate cores. Society of Petroleum Engineers 22 (05), 1–11.

Bear, J., 1972. Dynamics of fluids in porous media. American Elsevier Pub. Co.

Bear, J., 1988. Dynamics of fluids in porous media. Dover.

Benson, D. A., Wheatcraft, S. W., Meerschaert, M. M., 2000. Application of a fractional advection-dispersion equation. Water Resources Research 36 (6), 1403–1412.

Berg, S., Oedai, S., Landman, A. J., Brussee, N., Boele, M., Valdez, R., van Gelder, K., 2010. Miscible displacement of oils by carbon disulfide in porous media: Experiments and analysis. Physics of Fluids 22 (11), 113102.

Berg, S., Oedai, S., Ott, H., 2013. Displacement and mass transfer between saturated and unsaturated CO_2brine systems in sandstone. International Journal of Greenhouse Gas Control 12, 478–492.

Berg, S., Rücker, M., Ott, H., Georgiadis, A., van der Linde, H., Enzmann, F., Kersten, M., Armstrong, R., de With, S., Becker, J., Wiegmann, A., 2016. Connected pathway relative permeability from pore-scale imaging of imbibition. Advances in Water Resources 90, 24–35.

Berkowitz, B., Cortis, A., Dentz, M., Scher, H., 2006. Modeling Non-fickian transport in geological formations as a continuous time random walk. Reviews of Geophysics 44 (2), RG2003.

Berkowitz, B., Scher, H., 2009. Exploring the nature of non-Fickian transport in laboratory experiments. Advances in Water Resources 32 (5), 750–755.

Berkowitz, B., Scher, H., 2010. Anomalous transport in correlated velocity fields. Physical Review E 81 (1), 011128.

Berkowitz, B., Scher, H., Silliman, S. E., 2000. Anomalous transport in laboratory-scale, heterogeneous porous media. Water Resources Research 36 (1), 149–158.

Berkowitz, B., Singurindy, O., Lowell, R. P., 2003. Mixing-driven diagenesis and mineral deposition: $CaCO_3$ precipitation in salt water-fresh water mixing zones. Geophysical Research Letters 30 (5).

Berre, I., Doster, F., Keilegavlen, E., 2018. Flow in Fractured Porous Media: A Review of Conceptual Models and Discretization Approaches. Transport in Porous Media, 1–22.

Bertels, S. P., DiCarlo, D. A., Blunt, M. J., 2001. Measurement of aperture distribution, capillary pressure, relative permeability, and in situ saturation in a rock fracture using computed tomography scanning. Water Resources Research 37 (3), 649–662.

Bijeljic, B., Blunt, M. J., 2006. Pore-scale modeling and continuous time random walk analysis of dispersion in porous media. Water Resources Research 42 (1), 1–5.

Bijeljic, B., Mostaghimi, P., Blunt, M. J., 2011. Signature of Non-Fickian Solute Transport in Complex Heterogeneous Porous Media. Physical Review Letters 107 (20), 204502.

Bijeljic, B., Mostaghimi, P., Blunt, M. J., 2013. Insights into non-Fickian solute transport in carbonates. Water Resources Research 49 (5), 2714–2728.

Bijeljic, B., Muggeridge, A. H., Blunt, M. J., 2004. Pore-scale modeling of longitudinal dispersion. Water Resources Research 40 (11).

Blunt, M. J., 2001. Flow in porous media - Pore-network models and multiphase flow.

Blunt, M. J., Bijeljic, B., Dong, H., Gharbi, O., Iglauer, S., Mostaghimi, P., Paluszny, A., Pentland, C., 2013. Pore-scale imaging and modelling. Advances in Water Resources 51, 197–216.

Boek, E. S., Venturoli, M., 2010. Lattice-Boltzmann studies of fluid flow in porous media with realistic rock geometries. Computers & Mathematics with Applications 59 (7), 2305–2314.

Boon, M., Bijeljic, B., Krevor, S., 2017. Observations of the impact of rock heterogeneity on solute spreading and mixing. Water Resources Research 53 (6), 4624–4642.

Boutchko, R., Rayz, V. L., Vandehey, N. T., O'Neil, J. P., Budinger, T. F., Nico, P. S., Druhan, J. L., Saloner, D. A., Gullberg, G. T., Moses, W. W., 2012. Imaging and modeling of flow in porous media using clinical nuclear emission tomography systems and computational fluid dynamics. Journal of Applied Geophysics 76, 74–81.

Brattekås, B., Seright, R., 2018. Implications for improved polymer gel conformance control during low-salinity chase-floods in fractured carbonates. Journal of Petroleum Science and Engineering 163, 661–670.

Brattekås, B., Steinsbø, M., Graue, A., Fernø, M. A., Espedal, H., Seright, R. S., 2016. New Insight to Wormhole Formation in Polymer Gel During Water Chasefloods Using Positron Emission Tomography PET. In: SPE Bergen One Day Seminar. Society of Petroleum Engineers.

Bredehoeft, J. D., Pinder, G. F., 1973. Mass transport in flowing groundwater. Water Resources Research 9 (1), 194–210.

Brenner, H., Gaydos, L. J., 1977. The constrained brownian movement of spherical particles in cylindrical pores of comparable radius: Models of the diffusive and convective transport of solute molecules in membranes and porous media. Journal of Colloid and Interface Science 58 (2), 312–356.

Bretz, R., Specter, R., Orr, F., 1988. Effect of Pore Structure on Miscible Displacement in Laboratory Cores. SPE Reservoir Engineering 3 (03), 857–866.

Bretz, R. E., Orr, F. M., 1987. Interpretation of Miscible Displacements in Laboratory Cores. SPE Reservoir Engineering 2 (04), 492–500.

Brigham, W., 1974. Mixing Equations in Short Laboratory Cores. Society of Petroleum Engineers Journal 14 (01), 91–99.

Bui, M., Adjiman, C. S., Bardow, A., Anthony, E. J., Boston, A., Brown, S., Fennell, P. S., Fuss, S., Galindo, A., Hackett, L. A., Hallett, J. P., Herzog, H. J., Jackson, G., Kemper, J., Krevor, S., Maitland, G. C., Matuszewski, M., Metcalfe, I. S., Petit, C., Puxty, G., Reimer, J., Reiner, D. M., Rubin, E. S., Scott, S. A., Shah, N., Smit, B., Trusler, J. P. M., Webley, P., Wilcox, J., Mac Dowell, N., 2018. Carbon capture and storage (CCS): the way forward. Energy & Environmental Science 11 (5), 1062–1176.

Catania, F., Massabò, M., Valle, M., Bracco, G., Paladino, O., 2007. Assessment of quantitative imaging of contaminant distributions in porous media. Experiments in Fluids 44 (1), 167–177.

Chiogna, G., Cirpka, O. A., Grathwohl, P., Rolle, M., 2011a. Relevance of local compound-specific transverse dispersion for conservative and reactive mixing in heterogeneous porous media. Water Resources Research 47 (7).

Chiogna, G., Cirpka, O. A., Grathwohl, P., Rolle, M., 2011b. Transverse mixing of conservative and reactive tracers in porous media: Quantification through the concepts of flux-related and critical dilution indices. Water Resources Research 47 (2).

Chiogna, G., Hochstetler, D. L., Bellin, A., Kitanidis, P. K., Rolle, M., 2012. Mixing, entropy and reactive solute transport. Geophysical Research Letters 39 (20).

Chuang, P.-Y., Chia, Y., Liou, Y.-H., Teng, M.-H., Liu, C.-Y., Lee, T.-P., 2016. Characterization of preferential flow paths between boreholes in fractured rock using a nanoscale zero-valent iron tracer test. Hydrogeology Journal 24 (7), 1651–1662.

Cirpka, O. A., Kitanidis, P. K., 2000a. An advective-dispersive stream tube approach for the transfer of conservative-tracer data to reactive transport. Water Resources Research 36 (5), 1209–1220.

Cirpka, O. A., Kitanidis, P. K., 2000b. Characterization of mixing and dilution in heterogeneous aquifers by means of local temporal moments. Water Resources Research 36 (5), 1221–1236.

Cirpka, O. A., Schwede, R. L., Luo, J., Dentz, M., 2008. Concentration statistics for mixing-controlled reactive transport in random heterogeneous media. Journal of Contaminant Hydrology 98 (1-2), 61–74.

Clausnitzer, V., Hopmans, J., 1999. Determination of phase-volume fractions from tomographic measurements in two-phase systems. Advances in Water Resources 22 (6), 577–584.

Coats, K., Smith, B., van Genuchten, M. T., Wierenga, P. J., 1964. Dead-End Pore Volume and Dispersion in Porous Media. Society of Petroleum Engineers Journal 4 (01), 73–84.

Cortis, A., Berkowitz, B., 2004. Anomalous Transport in Classical Soil and Sand Columns. Soil Science Society of America Journal 68 (5), 1539–1548.

Cortis, A., Berkowitz, B., 2005. Computing Anomalous Contaminant Transport in Porous Media: The CTRW MATLAB Toolbox. Ground Water 43 (6), 947–950.

Cortis, A., Chen, Y., Scher, H., Berkowitz, B., 2004. Quantitative characterization of pore-scale disorder effects on transport in homogeneous granular media. Physical Review E 70 (4), 041108.

Cortis, A., Harter, T., Hou, L., Atwill, E. R., Packman, A. I., Green, P. G., 2006. Transport of Cryptosporidium parvum in porous media: Long-term elution experiments and continuous time random walk filtration modeling. Water Resources Research 42 (12).

Curry, T. S., Dowdey, J. E., Murry, R. C., Christensen, E. E., 1990. Christensen's physics of diagnostic radiology. Lea & Febiger.

Curtis, J. B., 2002. Fractured shale-gas systems. AAPG bulletin 86 (11), 1921–1938.

Cushman, J. H., Tartakovsky, D. M., 2016. The Handbook of groundwater engineering, 3rd Edition. CRC Press.

Danckwerts, P. V., 1952. The definition and measurement of some characteristics of mixtures. Applied Scientific Research 3 (4), 279–296.

de Anna, P., Le Borgne, T., Dentz, M., Tartakovsky, A. M., Bolster, D., Davy, P., 2013. Flow Intermittency, Dispersion, and Correlated Continuous Time Random Walks in Porous Media. Physical Review Letters 110 (18), 184502.

de Hoog, F. R., Knight, J. H., Stokes, A. N., 1982. An Improved Method for Numerical Inversion of Laplace Transforms. SIAM Journal on Scientific and Statistical Computing 3 (3), 357–366.

de. Marsily, G., 1986. Quantitative hydrogeology : groundwater hydrology for engineers. Academic Press.

Degueldre, C., Pleinert, H., Maguire, P., Lehman, E., Missimer, J., Hammer, J., Leenders, K., Böck, H., Townsend, D., 1996. Porosity and pathway determination in crystalline rock by positron emission tomography and neutron radiography. Earth and Planetary Science Letters 140 (1-4), 213–225.

Delgado, J., 2007. Longitudinal and transverse dispersion in porous media. Chemical Engineering Research and Design 85 (9), 1245–1252.

Deng, H., Fitts, J. P., Peters, C. A., 2016. Quantifying fracture geometry with X-ray tomography: Technique of Iterative Local Thresholding (TILT) for 3D image segmentation. Computational Geosciences 20 (1), 231–244.

Deng, J., Jiang, X., Zhang, X., Hu, W., Crawford, J. W., 2008. Continuous time random walk model better describes the tailing of atrazine transport in soil. Chemosphere 71 (11), 2150–2157.

Dentz, M., Carrera, J., Hidalgo, J., 2017. Upscaling and Scale Effects. Springer, Dordrecht, pp. 187–248.

Dentz, M., Cortis, A., Scher, H., Berkowitz, B., 2004. Time behavior of solute transport in heterogeneous media: transition from anomalous to normal transport. Advances in Water Resources 27 (2), 155–173.

Dentz, M., Icardi, M., Hidalgo, J. J., 2018. Mechanisms of dispersion in a porous medium. Journal of Fluid Mechanics 841, 851–882.

Dentz, M., Le Borgne, T., Englert, A., Bijeljic, B., 2011. Mixing, spreading and reaction in heterogeneous media: A brief review. Journal of Contaminant Hydrology 120-121, 1–17.

Dogan, M., Moysey, S. M. J., Ramakers, R. M., DeVol, T. A., Beekman, F. J., Groen, H. C., Powell, B. A., 2017. High-Resolution 4D Preclinical Single-Photon Emission Computed Tomography/X-ray Computed Tomography Imaging of Technetium Transport within a Heterogeneous Porous Media. Environmental Science & Technology 51 (5), 2864–2870.

Donaldson, E. C., Kendall, R. F., Manning, F. S., 1976. Dispersion and Tortuosity in Sandstones. In: SPE Annual Fall Technical Conference and Exhibition. Society of Petroleum Engineers.

Dullien, F. A. L., 1992. Porous media : fluid transport and pore structure. Academic Press.

Fatt, I., 1956. The network model of porous media III. Dynamic properties of networks with tube radius distribution. Petroleum Transactions, AIME 207, 144–181.

Fernø, M. A., Gauteplass, J., Hauge, L. P., Abell, G. E., Adamsen, T. C. H., Graue, A., 2015a. Combined positron emission tomography and computed tomography to visualize and quantify fluid flow in sedimentary rocks. Water Resources Research 51 (9), 7811–7819.

Fernø, M. A., Hauge, L. P., Uno Rognmo, A., Gauteplass, J., Graue, A., 2015b. Flow visualization of CO_2 in tight shale formations at reservoir conditions. Geophysical Research Letters 42 (18), 7414–7419.

Fetter, C. W. C. W., 1999. Contaminant hydrogeology, 2nd Edition. Prentice Hall, Upper Saddle River, NJ.

Fogler, H. S., 1999. Elements of chemical reaction engineering. Prentice Hall PTR.

Fourar, M., Radilla, G., 2009. Non-Fickian Description of Tracer Transport Through Heterogeneous Porous Media. Transport in Porous Media 80 (3), 561–579.

Ginn, T., 2001. Stochasticconvective transport with nonlinear reactions and mixing: finite streamtube ensemble formulation for multicomponent reaction systems with intra-streamtube dispersion. Journal of Contaminant Hydrology 47 (1), 1–28.

Ginn, T. R., Simmons, C. S., Wood, B. D., 1995. Stochastic-Convective Transport with Nonlinear Reaction: Biodegradation With Microbial Growth. Water Resources Research 31 (11), 2689–2700.

Gist, G. A., Thompson, A. H., Katz, A. J., Higgins, R. L., 1990. Hydrodynamic dispersion and pore geometry in consolidated rock. Physics of Fluids A: Fluid Dynamics 2 (9), 1533–1544.

Gjetvaj, F., Russian, A., Gouze, P., Dentz, M., 2015. Dual control of flow field heterogeneity and immobile porosity on non-Fickian transport in Berea sandstone. Water Resources Research 51 (10), 8273–8293.

Gladden, L. F., Mitchell, J., 2011. Measuring adsorption, diffusion and flow in chemical engineering: applications of magnetic resonance to porous media. New Journal of Physics 13 (3), 035001.

Goethals, P., Volkaert, A., Jacobs, P., Roels, S., Carmeliet, J., 2009. Comparison of Positron Emission Tomography and X-ray radiography for studies of physical processes in sandstone. Engineering geology 103 (3), 134–138.

Goldsack, D. E., Franchetto, R., 1977. The viscosity of concentrated electrolyte solutions. I. Concentration dependence at fixed temperature. Canadian Journal of Chemistry 55 (6), 1062–1072.

Gouze, P., Le Borgne, T., Leprovost, R., Lods, G., Poidras, T., Pezard, P., 2008a. Non-Fickian dispersion in porous media: 1. Multiscale measurements using single-well injection withdrawal tracer tests. Water Resources Research 44 (6).

Gouze, P., Melean, Y., Le Borgne, T., Dentz, M., Carrera, J., 2008b. Non-Fickian dispersion in porous media explained by heterogeneous microscale matrix diffusion. Water Resources Research 44 (11).

Grane, F., 1961. Measurements of Transverse Dispersion in Granular Media. Journal of Chemical & Engineering Data 6 (2), 283–287.

Gründig, M., Richter, M., Seese, A., Sabri, O., 2007. Tomographic radiotracer studies of the spatial distribution of heterogeneous geochemical transport processes. Applied Geochemistry 22 (11), 2334–2343.

Guedes de Carvalho, J., Delgado, J., 2005. Overall map and correlation of dispersion data for flow through granular packed beds. Chemical Engineering Science 60 (2), 365–375.

Haberer, C. M., Rolle, M., Liu, S., Cirpka, O. A., Grathwohl, P., 2011. A high-resolution non-invasive approach to quantify oxygen transport across the capillary fringe and within the underlying groundwater. Journal of Contaminant Hydrology 122 (1-4), 26–39.

Haggerty, R., Gorelick, S. M., 1995. Multiplerate mass transfer for modeling diffusion and surface reactions in media with porescale heterogeneity. Water Resources Research 31 (10), 2383–2400.

Han, N.-W., Bhakta, J., Carbonell, R. G., 1985. Longitudinal and lateral dispersion in packed beds: Effect of column length and particle size distribution. AIChE Journal 31 (2), 277–288.

Hansen, S. K., Berkowitz, B., Vesselinov, V. V., O'Malley, D., Karra, S., 2016. Push-pull tracer tests: Their information content and use for characterizing non-Fickian, mobile-immobile behavior. Water Resources Research 52 (12), 9565–9585.

Heidari, P., Li, L., 2014. Solute transport in low-heterogeneity sandboxes: The role of correlation length and permeability variance. Water Resources Research 50 (10), 8240–8264.

Herzig, J. P., Leclerc, D. M., Goff, P. L., 1970. Flow of Suspensions through Porous Media - Application to Deep Filtration. Industrial & Engineering Chemistry 62 (5), 8–35.

Hiby, J. W., 1962. Longitudinal and transverse mixing during single-phase flow through granular beds. Interaction between Fluids & Particles, 312–325.

Hidajat, I., Mohanty, K., Flaum, M., Hirasaki, G., 2004. Study of Vuggy Carbonates Using NMR and X-Ray CT Scanning. SPE Reservoir Evaluation & Engineering 7 (05), 365–377.

Hill, R., 1963. Elastic properties of reinforced solids: Some theoretical principles. Journal of the Mechanics and Physics of Solids 11 (5), 357–372.

Hirono, T., Takahashi, M., Nakashima, S., 2003. In situ visualization of fluid flow image within deformed rock by X-ray CT. Engineering Geology 70 (1-2), 37–46.

Hoff, W. D., Wilson, M. A., Benton, D. M., Hawkesworth, M. R., Parker, D. J., Flowles, P., 1996. The use of positron emission tomography to monitor unsaturated water flow within porous construction materials. Journal of Materials Science Letters 15 (13), 1101–1104.

Honari, A., Bijeljic, B., Johns, M. L., May, E. F., 2015. Enhanced gas recovery with CO_2 sequestration: The effect of medium heterogeneity on the dispersion of supercritical CH_4-CO_2. International Journal of Greenhouse Gas Control 39, 39–50.

Honari, A., Hughes, T. J., Fridjonsson, E. O., Johns, M. L., May, E. F., 2013. Dispersion of supercritical CO_2 and CH_4 in consolidated porous media for enhanced gas recovery simulations. International Journal of Greenhouse Gas Control 19, 234–242.

Honari, A., Zecca, M., Vogt, S. J., Iglauer, S., Bijeljic, B., Johns, M. L., May, E. F., 2016. The impact of residual water on CH_4-CO_2 dispersion in consolidated rock cores. International Journal of Greenhouse Gas Control 50, 100–111.

Hornung, U., 1997. Homogenization and Porous Media. Springer New York.

Hosseinzadeh Hejazi, S. A., Estupiñan Perez, L., Rajendran, A., Kuznicki, S., 2017. Cycle Development and Process Optimization of High-Purity Oxygen Production Using Silver-Exchanged Titanosilicates. Industrial & Engineering Chemistry Research 56 (19), 5679–5691.

Hu, Y., Armstrong, R. T., Lee, B., Shikhov, I., Mostaghimi, P., 2017. Analysing flow in rocks by combined positron emission tomography and computed tomography imaging. Society of Core Analysts 82, 1–9.

Hudson, H., Larkin, R., 1994. Accelerated image reconstruction using ordered subsets of projection data. IEEE Transactions on Medical Imaging 13 (4), 601–609.

Hulin, J. P., Plona, T. J., 1989. Echo" tracer dispersion in porous media. Physics of Fluids A: Fluid Dynamics 1 (8), 1341–1347.

Ilankoon, I., Cole, K., Neethling, S., 2013. Measuring hydrodynamic dispersion coefficients in unsaturated packed beds: Comparison of PEPT with conventional tracer tests. Chemical Engineering Science 89, 152–157.

Kandhai, D., Hlushkou, D., Hoekstra, A. G., Sloot, P. M. A., Van As, H., Tallarek, U., 2002. Influence of Stagnant Zones on Transient and Asymptotic Dispersion in Macroscopically Homogeneous Porous Media. Physical Review Letters 88 (23), 234501.

Khalili, A., Basu, A. J., Pietrzyk, U., 1998. Flow visualization in porous media via positron emission tomography. Physics of Fluids 10 (4), 1031–1033.

Kinahan, P. E., Defrise, M., Clackdoyle, R., 2004. Analytic Image Reconstruction Methods. Emission Tomography, 421–442.

Kitanidis, P., 2017. Teaching and communicating dispersion in hydrogeology, with emphasis on the applicability of the Fickian model. Advances in Water Resources 106, 11–23.

Kitanidis, P. K., 1994. The concept of the Dilution Index. Water Resources Research 30 (7), 2011–2026.

Kitanidis, P. K., McCarty, P. L., Abriola, L. M., 2012. Delivery and mixing in the subsurface : processes and design principles for in situ remediation. Springer New York.

Knox, J. H., 1999. Band dispersion in chromatography - a new view of A-term dispersion. Journal of Chromatography A 831 (1), 3–15.

Kosakowski, G., Berkowitz, B., Scher, H., 2001. Analysis of field observations of tracer transport in a fractured till. Journal of Contaminant Hydrology 47 (1), 29–51.

Krause, M., Krevor, S., Benson, S. M., 2013. A Procedure for the Accurate Determination of Sub-Core Scale Permeability Distributions with Error Quantification. Transport in Porous Media 98 (3), 565–588.

Krause, M. H., Benson, S. M., 2015. Accurate determination of characteristic relative permeability curves. Advances in Water Resources 83, 376–388.

Krause, M. H., Perrin, J.-C., Benson, S. M., 2009. Modeling Permeability Distributions in a Sandstone Core for History Matching Coreflood Experiments. In: SPE International Conference on CO2 Capture, Storage, and Utilization. Society of Petroleum Engineers.

Kukukova, A., Aubin, J., Kresta, S. M., 2009. A new definition of mixing and segregation: Three dimensions of a key process variable. Chemical Engineering Research and Design 87 (4), 633–647.

Kulenkampff, J., Gründig, M., Richter, M., Enzmann, F., 2008. Evaluation of positron-emission-tomography for visualisation of migration processes in geomaterials. Physics and Chemistry of the Earth 33 (14), 937–942.

Kulenkampff, J., Gründig, M., Zakhnini, A., Gerasch, R., Lippmann-Pipke, J., 2015. Process tomography of diffusion, using PET, to evaluate anisotropy and heterogeneity. Clay Minerals 50 (3), 369–375.

Kulenkampff, J., Gründig, M., Zakhnini, A., Lippmann-Pipke, J., 2016. Geoscientific process monitoring with positron emission tomography (GeoPET). Solid Earth 7, 1217–1231.

Kulenkampff, J., Stoll, M., Gründig, M., Mansel, A., Lippmann-Pipke, J., Kersten, M., 2018. Time-lapse 3D imaging by positron emission tomography of Cu mobilized in a soil column by the herbicide MCPA. Scientific Reports 8 (1), 7091.

Kurotori, T., Zahasky, C., Hosseinzadeh Hejazi, S. A., Shah, S. M., Benson, S. M., Pini, R., 2019. Measuring, imaging and modelling solute transport in a microporous limestone. Chemical Engineering Science 196, 366–383.

Lai, J., Wang, G., Fan, Z., Chen, J., Qin, Z., Xiao, C., Wang, S., Fan, X., 2017. Three-dimensional quantitative fracture analysis of tight gas sandstones using industrial computed tomography. Scientific Reports 7 (1), 1825.

Lai, P., Moulton, K., Krevor, S., 2015. Pore-scale heterogeneity in the mineral distribution and reactive surface area of porous rocks. Chemical Geology 411, 260–273.

Lasaga, A. C., 2014. Kinetic theory in the earth sciences. Princeton University Press.

Le Borgne, T., Dentz, M., Bolster, D., Carrera, J., de Dreuzy, J.-R., Davy, P., 2010. Non-Fickian mixing: Temporal evolution of the scalar dissipation rate in heterogeneous porous media. Advances in Water Resources 33 (12), 1468–1475.

Le Borgne, T., Dentz, M., Davy, P., Bolster, D., Carrera, J., de Dreuzy, J.-R., Bour, O., 2011. Persistence of incomplete mixing: A key to anomalous transport. Physical Review E 84 (1), 15301.

Le Borgne, T., Dentz, M., Villermaux, E., 2015. The lamellar description of mixing in porous media. Journal of Fluid Mechanics 770, 458–498.

Le Borgne, T., Ginn, T. R., Dentz, M., 2014. Impact of fluid deformation on mixing-induced chemical reactions in heterogeneous flows. Geophysical Research Letters 41 (22), 7898–7906.

Legatski, M. W., Katz, D. L., 1967. Dispersion Coefficients for Gases Flowing in Consolidated Porous Media. Society of Petroleum Engineers Journal 7 (01), 43–53.

Leroy, C., Hulin, J., Lenormand, R., 1992. Tracer dispersion in stratified porous media: influence of transverse dispersion and gravity. Journal of Contaminant Hydrology 11 (1-2), 51–68.

Levin, C. S., Hoffman, E. J., 1999. Calculation of positron range and its effect on the fundamental limit of positron emission tomography system spatial resolution. Physics in Medicine and Biology 44 (3), 781–799.

Levy, M., Berkowitz, B., 2003. Measurement and analysis of non-Fickian dispersion in heterogeneous porous media. Journal of Contaminant Hydrology 64 (3-4), 203–226.

Lippmann-Pipke, J., Gerasch, R., Schikora, J., Kulenkampff, J., 2017. Benchmarking PET for geoscientific applications: 3D quantitative diffusion coefficient determination in clay rock. Computers & Geosciences 101, 21–27.

Liu, G., Zheng, C., Tick, G. R., Butler, J. J., Gorelick, S. M., 2010. Relative importance of dispersion and rate-limited mass transfer in highly heterogeneous porous media: Analysis of a new tracer test at the Macrodispersion Experiment (MADE) site. Water Resources Research 46 (3).

Liyanage, R., Cen, J., Krevor, S., Crawshaw, J. P., Pini, R., 2019. Multidimensional Observations of Dissolution-Driven Convection in Simple Porous Media Using X-ray CT Scanning. Transport in Porous Media 126 (2), 355–378.

Lucia, F., 1983. Petrophysical Parameters Estimated From Visual Descriptions of Carbonate Rocks: A Field Classification of Carbonate Pore Space. Journal of Petroleum Technology 35 (03), 629–637.

Maclay, R. W., Land, L. F., 1988. Simulation of flow in the Edwards Aquifer, San Antonio Region, Texas and refinement of storage and flow concepts. U.S. Government Printing Office.

Maguire, R., Missimer, J., Emert, F., Townsend, D., Dollinger, H., Leenders, K., 1997. Positron emission tomography of large rock samples using a multiring PET instrument. IEEE Transactions on Nuclear Science 44 (1), 26–30.

Martinez, Z., 2016. Pore network connectivity in microbialites of the Green River Formation (Wyoming, USA): analogs for petroleum reservoir potential.

Mathur, S. M., 2008. Elements of geology. PHI Learning Pvt. Ltd.

Maucec, M., Dusterhoft, R., Rickman, R., Gibson, R., Buffler, A., Stankiewica, M., van Heerden, M., 2013. Dynamic Imaging of Fluid Mobility in Low-Permeability Rocks Using High-Resolution Positron Emission Tomography. In: SPE Asia Pacific Oil and Gas Conference and Exhibition. Society of Petroleum Engineers.

Menke, H. P., Bijeljic, B., Andrew, M. G., Blunt, M. J., 2015. Dynamic Three-Dimensional Pore-Scale Imaging of Reaction in a Carbonate at Reservoir Conditions. Environmental Science & Technology 49 (7), 4407–4414.

Metzler, R., Klafter, J., 2000. The random walk's guide to anomalous diffusion: a fractional dynamics approach. Physics Reports 339 (1), 1–77.

Montemagno, C., Pyrak-Nolte, L., 1999. Fracture network versus single fractures: Measurement of fracture geometry with X-ray tomography. Physics and Chemistry of the Earth, Part A: Solid Earth and Geodesy 24 (7), 575–579.

Moses, W. W., 2011. Fundamental limits of spatial resolution in PET. Nuclear Instruments and Methods in Physics Research Section A: Accelerators, Spectrometers, Detectors and Associated Equipment 648, S236–S240.

Muggeridge, A., Cockin, A., Webb, K., Frampton, H., Collins, I., Moulds, T., Salino, P., 2013. Recovery rates, enhanced oil recovery and technological limits. Philosophical Transactions of the Royal Society A: Mathematical, Physical and Engineering Sciences 372 (2006), 20120320.

Muniruzzaman, M., Haberer, C. M., Grathwohl, P., Rolle, M., 2014. Multicomponent ionic dispersion during transport of electrolytes in heterogeneous porous media: Experiments and model-based interpretation. Geochimica et Cosmochimica Acta 141, 656–669.

Muniruzzaman, M., Rolle, M., 2017. Experimental investigation of the impact of compound-specific dispersion and electrostatic interactions on transient transport and solute breakthrough. Water Resources Research 53 (2), 1189–1209.

Murphy, W. F., Roberts, J. N., Yale, D., Winkler, K. W., 1984. Centimeter scale heterogeneities and microstratifaction in sedimentary rocks. Geophysical Research Letters 11 (8), 697–700.

Nestle, N., Baumann, T., Wunderlich, A., Niessner, R., 2003. MRI observation of heavy metal transport in aquifer matrices down to sub-mg quantities. Magnetic Resonance Imaging 21 (3-4), 345–349.

Neuman, S. P., Tartakovsky, D. M., 2009. Perspective on theories of non-Fickian transport in heterogeneous media. Advances in Water Resources 32 (5), 670–680.

Ogilvie, S. R., Orribo, J. M., Glover, P. W. J., 2001. The influence of deformation bands upon fluid flow using profile permeametry and positron emission tomography. Geophysical Research Letters 28 (1), 61–64.

Ott, H., Pentland, C. H., Oedai, S., 2015. CO_2-brine displacement in heterogeneous carbonates. International Journal of Greenhouse Gas Control 33, 135–144.

Pan, C., Hilpert, M., Miller, C. T., 2004. Lattice-Boltzmann simulation of two-phase flow in porous media. Water Resources Research 40 (1).

Pedrotti, F. L., Pedrotti, L. S., Pedrotti, L. M., 2007. Introduction to optics. Pearson Prentice Hall.

Peksa, A. E., Wolf, K.-H. A., Slob, E. C., Chmura, Ł., Zitha, P. L., 2017. Original and pyrometamorphical altered Bentheimer sandstone; petrophysical properties, surface and dielectric behavior. Journal of Petroleum Science and Engineering 149, 270–280.

Perkins, T., Johnston, O., 1963. A Review of Diffusion and Dispersion in Porous Media. Society of Petroleum Engineers Journal 3 (01), 70–84.

Perrin, J.-C., Benson, S., 2010. An Experimental Study on the Influence of Sub-Core Scale Heterogeneities on CO_2 Distribution in Reservoir Rocks. Transport in Porous Media 82 (1), 93–109.

Perrodon, A., 1983. Dynamics of oil and gas accumulations. Elf Aquitaine.

Pfankuch, H., 1963. Contribution a l'étude des deplacements de fluides miscibles dans un milieu poreaux, Ins. Francais du Petrole, Paris, 54.

Pini, R., Benson, S. M., 2013. Simultaneous determination of capillary pressure and relative permeability curves from core-flooding experiments with various fluid pairs. Water Resources Research 49 (6), 3516–3530.

Pini, R., Krevor, S., 2019. Laboratory Studies to Understand the Controls on Flow and Transport for CO_2 Storage. Science of Carbon Storage in Deep Saline Formations, 145–180.

Pini, R., Krevor, S. C., Benson, S. M., 2012. Capillary pressure and heterogeneity for the CO_2/water system in sandstone rocks at reservoir conditions. Advances in Water Resources 38, 48–59.

Pini, R., Madonna, C., 2016. Moving across scales: a quantitative assessment of X-ray CT to measure the porosity of rocks. Journal of Porous Materials 23 (2), 325–338.

Pini, R., Vandehey, N. T., Druhan, J., O'Neil, J. P., Benson, S. M., 2016. Quantifying solute spreading and mixing in reservoir rocks using 3-D PET imaging. Journal of Fluid Mechanics 796, 558–587.

Rajagopalan, A. K., Avila, A. M., Rajendran, A., 2016. Do adsorbent screening metrics predict process performance? A process optimisation based study for post-combustion capture of CO2. International Journal of Greenhouse Gas Control 46, 76–85.

Ramstad, T., Idowu, N., Nardi, C., Øren, P.-E., 2012. Relative Permeability Calculations from Two-Phase Flow Simulations Directly on Digital Images of Porous Rocks. Transport in Porous Media 94 (2), 487–504.

Reeves, A. D., Chudek, J. A., 2001. Nuclear magnetic resonance imaging (MRI) of diesel oil migration in estuarine sediment samples. Journal of Industrial Microbiology and Biotechnology 26 (1-2), 77–82.

Reynolds, C. A., Krevor, S., 2015. Characterizing flow behavior for gas injection: Relative permeability of CO_2-brine and N_2-water in heterogeneous rocks. Water Resources Research 51 (12), 9464–9489.

Rolle, M., Chiogna, G., Hochstetler, D. L., Kitanidis, P. K., 2013. On the importance of diffusion and compound-specific mixing for groundwater transport: An investigation from pore to field scale. Journal of Contaminant Hydrology 153, 51–68.

Rolle, M., Eberhardt, C., Chiogna, G., Cirpka, O. A., Grathwohl, P., 2009. Enhancement of dilution and transverse reactive mixing in porous media: Experiments and model-based interpretation. Journal of Contaminant Hydrology 110 (3-4), 130–142.

Rolle, M., Hochstetler, D., Chiogna, G., Kitanidis, P. K., Grathwohl, P., 2012. Experimental Investigation and Pore-Scale Modeling Interpretation of Compound-Specific Transverse Dispersion in Porous Media. Transport in Porous Media 93 (3), 347–362.

Rolle, M., Kitanidis, P. K., 2014. Effects of compound-specific dilution on transient transport and solute breakthrough: A pore-scale analysis. Advances in Water Resources 71, 186–199.

Rolle, M., Sprocati, R., Masi, M., Jin, B., Muniruzzaman, M., 2018. Nernst-Planck-based Description of Transport, Coulombic Interactions, and Geochemical Reactions in Porous Media: Modeling Approach and Benchmark Experiments. Water Resources Research 54 (4), 3176–3195.

Ruthven, D. M. D. M., 1984. Principles of adsorption and adsorption processes. Wiley.

Saffman, P. G., 1959. A theory of dispersion in a porous medium. Journal of Fluid Mechanics 6 (03), 321.

Sahimi, M., 2011. Flow and Transport in Porous Media and Fractured Rock: From Classical Methods to Modern Approaches. Wiley.

Sahimi, M., Hughes, B. D., Scriven, L. E., Davis, H. T., 1986. Dispersion in flow through porous media—I. One-phase flow. Chemical Engineering Science 41 (8), 2103–2122.

Salles, J., Thovert, J., Delannay, R., Prevors, L., Auriault, J., Adler, P. M., 1993. Taylor dispersion in porous media. Determination of the dispersion tensor. Physics of Fluids A: Fluid Dynamics 5 (10), 2348–2376.

Sarma, D. D., 2009. Geostatistics with Applications in Earth Sciences. Springer Netherlands.

Schroth, M., Istok, J., Haggerty, R., 2000. In situ evaluation of solute retardation using single-well pushpull tests. Advances in Water Resources 24 (1), 105–117.

Seymour, J. D., Callaghan, P. T., 1997. Generalized approach to NMR analysis of flow and dispersion in porous media. AIChE Journal 43 (8), 2096–2111.

Shafer, J., 2013. Recent advances in core analysis. Petrophysics 54 (06), 554–579.

Shakas, A., Linde, N., Baron, L., Bochet, O., Bour, O., Le Borgne, T., 2016. Hydrogeophysical characterization of transport processes in fractured rock by combining push-pull and single-hole ground penetrating radar experiments. Water Resources Research 52 (2), 938–953.

Silliman, S. E., Simpson, E. S., 1987. Laboratory evidence of the scale effect in dispersion of solutes in porous media. Water Resources Research 23 (8), 1667–1673.

Simmons, C. S., Ginn, T. R., Wood, B. D., 1995. Stochastic-Convective Transport with Nonlinear Reaction: Mathematical Framework. Water Resources Research 31 (11), 2675–2688.

Singer, P., Mitchell, J., Fordham, E., 2016. Characterizing dispersivity and stagnation in porous media using NMR flow propagators. Journal of Magnetic Resonance 270, 98–107.

Slichter, C. S., 1905. Field measurements of the rate of movement of underground waters. Tech. rep.

Spence, A. P., Watkins, R. W., 1980. The Effect Of Microscopic Core Heterogeneity On Miscible Flood Residual Oil Saturation. In: SPE Annual Technical Conference and Exhibition. Society of Petroleum Engineers.

Sposito, G., Skipper, N. T., Sutton, R., Park, S., Soper, A. K., Greathouse, J. A., 1999. Surface geochemistry of the clay minerals. Proceedings of the National Academy of Sciences of the United States of America 96 (7), 3358–64.

Steefel, C. I., Maher, K., 2009. Fluid-Rock Interaction: A Reactive Transport Approach. Reviews in Mineralogy and Geochemistry 70 (1), 485–532.

Tartakovsky, A. M., Tartakovsky, D. M., Meakin, P., 2008. Stochastic Langevin Model for Flow and Transport in Porous Media. Physical Review Letters 101 (4), 044502.

Taylor, G. I., 1953. Dispersion of soluble matter in solvent flowing slowly through a tube. Proceedings of the Royal Society of London. Series A. Mathematical and Physical Sciences 219 (1137), 186–203.

Thorpe, C. L., Williams, H. A., Boothman, C., Lloyd, J. R., Morris, K., 2019. Positron emission tomography to visualise in-situ microbial metabolism in natural sediments. Applied Radiation and Isotopes 144, 104–110.

Toshiya, O., Hiroshi, O., Takao, N., 2000. Early Water Breakthrough: X-ray CT Visualizes How It Happens in Oil-Wet Cores. In: SPE Asia Pacific Conference on Integrated Modelling for Asset Management. Society of Petroleum Engineers.

Trevisan, L., Pini, R., Cihan, A., Birkholzer, J. T., Zhou, Q., González-Nicolás, A., Illangasekare, T. H., 2017. Imaging and quantification of spreading and trapping of carbon dioxide in saline aquifers using meter-scale laboratory experiments. Water Resources Research 53 (1), 485–502.

Trevisan, L., Pini, R., Cihan, A., Birkholzer, J. T., Zhou, Q., Illangasekare, T. H., 2015. Experimental analysis of spatial correlation effects on capillary trapping of supercritical CO_2 at the intermediate laboratory scale in heterogeneous porous media. Water Resources Research 51 (11), 8791–8805.

Turkington, T. G., 2011. PET Imaging Basics. In: Clinical PET-CT in Radiology. Springer New York, New York, NY, pp. 21–28.

Valvatne, P. H., Blunt, M. J., 2004. Predictive pore-scale modeling of two-phase flow in mixed wet media. Water Resources Research 40 (7).

Vasco, D. W., Pride, S. R., Zahasky, C., Benson, S. M., 2018. Calculating Trajectories Associated With Solute Transport in a Heterogeneous Medium. Water Resources Research 54 (9), 6890–6908.

Vogler, D., Ostvar, S., Paustian, R., Wood, B. D., 2018. A hierarchy of models for simulating experimental results from a 3D heterogeneous porous medium. Advances in Water Resources 114, 149–163.

Wadell, H., 1935. Volume, Shape, and Roundness of Quartz Particles.

Wakao, N., Funazkri, T., 1978. Effect of fluid dispersion coefficients on particle-to-fluid mass transfer coefficients in packed beds: Correlation of sherwood numbers. Chemical Engineering Science 33 (10), 1375–1384.

Walsh, M., Withjack, E., 1994. On Some Remarkable Observations of Laboratory Dispersion Using Computed Tomography (CT). Journal of Canadian Petroleum Technology 33 (09).

Whitaker, S., 1999. The Method of Volume Averaging. Vol. 13 of Theory and Applications of Transport in Porous Media. Springer Netherlands, Dordrecht.

Xiong, Q., Baychev, T. G., Jivkov, A. P., 2016. Review of pore network modelling of porous media: Experimental characterisations, network constructions and applications to reactive transport. Journal of Contaminant Hydrology 192, 101–117.

Ye, Y., Chiogna, G., Cirpka, O., Grathwohl, P., Rolle, M., 2015. Experimental investigation of compound-specific dilution of solute plumes in saturated porous media: 2-D vs. 3-D flow-through systems. Journal of Contaminant Hydrology 172, 33–47.

Yellig, W., Baker, L., 1981. Factors Affecting Miscible Flooding Dispersion Coefficients. Journal of Canadian Petroleum Technology 20 (04).

Zahasky, C., Benson, S. M., 2016. Phase saturation validation and tracer transport quantification using microPET in a heterogeneous sandstone core. In: International Symposium of the Society of Core Analysts.

Zahasky, C., Benson, S. M., 2018. Micro-positron emission tomography for measuring sub-core scale single and multiphase transport parameters in porous media. Advances in Water Resources 115, 1–16.

Zahasky, C., Kurotori, T., Pini, R., Benson, S. M., 2019. Positron emission tomography in water resources and subsurface energy resources engineering research. Advances in Water Resources 127, 39–52.

Zahasky, C., Thomas, D., Matter, J., Maher, K., Benson, S. M., 2018. Multimodal imaging and stochastic percolation simulation for improved quantification of effective porosity and surface area in vesicular basalt. Advances in Water Resources 121, 235–244.

Zecca, M., Vogt, S. J., Honari, A., Xiao, G., Fridjonsson, E. O., May, E. F., Johns, M. L., 2017. Quantitative dependence of CH_4-CO_2 dispersion on immobile water fraction. AIChE Journal 63 (11), 5159–5168.

Zhao, Y., Song, Y., Liu, Y., Liang, H., Dou, B., 2011. Visualization and Measurement of CO_2 Flooding in Porous Media Using MRI. Industrial & Engineering Chemistry Research 50 (8), 4707–4715.

Zhu, W. C., Liu, J., Elsworth, D., Polak, A., Grader, A., Sheng, J. C., Liu, J. X., 2007. Tracer transport in a fractured chalk: X-ray CT characterization and digital-image-based (DIB) simulation. Transport in Porous Media 70 (1), 25–42.

Zinn, B., Meigs, L. C., Harvey, C. F., Haggerty, R., Peplinski, W. J., von Schwerin, C. F., 2004. Experimental Visualization of Solute Transport and Mass Transfer Processes in Two-Dimensional Conductivity Fields with Connected Regions of High Conductivity. Environmental Science & Technology 38 (14), 3916–3926.